

**Project Report**  
**MTP-20**

# **Modeling of UHF and VHF Bistatic Scattering from WSMR Terrain**

**B.A. Francis**

**11 June 1999**

---

**Lincoln Laboratory**

**MASSACHUSETTS INSTITUTE OF TECHNOLOGY**

*LEXINGTON, MASSACHUSETTS*



---

Prepared for the Defense Advanced Research Projects Agency under  
Air Force Contract F19628-95-C-0002.

Approved for public release; distribution is unlimited.

**DTIC QUALITY INSPECTED 4**

**19990617 133**


This report is based on studies performed at Lincoln Laboratory, a center for research operated by Massachusetts Institute of Technology. The work was sponsored by the Defense Advanced Research Projects Agency under Air Force Contract F19628-95-C-0002.

This report may be reproduced to satisfy needs of U.S. Government agencies.

The ESC Public Affairs Office has reviewed this report, and it is releasable to the National Technical Information Service, where it will be available to the general public, including foreign nationals.

This project report has been reviewed and is approved for publication.

FOR THE COMMANDER

  
Gary Tutungian  
Administrative Contracting Officer  
Contracted Support Management

Non-Lincoln Receipts

PLEASE DO NOT RETURN

Permission is given to destroy this document  
when it is no longer needed.

MASSACHUSETTS INSTITUTE OF TECHNOLOGY  
LINCOLN LABORATORY

**MODELING OF UHF AND VHF BISTATIC SCATTERING  
FROM WSMR TERRAIN**

*B.A. FRANCIS  
Subcontractor  
Group 103*

PROJECT REPORT MTP-20

11 JUNE 1999

Approved for public release; distribution is unlimited.

LEXINGTON

MASSACHUSETTS

## ABSTRACT

Analysis was performed on bistatic radar data taken at White Sands Missile Range (WSMR) in support of the evaluation of Space-Time Adaptive Processing (STAP) algorithms and the characterization and modeling of monostatic and bistatic scattering. The analysis was confined to data from the flat semi-desert valley floor. Two sets of measurements were made, the first using the ground-based RSTER antenna for reception in combination with ground-based and airborne transmitters. The frequencies were at or near 435 MHz and included VV, VH, HV and HH polarization combinations. The second set of measurements used airborne platforms for both transmitting and receiving and were taken at 141 MHz and 431 MHz for VV, VH and HH polarization combinations. The two sets covered different spans of grazing angles. The data were analyzed to determine the bistatic scattering coefficient of the terrain as a function of out-of-plane angle and grazing angle, and to interpret the results in terms of the Generalized Lambertian Formula.

## **ACKNOWLEDGMENTS**

The analysis was conducted and this report prepared under the supervision of R. A. Gabel. The RSTER data were recorded under the supervision of G. W. Titi and R. A. Gabel. The air-to-air data were provided by Lisa Zurk as a by-product of her Propagation Experiment conducted in Sept./Oct. 1996.

# TABLE OF CONTENTS

	Abstract	iii
	Acknowledgments	v
	List of Illustrations	xi
	List of Tables	xvi
1.	INTRODUCTION	1
1.1	Presentation of Results	4
2.	SCATTERING MODELS	5
3.	STATISTICAL ANALYSIS METHODS	7
3.1	Determination of Noise Floor	7
3.2	Amplitude Distribution Functions	7
4.	SYSTEM CONFIGURATION	9
4.1	Configuration for Delay-Azimuth Measurements	9
4.2	Configuration for Delay-Doppler Measurements	11
5.	CALCULATION OF BISTATIC SCATTERING COEFFICIENT	13
5.1	Determination of Effective Scattering Area	13
6.	DATABASE	15
6.1	Bistatic Delay-Azimuth Data	15
6.2	Monostatic Delay-Azimuth Data	17
6.3	Bistatic Delay-Doppler Data	17
7.	DELAY-AZIMUTH DATA REDUCTION	19
7.1	RSTER Antenna Beamforming	19
7.2	Types of Modulation	20
7.3	Optimization of PN Pulse Compression	20
7.4	First Method for Optimizing PN Compression	21
7.5	Second Method for Optimizing PN Compression	22
7.6	Coherent Processing	22
7.7	Delay Tracking	24
8.	SYSTEM PARAMETERS FOR DELAY-AZIMUTH MEASUREMENTS	25
8.1	Transmitter Antenna Gain for Delay-Azimuth Measurements	25
8.2	Calculation of RSTER Receiver Antenna Gain	25
8.3	Measurement of Received Power	25
8.4	Measurement of RSTER Receiver Gain	25
8.5	Receiver Bandwidth	26
8.6	Receiver Equalization	26
8.7	Amplitude Calibration	26
8.8	Data Selection Criteria	27
9.	DELAY-DOPPLER DATA REDUCTION	29
9.1	Delay Tracking	29
9.2	Resolving Ambiguities in Delay-Doppler Processing	30

10.	SYSTEM PARAMETERS FOR DELAY-DOPPLER MEASUREMENTS	33
10.1	Operating Modes	33
10.2	Antenna Patterns for Delay-Doppler Measurements	33
10.3	Measurement of Receiver Gain	33
10.4	Verification of UHF System Parameters by Direct Signal Measurement	34
11.	WIDE-AREA DELAY-AZIMUTH VV-POL RESULTS	37
11.1	Database	37
11.2	VV-pol Ground-based Results from Socorro Peak	37
11.3	VV-pol Airborne Results from Socorro Peak	39
11.4	Ground-based and Airborne VV-pol Results from Salinas Peak	40
11.5	Ground-based and Airborne VV-pol Results from Sierra Blanca	40
11.6	Combined VV-pol Results	43
11.7	Monostatic VV-pol Results	47
11.8	Comparison of VV-pol Bistatic and Monostatic Results	50
12.	WIDE-AREA DELAY-AZIMUTH VH-POL RESULTS	51
12.1	Database	51
12.2	VH-pol Ground-based Results from Socorro Peak	51
12.3	VH-pol Airborne Results from Socorro Peak	51
12.4	Ground-based and Airborne VH-Pol Results from Salinas Peak	53
12.5	Ground-based and Airborne VH-Pol Results from Sierra Blanca	55
12.6	Combined VH-pol Results	55
13.	WIDE-AREA DELAY-AZIMUTH HH-POL RESULTS	59
13.1	Database	59
13.2	HH-pol Ground-based PCW Results from Socorro Peak	60
13.3	HH-pol Ground-based PN Results from Socorro Peak	62
13.4	Salina Peak Ground-based PCW Results	64
13.5	Salinas Peak Ground-based PN Results	67
13.6	Combined Bistatic HH-pol Results	70
13.7	Quasi-Monostatic HH-pol Results	72
13.8	Monostatic HH-pol Results	75
13.9	Comparison of HH-pol Quasi-Monostatic and True Monostatic Results	77
14.	WIDE-AREA DELAY-AZIMUTH HV-POL RESULTS	79
14.1	Database	79
14.2	Full Area	79
14.3	Limited Area	80
15.	DELAY-AZIMUTH RADIAL-FLIGHT RESULTS	83
15.1	Database	83
15.2	Fair Site	84
15.3	Harriet Site	86
15.4	Carrizozo	88
15.5	Comparison with Wide-Area Results	91

16.	DELAY-DOPPLER UHF VV-POL RESULTS	93
16.1	M3D21_1003 and M3E21_1003 Data	93
17.	DELAY-DOPPLER UHF HH-POL RESULTS	97
17.1	M3D21_1001 and M3E21_1001 Data	97
18.	DELAY-DOPPLER UHF VH-POL RESULTS	101
18.1	M3D21_1002 and M3E21_1002 Data	101
19.	COMBINED UHF VV-POL RESULTS	105
19.1	Full Area	105
19.2	Limited Area	106
20.	COMBINED UHF HH-POL RESULTS	109
20.1	Full Area	109
20.2	Limited Area	110
21.	COMBINED UHF VH-POL RESULTS	113
21.1	Full Area	113
21.2	Limited Area	113
22.	VHF VV-POL RESULTS	117
22.1	MOD318004	117
22.2	MOD318007	119
22.3	M3E22_1003	121
22.4	M3D22_1003	122
22.5	Combined VHF VV-pol Data	125
22.6	Comparison of VV-pol UHF and VHF Results	126
23.	VHF HH-POL RESULTS	129
23.1	MOD318002	129
23.2	M3E22_1001	131
23.3	MOD318005	133
23.4	M3D22_1001	135
23.5	Combined VHF HH-pol Data	137
23.6	Comparison of HH-pol UHF and VHF Data	138
24.	VHF VH-POL RESULTS	141
24.1	MOD318003	141
24.2	MOD318006	143
24.3	M3D22_1002	145
24.4	Combined VHF VH-pol Data	147
24.5	Comparison of VH-pol UHF and VHF Data	147
25.	STATISTICAL INDEPENDENCE WITH FREQUENCY VARIATION	151
25.1	Method	151
25.2	Results	151
26.	SUMMARY	153
26.1	Summary of Delay-Azimuth UHF Results	153



26.2	Summary of Combined Delay-Azimuth and Delay-Doppler UHF Results	155
26.3	Comparison of UHF Results	157
26.4	Comparison of UHF and VHF Results	157
26.5	Probable Error	158
27.	CONCLUSIONS	161
28.	APPENDIX	163
	REFERENCES	167

## LIST OF ILLUSTRATIONS

Figure 1.	TSI Threat Scenario	1
Figure 2.	Observed WSMR Terrain	2
Figure 3.	RSTER on North Oscura Peak	3
Figure 4.	RSTER antenna	9
Figure 5.	Little Frank antenna	10
Figure 6.	Lear Jet	11
Figure 7.	Cessna 421	11
Figure 8.	Beechcraft 90 King Air	12
Figure 9.	Site Locations	15
Figure 10.	RSTER Doppler Processing and Matched Filtering	23
Figure 11.	Typical Isodelay and Isodoppler Plot	30
Figure 12.	Measured Bistatic Scattering Coefficient, Socorro Peak, VV, PN	37
Figure 13.	Distribution of Bistatic Scattering Coefficient, Socorro Peak, VV, PCW	38
Figure 14.	Distribution of Bistatic Scattering Coefficients, Socorro Peak, VV, PN	38
Figure 15.	Distribution of Bistatic Scattering Coefficient, Socorro Peak, VV, PN, Airborne	39
Figure 16.	Distribution of Bistatic Scattering Coefficient, Socorro Peak, VV, PN, Limited Area	40
Figure 17.	Distribution of Bistatic Scattering Coefficient, Socorro Peak, VV, PN, Airborne, Limited Area	41
Figure 18.	Distribution of Bistatic Scattering Coefficient, Salinas Peak, VV, PN	41
Figure 19.	Distribution of Bistatic Scattering Coefficient, Salinas Peak, VV, PN, Airborne	42
Figure 20.	Distribution of Bistatic Scattering Coefficient, Sierra Blanca, VV, PN	42
Figure 21.	Distribution of Bistatic Scattering Coefficient, Sierra Blanca, VV, PN, Airborne	43
Figure 22.	Distribution of Bistatic Scattering Coefficient, VV	44
Figure 23.	Bistatic Scattering Coefficient vs. Product of Sines of Grazing Angles, VV	45
Figure 24.	Cumulative Amplitude Distribution, Bistatic, VV	45
Figure 25.	Distribution of Bistatic Scattering Coefficient, VV, Limited Area	46
Figure 26.	Cumulative Amplitude Distribution, Bistatic, VV, Limited Area	47
Figure 27.	Distribution of Monostatic Scattering Coefficient, VV	48
Figure 28.	Monostatic Scattering Coefficient vs. Squared Sine of Grazing Angle, VV	48
Figure 29.	Cumulative Amplitude Distribution, Monostatic, VV	49

Figure 30.	Cumulative Amplitude Distribution, Monostatic, VV, Limited Area	49
Figure 31.	Distribution of Bistatic Scattering Coefficient, Socorro Peak, VH, PCW	52
Figure 32.	Distribution of Bistatic Scattering Coefficient, Socorro Peak, VH, PN	52
Figure 33.	Distribution of Bistatic Scattering Coefficient, Socorro Peak, VH, PN, Airborne	53
Figure 34.	Distribution of Bistatic Scattering Coefficient, Salinas Peak, VH, PN	54
Figure 35.	Distribution of Bistatic Scattering Coefficient, Salinas Peak, VH, PN, Airborne	54
Figure 36.	Distribution of Bistatic Scattering Coefficient, Sierra Blanc, VH, PN	55
Figure 37.	Distribution of Bistatic Scattering Coefficient, VH	56
Figure 38.	Bistatic Scattering Coefficient vs. Product of Sines of Grazing Angles, VH	57
Figure 39.	Cumulative Amplitude Distribution, Bistatic, VH	57
Figure 40.	Cumulative Amplitude Distribution, Bistatic, VH, Limited Area	58
Figure 41.	RSTER-90 on North Oscura Peak	59
Figure 42.	Distribution of Bistatic Scattering Coefficient, Airborne, Socorro Peak, HH, PCW	60
Figure 43.	Bistatic Scattering Coefficient vs. Product of Sines of Grazing Angles, Airborne, Socorro Peak, HH, PCW	61
Figure 44.	Cumulative Amplitude Distribution, Bistatic, Airborne, Socorro Peak, HH, PCW	61
Figure 45.	Cumulative Amplitude Distribution, Bistatic, Airborne, Socorro Peak, HH, PCW, Limited Area	62
Figure 46.	Distribution of Bistatic Scattering Coefficient, Airborne, Socorro Peak, HH, PN	63
Figure 47.	Bistatic Scattering Coefficient vs. Product of Sines of Grazing Angles, Airborne, Socorro Peak, HH, PN	63
Figure 48.	Cumulative Amplitude Distribution, Bistatic, Airborne, Socorro Peak, HH, PN	64
Figure 49.	Cumulative Amplitude Distribution, Bistatic, Airborne, Socorro Peak, HH, PN, Limited Area	65
Figure 50.	Distribution of Bistatic Scattering Coefficient, Salinas Peak, HH, PCW	65
Figure 51.	Bistatic Scattering Coefficient vs. Product of Sines of Grazing Angles, HH, PCW	66
Figure 52.	Cumulative Amplitude Distribution, Bistatic, Salinas Peak, HH, PCW	66
Figure 53.	Cumulative Amplitude Distribution, Bistatic, Salinas Peak, HH, PCW, Limited Area	67
Figure 54.	Distribution of Bistatic Scattering Coefficient, Salinas Peak, HH, PN	68
Figure 55.	Bistatic Scattering Coefficient vs. Product of Sines of Grazing Angles, Salinas Peak, HH, PN	69
Figure 56.	Cumulative Amplitude Distribution, Bistatic, Salinas Peak, HH, PN	69
Figure 57.	Cumulative Amplitude Distribution, Bistatic, Salinas Peak, HH, PN, Limited Area	70
Figure 58.	Distribution of Bistatic Scattering Coefficient, HH	71

Figure 59.	Bistatic Scattering Coefficient vs. Product of Sines of Grazing Angles, HH	71
Figure 60.	Cumulative Amplitude Distribution, Bistatic, HH	72
Figure 61.	Cumulative Amplitude Distribution, Bistatic, HH, Limited Area	73
Figure 62.	Distribution of Quasi-Monostatic Scattering Coefficient, HH	73
Figure 63.	Quasi-Monostatic Scattering Coefficient vs. Squared Sine of Grazing Angle, HH	74
Figure 64.	Cumulative Amplitude Distribution, Quasi-Monostatic, HH	74
Figure 65.	Cumulative Amplitude Distribution, Quasi-Monostatic, HH, Limited Area	75
Figure 66.	Distribution of Monostatic Scattering Coefficient, HH	76
Figure 67.	Monostatic Scattering Coefficient vs. Squared Sine of Grazing Angle, HH	76
Figure 68.	Cumulative Amplitude Distribution, Monostatic, HH	77
Figure 69.	Cumulative Amplitude Distribution, Monostatic, HH, Limited Area	78
Figure 70.	Distribution of Bistatic Scattering Coefficient, HV	79
Figure 71.	Bistatic Scattering Coefficient vs. Product of Sines of Grazing Angles, HV	80
Figure 72.	Cumulative Amplitude Distribution, Bistatic, HV	81
Figure 73.	Cumulative Amplitude Distribution, Bistatic, HV, Limited Area	81
Figure 74.	Distribution of Bistatic Scattering Coefficient, Fair Site, VV	84
Figure 75.	Bistatic Scattering Coefficient vs. Product of Sines of Grazing Angles, Fair Site	85
Figure 76.	Cumulative Amplitude Distribution, Fair Site, VV	86
Figure 77.	Distribution of Bistatic Scattering Coefficient, Harriet Site, VV	87
Figure 78.	Bistatic Scattering Coefficient vs. Product of Sines of Grazing Angles, Harriet Site	88
Figure 79.	Cumulative Amplitude Distribution, Harriet Site, VV	88
Figure 80.	Distribution of Bistatic Scattering Coefficient, Carrizozo, VV	89
Figure 81.	Bistatic Scattering Coefficient vs. Product of Sines of Grazing Angles, Carrizozo	90
Figure 82.	Cumulative Amplitude Distribution, Carrizozo, VV	91
Figure 83.	Isodelay & Isodoppler Plots, M3E21_1003, VV	93
Figure 84.	Isodelay & Isodoppler Plots, M3D21_1003, VV	94
Figure 85.	Distribution of Bistatic Scattering Coefficient, M3D21 & M3E21, VV	94
Figure 86.	Log of Bistatic Scattering Coefficient vs. Log of Product of Sines of Grazing Angles, M3D21 & M3E21, VV	95
Figure 87.	Isodelay & Isodoppler Plots, M3D21_1001, HH	97
Figure 88.	Isodelay & Isodoppler Plots, M3E21_1001, HH	98
Figure 89.	Distribution of Bistatic Scattering Coefficient, M3D21 & M3E21, HH	98
Figure 90.	Log of Bistatic Scattering Coefficient vs. Log of Product of Sines of Grazing Angles, M3D21 & M3E21, HH	99

Figure 91.	Isodelay & Isodoppler Plots, M3D21_1002, VH	101
Figure 92.	Isodelay & Isodoppler Plots, M3E21_1002, VH	102
Figure 93.	Distribution of Bistatic Scattering Coefficient, M3D21 & M3E21, VH	102
Figure 94.	Log of Bistatic Scattering Coefficient vs. Log of Product of Sines of Grazing Angles, M3D21 & M3E21, VH	103
Figure 95.	Distribution of Bistatic Scattering Coefficient, Combined Data, UHF, VV	105
Figure 96.	Log of Bistatic Scattering Coefficient vs. Log of Product of Sines of Grazing Angles, Combined Data, UHF, VV	106
Figure 97.	Distribution of Bistatic Scattering Coefficient, Combined Data, Limited Area, UHF, VV	107
Figure 98.	Log of Bistatic Scattering Coefficient vs. Log of Product of Sines of Grazing Angles, Combined Data, Limited Area, UHF, VV	107
Figure 99.	Distribution of Bistatic Scattering Coefficient, Combined Data, UHF, HH	109
Figure 100.	Log of Bistatic Scattering Coefficient vs. Log of Product of Sines of Grazing Angles, Combined Data, UHF, HH	110
Figure 101.	Distribution of Bistatic Scattering Coefficient, Combined Data, Limited Area, UHF, HH	111
Figure 102.	Log of Bistatic Scattering Coefficient vs. Log of Product of Sines of Grazing Angles, Combined Data, Limited Area, UHF, HH	111
Figure 103.	Distribution of Bistatic Scattering Coefficient, Combined Data, UHF, VH	113
Figure 104.	Log of Bistatic Scattering Coefficient vs. Log of Product of Sines of Grazing Angles, Combined Data, UHF, VH	114
Figure 105.	Distribution of Bistatic Scattering Coefficient, Combined Data, Limited Area, UHF, VH	114
Figure 106.	Log of Bistatic Scattering Coefficient vs. Log of Product of Sines of Grazing Angles, Combined Data, Limited Area, UHF, VH	115
Figure 107.	Isodelay & Isodoppler Plots, MOD318004, VHF, VV	117
Figure 108.	Distribution of Bistatic Scattering Coefficient, MOD318004, VHF, VV	118
Figure 109.	Isodelay & Isodoppler Plots, MOD318007, VHF, VV	119
Figure 110.	Distribution of Bistatic Scattering Coefficient, MOD318007, VHF, VV	120
Figure 111.	Isodelay & Isodoppler Plots, M3E22_1003, VHF, VV	121
Figure 112.	Distribution of Bistatic Scattering Coefficient, M3E22_1003, VHF, VV	122
Figure 113.	Isodelay & Isodoppler Plots, M3D22_1003, VHF, VV	123
Figure 114.	Distribution of Bistatic Scattering Coefficient, M3D22_1003, VHF, VV	124
Figure 115.	Distribution of Bistatic Scattering Coefficient, Delay-Doppler Data, VHF, VV	125
Figure 116.	Log of Bistatic Scattering Coefficient vs. Log of Product of Sines of Grazing Angles, Delay-Doppler Data, VHF, VV	126

Figure 117.	Comparison of VHF and UHF VV-pol scattering	127
Figure 118.	Isodelay & Isodoppler Plots, MOD318002, VHF, HH	129
Figure 119.	Distribution of Bistatic Scattering Coefficient, MOD318, VHF, HH	130
Figure 120.	Isodelay & Isodoppler Plots, M3E22_1001, VHF, HH	131
Figure 121.	Distribution of Bistatic Scattering Coefficient, M3E22_1001, VHF, HH	132
Figure 122.	Isodelay & Isodoppler Plots, MOD318005, VHF, HH	133
Figure 123.	Distribution of Bistatic Scattering Coefficient, MOD318005, VHF, HH	134
Figure 124.	Isodelay & Isodoppler Plots, M3D22_1001, VHF, HH	135
Figure 125.	Distribution of Bistatic Scattering Coefficient, M3D22_1001, VHF, HH	136
Figure 126.	Distribution of Bistatic Scattering Coefficient, Delay-Doppler Data, VHF, HH	137
Figure 127.	Log of Bistatic Scattering Coefficient vs. Log of Product of Sines of Grazing Angles, Delay-Doppler Data, VHF, HH	138
Figure 128.	Comparison of VHF and UHF HH-pol scattering	139
Figure 129.	Isodelay & Isodoppler Plots, MOD318003, VHF, VH	141
Figure 130.	Distribution of Bistatic Scattering Coefficient, MOD318003, VHF, VH	142
Figure 131.	Isodelay & Isodoppler Plots, MOD318006, VHF, VH	143
Figure 132.	Distribution of Bistatic Scattering Coefficient, MOD318006, VHF, VH	144
Figure 133.	Isodelay & Isodoppler Plots, M3D22_1002, VHF, VH	145
Figure 134.	Distribution of Bistatic Scattering Coefficient, M3D22_1002, VHF, VH	146
Figure 135.	Distribution of Bistatic Scattering Coefficient, Delay-Doppler Data, VHF, VH	147
Figure 136.	Log of Bistatic Scattering Coefficient vs. Log of Product of Sines of Grazing Angles, Delay-Doppler Data, VHF, VH	148
Figure 137.	Comparison of VHF and UHF VH-pol scattering	149
Figure 138.	Generalized Lambertian Parameters, Delay-Azimuth, UHF	153
Figure 139.	Generalized Lambertian Parameters, Combined Data, UHF	156
Figure 140.	Comparison of VHF and UHF Scattering	158
Figure 141.	Gaussian Parameters	164

## LIST OF TABLES

Table 1.	Site Locations	15
Table 2.	Database for Delay-Azimuth Data	16
Table 3.	Operating Mode Parameters	33
Table 4.	UHF Direct Signal Measurements	34
Table 5.	Radial-Flight Database	83
Table 6.	Frequency Dependence	152
Table 7.	GLF Parameters	154

# 1. INTRODUCTION

This paper summarizes the analysis of bistatic radar data taken at White Sands Missile Range (WSMR), NM, in support of the evaluation of Space-Time Adaptive Processing (STAP) algorithms and the characterization and modeling of monostatic and bistatic scattering. Most of the measurements were made using a ground-based receiver at frequencies at or near 435 MHz. These measurements were made under the Mountaintop Program, which is a DARPA/NAVY sponsored initiative started in 1990 to study advanced processing techniques and technologies required to support the mission requirements of next-generation airborne early warning (AEW) platforms. Central to the Mountaintop Program is a surveillance radar measurements program executed from various mountaintop locations including field sites at the White Sands Missile Range (WSMR), New Mexico and the Pacific Missile Range Facility (PMRF), Hawaii. A second source of measurements were some air-to-air data recorded at 141 MHz and 431 MHz during a Propagation Experiment conducted in Sept./Oct. 1996. This experiment used two airborne platforms to obtain data on the effect of varying terrain types on electromagnetic propagation and bistatic clutter.

A typical radar surveillance scenario is shown in Figure 1. This diagram illustrates a jammer whose transmitted energy impacts the radar receiver performance both through the direct path and by way of a bistatic path from jammer to terrain patch to receiver. The direct-path jammer power can be nulled

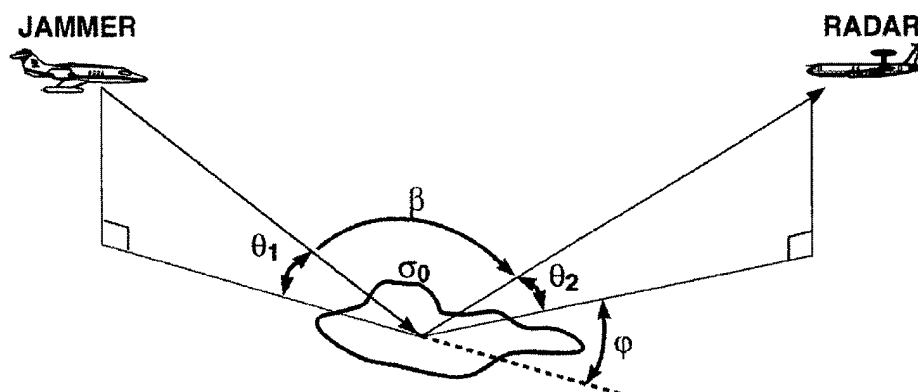


Figure 1. TSI Threat Scenario

spatially at the receiver by placing an array gain null at the jammer's azimuth; this represents a one-dimensional adaptive problem. The jammer power received due to terrain scattered interference (TSI) is a function of the radar - jammer geometry, the scattering characteristic of the terrain, the jammer and receiver antenna patterns, and the transmitted jammer power; its evaluation involves an integral of scattered power over the receive-beam footprint on the terrain. The terrain-scattered jammer power arrives in the target beam with the receiver's full main-beam gain; this interference cannot be mitigated with



spatial-only processing, since nulling the jammer would also attenuate the target returns. Thus, TSI mitigation will involve adaptive processing in both space and fast-time. A considerable amount of analysis has been directed at a variety of TSI mitigation algorithms operating in the absence of monostatic clutter [1,2,3,4,5] and initial studies have begun investigating the interaction between monostatic clutter nulling and TSI mitigation [6,7]. The focus of current activity [8, 9] has been to integrate monostatic clutter nulling and TSI mitigation more fully.

Bistatic radar data taken at White Sands Missile Range (WSMR) were analyzed to determine the bistatic scattering coefficient  $\sigma_0$  of the terrain. The primary objective was to derive graphs and formulae to enable designers to predict  $\sigma_0$  for various geometries. To this end the scattering characteristics were expressed as functions of out-of-plane angle and grazing angle relative to the local tangent. Since the grazing angles were expressed as relative to the local tangent, the results can be applied to terrain that is rougher than that measured if the local slopes are known or can be estimated. Other topics addressed by this report are the amplitude distribution of  $\sigma_0$  values, the comparison between monostatic and bistatic measurements and the statistical independence of measurements made at different frequencies.

The analysis reported here is confined to data from the flat semi-desert valley floor. A sample of this area is shown in Figure 2. This area was selected because of its uniformity and to ensure accuracy in determining the local tangent.

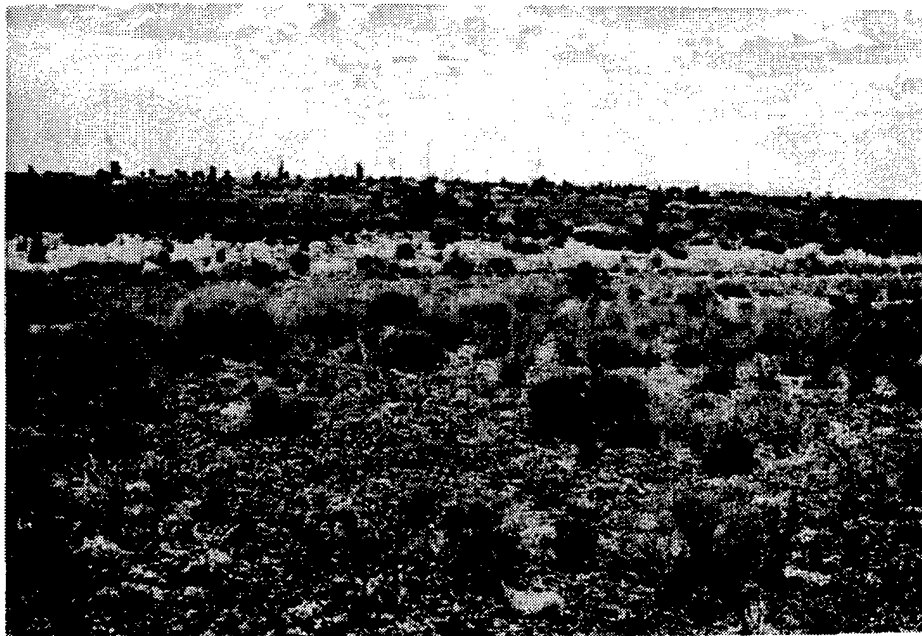


*Figure 2. Observed WSMR Terrain*

The data analyzed for this report are divided into two categories. In the first category, the receiver was ground-based and used the Radar Surveillance Technology Experimental Radar (RSTER) antenna for receiving. The transmitter was ground-based or airborne. For this set of data, the receiver grazing angle

was always five degrees or less. In the second category, both transmitter and receiver were airborne. For this air-to-air data, the grazing angle ranged from 5 to 40 degrees. By combining the two sets of data, it is possible to determine the dependence of  $\sigma_0$  on grazing angles over a wider range than with either set of data independently. The out-of-plane angles covered in the analysis were in the range from 8 to 180 degrees. Because of resolution limitations in the measurement of range, angle and Doppler, no attempt was made to determine  $\sigma_0$  for the glistening region.

The two categories of data required the use of different methods of selecting the ground area to be measured. For the RSTER data, the scattering areas were selected on the basis of time delay and azimuth at the receiver. These data are therefore referred to in the text as delay-azimuth data. For the air-to air data, the scattering areas were selected using time delay and Doppler shift. These are therefore referred to as delay-Doppler data.

From April 1993 through April 1994, RSTER was deployed at WSMR in support of DARPA's Mountaintop Program. A major objective of this program was to measure bistatic reflectivity of desert and

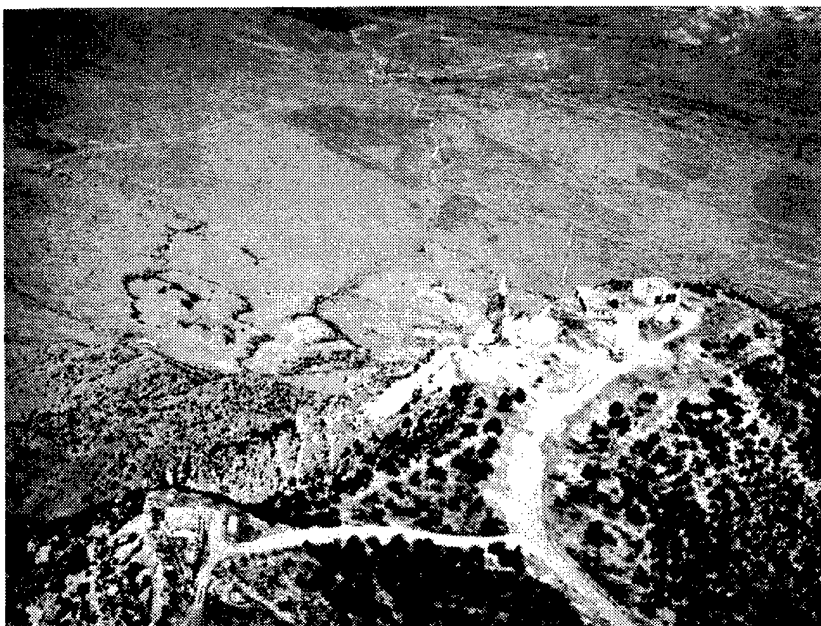


*Figure 3. RSTER on North Oscura Peak*

mountainous terrain using RSTER, a highly-directive low-sidelobe receiver array, with both static and airborne transmitters serving as radiation sources. Figure 3 shows the RSTER antenna at North Oscura Peak. Tests were conducted at frequencies in the neighborhood of 435 MHz with CW, pulsed CW (PCW), and pseudorandom (PN) waveforms.

In addition to the analysis of the wide-area measurements, analysis of the scattering at specific sites is reported. The wide-area measurements were conducted with the transmitter in a limited number of

positions, so the scattering characteristics over a range of transmitter grazing angles, receiver grazing angles and out-of-plane angles had to be deduced on the assumption that the scattering characteristics were uniform over the area measured. The analysis of the measurements from specific sites over a range of transmitter grazing angles and out-of-plane angles was designed to validate the wide-area measurements.

The air-to-air data were recorded during the Propagation Experiment in Sept./Oct. 1996. The experiment used an airborne transmitter and an airborne receiver to obtain data on the effect of various terrain types on electromagnetic propagation and bistatic clutter. The ground area selected for the current analysis was confined to that observed using the RSTER set up. Although not as abundant as the RSTER data, the two-aircraft data complemented the RSTER data in terms of the range of grazing angles covered. Measurements were taken at 141 MHz and 431 MHz using PCW modulation.

The remainder of this report explains the methodology of the analysis and presents the results. The scattering models and analysis methods are first considered. Results are then presented for the wide-area delay-azimuth data, the delay-azimuth radial-flight data and the delay-Doppler UHF data. The results of combining all the UHF data is then considered. The results from the VHF, delay-doppler data are reported and compared with the UHF results. Finally, the results are summarized in Section 26.

## **1.1 Presentation of Results**

Many of the results are displayed with reference to the out-of-plane angle. This is the angle between the line of site from the transmitter to the scatterer, projected onto the horizontal plane, and the line of site from the scatterer to the receiver projected onto the horizontal plane. An out-of-plane angle of 180 degrees implies backscatter; an out-of-plane angle of zero implies forward scattering.

Two of the parameters used in this analysis are the transmitter and receiver grazing angles. The grazing angle is the angle between the radar line-of-sight and the plane tangent to the scattering surface. The slope of the surface is taken into account in calculating the grazing angles and is calculated from the DMA maps at the center of the scattering area for the signals under consideration.

In many of the figures, a plot is given showing the transmitter position (represented by circles), the position of the reflection point on the ground (represented by dots), and the receiver position (indicated by an asterisk). The ground altitude is represented by a grey scale, with the higher altitudes darker. For most of the plots, the dots representing the ground reflection point cannot be seen since they are hidden by the circles showing transmitter position. For most of the airborne missions, the transmitter position cannot be seen since it is outside the area plotted.

Various transmitter-receiver polarization combinations were recorded. All were linear vertical or horizontal. Throughout this report, the polarization pairs will be referred to as VV-pol, HH-pol, VH-pol and HV-pol, where the first character refers to the polarization of the receiver and the second to the polarization of the transmitter.

## 2. SCATTERING MODELS

A number of models have been proposed for the dependence of bistatic scattering on grazing angle [10,14,16]. A selection of these models are listed below. These are known as constant-gamma models.

$$\sigma_0 = \gamma(\sin\theta_t \sin\theta_r)^\alpha \quad (\text{EQ 1})$$

$$\sigma_0 = \gamma\sqrt{\sin\theta_t \sin\theta_r} \quad (\text{EQ 2})$$

$$\sigma_0 = \gamma\left(\frac{\sin\theta_t + \sin\theta_r}{2}\right) \quad (\text{EQ 3})$$

$$\sigma_0 = \gamma\sin\left[\frac{(\theta_t + \theta_r)}{2}\right] \quad (\text{EQ 4})$$

$$\sigma_0 = \frac{2\gamma\sin\theta_t \sin\theta_r}{\sin\theta_t + \sin\theta_r} \quad (\text{EQ 5})$$

where  $\theta_t$  and  $\theta_r$  are transmitter and receiver grazing angles, respectively.

Equation 1 above is the Generalized Lambertian Formula (GLF). When  $\alpha$  is set to 0.5, it reduces to Equation 2, which represents  $\sigma_0$  as being proportional to the geometric mean of the grazing angles. Equation 3 and Equation 4 use the arithmetic mean of the sines and the sine of the arithmetic mean respectively. Because the GLF is the only formula that uses more than one parameter, the data have been analyzed in terms of this model.

The GLF relationship is graphically illustrated by plotting the log of the measured  $\sigma_0$  against the log of the product of the sines. A straight line on this plot represents the GLF, where the intercept on the Y axis gives the value of  $\log(\gamma)$  and the slope give the value of  $\alpha$ . The data were separated into bins of out-of-plane angle  $\phi$ , to test whether the relationship between  $\sigma_0$  and grazing angle varied with  $\phi$ . The GLF was fitted to the data, using a single value of  $\gamma$  for each polarization combination and an  $\alpha$  that varied with polarization and out-of-plane angle. This fitting was performed for each polarization of the UHF data, and the solution plotted as straight lines on the data plots.

The fitting of the GLF to the data was performed as follows. With  $\alpha$  varying with out-of-plane angle, Equation 1 takes the form

$$\sigma_0 = \gamma(\sin\theta_t \sin\theta_r)^{\alpha(\phi)} \quad (\text{EQ 6})$$

Taking the log of both sides of Equation 6 yields  $\log\sigma_0 = \log(\gamma) + \alpha(\phi)\log(\sin\theta_t \sin\theta_r)$ , which is a linear

relationship that can be solved by classical means. Let  $\underline{z} = H\underline{x} + \underline{\epsilon}$ , where  $\underline{z} = \begin{bmatrix} \log(\sigma_{0,1}) \\ \log(\sigma_{0,2}) \\ \log(\sigma_{0,3}) \\ \dots \end{bmatrix}$ , a vector of

$$\text{measured values, } H = \begin{bmatrix} 1 & \log(\sin(\theta_{t,1,1})\sin(\theta_{r,1,2})) & \log(\sin(\theta_{t,1,1})\sin(\theta_{r,1,3})) & \dots \\ 1 & \log(\sin(\theta_{t,2,1})\sin(\theta_{r,2,2})) & \log(\sin(\theta_{t,1,1})\sin(\theta_{r,2,3})) & \dots \\ 1 & \log(\sin(\theta_{t,3,1})\sin(\theta_{r,3,2})) & \log(\sin(\theta_{t,1,1})\sin(\theta_{r,3,3})) & \dots \\ \dots & \dots & \dots & \dots \end{bmatrix}, \quad \underline{x} = \begin{bmatrix} \log(\gamma) \\ \alpha(\phi_1) \\ \alpha(\phi_2) \\ \dots \end{bmatrix},$$

a vector of parameters, and  $\epsilon$  is an error term. A least-squares fit is given by  $\hat{\underline{x}} = [H^T H]^{-1} H^T \underline{z}$  which gives the values of  $\gamma$  and  $\alpha$ .

For the UHF HH-pol delay-azimuth data taken with the RSTER receiving antenna, it was found that the  $\sigma_0$  showed a drop in value in the region of 90 degrees out-of-plane angle. There is some theoretical basis for this effect [12]. The same decrease in  $\sigma_0$  was not observed in the air-to-air delay-Doppler data, due probably to inadequate cross-polarization isolation in one or both antennas. In Section 20, which reports the combined result from the UHF HH-pol delay-azimuth and delay-Doppler measurements, the variation of  $\sigma_0$  in the RSTER data was included in the model by adding a simple cosine term to the GLF. Thus

$$\sigma_0' = \gamma \vartheta(\phi) (\sin\theta_t \sin\theta_r)^{\alpha(\phi)}, \quad (\text{EQ 7})$$

where

$$\vartheta(\phi) = \frac{1 + a + (1 - a)\cos 2\phi}{2} \quad (\text{EQ 8})$$

and  $a$  determines the depth of the null. This formula will be referred to as the Modified Generalized Lambertian Formula. The value of  $a$  was chosen to minimize the variation in  $\alpha$  over the data analyzed. The depth of the null is probably determined more by the degree of cross-polarization coupling in the transmitter and receiver antennas than by the phenomenon. For an infinitely deep null,  $a$  is zero and Equation 7 reduced to

$$\sigma_0' = \frac{(1 + \cos 2\phi)}{2} (\sin\theta_t \sin\theta_r)^{\alpha(\phi)} \quad (\text{EQ 9})$$

Taking the log of both sides of Equation 7, and rearranging the terms, gives

$$\log \sigma_0' - \log \vartheta(\phi) = \log(\gamma) + \alpha(\phi) \log(\sin\theta_t \sin\theta_r) \quad (\text{EQ 10})$$

The values of  $\alpha$  and  $\gamma$  were estimated by fitting this function to the measured values of  $\sigma_0$  in a least squares sense, the  $-\log \vartheta(\phi)$  term being applied to the RSTER data and not to the air-to-air data.

### 3. STATISTICAL ANALYSIS METHODS

One of the purposes of the analysis was to look for the sensitivity of  $\sigma_0$  to various parameters such as out-of-plane angle and grazing angles. To assemble data for statistical analysis, a matrix was formed, each row of which containing a set of variable values for a single data point. The matrix included columns for  $\sigma_0$ , noise floor, ground scatterer position and altitude, transmitter position and altitude, receiver position and altitude, grazing angles for transmitter and receiver, out-of-plane angle and visibility flags for transmitter and receiver. For the various statistics derived, the data points were selected according to certain criteria that confined the terrain to the valley floor.

Different methods were used to compile the data for the various modes of measurements. For the ground-based delay-azimuth missions, the positions of the transmitter and receiver were fixed. This allowed a shadowing map to be calculated once for each particular geometry and used for all appropriate data sets. Under these conditions the range profile data were interpolated into a cartesian grid and the data for the statistics taken from the cartesian grid of  $\sigma_0$ . For the airborne delay-azimuth missions, the shadowing varied with the position of the two aircraft. For these data, the data points were taken directly from the radial range profiles and the shadowing relative to the moving transmitter calculated for each range profile. For the air-to-air delay-Doppler missions, shadowing was not considered, since the grazing angles were large. The data were taken from the range profiles.

#### 3.1 Determination of Noise Floor

The validity of the calculation of the scattering coefficient depends on the level of noise or other extraneous signals present in the measurement. The principal source of corruption was either receiver noise or range sidelobes, depending on the strength of the direct signal. For both PCW and PN modulation, the range sidelobes were due to leakage and other imperfections in the transmitter modulator. The noise/sidelobe floor was measured by measuring the signal immediately preceding the reception of each direct signal.

#### 3.2 Amplitude Distribution Functions

In analyzing the statistics of the amplitudes of the scattering coefficients, the results were compared with three types of distributions. These are the Rayleigh (exponential in signal amplitude squared), Weibull [11] and lognormal distributions. The Rayleigh distribution is that expected from a large number of scatterers of approximately equal size. The lognormal distribution can approximate that of the sum of several different Rayleigh distributions. The Weibull distribution is similar to the Rayleigh distribution but is more general since it contains a shape factor.

In terms of signal amplitude squared, the Weibull distribution is given by [11]

$$p(x) = \frac{\eta}{\sigma_w} \left( \frac{x}{\sigma_w} \right)^{\eta-1} e^{-\left( \frac{x}{\sigma_w} \right)^\eta}, x > 0, \sigma_w > 0, \eta > 0 \text{ and } p(x) = 0 \text{ otherwise.} \quad (\text{EQ 11})$$

where  $\sigma_w$  and  $\eta$  are the scale and shape parameters respectively. For  $\eta = 1$  we get the exponential distribution

$$p(x) = \frac{1}{\sigma} e^{-\left( \frac{x}{\sigma} \right)}. \quad (\text{EQ 12})$$

## 4. SYSTEM CONFIGURATION

### 4.1 Configuration for Delay-Azimuth Measurements

#### 4.1.1 RSTER Configuration

The RSTER antenna [13] is a rectangular planar array of 14 linear arrays in which the spacing of the linear arrays is one half wavelength at 450 MHz. The antenna gain function of each linear array is approximately equivalent to a line of dipoles in front of a reflecting plane. The polarization of the dipoles is perpendicular to the length of the linear array. For the VV-pol and VH-pol measurements, the linear elements were horizontal (RSTER-0 configuration). For the HH-pol and HV-pol measurements, the antenna was rotated about boresight by 90 degrees so that elements were vertical (RSTER-90 configuration). In the RSTER-0 configuration, the antenna beam was steered electronically in elevation and mechanically in azimuth. In the RSTER-90 configuration, the beam was fixed at zero elevation and was steered electronically in azimuth. Figure 4 shows the antenna in the RSTER-0 configuration.

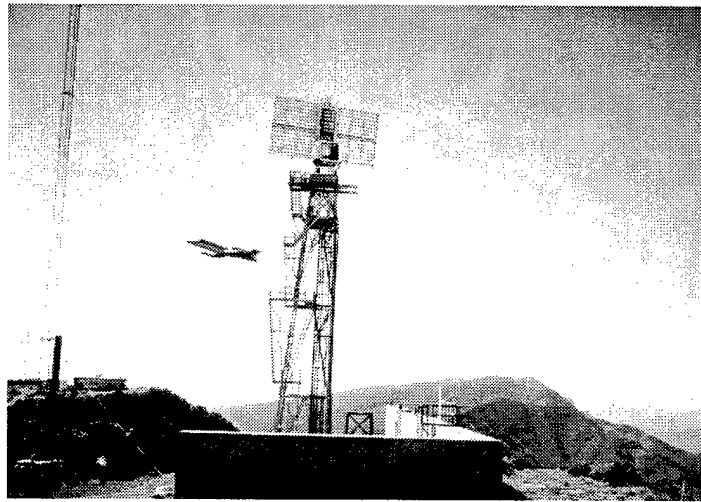


*Figure 4. RSTER antenna*

The RSTER Receiver system consists of fourteen independent, triple-conversion channels that downconvert input signals in the 400 MHz to 500 MHz range to a 1 MHz center frequency. Remote Front Ends are employed to optimize sensitivity. The noise figure for each channel is 5 dB. The three intermediate frequencies are 62 MHz at 3 MHz bandwidth, 6 MHz at 200 kHz bandwidth and 1 MHz at 800 kHz bandwidth. The overall bandwidth is determined at the 6 MHz frequency, where the response shape is approximately gaussian and is nominally 200 kHz wide at the  $-3$  dB point. For a gaussian shape, the noise bandwidth is 1.064 times the  $-3$  dB bandwidth, i.e. nominally 212.8 kHz.



The analogue output of each channel, centered at 1 MHz, is fed to an A/D, the output of which is digitally filtered, converted to baseband and recorded. Post-mission on-site processing was then performed to generate a set of files on 4 mm DAT tapes. These tapes were the data source for this analysis.

#### **4.1.2 Ground-based Transmitter Configuration**

Figure 5 shows the "Little Frank" antenna used for the bistatic delay-azimuth measurements. This



*Figure 5. Little Frank antenna*

antenna consists of four circular patches, arranged vertically, one half wavelength apart, in front of a ground plane. For the current experiment, either the vertical or the horizontal feedpoints were excited in phase depending on the polarization required.

#### **4.1.3 Airborne Transmitter Configuration**

Figure 6 shows the Lear Jet used for the airborne delay-Doppler measurements. This aircraft was equipped with antennas in the nose and tail. Each antenna consisted of crossed dipoles one quarter wavelength in front of a ground plane. For the current experiment, the dipoles were excited to give vertical or horizontal polarization as required. The boresight direction for the nose antenna was along the aircraft axis in the forward direction. Similarly, the boresight direction for the tail antenna was rearward along the aircraft axis.



*Figure 6. Lear Jet*

## **4.2 Configuration for Delay-Doppler Measurements**

The delay-Doppler data were obtained during the Propagation Experiment in Sept./Oct. 1996. The experiment used two airborne platforms to obtain data illustrating the effect of varying terrain types on electromagnetic propagation and bistatic clutter. The two aircraft used in the experiment were a Cessna 421, shown in Figure 7, and a Beechcraft 90 King Air, shown in Figure 8.



*Figure 7. Cessna 421*

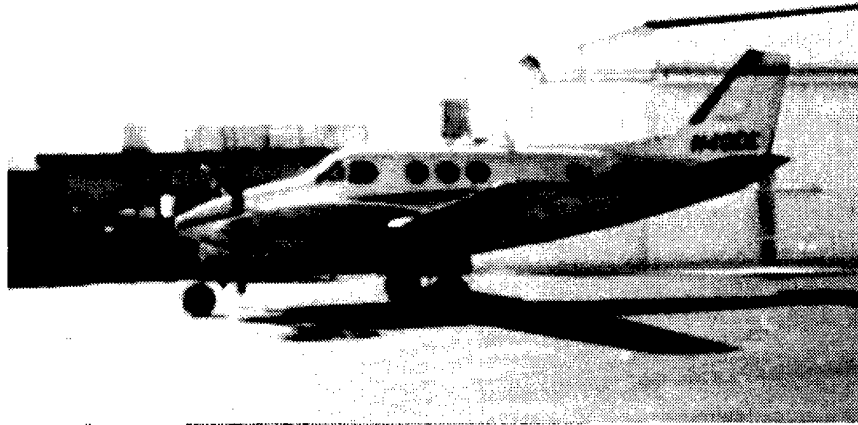


*Figure 8. Beechcraft 90 King Air*

Both aircraft were equipped with VHF and UHF H-pol and V-pol antennas operating at 141 MHz and 431 MHz. For the Cessna, the VHF H-pol half loop ("towel bar") antenna was mounted on the starboard side, and the VHF V-pol monopole was mounted under the belly of the aircraft. The UHF patch antenna on the Cessna was attached to the port side, and radiated both polarizations. The V-pol and H-pol antennas on the King Air had interchangeable elements for UHF and VHF. The H-pol antenna was mounted on the rear of the aircraft and the V-pol antenna was attached to the belly. The patterns of these antennas were symmetrical about the longitudinal axis of the aircraft. Measurements from calibration flights were used to produce antenna patterns [19].

The Cessna transmitted a PCW signal that was received by the King Air and recorded. GPS data for the two aircraft were also recorded. The system was operated in three distinct modes for various data-gathering purposes. For this analysis Mode 3 data were used for measuring  $\sigma_0$ . In this mode, the pulse length was 5 microseconds and the transmitter PRF was 2 kHz. The receiver sampled the signal at a rate of 200 kHz and recorded 110 samples every 2 milliseconds for UHF and every 4 milliseconds for VHF. Mode 2 data were used for measuring antenna patterns. In this mode, the pulse length was 0.333 microseconds and the transmitter PRF was 5.25 kHz. The receiver sampled the signal at a rate of 4 MHz and recorded 786 samples every 4 milliseconds.

## 5. CALCULATION OF BISTATIC SCATTERING COEFFICIENT

The bistatic radar equation is as follows:

$$P_R = \frac{P_J G_J \sigma_0 A_B \lambda^2 G_R}{(4\pi)^3 R_{JG}^2 L_{JG} R_{GR}^2 L_{GR}} , \quad (\text{EQ 13})$$

where  $P_R$  is the received power,  $P_J$  is the transmitted power,  $G_J$  is the transmitter antenna gain,  $\sigma_0$  is the bistatic scattering coefficient,  $A_B$  is the effective scattering area,  $\lambda$  is the wavelength,  $G_R$  is the receiver antenna gain,  $R_{JG}$  is the distance between the transmitter and the scatterer,  $L_{JG}$  is the excess loss in the propagation from transmitter to scatterer,  $R_{GR}$  is the distance between the scatterer and the receiver and  $L_{GR}$  is the excess loss in the propagation from the scatterer to the receiver.

Solving the equation above for  $\sigma_0$  yields,

$$\sigma_0 = \frac{(4\pi)^3 P_R R_{JG}^2 L_{JG} R_{GR}^2 L_{GR}}{P_J G_J A_B \lambda^2 G_R} . \quad (\text{EQ 14})$$

After the appropriate beamforming, calibration, and matched filtering, files were generated giving  $P_R$  for each time sample. The geometry-dependent factors  $R_{JG}$ ,  $R_{GR}$ ,  $G_J$  and  $A_B$  were then calculated as functions of sample number, and combined with  $P_R$  and the constant factors  $L_{JG}$ ,  $L_{GR}$ ,  $\lambda$  and  $G_R$  to yield range profiles of  $\sigma_0$  for each azimuth direction. The excess losses in propagation are assumed to be small so the terms  $L_{JG}$  and  $L_{GR}$  are given values of unity. A cartesian map of  $\sigma_0$  was then obtained by interpolating between the radial range profiles.

### 5.1 Determination of Effective Scattering Area

For both delay-azimuth and delay-Doppler measurements, the calculation of  $\sigma_0$  requires a knowledge of the effective scattering area,  $A_B$ . For the delay-azimuth data, this scattering area is determined by the combined effects of the receiving antenna beamwidth, the time delay resolution cell size and, in the case of an airborne transmitter, the Doppler resolution cell size. For the delay-Doppler data, the scattering area is determined by the time delay resolution cell size and the Doppler resolution cell size. The transmitting antenna beamwidth is always considered to be too broad to affect the effective scattering area. With reference to the ground, each of these three elements can be considered to be a spatial filter. If the receiver antenna gain and the processing gain are calculated for the maximum response, each of the spacial filters will have a maximum value of unity.  $A_B$  will then be equal to the integral over the ground of the squared product of the filter functions.

Two methods are available in the programs for calculating this area. In the first method, which does not include the effects of Doppler cell and is applicable only to the delay-azimuth measurements, both the range and azimuth windows are considered to be rectangular, and the effective scattering area is assumed to be equal to the geometric area bounded by these two functions. Willis [10] gives the effective scattering area as

$$A_B = \frac{c\tau R_{GR}\alpha}{2\left[\cos\left(\frac{\beta}{2}\right)\right]^2} \quad (\text{EQ 15})$$

where  $\tau$  is the radar's compressed pulse width,  $R_{GR}$  is the distance from the scatterer to the receiver,  $\alpha$  is the receiver beamwidth in radians, and  $\beta$  is the bistatic angle as defined in Figure 1. This expression reduces to

$$A_B = \frac{R_{GR}r_d\alpha}{1 + \cos\beta}, \quad (\text{EQ 16})$$

where  $r_d = c\tau$ .

The second method for calculating the effective scattering area takes into consideration the effects of Doppler cell size as well as range and azimuth cell sizes. With three intersecting functions, an assumption of rectangular windows makes the calculations difficult. To make the problem more tractable and more accurate, each window was approximated by a gaussian function. The details of the method are given in Appendix I. This second method was found to give similar results to the first method in the delay-azimuth measurements when both transmitter and receiver were static and there was no Doppler resolution.

The first method was used for the delay-azimuth measurements with the ground-based transmitter. The second method was used for the delay-azimuth measurements with airborne transmitter and for the delay-Doppler measurements.

## 6. DATABASE

### 6.1 Bistatic Delay-Azimuth Data

Data were taken using the RSTER receiver in combination with ground-based and airborne transmitters. For all missions, the receiver was located on North Oscura Peak, White Sands Missile Range, NM. For the ground-based measurements, the transmitter was positioned at three different locations at various times. The transmitter sites were Socorro Peak, Salinas Peak and Sierra Blanca; their locations and altitudes are given in Table 1 and are illustrated in Figure 9. For the airborne missions, the aircraft was

Table 1. Site Locations

Site	Altitude (m)	Position East (km)	Position North (km)	Range (km)	Bearing (deg true)	Latitude (deg N)	Longitude (deg E)
RSTER	2407	0	0	0	0	33.75158	-106.3702
Socorro Peak	2134	-55.05	35.11	65.29	302.5	34.0680	-106.9667
Salinas Peak	2652	-15.60	-49.68	52.07	197.4	33.3036	-106.5401
Sierra Blanca	3537	52.26	-41.86	66.96	128.7	33.3741	-105.8070

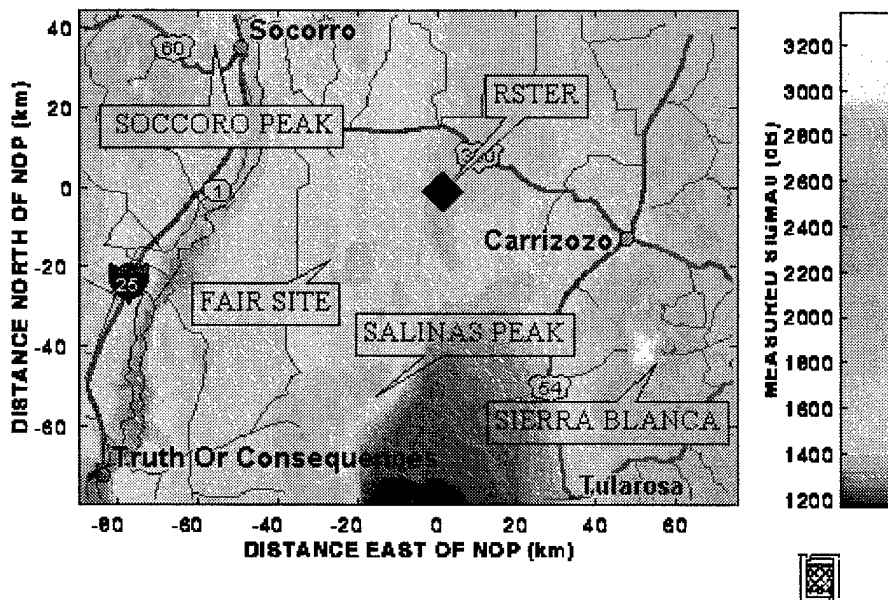


Figure 9. Site Locations

flown along straight lines that were radials approximately in line with each of the listed ground sites and the receiver. Measurements were also made to evaluate the scattering at specific sites. These measurements were made at three sites: Fair Site, Harriet Site and Carrizozo. The positions of each of these sites is given in Table 5. The aircraft was flown along several radials toward or away from each site. In this report, these flights are referred to as radial flights.

The measurements covered a range of frequencies, polarizations, waveforms, transmitter positions and receiver azimuths. For the missions using the ground-based transmitter, the transmitting antenna was directed toward the receiver. For the airborne missions, the forward-facing transmitter antenna was used while the aircraft was flying toward the receiver and the rearward-facing antenna used when it was flying away. The aircraft was equipped with a GPS receiver and recorder, which allowed the position and velocity of the aircraft to be available for post-mission analysis.

To obtain comprehensive statistics, the measurements were taken at four combinations of linear polarizations, that is VV-pol, HH-pol, VH-pol and HV-pol. The measurements for each polarization were taken for a combination of sites, frequencies and waveforms. For the ground-based measurements, the transmitted frequencies were 434.8, 435.0, 435.2 and 435.4 MHz. These measurement frequencies were spaced at multiples of the receiver bandwidth to obtain statistically independent scattering data. For the airborne missions, a single frequency of 435.0 MHz was used.

Table 2 below summarizes the number of frequencies and sites for each of the polarizations. This table does not include the radials flown over Fair Site, Harriet Site and Carrizozo discussed in Section 15.

**Table 2. Database for Delay-Azimuth Data**

VV-pol GROUND BASED	3 SITES	4 FREQ	VH GROUND BASED	3 SITES	4 FREQ
VV-pol AIR- BORNE	3 TRACKS 3 RADIALS	1 FREQ	VH AIR- BORNE	3 TRACKS	1 FREQ
VV-pol MONO- STATIC		4 FREQ	VH MONO- STATIC		
HV GROUND BASED	2 SITES	4 FREQ	HH GROUND BASED	2 SITES	4 FREQ
HV AIR- BORNE			HH AIR- BORNE	1 TRACK	1 FREQ
HV MONO- STATIC			HH MONO- STATIC		4 FREQ

## 6.2 Monostatic Delay-Azimuth Data

The monostatic data were reduced and analyzed as reported in an internal memo by John Jayne [21]. This processing also generated MATLAB files containing arrays of values of  $\sigma_0$  as functions of ground position.

## 6.3 Bistatic Delay-Doppler Data

Data were taken at VV, HH and VH polarizations. Four sets of data were available for VV-pol, four for VH-pol and three for HH-pol. Details are discussed in Sections 16, 17 and 18.



## 7. DELAY-AZIMUTH DATA REDUCTION

### 7.1 RSTER Antenna Beamforming

The RSTER antenna is a rectangular planar array of 14 linear arrays. The spacing of the linear arrays is one half wavelength at 450 MHz. Each linear array has a radiation pattern approximating that of a line of dipoles in front of a reflecting plane. The polarization of the dipoles is perpendicular to the length of the linear array. For the VH and VV-pol measurements, the linear elements were horizontal (RSTER-0 configuration). For the HH-pol and HV-pol measurements, the antenna was rotated about boresight by 90 degrees so that the linear elements were vertical (RSTER-90 configuration). The linear elements are numbered 1 through 14. In the RSTER-0 configuration, element #1 is at the top. For the RSTER-90 configuration, #1 element is to the right when viewed from behind the antenna.

In the RSTER-0 configuration, the antenna beam was steered electronically in elevation and mechanically in azimuth. Only arrays 2 through 14 were used, the receiver channel normally used for element #1 being connected to a non-directional monopole antenna. The connection to the omnidirectional antenna was made to ensure that a clean direct signal was available when the main beam was steered away from the transmitter. The outputs of the thirteen receivers connected to elements #2 through #14 were combined to form a beam centered on an elevation of  $-3.65$  degrees. Dolph-Chebyshev weighting giving a sidelobe level of  $-50$  dB was used. At a frequency of 435 MHz, the  $-1$  dB beamwidth in elevation was  $7.9$  degrees. The beam therefore covered the range of  $0.3$  to  $-7.6$  degrees. In the files containing the bistatic range profiles, the signal from the monopole antenna was recorded along with the beamformed data. The antenna was moved in five degree increments in azimuth, one file of data being recorded for each azimuth position.

In the RSTER-90 configuration, the beam was fixed at zero elevation and was steered electronically in azimuth. All 14 elements were used in beam forming. Dolph-Chebyshev weighting giving a sidelobe level of  $-40$  dB and a  $-3$  dB beamwidth of  $10.6$  degrees broadside to the array was used. The higher sidelobe level was tolerated in exchange for a narrower beam. Data were taken with the array facing  $210$ ,  $270$  and  $330$  degrees azimuth. For each data file a set of beams at five degree intervals covering  $30$  degrees either side of broadside.

Since the antenna elements and receivers varied in their amplitude and phase responses, it was necessary to determine their responses in order to fix the beamforming weights. The calibration of the antennas and receiver channels for the purpose of beamforming was performed using the direct signal from a boresight antenna. The data sets used for this calibration were those taken when the antenna azimuth was directly toward the transmitter and when the transmitter antenna had the same polarization as the receiving antenna. The signal was measured for each channel at the first peak of the return. Beamforming weights were then calculated by multiplying the inverse of the complex response by a Dolph-Chebyshev function.

This calibration was carried out for each of the VV-pol and HH-pol data sets. For the VH-pol and HV-pol data sets, the weights derived for an appropriate co-pol data set were used.

## 7.2 Types of Modulation

Two types of modulation were employed in the delay-azimuth experiments; these were Pulsed Continuous Wave (PCW) modulation and Binary-Phase Pseudo-Noise (PN) modulation. For PCW modulation, the transmitter periodically radiated at a constant frequency for either  $5\mu s$  or  $13\mu s$ . For the  $5\mu s$  mode, the pulse repetition period (PRP) was 255 times the pulse length, i.e.  $1275\mu s$ . For the  $13\mu s$  mode the PRP was 127 times the pulse length, i.e. 1651 microseconds. The sampling interval was  $1\mu s$ .

With PN modulation, the transmitter radiated at a nominally constant amplitude with the phase switching to 0 or 180 degrees at  $5\mu s$  or  $13\mu s$  intervals. The pseudorandom binary phase sequence was a maximum-length sequence from a feedback shift register. In the  $5\mu s$  mode, the length of the shift register was 8, giving a sequence of 255 chips. In the  $13\mu s$  mode, the length was 7, giving 127 chips. Again, the sampling interval was  $1\mu s$ . In the processing for analysis, the PN waveform was compressed to a short pulse by convolving the signal with a time-reversed sequence, which was modified in a manner detailed in Section 7.3. It can be seen that the PCW and PN waveforms had similar parameters and hence could share much of the processing.

## 7.3 Optimization of PN Pulse Compression

With a bistatic radar, the high sidelobe level inherent in the standard PN pulse compression techniques can be reduced by a simple modification to the compression algorithm. Assume a PN modulating function,  $x(t)$ , of unit magnitude composed of a maximum length sequence of length  $N$  with each chip of duration  $\tau$ . Assume that this sequence has  $(N+1)/2$  values of  $-1$  and  $(N-1)/2$  values of  $1$ . One property of this function is that the convolution  $x(t)*1 = -\tau$ . Such a function is usually compressed by convolving the received signal with the complex conjugate of the reverse sequence,  $x^*(-t)$ . The convolution  $x(t)*x^*(-t)$  produces a pulse of maximum amplitude  $N\tau + j0$  and sidelobes of  $-\tau + j0$ . In a monostatic radar, where the receiver is turned off during transmission and only a part of the PN sequence is available, this is the lowest sidelobe level achievable. With  $N = 127$ , the sidelobe level is  $-42$  dB with respect to the maximum. With a bistatic radar, where the signal can be processed over a complete cycle of the code and circular convolution can be employed, the sidelobes can, in theory, be reduced to zero by subtracting a constant,  $\Delta$ , from the pulse-compression.

In the current data, imperfections in the transmitter modulator cause the sidelobe level to be raised. In the biphasic PN code, the two phases should be 180 degrees apart. The imperfections appeared as a consistent error of several degrees in the phase swing. Fortunately, it was possible to reduce the sidelobes due to this imperfection by making  $\Delta$  complex-valued and adjusting the real and imaginary parts.

In this analysis, two methods were used to determine the optimum value of  $\Delta$ . For each data set the results of the two methods were compared and the value of  $\Delta$  giving the lower range sidelobe level selected. The range sidelobe level achieved ranged from  $-50$  to  $-80$  dB. Both methods made use of the cleanest available direct signal from the transmitter. The sample signal used depended on whether the transmitter and receiver had the same polarization or not. In the co-pol case, the sample signal was taken from the RSTER antenna when it was pointing directly toward the source. This gave the minimum multipath effect, since azimuth and elevation sidelobes constrained the multipath leakage. For the cross-pol case, the signal from the wide-angle monopole antenna was used when available or from a single element when it was not.

## 7.4 First Method for Optimizing PN Compression

The first method for optimizing PN compression derives the value of the constant  $\Delta$  directly from the observed range sidelobe level. Let the modulating function  $x(t)$  be a bipolar  $\pm 1$  maximum length sequence of length  $N$  with each chip having a time duration of  $\tau$  seconds. Let the system impulse response, including multipath effects be  $g(t)$ . The received signal will then be  $[g(t)*x(t)]$ . This received signal is compressed by circularly convolving with  $[x^*(-t) - \Delta]$ . After compression the received signal will be  $g(t)*x(t)*[x^*(-t) - \Delta]$ .

$$\text{Let } y(t) = x(t)*[x^*(-t) - \Delta] ; \quad (\text{EQ 17})$$

$$\text{then } y(t) = x(t)*x^*(-t) - x(t)*\Delta . \quad (\text{EQ 18})$$

$$y(t) = x(t)*x^*(-t) + \tau\Delta \quad (\text{EQ 19})$$

The term  $x(t)*x^*(-t)$  has a peak value of  $N\tau + j0$  and a constant sidelobe level of  $-\tau + j0$ . For  $y(t)$  to have a sidelobe level of zero,  $\tau\Delta = \tau + j0$ , i.e.,  $\Delta = 1 + j0$ .

Suppose now that, due to imperfections in the modulator, the transmitted waveform is  $x(t) + v$ . If  $\Delta$  is subtracted from the convolving function, then the pulse-compressed signal becomes

$$\begin{aligned} y''(t) &= g(t)*[x(t) + v]*[x^*(-t) - \Delta] \\ y''(t) &= g(t)*[x(t)*x^*(-t) + v*x^*(-t) - x(t)*\Delta - v*\Delta] . \end{aligned} \quad (\text{EQ 20})$$

The right-hand side of this equation reduces to  $g(t)*[x(t)*x^*(-t) + (\Delta - v)\tau - v\Delta N\tau]$ . For zero sidelobe level, the second and third terms must cancel out the sidelobes due to the first term, i.e.,

$(\Delta - v)\tau - v\Delta N\tau = \tau$ . Substituting the expression for  $v$  in terms of measured sidelobe level yields

$$\Delta = \frac{S}{\tau - (S + \tau)N} .$$

For the test signal, it is assumed that there is negligible multipath effect, and that the system impulse response can be expressed as  $g(t) = |g|e^{j(\omega t + \theta)}$ . The  $\omega$  term accounts for the slight difference between the transmitter and receiver reference oscillators and the  $\theta$  term accounts for the delay in transmission and other fixed phase shifts. The first step in deriving  $\Delta$  is to obtain values of  $\omega$  and  $\theta$ . This is done by extracting the phase of the signal at each sample, doubling the phase angle, resolving the  $2\pi$  ambiguity and fitting a linear function to the result. The initial phase and phase slope are then halved to yield values of  $\theta$  and  $\omega$ . The sample signal is then multiplied by  $e^{-j(\omega t + \theta)}$ , the resultant signal compressed by convolving with  $x^*(-t)$ , and the range sidelobe level measured. The value of  $\Delta$  is then calculated.

## 7.5 Second Method for Optimizing PN Compression

In the second method for optimizing the PN compression, the value of  $\Delta$  is derived by an iterative process which minimizes a selected measure of the range sidelobe level. The user is given the option of minimizing the peak signal level in a selected range of cells (usually those preceding the direct signal), minimizing the RMS signal in these cells, or minimizing the overall RMS signal. The starting values for this iterative process are those determined by the first method. In practice it has been found that in most cases the second method gives a small (1 to 3 dB) improvement over the first. If no improvement can be made, the parameters from the first method are used. The second method makes use of the MINIMIZE function provided by MATLAB, which employs the SIMPLEX minimization method.

## 7.6 Coherent Processing

An outline of the initial processing is shown in Figure 10. The data for each of the 14 elements is provided in a rectangular data array. These data arrays are combined to form a new set of data arrays, one for each beam. These arrays are represented by the rectangle at the top left of Figure 10. Each array contains a specific number of PRIs. For the  $5\mu s$  mode, this number was 96; for the  $13\mu s$  mode it was 64. The recorded PRIs were not contiguous but were spaced two periods apart to match the expected Doppler. The number of samples for each PRI was two to three percent longer than a full PN sequence period.

The first step illustrated in the diagram is Doppler processing and frequency offset compensation. To improve the S/N ratio over that from a single pulse, the sets of returns are coherently combined using a DFT by applying the transform over the 96 or 64 samples for each time delay. The reason that this processing is carried out first is that the pulse compression applied later to the PN signal is sensitive to frequency errors. Even with a stationary transmitter and receiver, the pulse compression is affected by the small offset between transmitter and receiver reference frequencies.

The next step in the processing is to apply a phase shift that is proportional to both Doppler shift and time delay. This has the effect of reducing the phase shift over the PN cycle to zero. Finally, the data

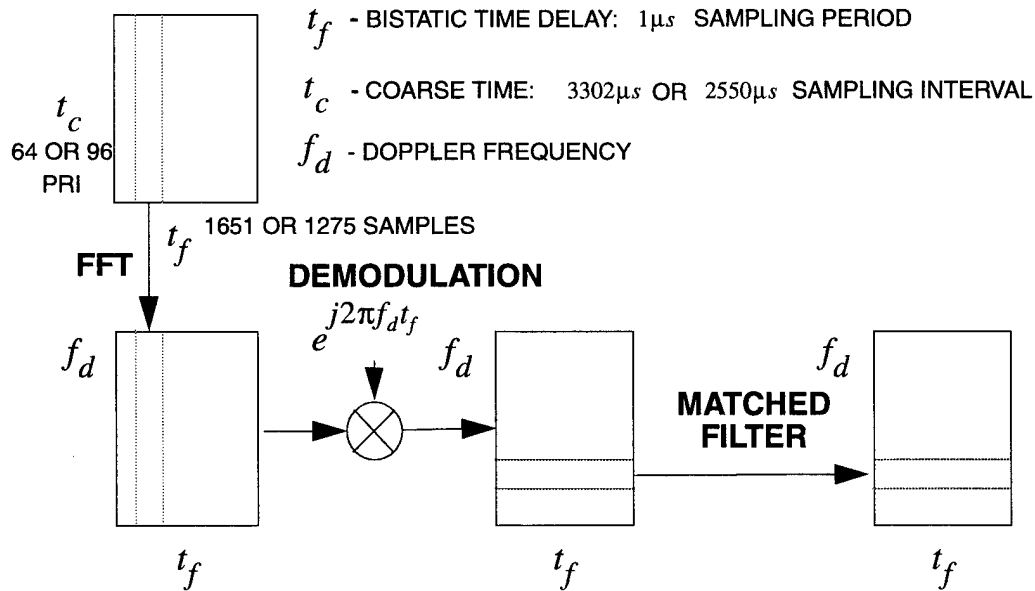


Figure 10. RSTER Doppler Processing and Matched Filtering

are passed through a matched filter, which is a convolution by the time-reversed pulse shape. This process is also termed pulse compression. As was seen, the time-reversed pulse shape is modified for PN to reduce sidelobe levels. The convolution is performed by taking the inverse Fourier transform of the product of the Fourier transform of the signal and the complex conjugate of the Fourier transform of the (modified) transmitted waveform. This processing generated a set of bistatic range profiles separated into Doppler frequency bands. A range profile was extracted from this array as follows. For the ground-based transmitter measurements, the frequency of the bin in which the maximum return appeared was deemed to represent the frequency offset between transmitter and receiver. The signals at all time delays were then taken from this frequency bin. For the airborne transmitter measurements, the signals were shifted in Doppler because of the motion of the aircraft, the Doppler shift being different for different scatterers. For each time delay and azimuth beam, the signal was extracted from the Doppler bin that contained the largest signal.

For the airborne measurements, it had been hoped that the effective scattering area could be reduced and the noise minimized by the Doppler processing. This would have entailed determining the expected Doppler shift from the aircraft velocity and selecting the appropriate Doppler cell at each delay. However, it was found that the frequency of the maximum response varied over a range of approximately two cells on either side of the expected value. This variation has been attributed to a variable latency in recording the aircraft velocity. Since no inertial data were available, this defect could not be corrected.

The choice in processing the aircraft signals was between taking the maximum of the five cells in the vicinity of the calculated Doppler shift, or taking the maximum of all 64 cells. Assuming an

exponential probability distribution of noise power, the level for 99% cumulative probability when taking the greatest of five cells is 1.3 dB higher than for the individual cells. When taking the maximum of 64 cells, the level for 99% cumulative probability is 2.8 dB higher than for the individual cells. In the interest of conserving time and maintaining simplicity in processing, it was decided to forego the 1.5 dB SNR advantage of using five cells in favor of the simpler approach of using all 64 cells.

## **7.7 Delay Tracking**

The determination of the range of a scatterer is based on the measurement of the difference in the arrival time between the direct signal and the reflected signal. In most cases, the time of arrival of the direct signal received by the monopole antenna was used as the time reference on a pulse-by-pulse basis. However, in a number of cases, the direct signal was corrupted by multipath effects and could not be used directly. In these cases a variety of tracking schemes were employed. Because the transmitter and receiver oscillators were unsynchronized, there was a slow drift in the arrival time relative to the local time base. The simplest tracking scheme employed was to assume a constant drift rate and to experimentally determine and apply an initial timing offset and drift rate; for the airborne transmitters, the changes in timing due to the aircraft motion were taken into account before applying a correction. On some missions, events occurred during the data-taking that introduced discontinuities in the timing. In these cases a list of the positions and displacements was manually generated and applied, along with the constant drift rate. As an alternative to manually determining the drift rate, provision was also made to perform piece-wise polynomial fits to the tracking data.

## **8. SYSTEM PARAMETERS FOR DELAY-AZIMUTH MEASUREMENTS**

### **8.1 Transmitter Antenna Gain for Delay-Azimuth Measurements**

The gain of the transmitting antenna used for the ground-based measurement was calculated as a function of azimuth and elevation using a model consisting of a vertically-stacked array of four dipoles in front of an infinite ground plane. The beam center was directed horizontally and toward the receiver in azimuth. The dipoles were vertically or horizontally polarized as required and were spaced one half wavelength apart.

For the airborne transmitting antenna, the model used was a single dipole in front of an infinite ground plane. The beam center was directed horizontally and in the direction of flight, or in the reversed direction of flight, depending on whether the transmission was from the nose or tail of the aircraft. The dipole was vertically or horizontally polarized as required.

### **8.2 Calculation of RSTER Receiver Antenna Gain**

The RSTER antenna consisted of 14 rows of 24 elements in front of a ground plane, the pattern of each element being approximately that of a dipole. The antenna was oriented with the plane of the elements vertical and with the rows horizontal (RSTER-0 configuration). At this orientation, the elements were vertically polarized. The horizontal beamwidth of each row was 5.8 degrees. The gain of each row was independently determined to be 17.5 dB over isotropic.

### **8.3 Measurement of Received Power**

The measurement of  $P_R$  involves a number of steps. These include beamforming, pulse compression, coherent averaging for static data, and Doppler processing for airborne data. Each of these processes will be discussed in the following paragraphs.

### **8.4 Measurement of RSTER Receiver Gain**

For the purpose of estimating the overall receiver gain, the receiver chain was considered to be divided into two sections. The first section was from the antennas to the input of the low-noise amplifiers. The second section was from the low-noise amplifiers to the recorded digital output. The loss in the receiver chain from the antenna to the low-noise amplifier was measured as 1.5 dB. The measurement of receiver gain from the low-noise amplifiers to the digitized recording was based on the measured receiver noise. The low-noise amplifiers were terminated at their inputs by matched loads and the noise at the

output recorded. The noise power  $P_N$ , generated by the terminating resistors, was calculated from  $P_n = kTB$ , where  $k$  is Boltzman's constant  $1.38 \times 10^{-23}$ ,  $T$  is the absolute temperature (290 degrees Kelvin), and  $B$  is the bandwidth. The effective noise is increased by the noise figure  $N_F$  of the receiver, which was independently measured at 5 dB. In connection with most missions, recordings were made of the receiver noise. In the analysis, the average noise across the receivers was taken from a suitable recording and the receiver gain calculated.

## 8.5 Receiver Bandwidth

The RSTER receiver passband is gaussian in shape and has a nominal -3 dB bandwidth of 200kHz and a nominal noise bandwidth of 212.8 kHz. To obtain an accurate measure of the noise bandwidth, the noise over a known narrow band in the center of the passband was measured and compared with the noise over the full receiver bandwidth. From this measurement the effective noise bandwidth was calculated to be 232.8 kHz.

## 8.6 Receiver Equalization

For other applications of these data, particularly those involving nulling of broadband signals, it is important that all receivers should have identical frequency responses across their full bandwidths, thus some of the RSTER data used for this study had been processed to equalize the receiver frequency responses. For the current application, there was no requirement for accurate equalization; however whenever equalized data were available, they were used.

## 8.7 Amplitude Calibration

Measurement of the receiver gain was performed by measuring the noise output of the receiver system and incorporating the nominal receiver noise figure (see Section 8.4). The overall receiver gain,  $G_R$  was then calculated by including the measured loss between the antenna and the receiver front end. In association with many of the missions, a recording was made of receiver noise. If such a record was available for a particular mission, it was used for receiver gain calculations. If a record was not available, an average figure was used.

As a check on the calibration based on receiver noise, calculations were made based on the direct signal from the transmitter. For those missions where both transmitter and receiver antennas had the same polarization, the theoretical direct signal was calculated and compared with the recorded signals. The results of these observations will be discussed along with the other results.



## 8.8 Data Selection Criteria

The principal objective in this analysis was to derive statistics of the scattering from the valley floor. Data from this area were selected by limiting the altitude to a maximum of 1600 m above sea level. This limit was designed to exclude the sloping surfaces at the base of the surrounding mountains. To exclude low-amplitude returns due to anomalous propagation, those ground positions that were shadowed from either the transmitter or the receiver were eliminated.

Beyond 90 degrees from the transmitter antenna boresight, the transmitter antenna gain was not known. Returns due to radiation in these directions were therefore rejected.

For the delay-Doppler bistatic data, certain other signals were rejected. When the receiving antenna azimuth is near that of the transmitter, the calculated values of the ground position for each delay/azimuth resolution cell is inaccurate. Because of this, data taken at azimuths within six degrees of the azimuth of the transmitter were rejected. The very strong specular signals from the ground area near the direct line between the transmitter and receiver can cause spurious results by entering the receiver in the skirts of the antenna response. These signals had a very short differential delay and hence were easily eliminated by rejecting signals with a differential delay of less than 13 microseconds.

In examining and comparing the amplitude distributions of the values of  $\sigma_0$  obtained from the delay-Doppler wide-area measurements, certain characteristics were noted. To further investigate these effects, the calculations were repeated for a smaller selected area of the terrain.

## 9. DELAY-DOPPLER DATA REDUCTION

The data presented for analysis was the digitized baseband output of the Beechcraft 90 King Air receiver. Mode 3<sup>1</sup> data were used for measuring  $\sigma_0$ . In this mode the modulation was PCW. The carrier frequency was 431 MHz, the pulse length was 5 microseconds and the transmitter PRF was 2 kHz. The receiver sampled the signal at 5 microsecond intervals and recorded 110 samples every 2 milliseconds for UHF and every 4 milliseconds for VHF. The receiving PRI sampling rate was not synchronized to the transmitter PRF but was adjusted to be close in frequency. The 110 samples recorded for each PRI provided a 10 percent margin.

The sequence of operations performed on the data were as follows. The sampling rate was doubled by interpolating with a low-pass filter. The data from each recorded pulse repetition interval (PRI) were truncated to 200 samples (one transmitter PRI) and shifted (with wrap around) to position the direct signal in a specific cell near the beginning of the array, typically cell #50.

The data were divided into segments of 64 PRI each, the data span for each data set generally yielding 35 segments. In the receiving system, the signal is translated to baseband before sampling. The sampling process introduced a small constant component. For each segment of the data, the constant detector bias was first measured by averaging the complex signals that were delayed sufficiently to avoid direct and scattered returns. The sampling bias was then removed from all the data in the section. Each delay cell was then multiplied by a -50 dB Chebychev weighting function and processed in a FFT to obtain an estimate of its Doppler spectrum. The squared amplitudes of the signals in each delay cell were then averaged over the number of segments.

A matrix of ground positions was specified for the area of interest. For each ground position, the delay and Doppler shift were calculated from the aircraft trajectories and the ground elevation. The signal was then extracted from the nearest delay-Doppler bin. Because neither the delay nor the Doppler shift measurements were absolute, the differences between the direct path signal and the ground-reflected signal were used for both. Values of  $\sigma_0$  were then calculated from the signal amplitude using the bistatic radar equation and parameters described elsewhere in this report.

### 9.1 Delay Tracking

The determination of the position of a scatterer was based in part on the measurement of the difference in the arrival time between the direct signal and the signal reflected from the scatterer. Because the transmitter and receiver oscillators were unsynchronized, there was a slow drift in the arrival time relative to the local time base. The simplest method of measuring the difference in the time of arrival would be to align the direct signal in a specific cell on a pulse-by-pulse basis. However, in these data, the

---

1. The parameters of the various modes of operation are given by Zurk [17].

signal was critically sampled (one sample per pulse length) and a quantization error would be incurred by this simple method. Instead, the method employed was to first correct for the known distance between the aircraft and then to assume an initial offset and a constant drift rate, the values of which were determined experimentally for each data set.

## 9.2 Resolving Ambiguities in Delay-Doppler Processing

In delay-Doppler processing, the scattered signal from each ground patch was extracted from the data on the basis of the delay and Doppler shift expected for a scatterer in that position. Figure 11 shows a

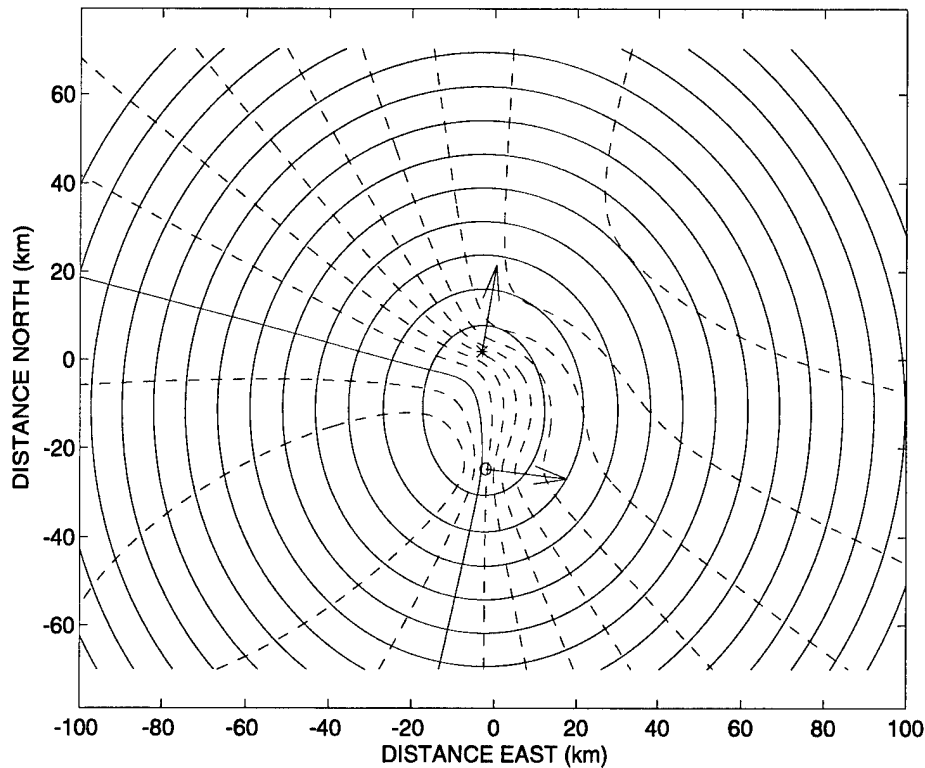


*Figure 11. Typical Isodelay and Isodoppler Plot*

typical plot of constant delay (solid lines) and constant Doppler (broken lines) for the ground reflection points. The position of the east-bound transmitter is shown by a circle and that of the north-bound receiver by an asterisk. The solid Doppler contour indicates zero Doppler shift. To the north and east of this line the Doppler shift is positive, i.e. negative range rate. The interval between the constant delay lines is 10 resolution cells. The interval between constant Doppler lines is 5 resolution cells.

It can be seen that each line of constant delay crosses each line of constant Doppler shift at an even number of points. This means that for each selected point on the ground, there is at least one other

point that could potentially give returns with the same delay and Doppler values. This ambiguity was resolved differently for the various polarization combinations.

For all cases except VHF VV-pol measurements the delay-Doppler ambiguities were resolved by exploiting the antenna patterns. For UHF V-pol and H-pol, and for VHF H-pol, the transmitting antenna was mounted on one side of the aircraft or the other and thus did not radiate significant energy to the opposite side. If there were only two ambiguous ground points at a particular delay and Doppler with one of them in the beam and the other out of the beam, the one in the beam would be the only contributor to the signal. In selecting data for statistical purposes, the appropriate ground area and Doppler range were selected to eliminate ambiguities.

For VHF VV-pol measurements, both transmitting and receiving antennas were omnidirectional in azimuth. Ambiguities could not then be resolved using antenna patterns. For these experiments, the aircraft were flown along the same track, with appropriate spacing (chase mode). The delay-Doppler patterns, shown in Figures 107, 109, 111 and 113, were therefore symmetrical about the aircraft track, as were the out-of-plane angles and the grazing angles. If the terrain was uniform, there would be no need to resolve the ambiguities in assembling data for the statistics.

## 10. SYSTEM PARAMETERS FOR DELAY-DOPPLER MEASUREMENTS

### 10.1 Operating Modes

The measurement system was operated with three distinct combinations of PRF pulse lengths and sampling rates. The parameters for the three modes are given in Table 3. The analysis for the determination

Table 3. Operating Mode Parameters

Mode	Transmitter PRF (Hz)	Transmitter pulse length (mms)	Receiver PRF (Hz)	Sampling frequency (MHz)
1	2500	0.333	2	4.0
2	5250	0.333	250	4.0
3 VHF	2000	5.00	250	0.2
3 UHF	2000	5.00	500	0.2

of  $\sigma_0$  made use of Mode 3 data only. However, some Mode 2 data was used for calibration purposes.

### 10.2 Antenna Patterns for Delay-Doppler Measurements

The antenna patterns of the two aircraft antennas were measured by transmitting from the aircraft and receiving on the ground. These measurements and data reduction are detailed by Kove et. al.[19]. Due to scheduling constraints no antenna patterns could be measured for the King Air receiving antenna at UHF. These patterns were assumed to be those of dipoles in free space.

The measurements were taken at an elevation of approximately -7.5 degrees with respect to the aircraft axes. This is at the extreme of the range for the scattering measurements, in which the elevation angle varied from approximately -7.5 to -25 degrees. In reducing the ground-scattered data, and in calculating the theoretical direct signal, the gains of the H-pol antennas were assumed to be constant with varying elevation angle and those of the V-pol antennas to be similar to vertical dipoles.

### 10.3 Measurement of Receiver Gain

For the delay-Doppler experiments, the calibration of the King Air receiver was performed by methods similar to those described in Section 8.4. These measurement were reported in detail by S. Coutts [18].

## 10.4 Verification of UHF System Parameters by Direct Signal Measurement

UHF system parameters were calculated from independent measurements as discussed in previous paragraphs. Measured direct signals were then used to validate these results as follows. In measuring the direct signal, multipath effect were avoided by taking readings at the shortest possible delay.

Table 4 shows the UHF direct signal amplitudes compared to the values calculated using the independently-determined parameters. The measured signal minus the calculated is shown in the right-most column and is labeled "EXCESS". The left-most column shows the data set title, the second column shows the polarization, the third column shows the mode and the fourth and fifth shows the azimuth of the RLOS with respect to boresight.

**Table 4. UHF Direct Signal Measurements**

DATA SET	POL	MODE	TRANS-MITTER AZIMUTH (deg)	RECEIVER AZIMUTH (deg)	EXCESS
M3B21_1002	HH	2	-1	7	-3
M3D21_1001	HH	3	26	-66	6
M3D21_2001	HH	3	35	-50	-2
M3E21_1001	HH	3	83	-63	3
M3E21_2001	HH	3	34	-46	-2
M3B21_1001	VV	2	-2	7	-2
M3D21_1003	VV	3	-8	-78	-11
M3D21_2003	VV	3	15	-67	-9
M3E21_1003	VV	3	13	-85	-12
M3E21_2003	VV	3	27	-55	-8
M3D21_1002	VH	3	13	-79	-19
M3E21_1002	VH	3	29	-67	-14

For the transmitter on the Cessna, boresight was perpendicular to the aircraft on the port side. For the receiving antennas on the King Air, boresight was to the port or starboard, depending on the geometry of the measurement. Positive azimuths were toward the nose in either case.

The first and sixth rows in the table show Mode 2 data. For this mode, the two aircraft flew along parallel tracks and were approximately broadside to each other. The azimuth of the RLOS with respect to boresight was small for both transmitter and receiver, as is seen in the columns four and five of the table. The excess of the measured direct signal over the calculated is -3 dB for HH-pol and -2 dB for the VV-pol. One possible contributor to the error is a difference in the antenna gain due to the different elevation angles for the direct signal measurement and for the antenna pattern measurement.

Rows two to five of the table show the HH-pol Mode 3 data. The largest error (6 dB) in HH-pol is seen on the second row of the table. This occurs when the receiver RLOS is 66 degrees from broadside, and is probably due to an inaccuracy in measured antenna gain.

Rows 7 to 10 show the VV-pol data. The two largest errors in the Mode 3 direct signal VV-pol measurements are 11 and 12 dB. These are likely to be due to a null in the receiver antenna when receiving from tail-on, since there are communication antennas projecting from the aircraft belly to the rear of the V-pol receiving antenna.

The bottom two rows of the table show the VH-pol measurement. These are included in the table to give an indication of the cross-polarization coupling.

## 11. WIDE-AREA DELAY-AZIMUTH VV-POL RESULTS

### 11.1 Database

Data were available for both bistatic and monostatic configurations. The bistatic data analyzed included both ground-based and airborne data. For the ground-based bistatic data, measurements were taken at 434.8, 435.0, 435.2 and 435.4 MHz with the transmitter positioned on Socorro Peak, Salinas Peak and Sierra Blanca. The single frequency of 435.0 MHz was used for the airborne missions in which the aircraft flew along a radial line from the receiver over each of the sites. The ground-based data was taken from the cartesian representation of  $\sigma_0$  whereas the airborne data was taken from the polar representation. The results of the missions associated with Socorro Peak are dealt with in some detail. Other results are dealt with briefly. For the monostatic data, RSTER was situated on North Oscura Peak and was used for both transmitting and receiving.

### 11.2 VV-pol Ground-based Results from Socorro Peak

Figure 12 shows a typical cartesian plot of  $\sigma_0$ . The results were first reported in an internal Lincoln Laboratory internal memo [20]. The data for this plot were taken with the transmitter on Socorro

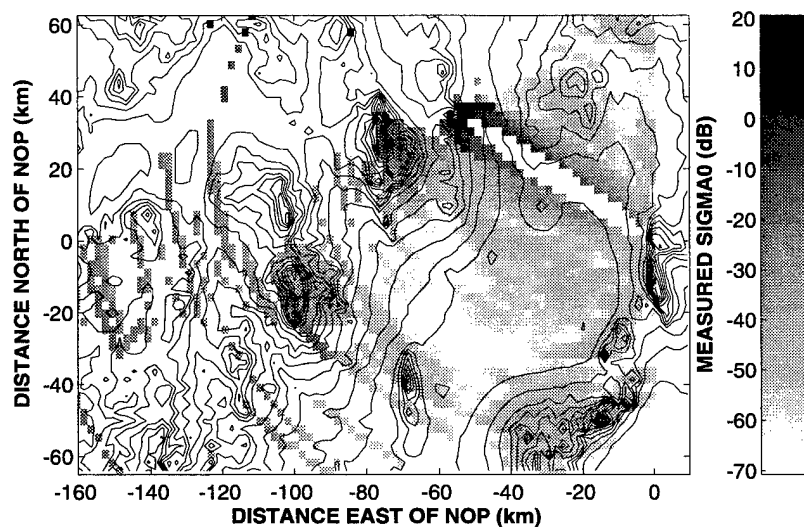


Figure 12. Measured Bistatic Scattering Coefficient, Socorro Peak, VV, PN

Peak, which is situated at -55 km east and 35 km north of the receiver. The polarization of both transmitter and receiver were vertical and the modulation was PN. The threshold was set 6 dB above the noise/



sidelobe level; signals below the threshold are not plotted. It is apparent that  $\sigma_0$  is high on the mountain slopes and low on the valley floor.

Figures 13 and 14 show some statistical results from the returns with the transmitter at Socorro Peak; Figure 13 is for PCW modulation and Figure 14 is for PN. The upper left-hand frame in each figure

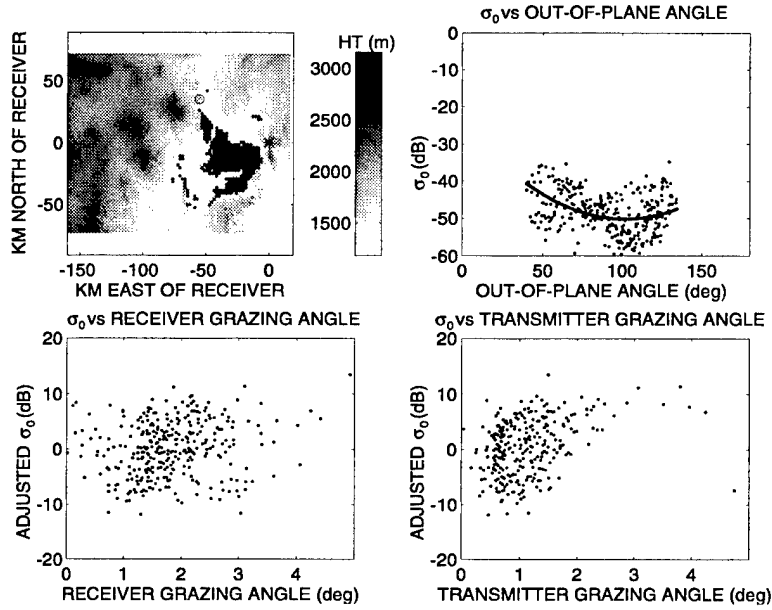


Figure 13. Distribution of Bistatic Scattering Coefficient, Socorro Peak, VV, PCW

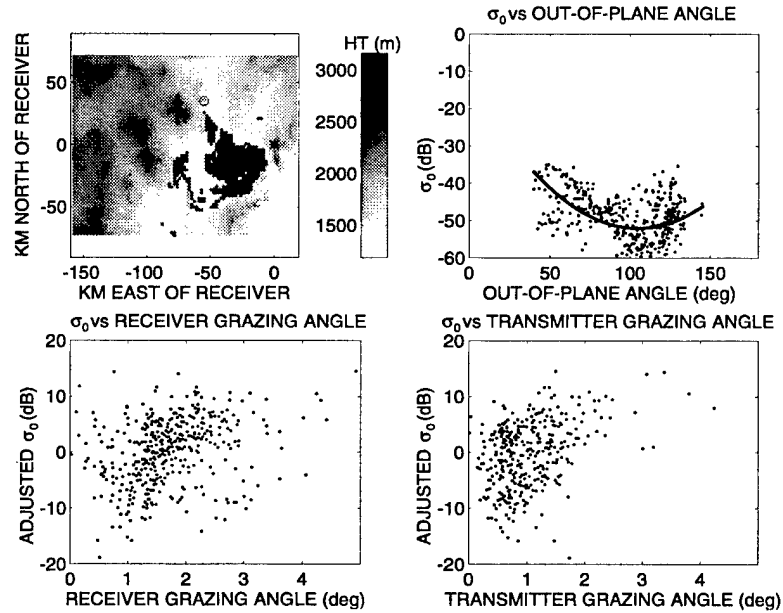


Figure 14. Distribution of Bistatic Scattering Coefficients, Socorro Peak, VV, PN

shows the locations of the points of reflection where the returns are above threshold. It can be seen that there are more returns on the PN plot because of the greater signal to noise/sidelobe level. The upper right frame in each figure shows the distribution of  $\sigma_0$  with respect to out-of-plane angle. It can be seen that there is close agreement between the PCW and PN results and that there is a variation of  $\sigma_0$  with out-of-plane angle. The smooth curve on this plot represents a parabola fitted to the points.

The lower two frames show the values of  $\sigma_0$  with the parabolic function subtracted from them. The values are plotted against receiver grazing angle and transmitter grazing angle. The value of  $\sigma_0$  tends to rise with increasing transmitter and receiver grazing angles.

### 11.3 VV-pol Airborne Results from Socorro Peak

Figure 15 shows the values of  $\sigma_0$  obtained with the transmitter in an aircraft flying along a radial aligned with Socorro Peak. The geometry of the scenario is somewhat different than with the ground-based

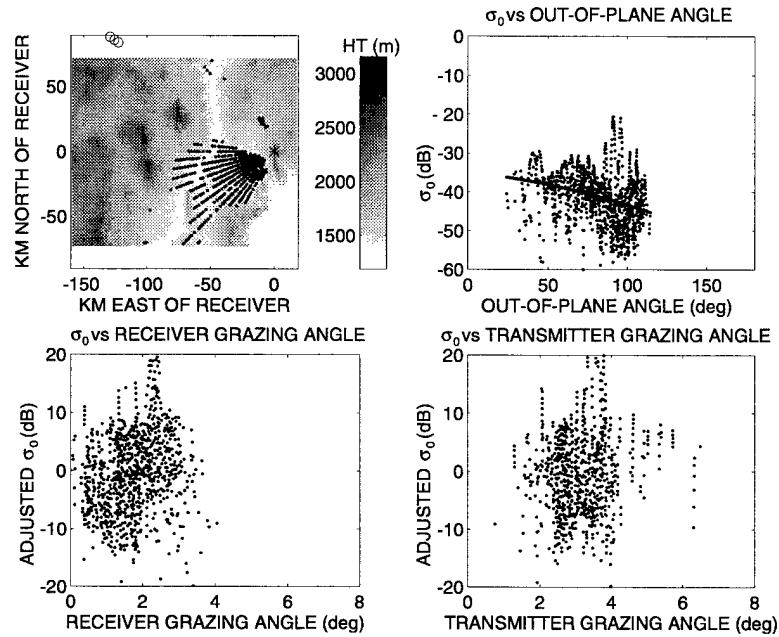


Figure 15. Distribution of Bistatic Scattering Coefficient, Socorro Peak, VV, PN, Airborne

transmitter in that the aircraft was at a much greater range and the transmitter grazing angle varied over a wider range. It can be seen that  $\sigma_0$  is higher and that its dependence on out-of-plane angle appears to be less than for the static transmitter. Since these two missions do not cover the same range of transmitter grazing angles, these results suggest a dependence of  $\sigma_0$  on grazing angle.

One possible reason for the different values of  $\sigma_0$  for the ground-based and airborne data is that for the different geometries, different areas are active at the same angles, and that the scattering

characteristics of the ground might not be uniform over the area selected. To investigate this possibility, the analysis of the airborne data was repeated using a smaller ground area. The area selected was a 20 km by 30 km area centered at 30 km west and 15 km south of the receiver. The results for the ground-based and airborne data are shown in Figures 16 and 17 respectively. It can be seen that the results agree with

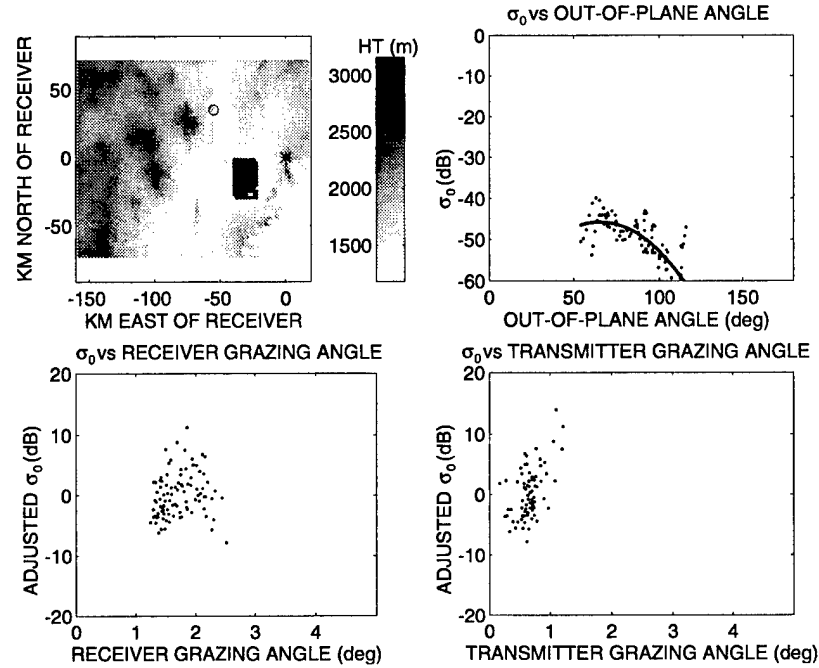


Figure 16. Distribution of Bistatic Scattering Coefficient, Socorro Peak, VV, PN, Limited Area

those obtained from the larger area. This indicates that variations in terrain within the larger area do not significantly contribute to the observed differences in  $\sigma_0$  between ground-based and airborne tests.

#### 11.4 Ground-based and Airborne VV-pol Results from Salinas Peak

Figure 18 shows the VV-pol  $\sigma_0$  values obtained from the ground-based data associated with Salinas Peak. Figure 19 show the corresponding air-borne data. Data from four frequencies are shown. Results from the PN data are shown rather than PCW as the S/N was higher. These results are very similar to those associated with Socorro Peak shown in Figures 14 and 15.

#### 11.5 Ground-based and Airborne VV-pol Results from Sierra Blanca

Figure 20 and 21 show the VV-pol  $\sigma_0$  values for the data associated with Sierra Blanca. The static results are similar to those obtained at Socorro Peak and Salinas Peak. In contrast to the ground-based results, the values of  $\sigma_0$  for the airborne mission are very low. It is apparent from the locations of

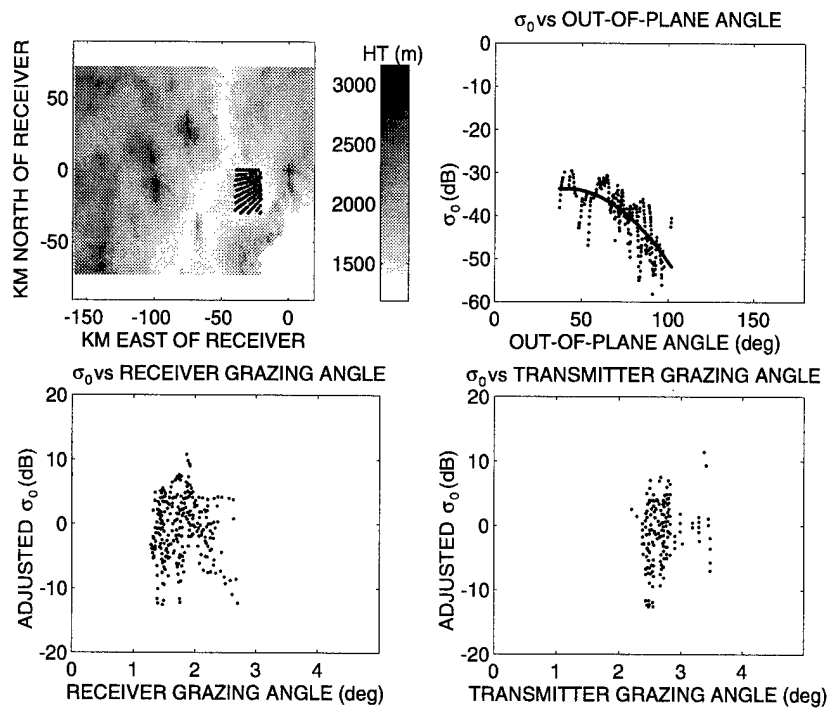


Figure 17. Distribution of Bistatic Scattering Coefficient, Socorro Peak, VV, PN, Airborne, Limited Area

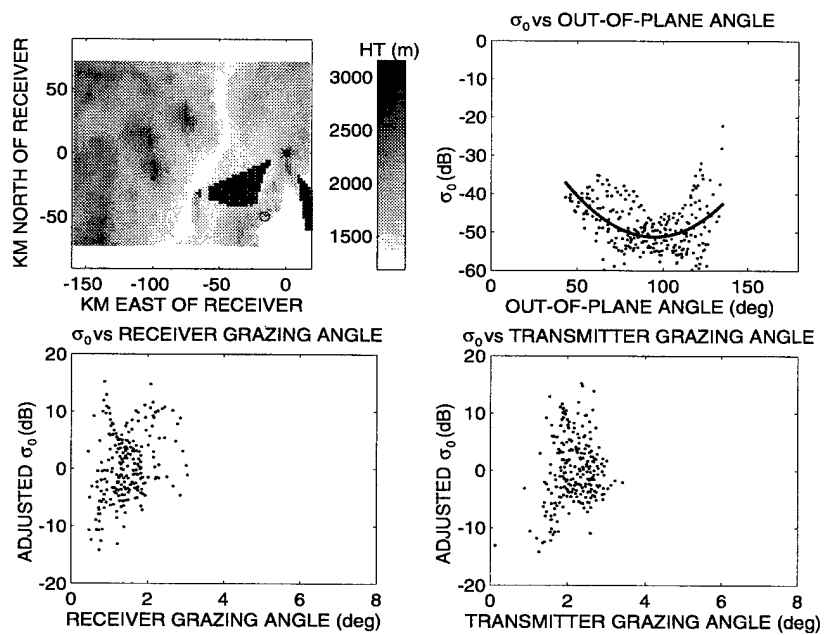


Figure 18. Distribution of Bistatic Scattering Coefficient, Salinas Peak, VV, PN

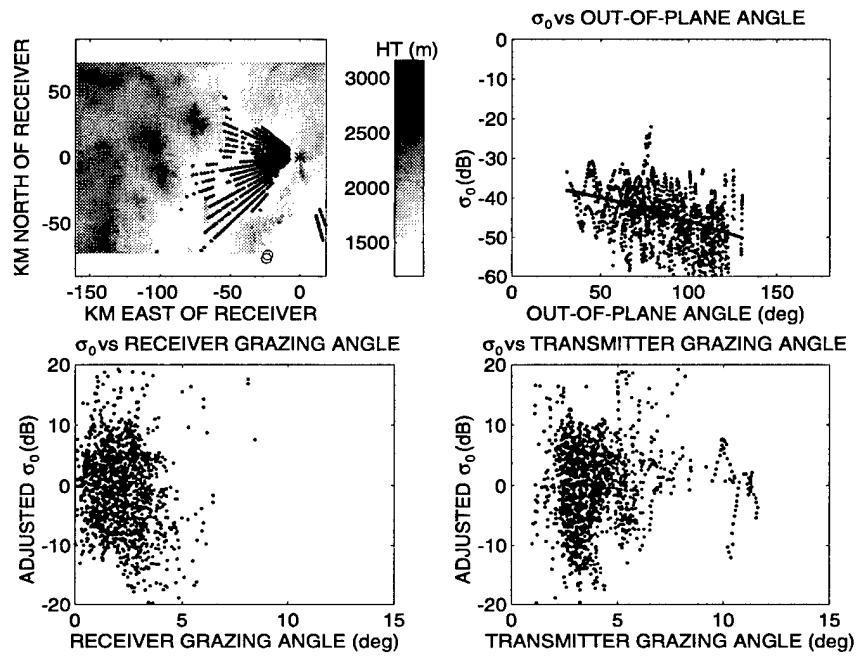


Figure 19. Distribution of Bistatic Scattering Coefficient, Salinas Peak, VV, PN, Airborne

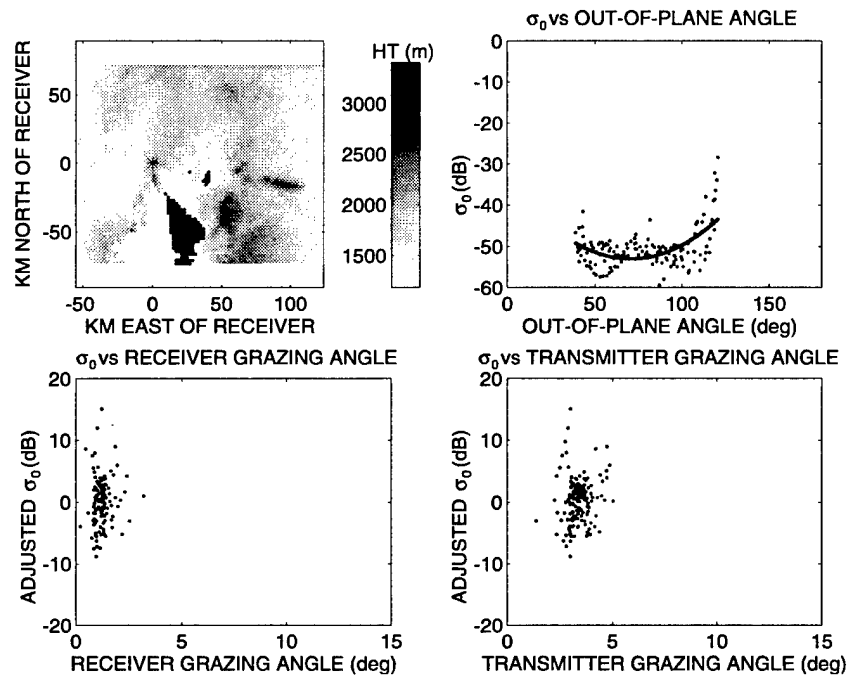


Figure 20. Distribution of Bistatic Scattering Coefficient, Sierra Blanca, VV, PN

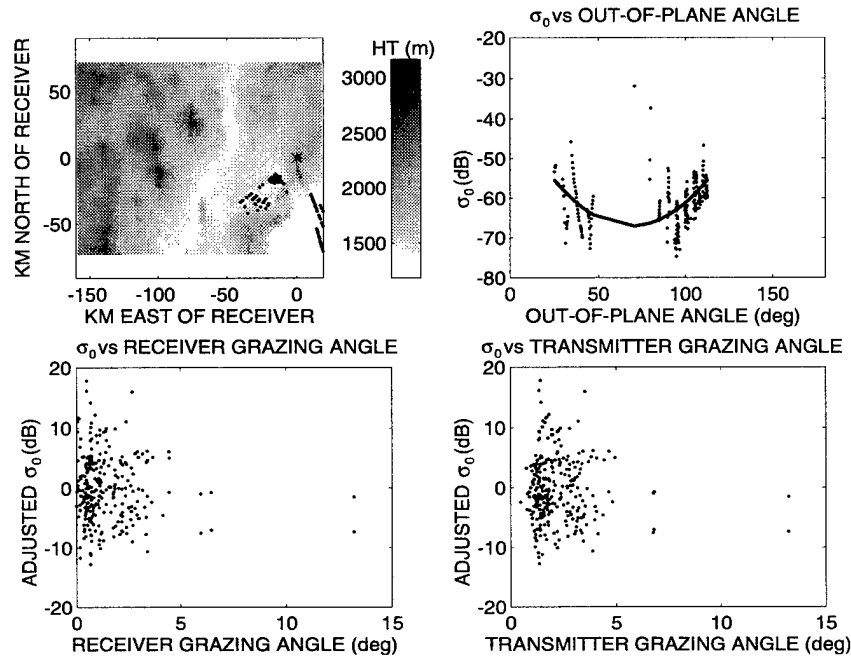


Figure 21. Distribution of Bistatic Scattering Coefficient, Sierra Blanca, VV, PN, Airborne

the scattering points that the area illuminated by the airborne transmitter was very different from that illuminated by the static transmitter. These airborne results are not considered representative of the scattering from the valley floor and have not been included in the overall assessment.

## 11.6 Combined VV-pol Results

### 11.6.1 Full Area

The ground-based and airborne returns associated with Socorro Peak and Salinas Peak, and the ground-based returns associated with Sierra Blanca were combined. The area active in the Sierra Blanca data was separate and distinct from that involved in the Socorro Peak and Salinas Peak measurements; however, the terrains were similar in appearance and were assumed to have similar scattering characteristics.

Figure 22 shows the VV-pol  $\sigma_0$  values obtained by combining the measurements. The upper left-hand frame shows the locations of the points of reflection. The upper right frame shows the distribution of  $\sigma_0$  with respect to out-of-plane angle. The curve fitted to the data in the upper right hand frame is a quadratic function of the out-of-plane angle. The coefficients of the quadratic, in descending order, are,  $-0.000292$ ,  $-0.067$  and  $-36.1$ ; the units are dB and degrees. The values of the function at 0, 90 and 180 degrees are  $-36.1$ ,  $-44.5$  and  $-57.7$  dB.

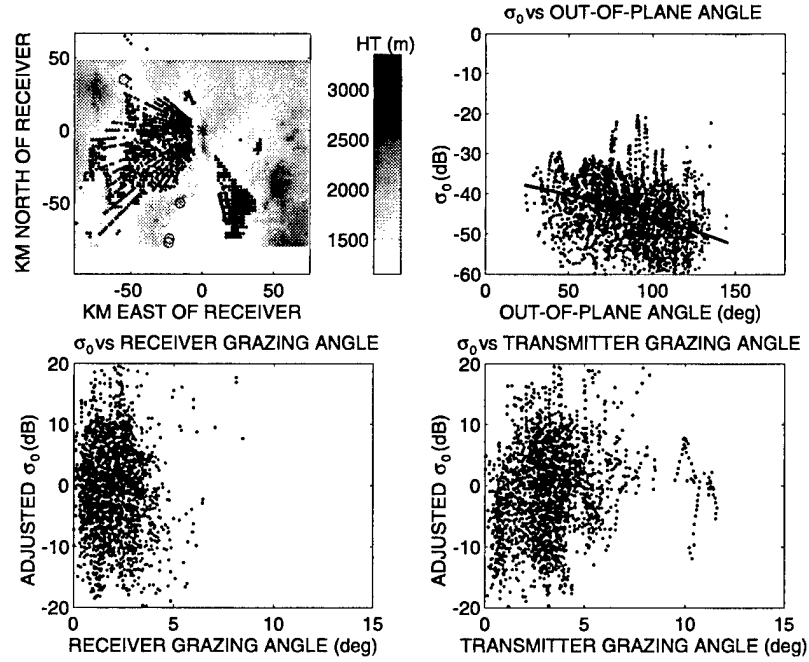


Figure 22. Distribution of Bistatic Scattering Coefficient, VV

The lower two frames of Figure 22 show the values of  $\sigma_0$  with the parabolic function subtracted from them. This quantity is termed “adjusted  $\sigma_0$ ”. The values are plotted against receiver grazing angle and transmitter grazing angle.

To determine the value of  $\alpha$  in the GLF model  $\sigma_0 = \gamma(\sin\theta_t \times \sin\theta_r)^\alpha$ , the log (to the base 10) of  $\sigma_0$  is plotted against the log of the product of the sines. The plots for VV-pol are shown in Figure 23. Each of the subplots in the figure shows the data for a 20 degree range of out-of-plane angle. Superimposed on each frame is a straight line representing the best fit to the GLF. Note that in fitting,  $\alpha$  is allowed to vary with out-of-plane angle while  $\gamma$  is held constant. The value of  $\sigma_0$  at zero on the horizontal axis gives the value of  $\gamma$ . For this data set  $\gamma$  is equivalent to -31 dB and  $\alpha$  varies from 0.32 to 0.54 depending on the out-of-plane angle. Each of the subplots is labeled with the slope of the straight line fitted to the data points. This slope is equal to the value of  $\alpha$  in the formula above.

Figure 24 shows the distribution of the amplitudes of  $\sigma_0$  for the VV-pol wide-area data. These statistics are obtained by combining the subsets shown in Figure 23. For each subset, the fitted straight line is subtracted from the value of  $\log\sigma_0$  and the result multiplied by 10 to convert to dB. The values from each subset are then assembled and sorted in order of magnitude. The index of the sorted values, divided by the total number of values, is shown plotted against adjusted  $\sigma_0$  in Figure 24. This curve then gives the proportion of values below the value indicated on the horizontal axis.

Three other curves have been plotted on this figure, each representing a different probability distribution. These distributions are Rayleigh, Weibull and lognormal. For each distribution law, the

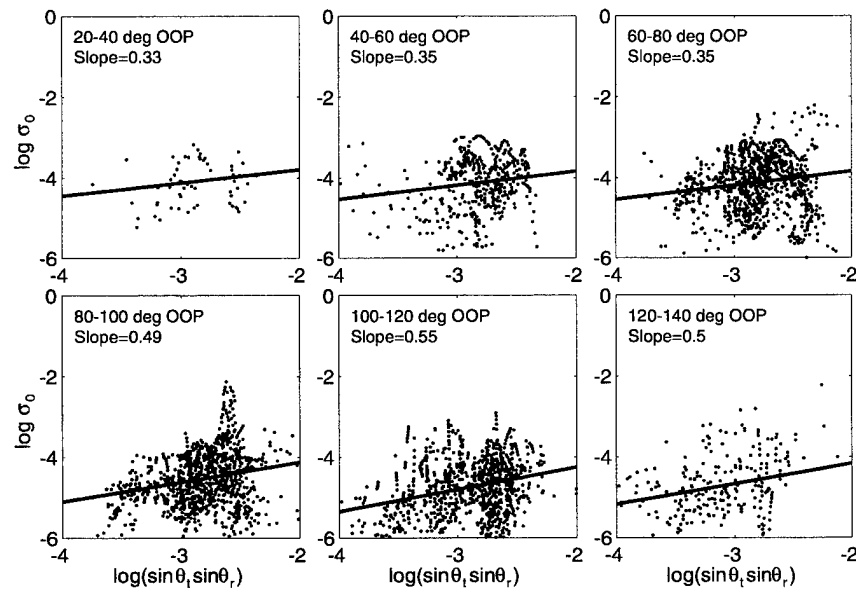


Figure 23. Bistatic Scattering Coefficient vs. Product of Sines of Grazing Angles, VV

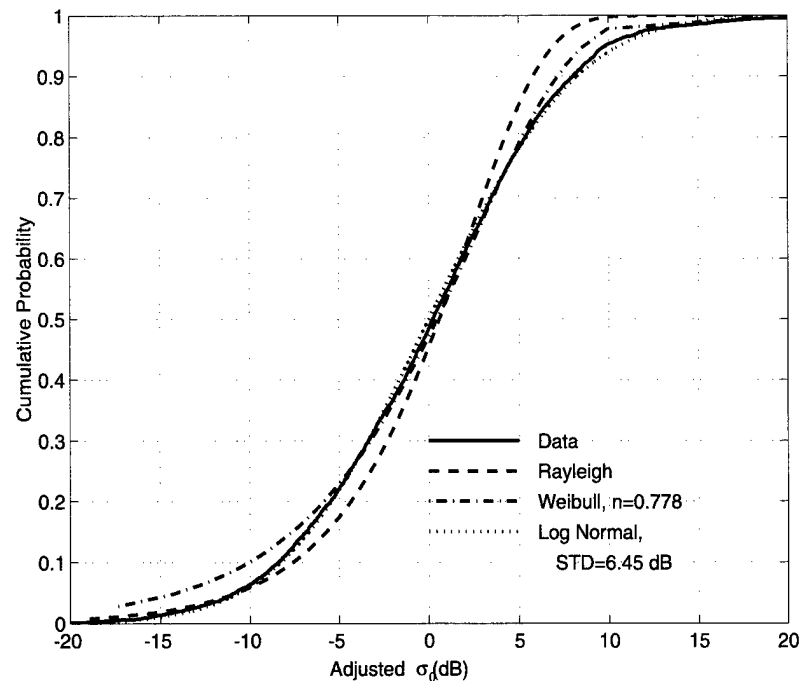


Figure 24. Cumulative Amplitude Distribution, Bistatic, VV

parameters were adjusted to give a least-squares fit to the data. It can be seen that the distribution in the data points is broader than the Rayleigh distributions, with the data having more points at the higher amplitudes. The Weibull distribution fits the higher amplitudes better but shows increased errors at the low end. The best fit is with the lognormal distribution law, with a scale width of 6.45 dB.



## 11.6.2 Limited Area

Since the amplitude distribution of  $\sigma_0$ , when measured over a large area of dessert terrain, proved to be broader than the Rayleigh distribution, the calculations were repeated over a smaller central area measuring 20x30 km. The extent of this smaller sample area was from 40 km west to 20 km west of NOP in the E-W direction and from 30 km south to NOP in the N-S direction.

Figures 25 and 26 show the  $\sigma_0$  values obtained when the scattering area was confined to this smaller area. It can be seen that the distribution of amplitudes is closer to Rayleigh than to lognormal. In

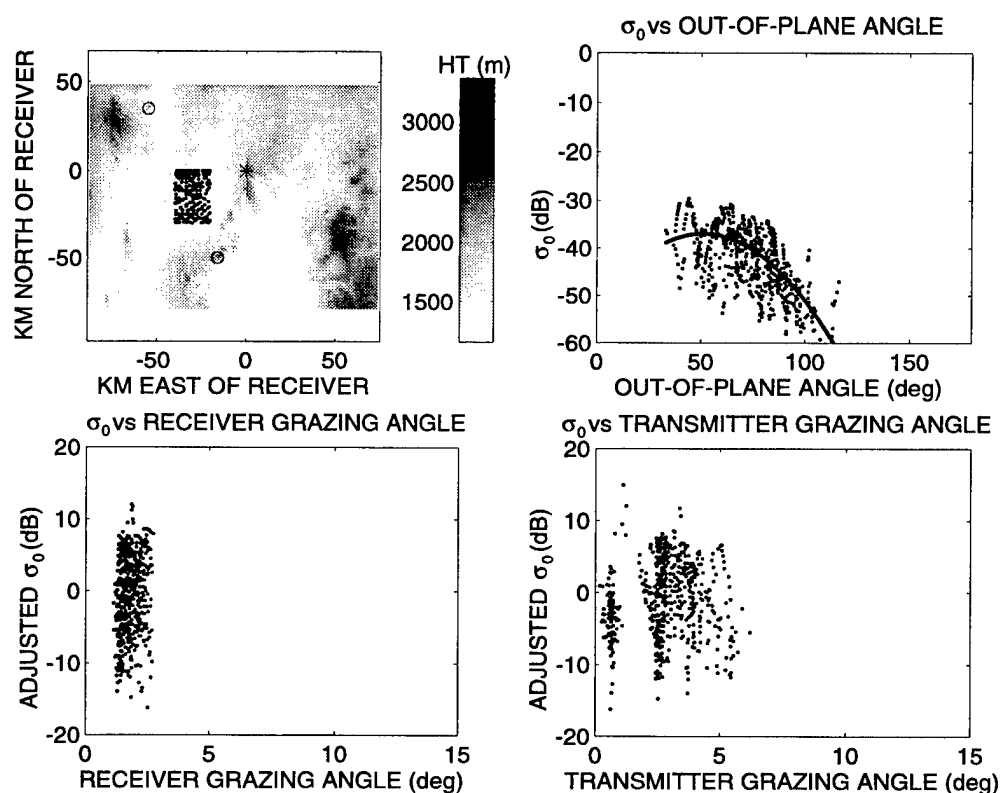


Figure 25. Distribution of Bistatic Scattering Coefficient, VV, Limited Area

terms of the lognormal parameters, the distribution has been narrowed from 6.45 dB to 5.28 dB by reducing the area. The fact that the full area gives a broader amplitude distribution than the smaller area suggests that there the local statistics are not uniform over the full area.

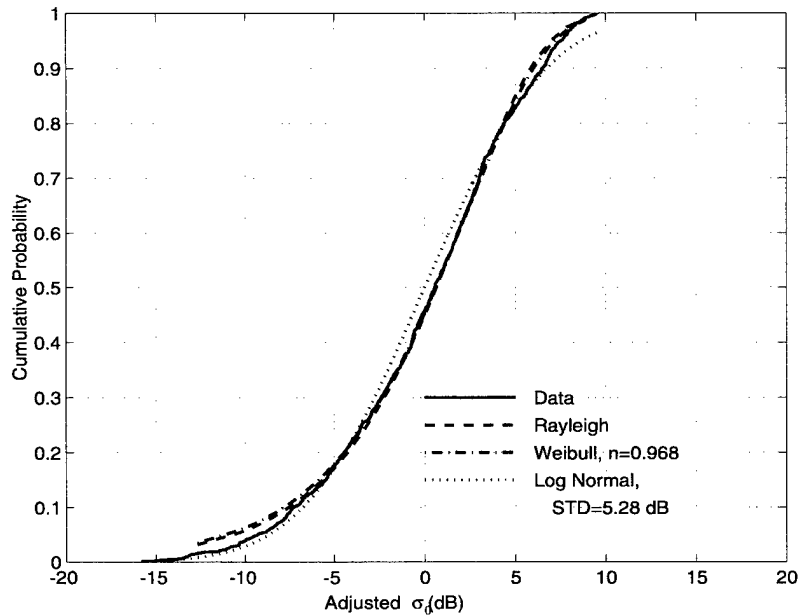


Figure 26. Cumulative Amplitude Distribution, Bistatic, VV, Limited Area

## 11.7 Monostatic VV-pol Results

The monostatic data were collected on 27th March 1993 at WSMR. RSTER was situated on North Oscura Peak (NOP) and was used for both transmitting and receiving. The data were reduced and analyzed, and the results reported in an internal memo by John Jayne, dated October 18, 1993. The reduced data were made available in MATLAB files; the variables contained in these files were raw clutter power, clutter to noise ratio, reflectivity and  $\sigma_0$ , all as functions of range and azimuth.

In deriving the statistics for this report, the values of  $\sigma_0$  were extracted from the MATLAB files and processed in a fashion similar to that used for the bistatic data. Statistics are shown for both the full area and for the limited area.

### 11.7.1 Full Area

Figure 27 shows the locations of the ground scattering points and the values of  $\sigma_0$  vs. grazing angle while Figure 28 shows the log (to the base 10) of  $\sigma_0$  plotted against the two times the log of the sine of the grazing angle. A straight line fitted to the points was found to have a slope of 0.77; this is the value of the exponent in the Generalized Lambertian Formula. The value of the straight line at  $2\log \sin \theta_1 = -3$  was  $-5.6$ .

Figure 29 shows the cumulative amplitude distribution for the monostatic data. It can be seen that the distribution is considerably broader than Rayleigh. The data appears to be approximately lognormal, except at the lower values, where it is closer to Weibull.

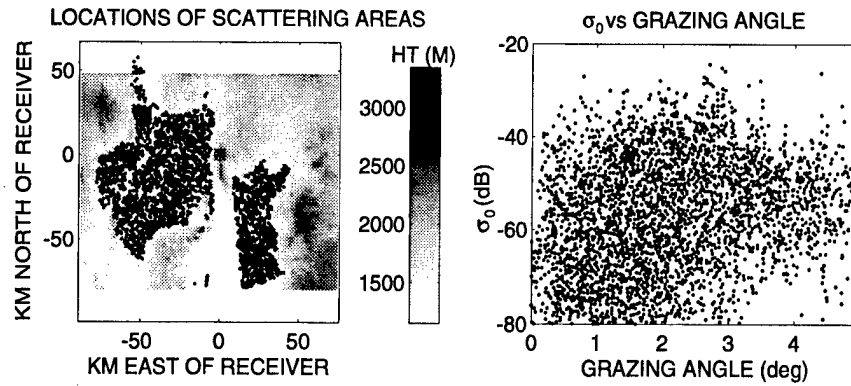


Figure 27. Distribution of Monostatic Scattering Coefficient, VV

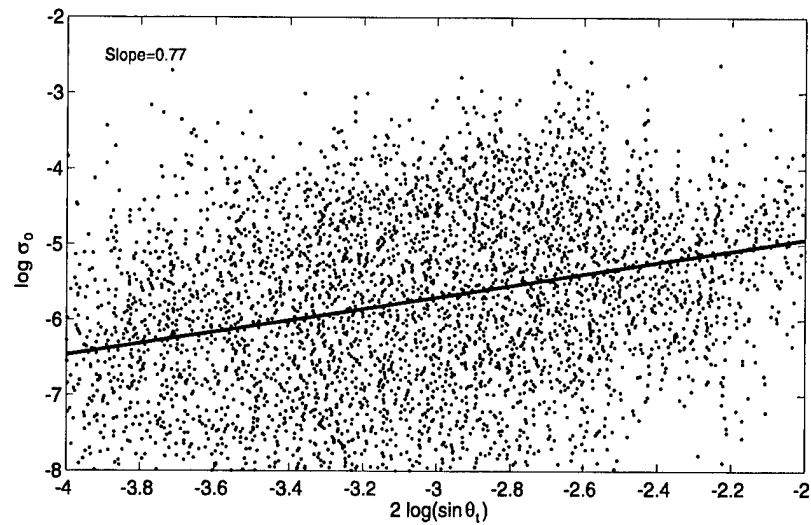


Figure 28. Monostatic Scattering Coefficient vs. Squared Sine of Grazing Angle, VV

### 11.7.2 Limited Area

Figure 30 shows the monostatic cumulative amplitude distribution obtained by limiting the scattering area to the 10x20 m area described in Section 11.6.2. The amplitude distribution is narrower than that for the full area but, is still considerably broader than Rayleigh.

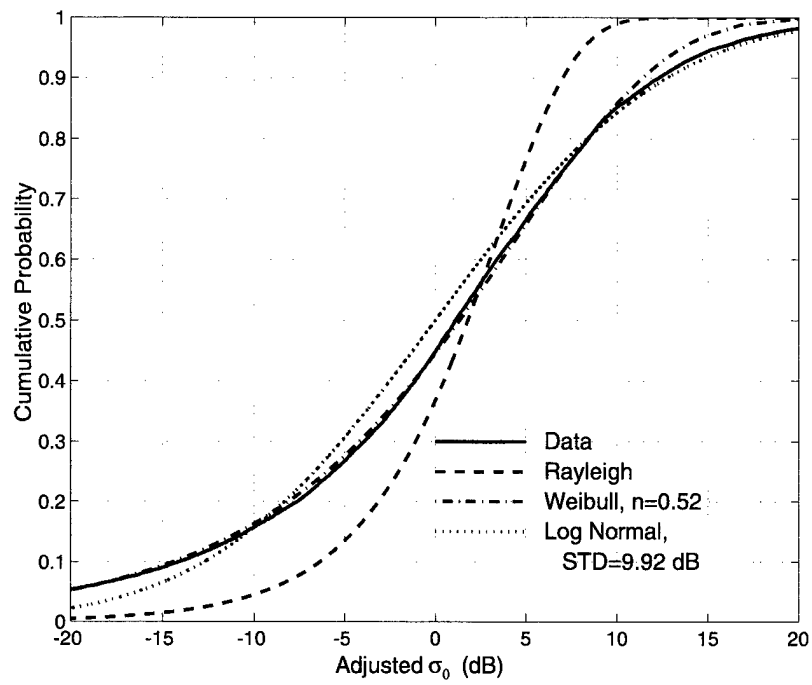


Figure 29. Cumulative Amplitude Distribution, Monostatic, VV

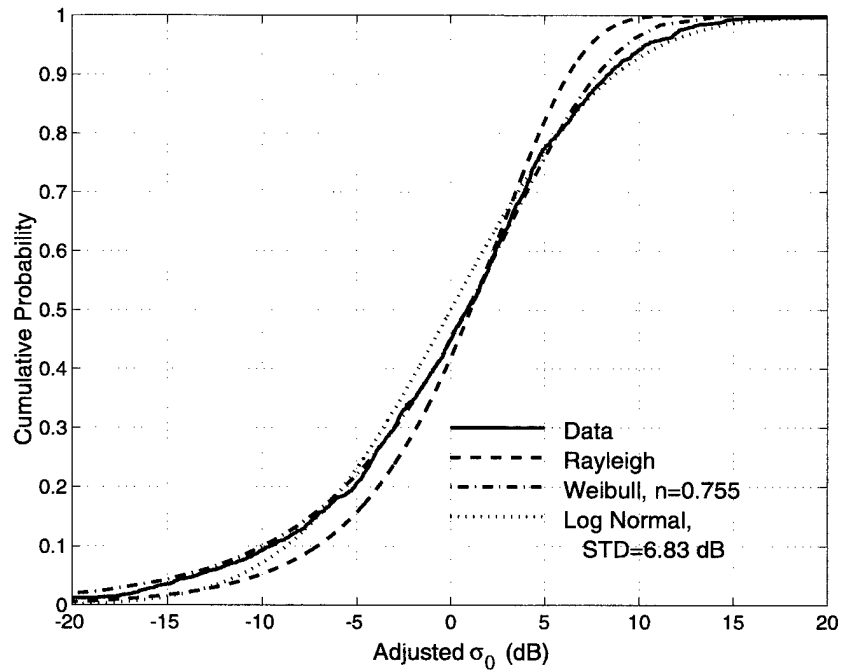


Figure 30. Cumulative Amplitude Distribution, Monostatic, VV, Limited Area

## 11.8 Comparison of VV-pol Bistatic and Monostatic Results

The bistatic and monostatic results were compared as follows: The mean receiver grazing angle for the bistatic measurements discussed in section 11.6.1 was approximately 2.0 degrees and the mean transmitter grazing angle was approximately 3.0 degrees. The log of the product of the sines of the grazing angles was therefore approximately  $-2.7$ . The value of  $\log \sigma_0$  for the GLF fitted to each OOP angle bin was extracted from Figure 23. A straight line was fitted to these values and was extrapolated to 180 degrees OOP angle to give a value of  $-4.8$ , equivalent to  $-48$  dB. For the same value of the product of the sines, the monostatic value of  $\sigma_0$  was read from the straight-line fit shown in Figure 28 to give a value of  $-56.0$  dB. It can be seen then that the results of the monostatic experiment are 8 dB below that from the bistatic data.

## 12. WIDE-AREA DELAY-AZIMUTH VH-POL RESULTS

### 12.1 Database

The analysis described in this section is based on data taken with both ground-based and airborne data transmitters. For the ground-based transmitters, measurements were taken at 434.8 , 435.0 , 435.2 and 435.4 MHz with the transmitter positioned on Socorro Peak, Salinas Peak and Sierra Blanca. A single frequency of 435.0 MHz was used for the airborne missions in which the aircraft was flown along a radial line from the receiver over the site. For the ground-based statistics, the delay-azimuth values were first mapped into a ground cartesian grid. The statistics were then derived from the cartesian representation of  $\sigma_0$ . For the airborne data statistics were derived directly from the delay-azimuth data.

For the ground-based Socorro Peak measurements, data were taken with both PCW and PN modulation at four frequencies each, i.e., a total of eight data sets. For the airborne Socorro Peak measurements, data were taken at a single frequency for both PCW and PN modulation. The data presented included one ground-based measurement and one airborne measurement associated with Salinas Peak, both taken using PN modulation, and a single ground-based measurement with the transmitter on Sierra Blanca using PN modulation.

### 12.2 VH-pol Ground-based Results from Socorro Peak

Figures 31 and 32 show the VH-pol, ground-based transmitter values of  $\sigma_0$  for PCW and PN, respectively. The two results fail to agree, the PCW values being about 6 dB higher than the PN values. This difference is consistent across all four frequencies used. The reason for this is not known but it is suspected that an error was made in the taking or processing of one or other of these two data sets. The PCW results are consistent with the results from other sites; it is therefore likely that the PN results are in error. In the PCW data, the values of  $\sigma_0$  for VH-pol are about 6 dB lower than for VV-pol, as can be seen by comparing Figure 31 with Figure 14.

### 12.3 VH-pol Airborne Results from Socorro Peak

Figure 33 shows the VH-pol values of  $\sigma_0$  for the airborne mission over Socorro Peak. The returns are two or three dB below the airborne VV-pol values seen in Figures 15; however, the variation of  $\sigma_0$  with out-of-plane angle is similar in shape. Note that the roll angle of the aircraft is not fixed at zero and the transmission is therefore not purely horizontal but has a vertical component proportional to the sine of the roll angle. The maximum roll angle was probably no more than 6 degrees. At this angle, the VV-pol component would be -20 dB relative to the signal received from a vertically polarized transmitting antenna. This amount of cross-coupling would not make a significant contribution to the returns.

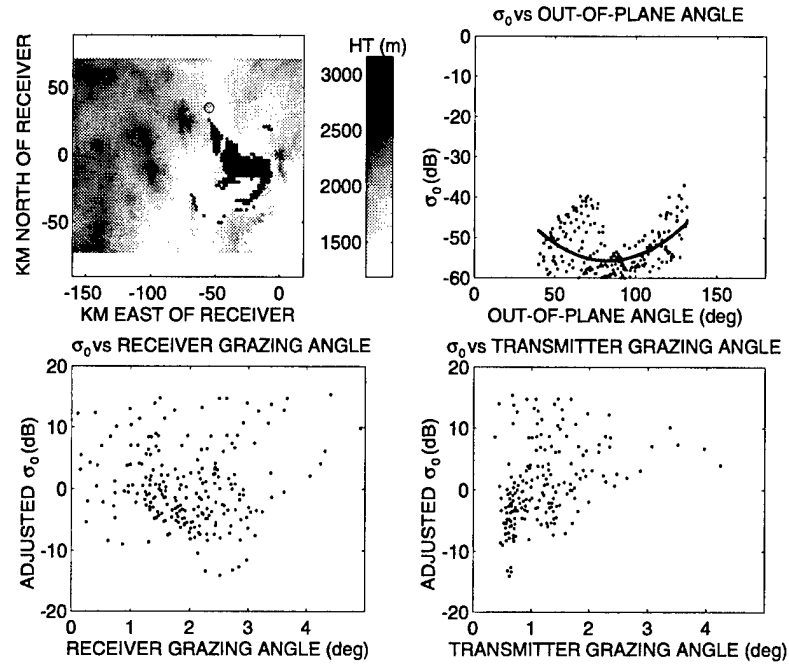


Figure 31. Distribution of Bistatic Scattering Coefficient, Socorro Peak, VH, PCW

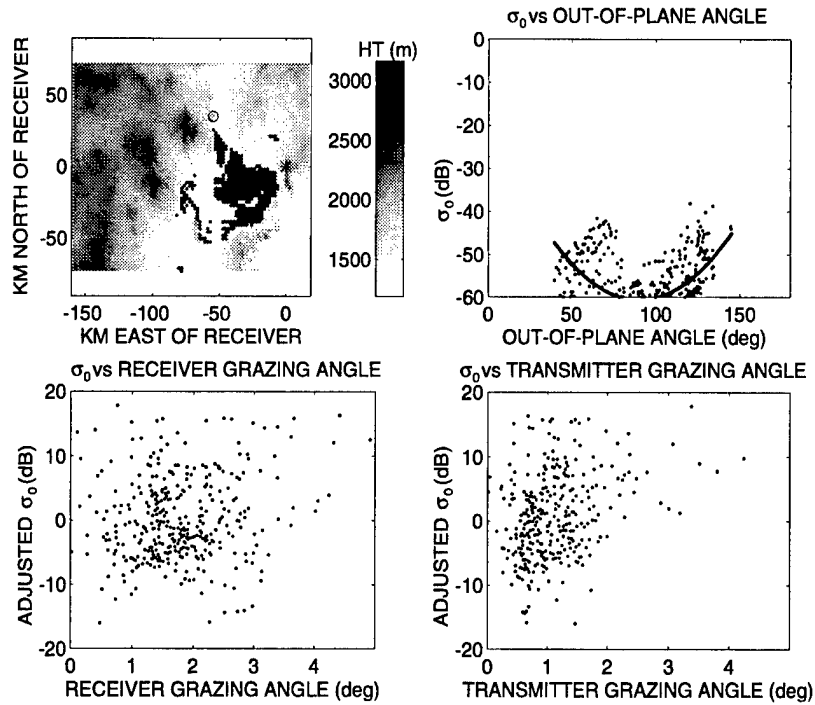


Figure 32. Distribution of Bistatic Scattering Coefficient, Socorro Peak, VH, PN

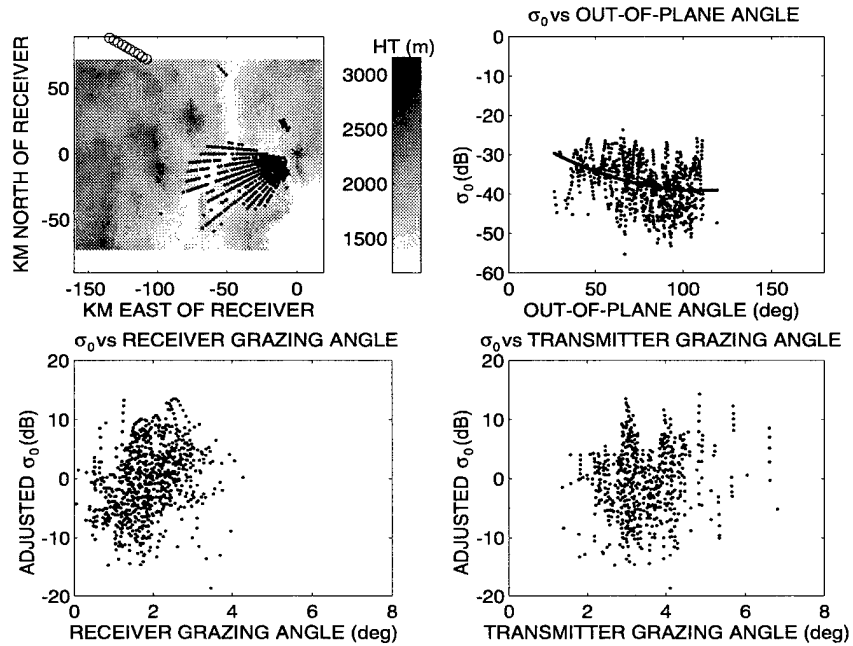


Figure 33. Distribution of Bistatic Scattering Coefficient, Socorro Peak, VH, PN, Airborne

## 12.4 Ground-based and Airborne VH-Pol Results from Salinas Peak

Figures 34 and 35 show the ground-based and airborne VH-pol  $\sigma_0$  values for the data associated with Salinas Peak. The PN data are shown in both cases; the PCW data for the airborne transmitter appeared to be defective. For the ground-based transmitter, the results are very similar to those shown in Figure 32 from Socorro Peak. For the airborne transmitter, the values are several dB lower than those associated with Socorro Peak shown in Figure 33. The reason for this difference might be due to poorer cross-polarization isolation expected with the airborne antenna. Cross-polarization coupling could also account for the lack of the null at 90 degrees out-of-plane angle seen in Figure 34.



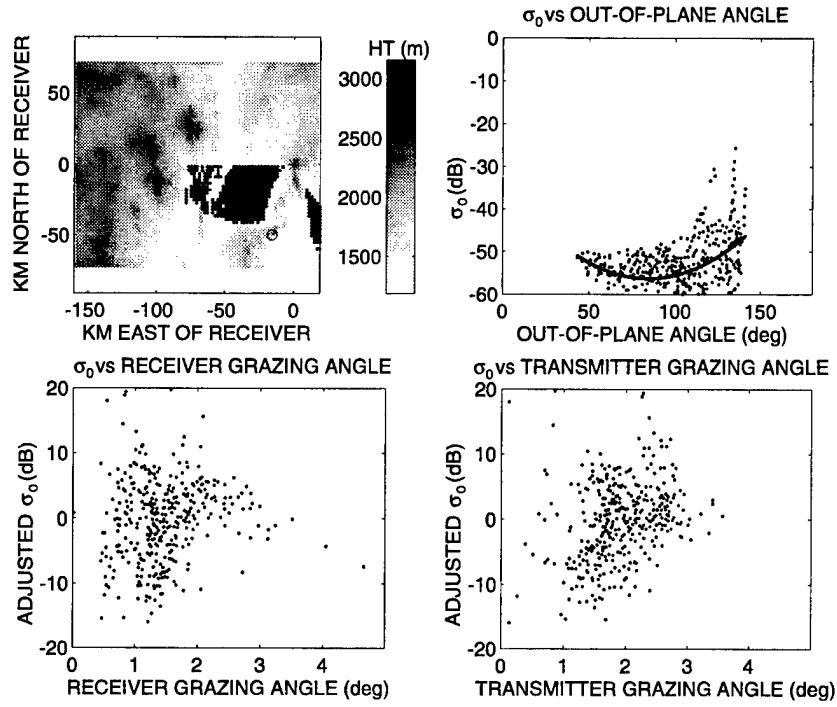


Figure 34. Distribution of Bistatic Scattering Coefficient, Salinas Peak, VH, PN

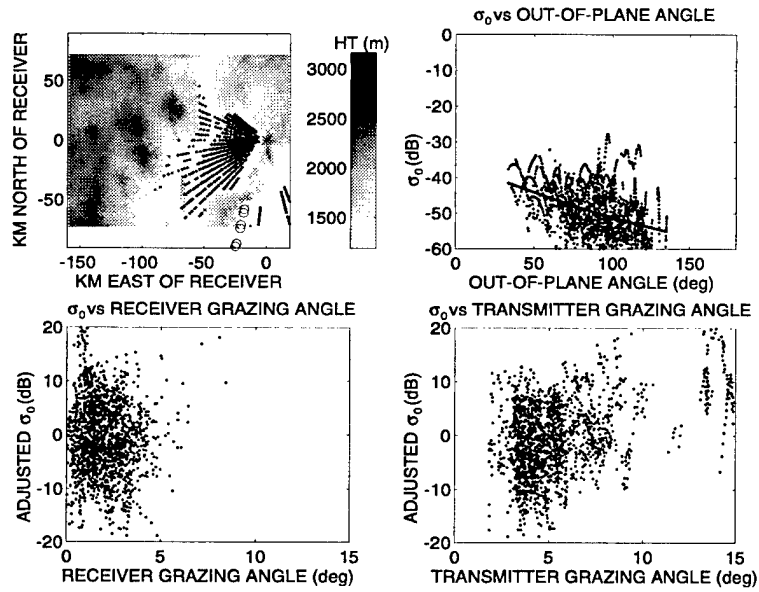


Figure 35. Distribution of Bistatic Scattering Coefficient, Salinas Peak, VH, PN, Airborne

## 12.5 Ground-based and Airborne VH-Pol Results from Sierra Blanca

Figure 36 shows the VH polarization values for  $\sigma_0$  with the transmitter on Sierra Blanca. These values agree with the results from Socorro Peak and Salinas Peak. The airborne VH-pol data (not shown)

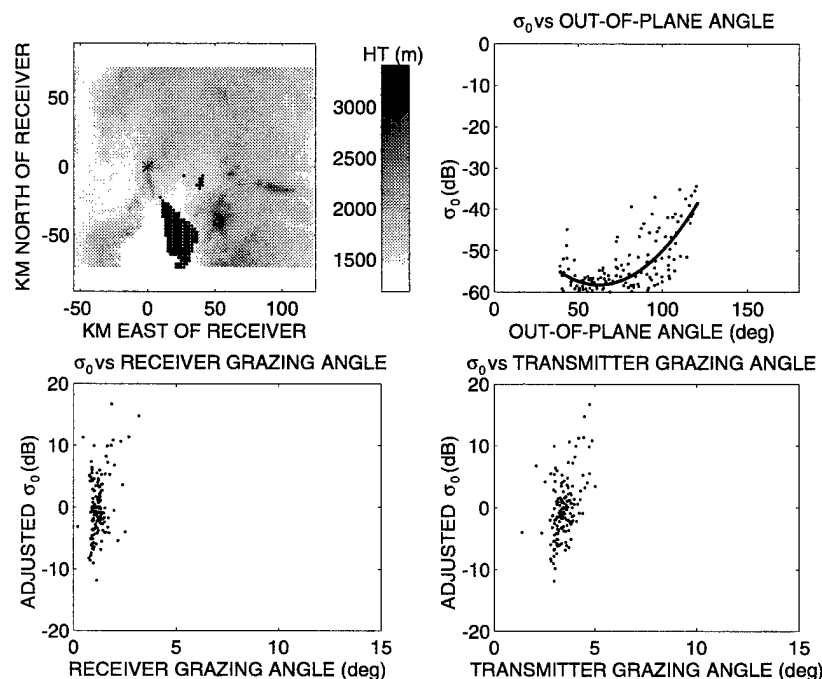


Figure 36. Distribution of Bistatic Scattering Coefficient, Sierra Blanc, VH, PN

exhibit characteristics similar to the VV-pol data associated with the same site (see Paragraph 11.5) in that the scattering is sparse and the  $\sigma_0$  values low. It is apparent from the locations of the scattering points that the area illuminated by the airborne transmitter was very different from that illuminated by the static transmitter. These airborne results are not considered representative of the scattering from the valley floor and therefore have not been included in the overall assessment.

## 12.6 Combined VH-pol Results

The ground-based and airborne returns associated with Socorro Peak and Salinas Peak, and the ground-based returns associated with Sierra Blanca were combined. The area active in the Sierra Blanca data was separate and distinct from that involved in the Socorro Peak and Salinas Peak measurements; however, the terrains were similar in appearance and were assumed to have similar scattering characteristics.

### 12.6.1 Full Area

Figure 37 shows the VH-polarized  $\sigma_0$  values obtained by combining the data described in the previous section. The upper left-hand frame shows the locations of the points of reflection. The upper right

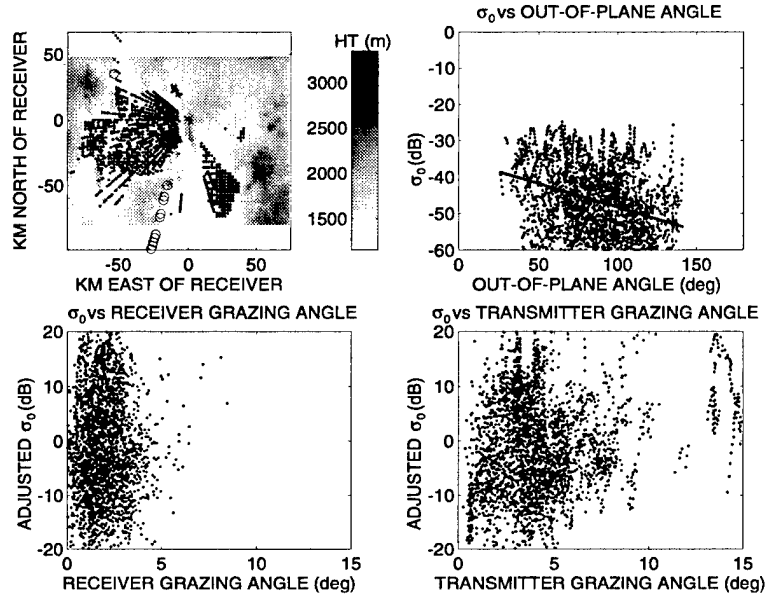


Figure 37. Distribution of Bistatic Scattering Coefficient, VH

frame shows the distribution of  $\sigma_0$  with respect to out-of-plane angle. The curve fitted to the data in the upper right hand frame is a quadratic function of the out-of-plane angle. The coefficients of the quadratic, in descending order, are 0.000785 -0.252 -30.9 ; the units are dB and degrees. The values of the function at 0, 90 and 180 degrees are -30.9 -47.2 -50.8 dB. The lower two frames show the values of  $\sigma_0$  with the parabolic function subtracted. The values are plotted against receiver grazing angle and transmitter grazing angle.

Figure 38 shows  $\log \sigma_0$  plotted against the log of the product of the sines of the grazing angles for various ranges of out-of-plane angle. The straight lines superposed represents the GLF fitted to the data. Note that  $\alpha$  in the GLF is allowed to vary with out-of-plane angle while  $\gamma$  is held constant. The value of  $\sigma_0$  at zero on the horizontal axis gives the value of  $\gamma$ . For this data set  $\gamma$  is equivalent to -35 dB and  $\alpha$  varies from 0.05 to 0.57.

Figure 39 shows the distribution of the amplitudes of  $\sigma_0$  compared with Rayleigh, Weibull and lognormal distributions. It can be seen that the best fit is obtained with a lognormal distribution of 9.3 dB scale width.

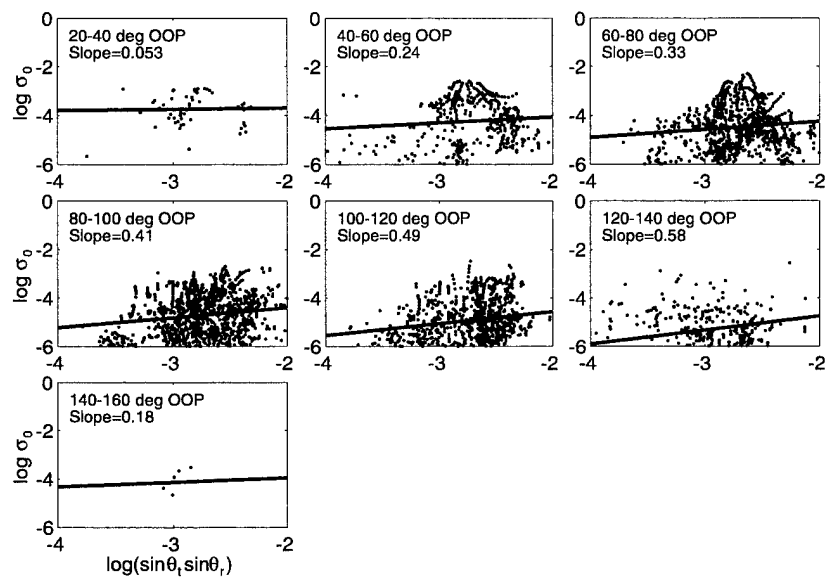


Figure 38. Bistatic Scattering Coefficient vs. Product of Sines of Grazing Angles, VH

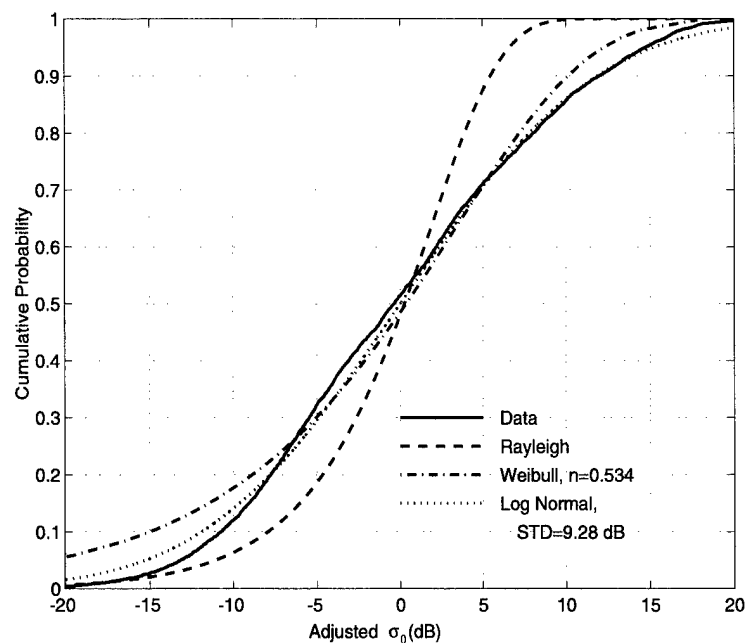


Figure 39. Cumulative Amplitude Distribution, Bistatic, VH

## 12.6.2 Limited Area

Figure 40 shows the cumulative amplitude distribution for the 20x30 km scattering area centered on a point 30 km to the west and 15 km to the south of NOP. The amplitude distribution is only slightly narrower than that for the full area, rather than being close to Rayleigh as expected. It is thought that this broad amplitude distribution could be due to high-RCS depolarizing scatterers, such as dihedral structures.

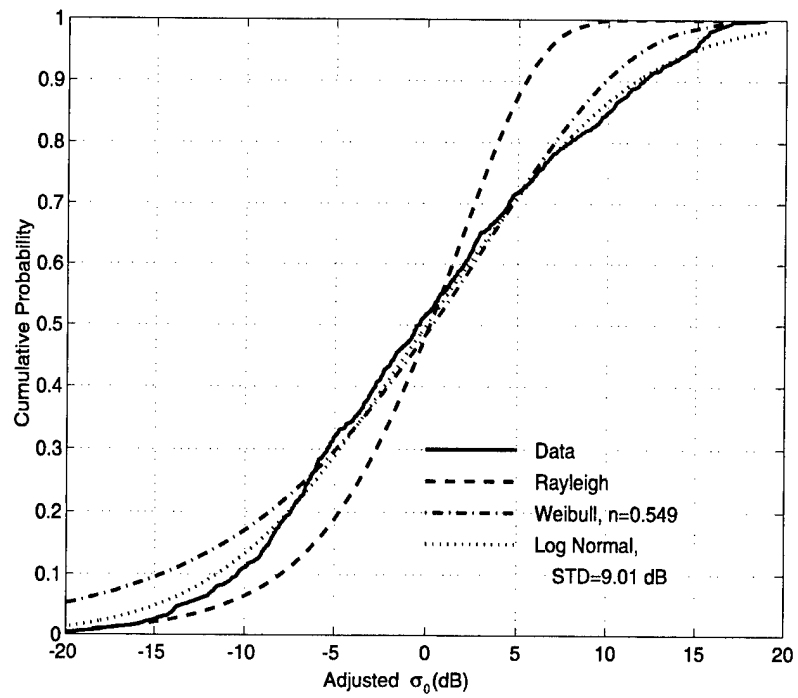
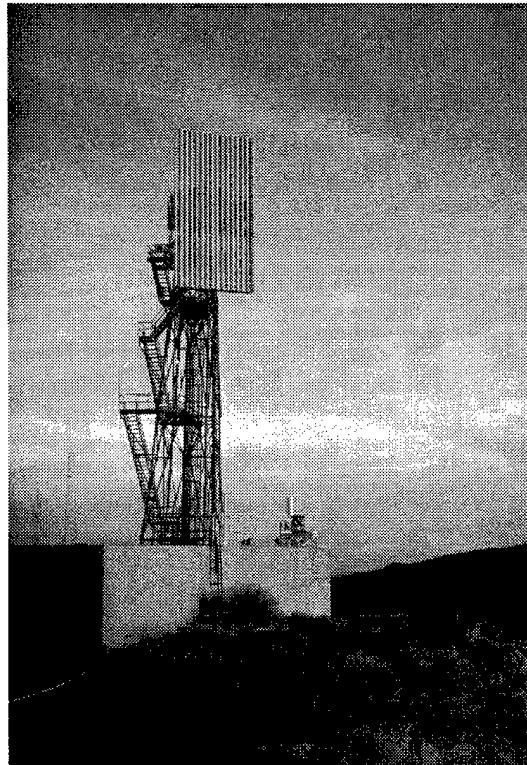


Figure 40. Cumulative Amplitude Distribution, Bistatic, VH, Limited Area

## 13. WIDE-AREA DELAY-AZIMUTH HH-POL RESULTS

### 13.1 Database

HH-pol measurements were made using the RSTER antenna on NOP as the receiver. Since H-pol reception was required, the antenna was set in the RSTER-90 configuration, as illustrated in Figure 41.



*Figure 41. RSTER-90 on North Oscura Peak*

Ground-based measurements were made with the transmitter on Socorro Peak and included combinations of two pulse lengths ( $5 \mu s$  and  $13 \mu s$ ), two modulations (PCW and PN) and four frequencies, for a total of 16 data sets. Each data set was made at three antenna boresight azimuths, with the beam steered electronically in five-degree increments. Similar ground-based measurements were made with the transmitter on Salinas Peak.

The airborne measurements were made with the aircraft flying along a radial course over Socorro Peak. On the inbound course, six sets of data were taken using  $5 \mu s$  PN modulation. On the outbound leg, four sets of data were gathered using  $13 \mu s$  PCW modulation. A single frequency was used for all these airborne measurements.

## 13.2 HH-pol Ground-based PCW Results from Socorro Peak

### 13.2.1 Full Area

Figure 42 shows the  $\sigma_0$  values obtained by combining all the HH-pol PCW data taken with two pulse lengths and four frequencies and with the transmitter on Socorro Peak. The upper left-hand frame

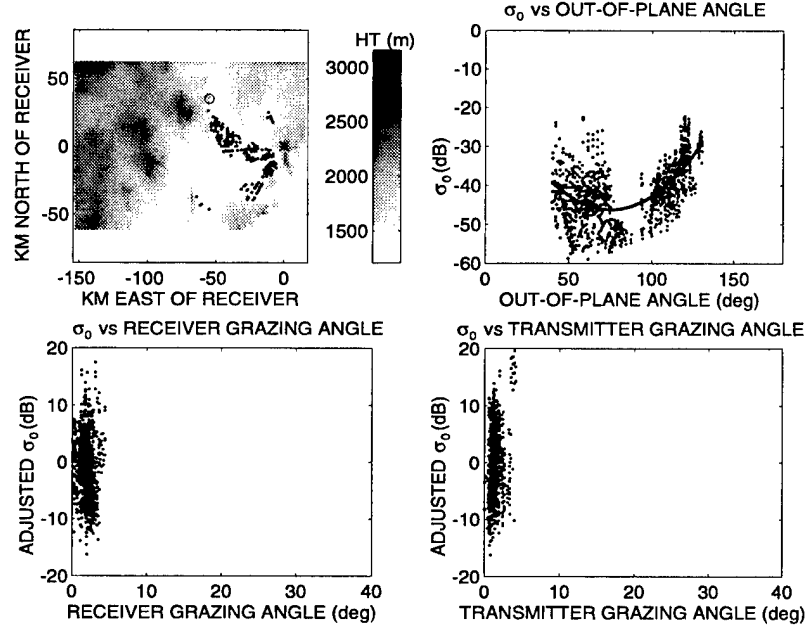


Figure 42. Distribution of Bistatic Scattering Coefficient, Airborne, Socorro Peak, HH, PCW

shows the locations of the points of reflection. It can be seen that the returns are sparse; this is due to the low sensitivity for PCW and the fact that the signals were thresholded at 10 dB above noise.

The upper right frame of Figure 42 shows the distribution of  $\sigma_0$  with respect to out-of-plane angle. The curve fitted to the data in the upper right hand frame is a quadratic function of the out-of-plane angle. The coefficients of the quadratic, in descending order, are 0.005622 , -0.847 and -14.3 , in units of dB and degrees. The values of the function at 0, 90 and 180 degrees are -14.3 , -45.0 and 15.4 dB. The lower two frames of Figure 42 show the values of  $\sigma_0$  with the parabolic function subtracted from them. The values are plotted against receiver grazing angle and transmitter grazing angle.

Figure 43 shows  $\log \sigma_0$  plotted against the log of the product of the sines of the grazing angles for various ranges of out-of-plane angle. The slope of the straight line fitted to the points gives the value of  $\alpha$  in the fitted GLF. Note that in fitting,  $\alpha$  is allowed to vary with out-of-plane angle while  $\gamma$  is held constant. The value of  $\sigma_0$  at zero on the horizontal axis gives the value of  $\gamma$ . For this data set  $\gamma$  is equivalent to -36 dB and  $\alpha$  varies from -0.12 to 0.41.

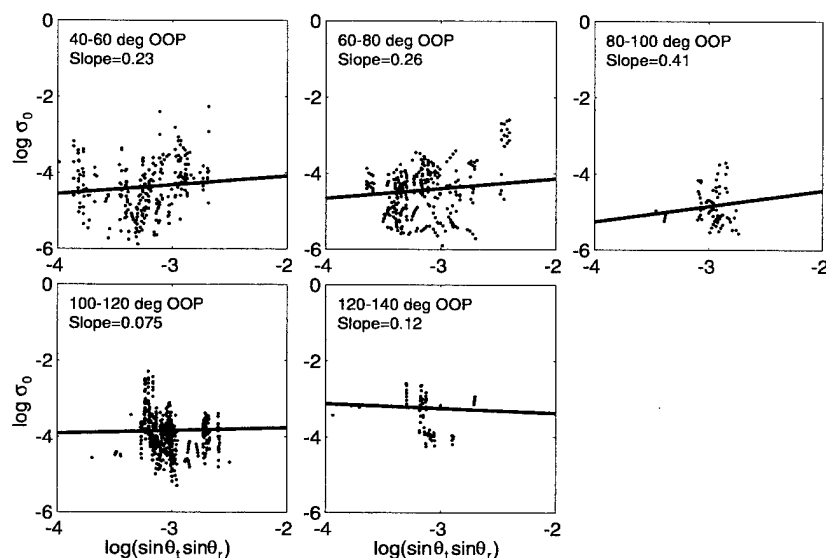


Figure 43. Bistatic Scattering Coefficient vs. Product of Sines of Grazing Angles, Airborne, Socorro Peak, HH, PCW

Figure 44 shows the distribution of the amplitudes of  $\sigma_0$  for the HH-pol wide-area PCW data. Rayleigh, Weibull and lognormal cumulative probability curves are shown fitted to these data. The data curve is close to lognormal with a standard deviation of 5.5 dB.

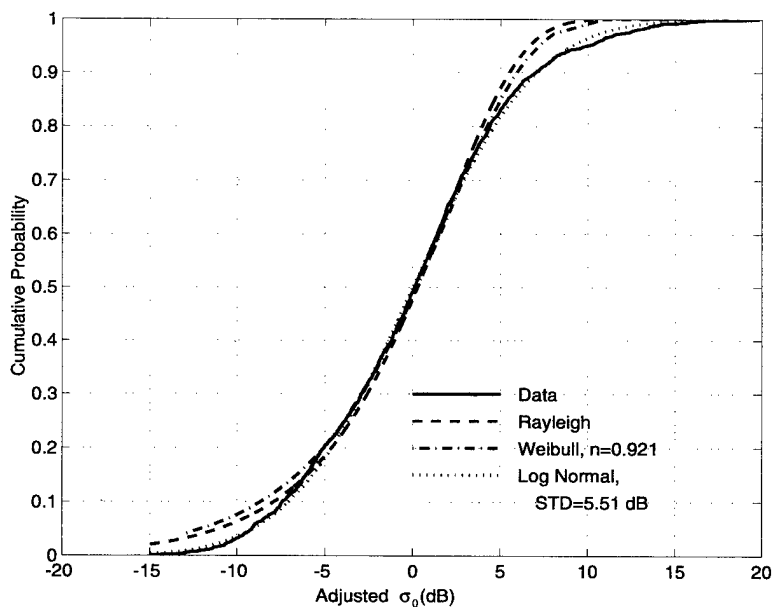


Figure 44. Cumulative Amplitude Distribution, Bistatic, Airborne, Socorro Peak, HH, PCW



### 13.2.2 Limited Area

Figure 45 shows the  $\sigma_0$  amplitude distribution obtained when the scattering area was confined to a 10 km by 20 km rectangle area. The distribution appears to be narrower than Rayleigh. This is probably due to the lower values being rejected by the thresholding.

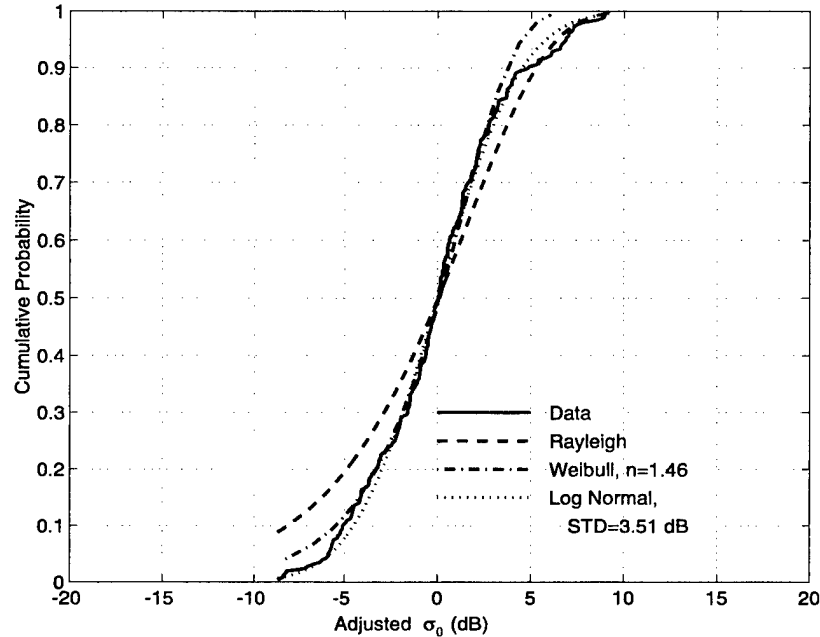


Figure 45. Cumulative Amplitude Distribution, Bistatic, Airborne, Socorro Peak, HH, PCW, Limited Area

## 13.3 HH-pol Ground-based PN Results from Socorro Peak

### 13.3.1 Full Area

Figure 46 shows the HH-pol  $\sigma_0$  values obtained by combining four sets of PN measurement taken with the transmitter on Socorro Peak. The upper left-hand frame shows the locations of the points of reflection. The upper right frame shows the distribution of  $\sigma_0$  with respect to out-of-plane angle. The curve fitted to the data in the upper right hand frame is a quadratic function of the out-of-plane angle. The coefficients of the quadratic, in descending order, are 0.00293, -0.464 and -28.72 ; the units are dB and degrees. The values of the function at 0, 90 and 180 degrees are -28.7, -46.8 and -17.3 dB. The lower two frames show the values of  $\sigma_0$  with the parabolic function subtracted from them. The values are plotted against receiver grazing angle and transmitter grazing angle.

Figure 47 shows  $\log \sigma_0$  plotted against the log of the product of the sines of the grazing angles for various ranges of out-of-plane angle. The slope of the straight line fitted to the points gives the value of  $\alpha$  in the fitted GLF. Note that in fitting,  $\alpha$  is allowed to vary with out-of-plane angle while  $\gamma$  is held

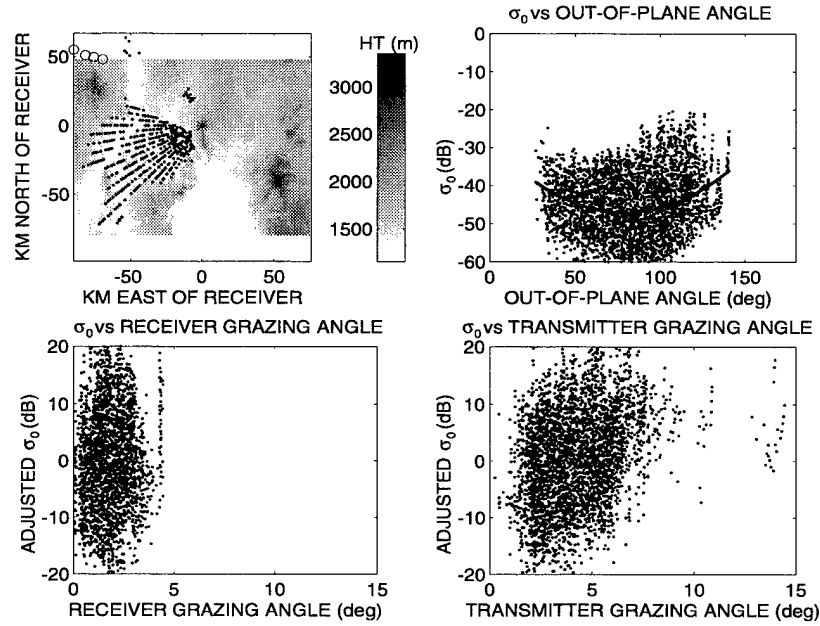


Figure 46. Distribution of Bistatic Scattering Coefficient, Airborne, Socorro Peak, HH, PN

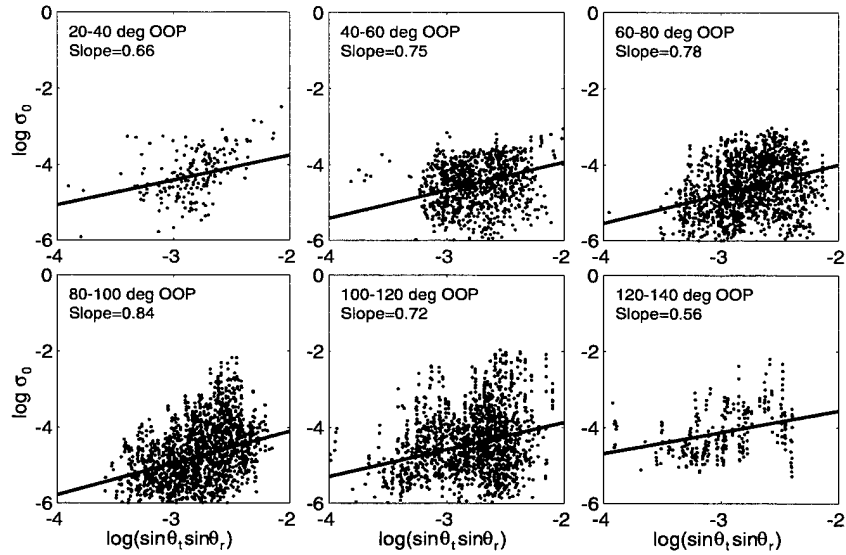


Figure 47. Bistatic Scattering Coefficient vs. Product of Sines of Grazing Angles, Airborne, Socorro Peak, HH, PN

constant. The value of  $\sigma_0$  at zero on the horizontal axis gives the value of  $\gamma$ . For this data set  $\gamma$  is equivalent to -24 dB and  $\alpha$  varies from 0.56 to 0.84.

Figure 48 shows the distribution of the amplitudes of  $\sigma_0$  for the HH-pol wide-area data. The data is a close fit to the lognormal curve with a 6.3 dB standard deviation.

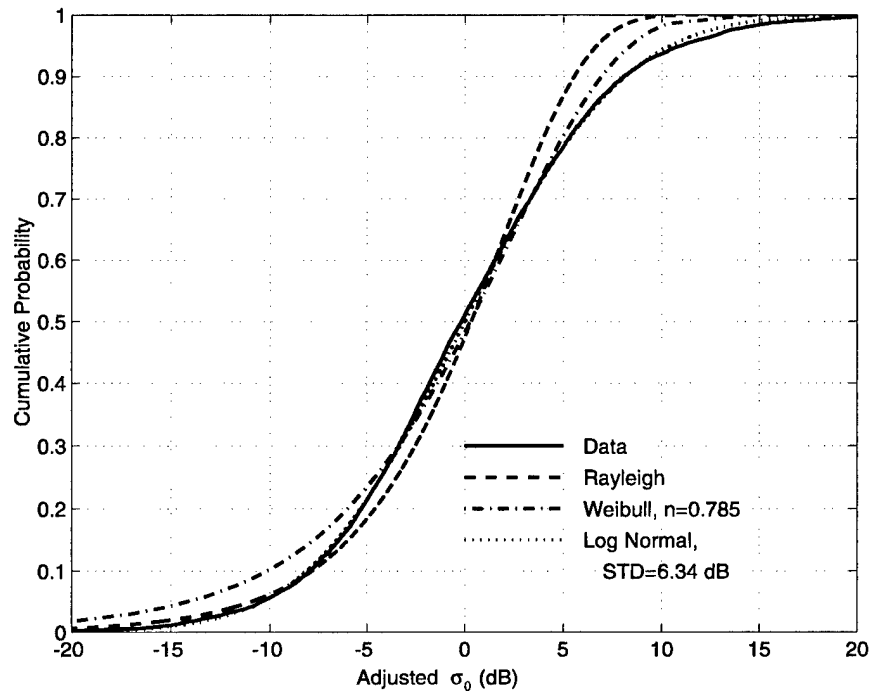


Figure 48. Cumulative Amplitude Distribution, Bistatic, Airborne, Socorro Peak, HH, PN

### 13.3.2 Limited Area

Figure 49 show the  $\sigma_0$  cumulative amplitude distribution obtained when the scattering area was confined to a 10 km by 20 km rectangle. The distribution of the higher values is now much closer to Rayleigh than it was with the full area, suggesting that the local statistics are not uniform over the full area.

## 13.4 Salina Peak Ground-based PCW Results

### 13.4.1 Full Area

The upper left subplot of Figure 50 shows the locations of the ground scattering points for the HH-pol data taken with the transmitter on Salinas Peak. The upper right frame shows the distribution of  $\sigma_0$  with respect to out-of-plane angle. The curve fitted to the data in the upper right hand frame is a quadratic function of the out-of-plane angle. The coefficients of the quadratic, in descending order, are 0.000457 , -0.00138 and -54.1 in units of dB and degrees. This curve has very little linear component when the origin is moved to the center of the range. The values of the function at 0, 90 and 180 degrees are -54.1 , -50.5 and -39.5 dB. The lower two frames of Figure 50 show the values of  $\sigma_0$  with the parabolic function subtracted from them, plotted against receiver grazing angle and transmitter grazing angle.

Figure 51 shows  $\log \sigma_0$  plotted against the log of the product of the sines of the grazing angles for various ranges of out-of-plane angle. The slope of the straight line fitted to the points gives the value of

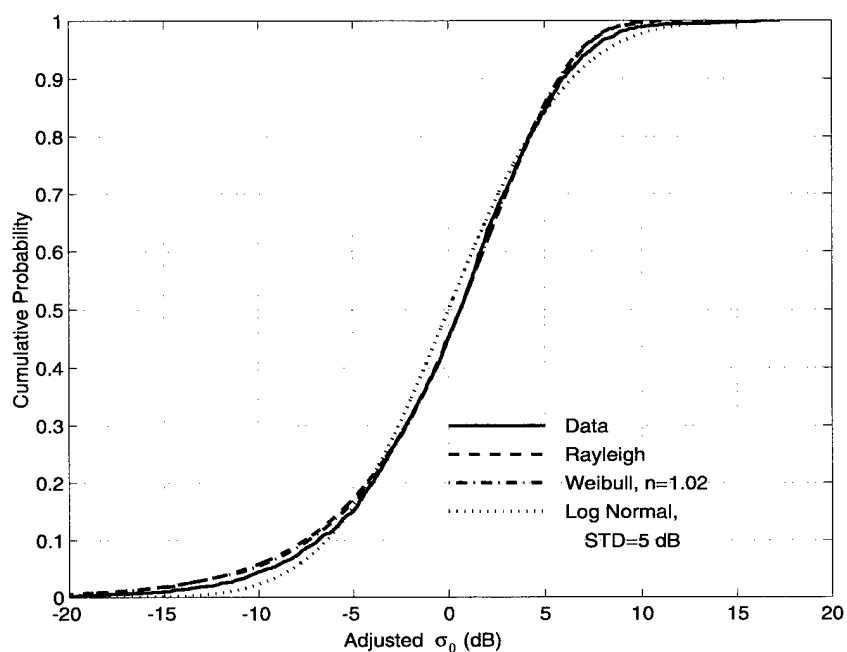


Figure 49. Cumulative Amplitude Distribution, Bistatic, Airborne, Socorro Peak, HH, PN, Limited Area

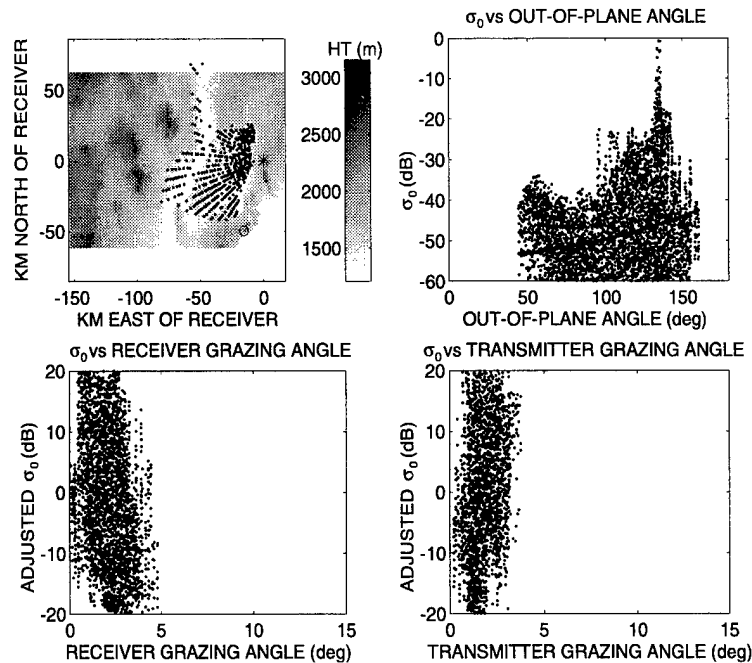


Figure 50. Distribution of Bistatic Scattering Coefficient, Salinas Peak, HH, PCW

$\alpha$  in the fitted GL. Note that in fitting,  $\alpha$  is allowed to vary with out-of-plane angle while  $\gamma$  is held constant. The value of  $\sigma_0$  at zero on the horizontal axis gives the value of  $\gamma$ . For this data set  $\gamma$  is equivalent to -45 dB and  $\alpha$  varies from 0.001 to 0.26.

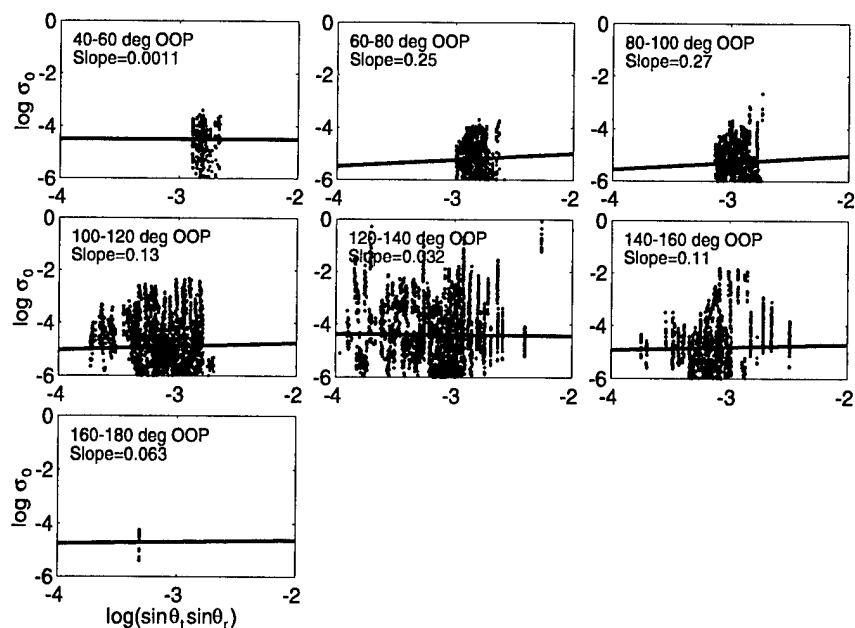


Figure 51. Bistatic Scattering Coefficient vs. Product of Sines of Grazing Angles, HH, PCW

Figure 52 shows the distribution of the amplitudes of  $\sigma_0$  for the HH-pol wide-area data. These statistics are obtained by combining the subsets shown in Figure 51. For each subset, the fitted straight line is subtracted from the value of  $\log \sigma_0$  and the result multiplied by 10 to convert to dB. The results are

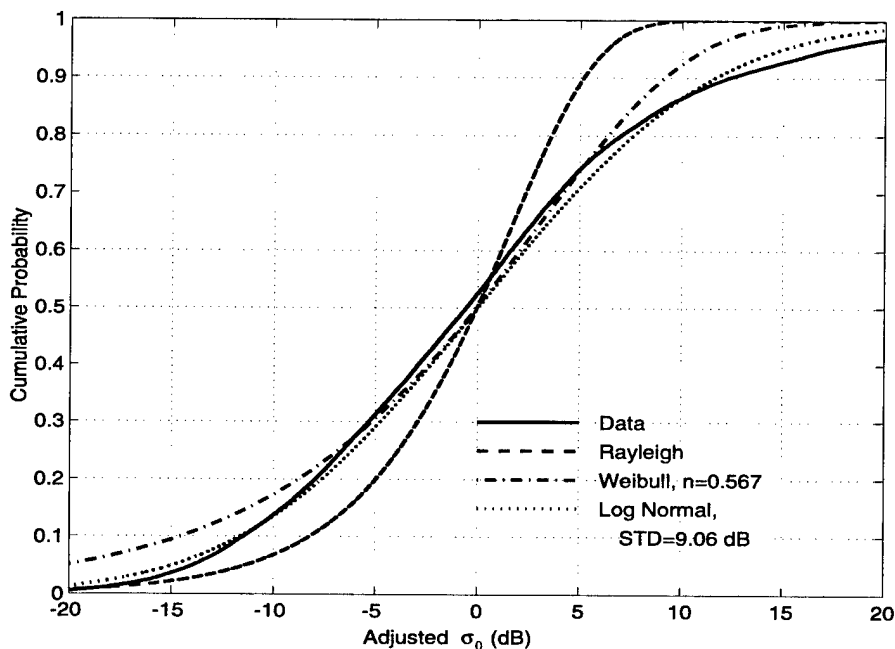


Figure 52. Cumulative Amplitude Distribution, Bistatic, Salinas Peak, HH, PCW

termed “adjusted  $\sigma_0$ .” The values from each subset are then assembled and sorted in order of magnitude. The index of the sorted values, divided by the total number of values, is shown plotted against adjusted  $\sigma_0$ . This curve then gives the proportion of values below the value indicated on the horizontal axis. It can be seen that the distribution of amplitudes is broader than Rayleigh and is best represented by a lognormal distribution with a scale width of 9.1 dB.

### 13.4.2 Limited Area

Figure 53 shows the cumulative distribution of amplitudes of  $\sigma_0$  obtained when the scattering area was confined to a 10 km by 20 km rectangle. The distribution of the higher values is now much closer to Rayleigh than it was with the full area.

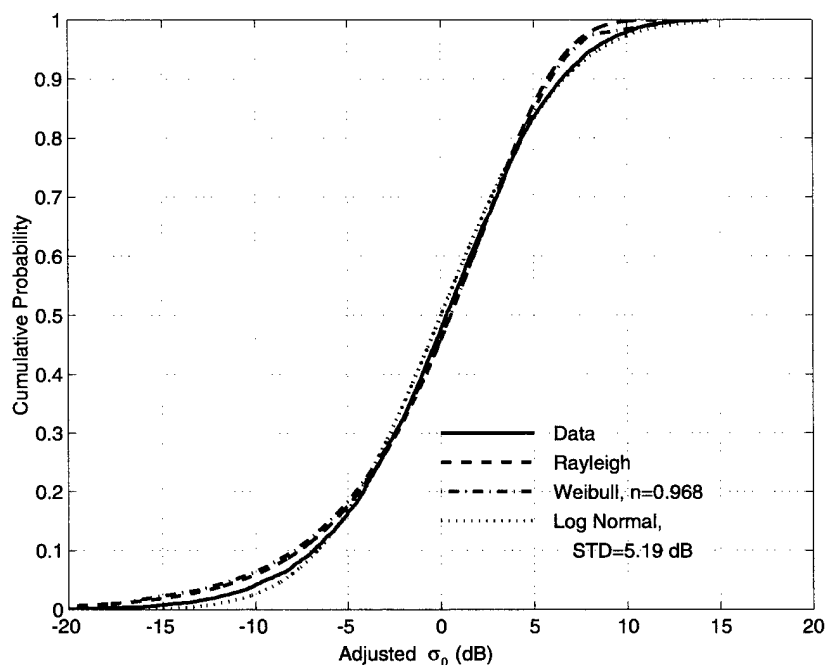


Figure 53. Cumulative Amplitude Distribution, Bistatic, Salinas Peak, HH, PCW, Limited Area

## 13.5 Salinas Peak Ground-based PN Results

### 13.5.1 Full Area

The upper left subplot of Figure 54 shows the locations of the ground scattering points for the HH-pol data taken with the transmitter on Salinas Peak. The upper right frame shows the distribution of  $\sigma_0$  with respect to out-of-plane angle. The curve fitted to the data in the upper right hand frame is a quadratic function of the out-of-plane angle. The coefficients of the quadratic, in descending order, are 0.001135 ,

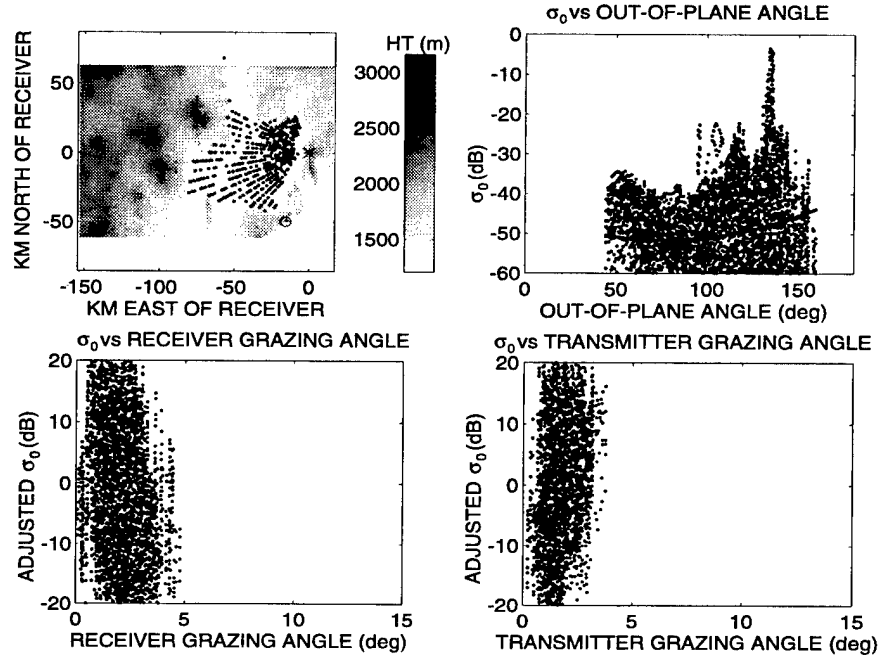


Figure 54. Distribution of Bistatic Scattering Coefficient, Salinas Peak, HH, PN

−0.173 and −44.9; the units are dB and degrees. The values of the function at 0, 90 and 180 degrees are −44.9, −51.4 and −39.5 dB. The lower two frames of Figure 54 show the values of  $\sigma_0$  with the parabolic function subtracted from them, plotted against receiver grazing angle and transmitter grazing angle.

Figure 55 shows  $\log \sigma_0$  plotted against the log of the product of the sines of the grazing angles for various ranges of out-of-plane angle. The slope of the straight line fitted to the points gives the value of  $\alpha$  in the fitted GLF. Note that in fitting,  $\alpha$  is allowed to vary with out-of-plane angle while  $\gamma$  is held constant. The value of  $\sigma_0$  at zero on the horizontal axis gives the value of  $\gamma$ . For this data set  $\gamma$  is equivalent to −38 dB and  $\alpha$  varies from 0.25 to 0.52.

Figure 56 shows the cumulative amplitude distribution for the Salinas Peak data. It can be seen that the distribution is considerably broader than Rayleigh. The data is close to both lognormal and Weibull functions. For the matching lognormal function, the standard deviation is 8.75 dB.

### 13.5.2 Limited Area

Figure 57 shows the  $\sigma_0$  cumulative distribution of amplitudes obtained when the scattering area was confined to a 10 km by 20 km rectangle. It can be seen that the distribution of amplitudes is close to lognormal. The scale width of the distribution is 5.7 dB.

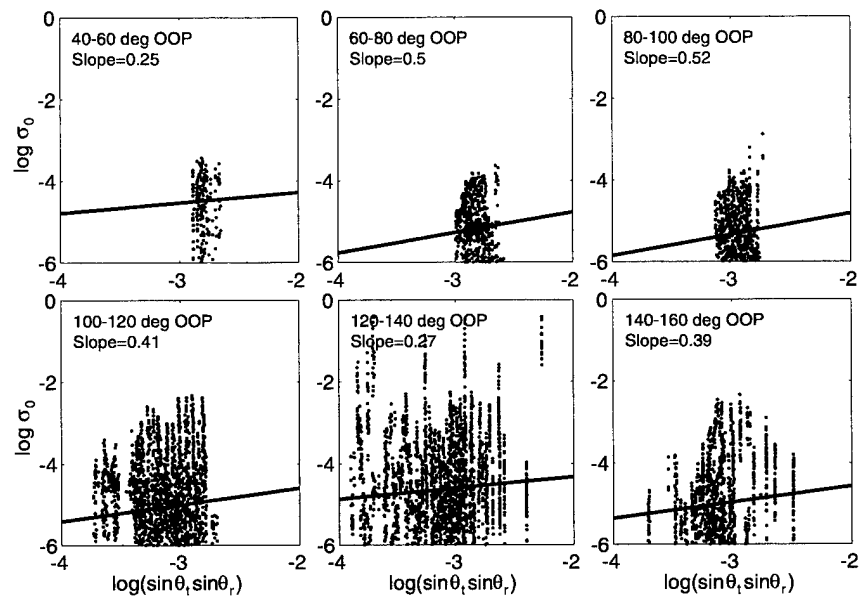


Figure 55. Bistatic Scattering Coefficient vs. Product of Sines of Grazing Angles, Salinas Peak, HH, PN

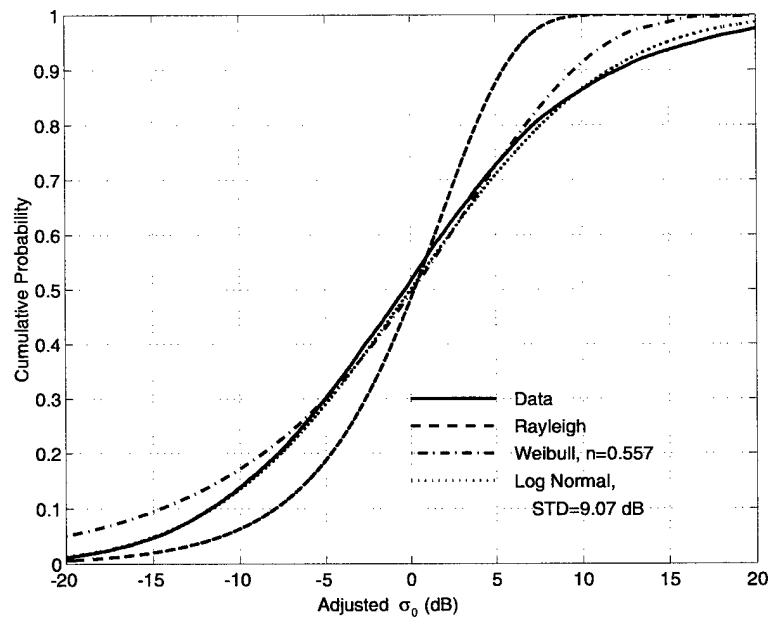


Figure 56. Cumulative Amplitude Distribution, Bistatic, Salinas Peak, HH, PN



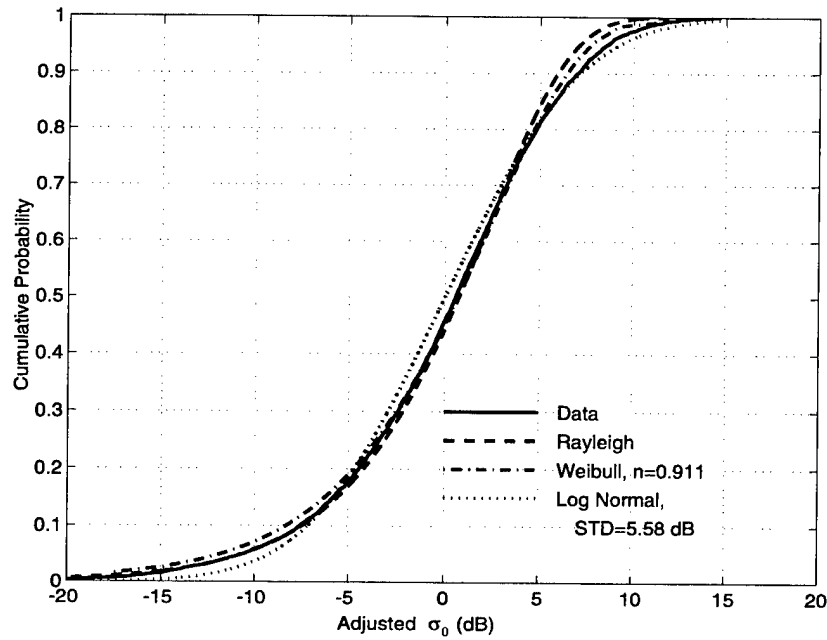


Figure 57. Cumulative Amplitude Distribution, Bistatic, Salinas Peak, HH, PN, Limited Area

## 13.6 Combined Bistatic HH-pol Results

### 13.6.1 Full Area

Figure 58 shows the HH-pol  $\sigma_0$  values obtained by combining several sets of HH-pol measurements. The data included are the single-frequency airborne returns associated with Socorro Peak and the multi-frequency ground-based returns associated with Salinas Peak. The upper left-hand frame shows the locations of the points of reflection where the returns are above the noise threshold. The upper right frame shows the distribution of  $\sigma_0$  with respect to out-of-plane angle. The curve fitted to the data in the upper right hand frame is a quadratic function of the out-of-plane angle. The coefficients of the quadratic, in descending order, are 0.00135, -0.194 and -45.1; the units are dB and degrees. The values of the function at 90 and 180 degrees are -45.1, -51.6 and -36.1 dB.

The lower two frames of Figure 58 show the values of  $\sigma_0$  with the parabolic function subtracted from them. The values are plotted against receiver grazing angle and transmitter grazing angle. These plots suggest that there is a very broad spread in the amplitudes. This appearance is an artifact of the plotting algorithm and is a result of attempting to plot a very large number of data points.

Figure 59 shows  $\log \sigma_0$  plotted against the log of the product of the sines of the grazing angles for various ranges of out-of-plane angle. Superimposed on each frame is a straight line representing the best fit of the model  $\sigma_0 = \gamma (\sin \theta_t \times \sin \theta_r)^{\alpha(\theta)}$ . Note that  $\alpha$  is allowed to vary with out-of-plane angle while  $\gamma$  is

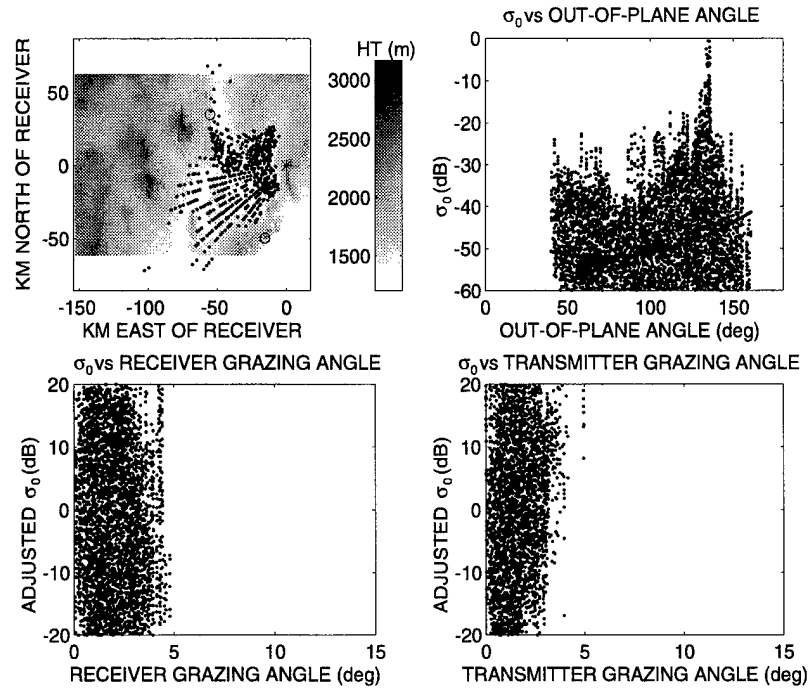


Figure 58. Distribution of Bistatic Scattering Coefficient, HH

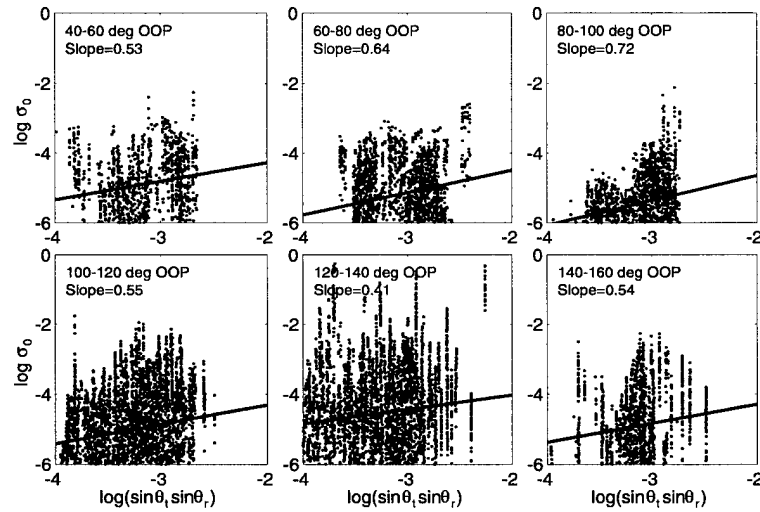


Figure 59. Bistatic Scattering Coefficient vs. Product of Sines of Grazing Angles, HH

held constant. The value of  $\sigma_0$  at zero on the horizontal axis gives the value of  $\gamma$ . For this data set  $\gamma$  is equivalent to -32 dB and  $\alpha$  varies from 0.53 to 0.72.

Figure 60 shows the cumulative amplitude distribution for the combined bistatic HH-pol measurement. It can be seen that the distribution is broader than Rayleigh. For the matching lognormal function, the standard deviation is 8.95 dB.

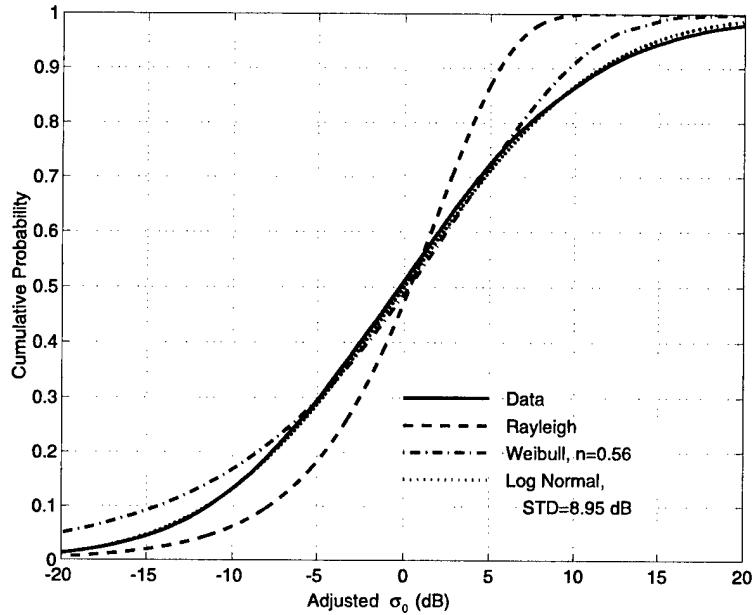


Figure 60. Cumulative Amplitude Distribution, Bistatic, HH

### 13.6.2 Limited Area

Figure 61 shows the  $\sigma_0$  cumulative distribution of amplitudes obtained when the scattering area was confined to a 10 km by 20 km rectangle. It can be seen that the distribution of amplitudes is close to lognormal at the higher values. The scale width of the distribution is 5.8 dB.

## 13.7 Quasi-Monostatic HH-pol Results

Mission BINOP (Bistatic at NOP) was conducted on April 4, 1994 at North Oscura Peak on the White Sands Missile Range. This experiment was designed to collect backscattered radiation using the bistatic measurement equipment in a quasi-monostatic geometry. The transmitter antenna was sited near the receiver on North Oscura Peak and was set for horizontal polarization. The receiver antenna was also set for horizontal polarization (RSTER-90 configuration). The boresight direction for both transmitting and receiving arrays was 240 degrees with respect to true north.

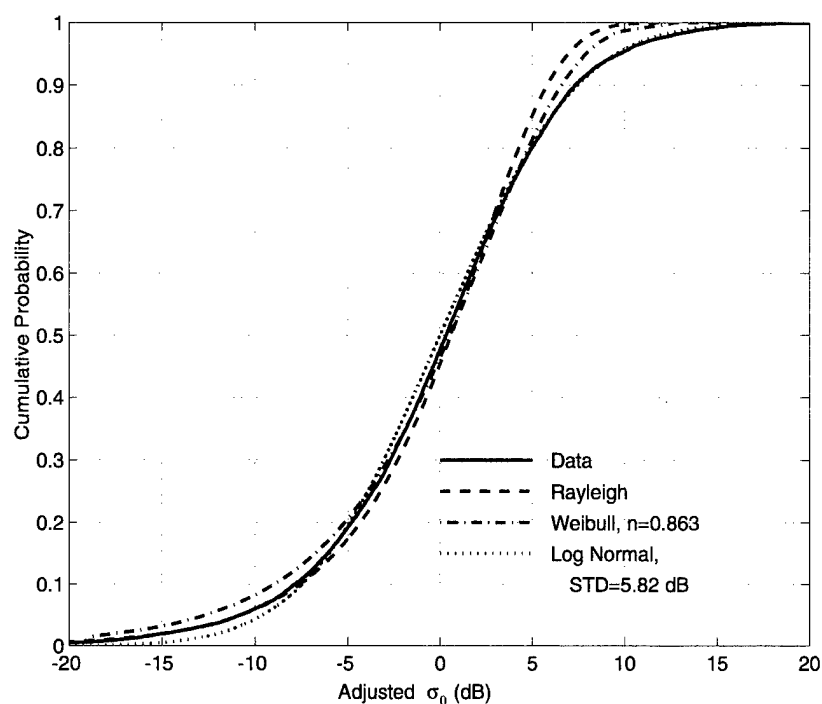


Figure 61. Cumulative Amplitude Distribution, Bistatic, HH, Limited Area

### 13.7.1 Full Area

Figure 62 shows the locations of the ground scattering points and the values of  $\sigma_0$  vs. grazing angle for the HH-pol quasi-monostatic data. Figure 63 shows the log (to the base 10) of  $\sigma_0$  plotted against

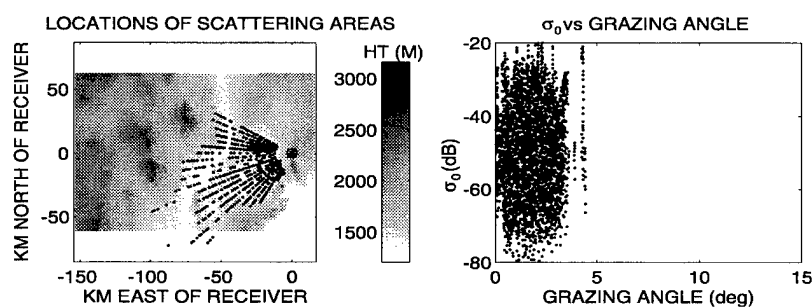


Figure 62. Distribution of Quasi-Monostatic Scattering Coefficient, HH

the log of the product of the sines of the transmitter and receiver grazing angles. Since the configuration was monostatic, the transmitter and receiver grazing angles were the same.

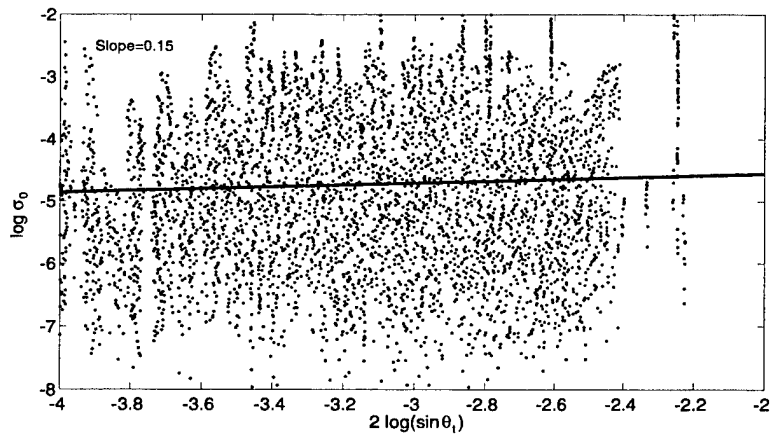


Figure 63. *Quasi-Monostatic Scattering Coefficient vs. Squared Sine of Grazing Angle, HH*

A straight line fitted to the points was found to have a slope of 0.15; this corresponds to the value of the exponent  $\alpha$  in the Generalized Lambertian Formula. The value of the straight line at  $-3.0$  was  $-4.7$ . Note that the value of  $\alpha$  is low compared to that obtained from the bistatic measurements.

Figure 64 shows the cumulative amplitude distribution for the quasi-monostatic HH-pol data. It can be seen that the distribution is broader than Rayleigh. For the matching lognormal function, the standard deviation is 7.9 dB.

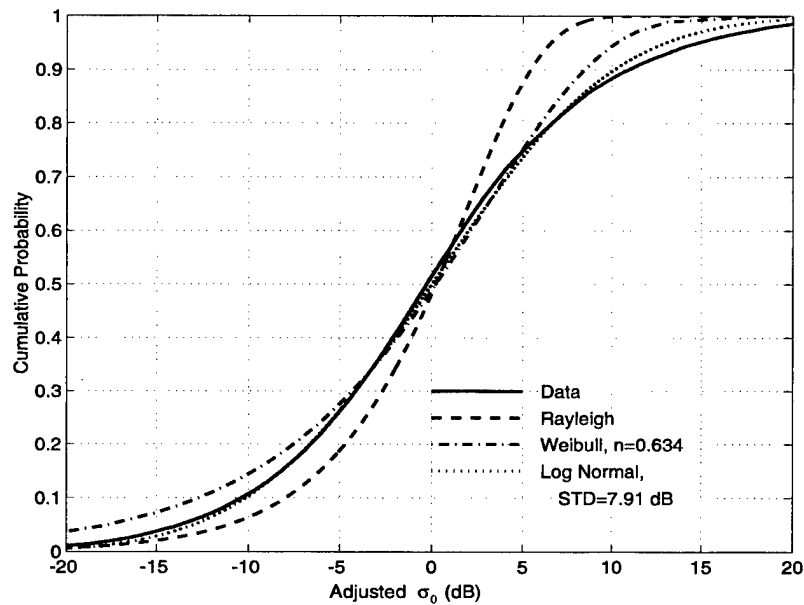


Figure 64. *Cumulative Amplitude Distribution, Quasi-Monostatic, HH*

### 13.7.2 Limited Area

Figure 65 shows the cumulative amplitude distribution for the quasi-monostatic HH-pol data for the limited area. It can be seen that the distribution is closer to Rayleigh than for the full area. For the

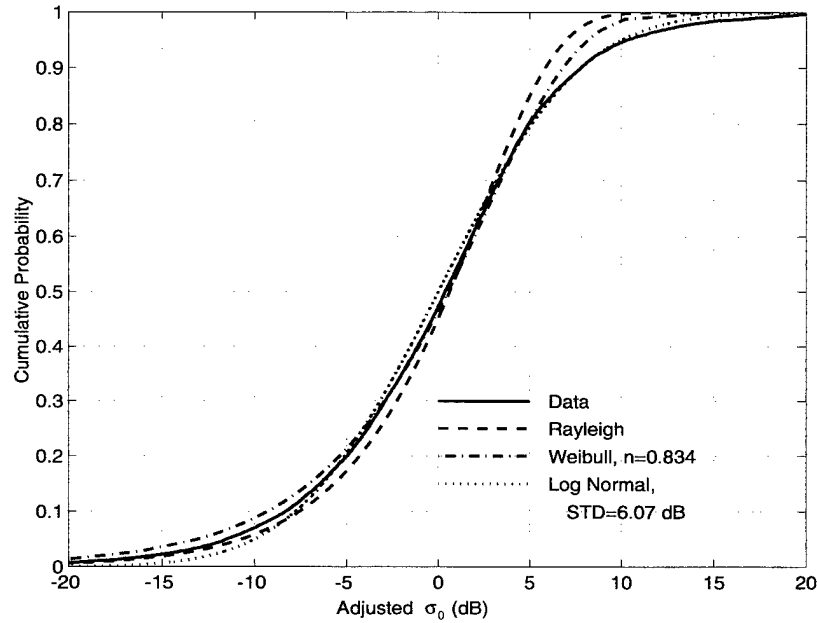


Figure 65. Cumulative Amplitude Distribution, Quasi-Monostatic, HH, Limited Area

matching lognormal function, the standard deviation is 6.1 dB. The value of  $\log \sigma_0$  is  $-4.8$  when  $2\log \sin \theta_t$  is  $-3.0$ , as compared to  $-4.7$  for the full area.

## 13.8 Monostatic HH-pol Results

Monostatic data were collected on 27th August 1993 at WSMR. RSTER was situated on North Oscura Peak, and was used for both transmitting and receiving. The data were reduced and analyzed, and the results reported in an internal memo by John Jayne, dated October 18, 1993. The reduced data were made available in MATLAB files; the variables contained in these files were raw clutter power, clutter to noise ratio, reflectivity and  $\sigma_0$ , all as functions of range and azimuth.

In deriving the statistics for this report, the values of  $\sigma_0$  were extracted from the MATLAB files and processed in a fashion similar to that used for the bistatic data. Statistics are shown for both the full area and for the limited area.

### 13.8.1 Full Area

Figure 66 shows the locations of the ground scattering points and the values of  $\sigma_0$  vs. grazing angle. Figure 67 shows the log (to the base 10) of  $\sigma_0$  plotted against the log of the product of the sines of

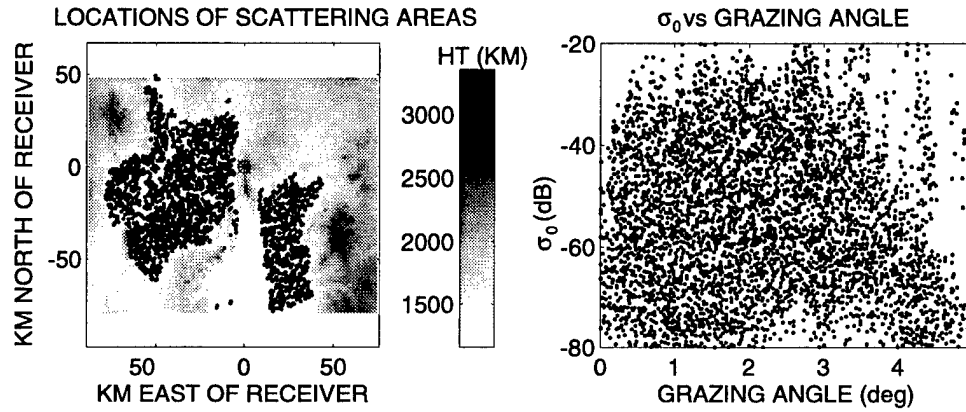


Figure 66. Distribution of Monostatic Scattering Coefficient, HH

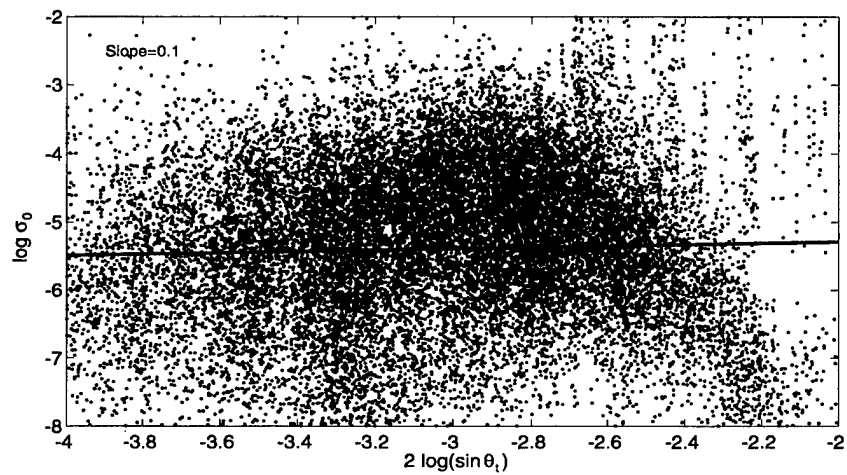


Figure 67. Monostatic Scattering Coefficient vs. Squared Sine of Grazing Angle, HH

the transmitter and receiver grazing angles. Since the configuration was monostatic, the grazing angles were the same. A straight line fitted to the points was found to have a slope of 0.1; this corresponds to the

value of the exponent  $\alpha$  in the Generalized Lambertian Formula. The value of the straight line at  $-3$  was  $-5.3$ . As in the quasi-monostatic case, the value of  $\alpha$  is low compared to that obtained from the bistatic measurements.

Figure 68 shows the cumulative amplitude distribution for the monostatic data. It can be seen that the distribution is considerably broader than Rayleigh. The data is close to both lognormal and Weibull functions. For the matching lognormal function, the standard deviation is 11.3 dB.

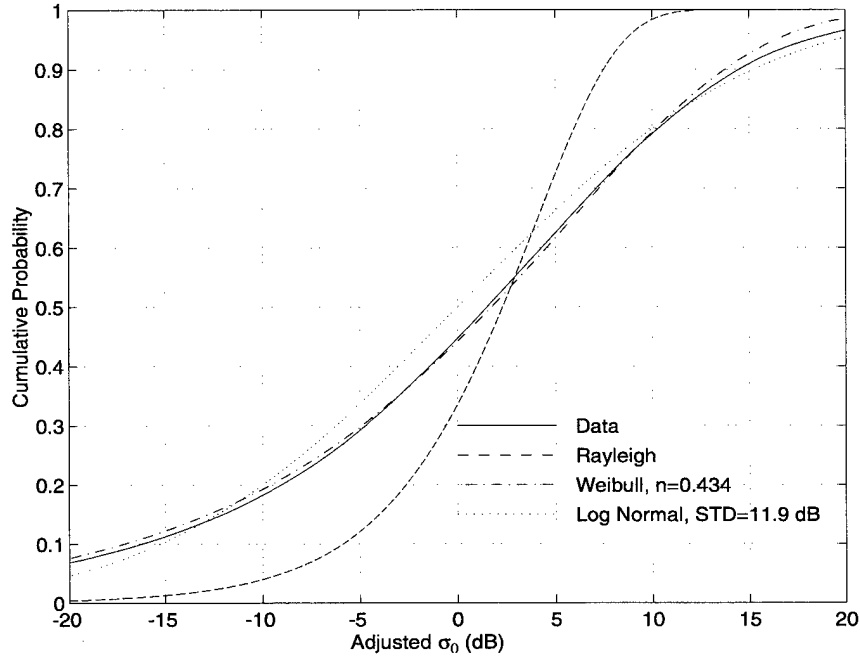


Figure 68. Cumulative Amplitude Distribution, Monostatic, HH

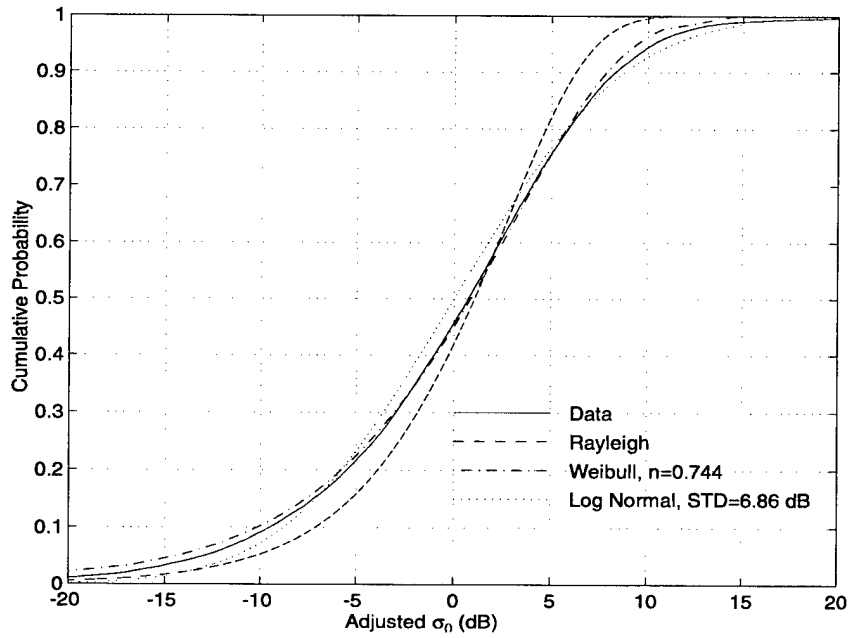
### 13.8.2 Limited Area

Figure 69 shows the cumulative amplitude distribution for the monostatic results for the limited area. The amplitude distribution is now much closer to Rayleigh. In terms of the lognormal distribution, the standard deviation has been reduced to 6.6 dB. The value of  $\log \sigma_0$  is  $-5.0$  when  $2 \log \sin \theta_t$  is  $-3.0$ , as opposed to  $-5.3$  for the full area.

## 13.9 Comparison of HH-pol Quasi-Monostatic and True Monostatic Results

Figures 63 and 67 show  $\log \sigma_0$  plotted against  $2 \log \sin \theta_t$  for quasi-monostatic and true monostatic data respectively. At a grazing angle of 1.8 degrees, the value on the abscissa is 3. For Quasi-monostatic data, the value of  $\log \sigma_0$  for the fitted straight line at this point is  $-4.7$ , equivalent to  $-47$  dB. For the true





*Figure 69. Cumulative Amplitude Distribution, Monostatic, HH, Limited Area*

monostatic data, the value is equivalent to  $-53$  dB, a difference of 6 dB. Some of this difference is due to the fact that the active ground area was different for the two test, as can be seen in the left-hand plot of Figures 62 and 66. When the active area was reduced to a  $10 \times 20$  m common area, the  $\sigma_0$  values changed to  $-48$  and  $-50$  dB respectively, a difference of only 2 dB. In view of the fact that the Quasi-monostatic and true monostatic tests were analyzed by different methods using different software, this close agreement validates the processing methodology.

## 14. WIDE-AREA DELAY-AZIMUTH HV-POL RESULTS

### 14.1 Database

Ground-based HV-pol measurements were made with the transmitter on Socorro Peak and Salinas Peak. For each transmitter site the measurements were made with two modulations (PCW and PN), two pulse lengths ( $5 \mu s$  and  $13 \mu s$ ) and four frequencies, for a total of 16 data sets. The receiving antenna was set in the RSTER-90 configuration and steered in azimuth electrically on each side of three boresight azimuths.

### 14.2 Full Area

The upper left subplot of Figure 70 shows the locations of the ground scattering points for the combined delay-azimuth HV-pol data. The upper right frame shows the distribution of  $\sigma_0$  with respect to

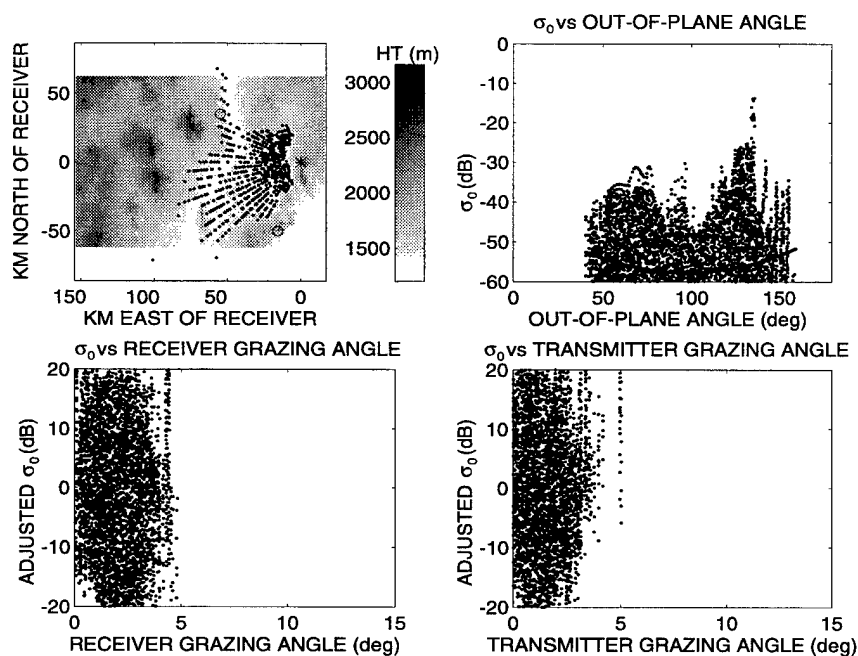


Figure 70. Distribution of Bistatic Scattering Coefficient, HV

out-of-plane angle. The curve fitted to the data in the upper right hand frame is a quadratic function of the out-of-plane angle. The coefficients of the quadratic, in descending order, are 0.00155,  $-0.304$  and  $-42.9$ ;

the units are dB and degrees. The values of the function at 0, 90 and 180 degrees are  $-42.9$ ,  $-57.6$  and  $-47.1$ .

Figure 71 shows the  $\log$  of  $\sigma_0$  plotted against the  $\log$  of the product of the sines of the transmitter and receiver grazing angles for a set of ranges of out-of-plane angle. Superimposed on each frame is a

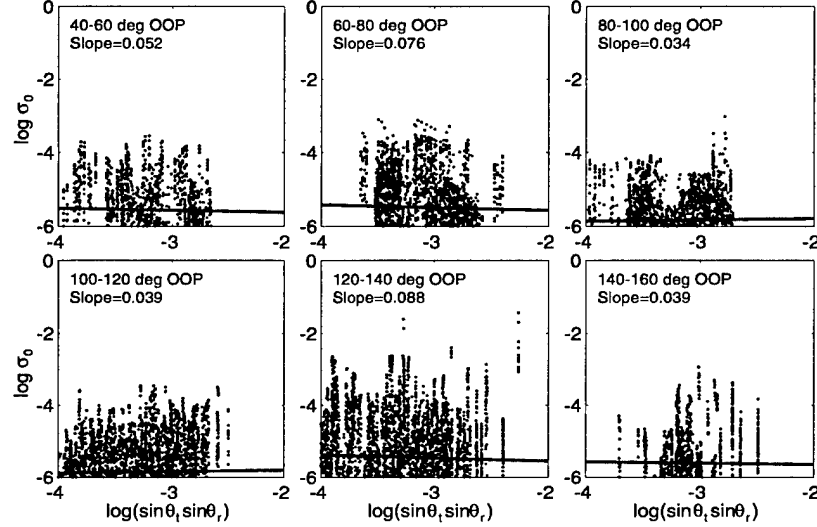


Figure 71. Bistatic Scattering Coefficient vs. Product of Sines of Grazing Angles, HV

straight line representing the best fit of the model  $\sigma_0 = \gamma(\sin \theta_t \times \sin \theta_r)^{\alpha(\theta)}$ . Note that  $\alpha$  is allowed to vary with out-of-plane angle while  $\gamma$  is held constant. The value of  $\sigma_0$  at zero on the horizontal axis gives the value of  $\gamma$  and the slope gives the value of  $\alpha$ . For this data set  $\gamma$  is equivalent to  $-32$  dB and  $\alpha$  varies from  $-0.088$  to  $0.039$ .

Figure 72 shows the distribution of the amplitudes of  $\sigma_0$  for the HV-pol wide-area data. These statistics are obtained by combining the subsets shown in Figure 71. For each subset, the fitted straight line is subtracted from the value of  $\log \sigma_0$  and the result multiplied by 10 to convert to dB. The result is termed “adjusted  $\sigma_0$ ”. The values from each subset are then assembled and sorted in order of magnitude. The index of the sorted values, divided by the total number of values, is shown plotted against adjusted  $\sigma_0$ . This curve then gives the proportion of values below the value indicated on the horizontal axis. It can be seen that the data closely fit a lognormal distribution with a scale width of 7.7 dB.

### 14.3 Limited Area

Figure 73 shows the  $\sigma_0$  cumulative distribution of amplitudes obtained when the scattering area was confined to a 20 km by 30 km rectangle. It can be seen that the distribution of amplitudes is closer to Rayleigh than for the full area but is still closer to a lognormal distribution with a scale width of 6.1 dB.

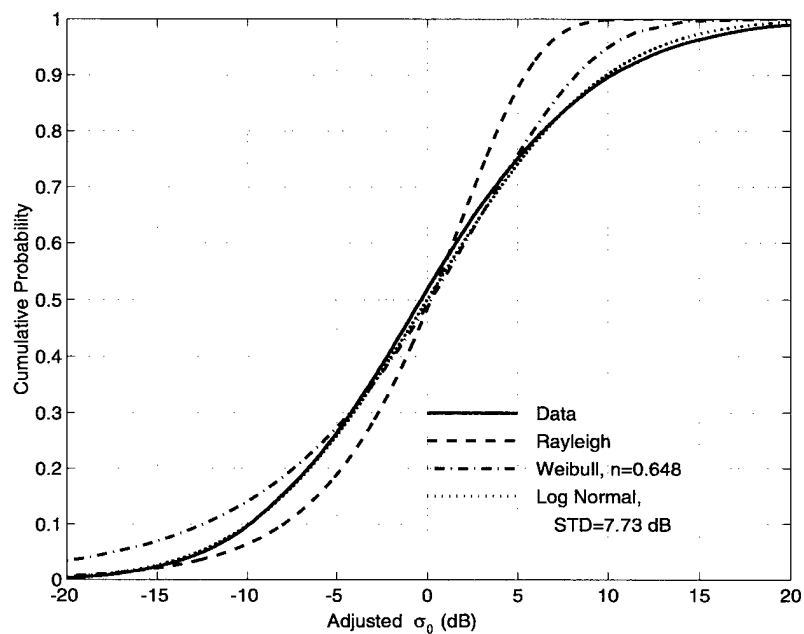


Figure 72. Cumulative Amplitude Distribution, Bistatic, HV

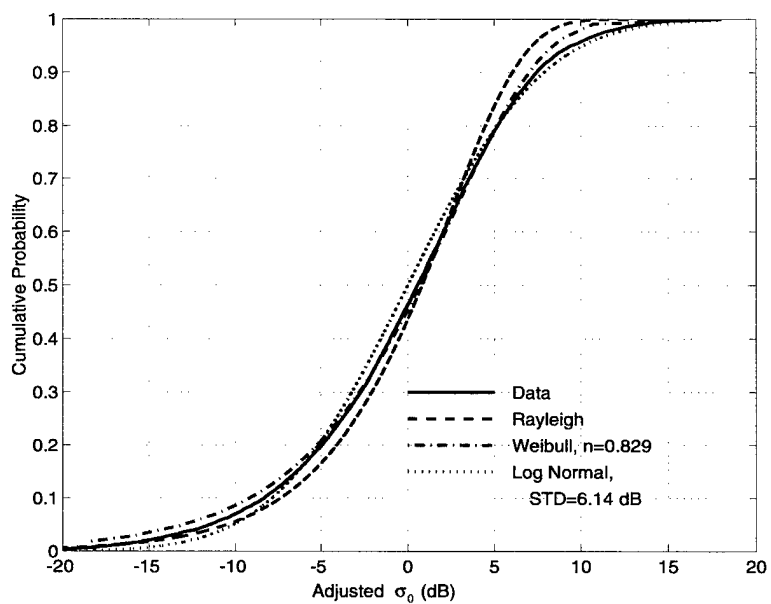


Figure 73. Cumulative Amplitude Distribution, Bistatic, HV, Limited Area

## 15. DELAY-AZIMUTH RADIAL-FLIGHT RESULTS

The wide-area measurements described in the preceding sections were conducted with the receiver at a single site (NOP) and the transmitter at a limited number of positions. To derive the scattering characteristics over a range of transmitter grazing angles, receiver grazing angles and out-of-plane angles it was necessary to assume that the scattering characteristics were uniform over a large area.

To validate the results of the wide-area analysis, analysis was performed on a particular set of VV-pol measurements designed to measure the scattering characteristics at specific sites. These measurements were taken with the transmitter at many positions. This provided data for specific areas over a considerable range of transmitter grazing angles and out-of-plane angles.

The measurements were made at three sites: Fair Site, Harriet Site and Carrizozo. Fair Site and Harriet Site were chosen as representative of WSMR desert terrain. Carrizozo is a small town that was included in the measurement for comparison with the desert sites. At each site, the aircraft was flown along several radials toward or away from the site (with transmission from the nose or tail antennas respectively) with the aircraft altitude constant at 3,000 or 10,000 feet above the site elevation. GPS aircraft position information was recorded during measurements. Tests were conducted at 432, 435 and 438 MHz using a pulsed CW (PCW) waveform. Signals from a vertically-polarized airborne transmitter were scattered from the terrain and received at the vertically-polarized RSTER situated at North Oscura Peak. The receiver beam was fixed, with its azimuth centered on the selected site.

In this section we present the database and detail the results from each site. We then compare the results with those from the wide-area measurements.

### 15.1 Database

Data were gathered at three sites, Fair, Harriet and Carrizozo. The mission designators and dates are given in the table below. The bearing and distance from the receiver are given in the two right-hand

**Table 5. Radial-Flight Database**

	Date	Mission	Distributed as	Frequencies (MHz)	Bearing (deg)	Dist. (km)
Fair Site	Sept. 13, 1993	HOT12	930913HOT	435	242	32
Fair Site	Sept. 16, 1993	HOT15	930916HOT	432, 435, 438	242	32
Fair Site	Sept. 17, 1993	HOT16	930917HOT	432, 435, 438	242	32
Harriet Site	Sept. 14, 1993	HOT13	930914HOT	435	220	33
Carrizozo	Sept. 15, 1993	HOT14	930915HOT	435	104	48

columns. The locations of Fair site and Carrizozo are shown in Figure 9. Harriet site is located 10 km to the south and 7 km to the east of Fair Site.

## 15.2 Fair Site

Fair Site was located at a distance of 32 km from the receiver at North Oscura Peak. The receiver beam-width was approximately 6 degrees, which gave a footprint width at the site of 3.4 km. The range extent selected for processing was 10 km and was centered on the selected site.

Figure 74 shows some statistical results from the returns from Fair Site. The upper left-hand frame shows the locations of the aircraft, the points of reflection and the receiver location. The aircraft

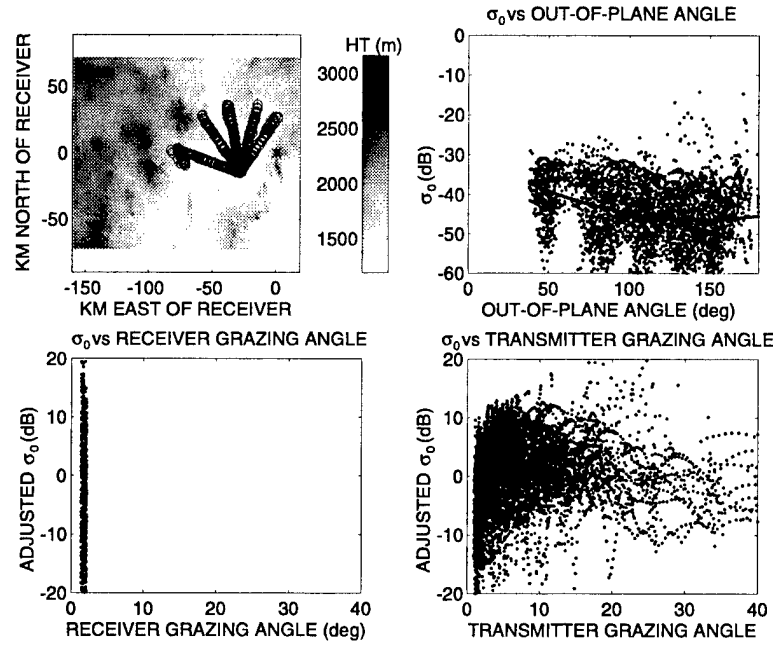


Figure 74. Distribution of Bistatic Scattering Coefficient, Fair Site, VV

positions are shown by a series of circles with each circle corresponding to a recorded range profile. Because of the rapid rate of data gathering, these circles overlap in this diagram. The reflection points on the ground are shown by dots, which are concentrated on the site. These dots are hidden by the circles representing aircraft position. The receiver position is at coordinates 0,0 and is marked by an asterisk.

The upper right frame of Figure 74 shows the distribution of  $\sigma_0$  with respect to out-of-plane angle. It can be seen that there is a decrease in  $\sigma_0$  with increasing out-of-plane angle. A quadratic representing a least-squares fit to the points is shown. The coefficients of the quadratic, in descending order, are 0.000815, -0.235 and -29.3; the units are degrees and dB. The values of the quadratic at 0, 90 and 180 degrees are -29.3, -43.9 and -45.3 dB.

The lower two frames of Figure 74 show adjusted  $\sigma_0$  plotted against receiver grazing angle and transmitter grazing angle. The adjusted  $\sigma_0$  is  $\sigma_0$  with the quadratic dependence on out-of-plane angle subtracted.

In the lower left figure, it can be seen that the receiver grazing angle covers only a small range, since the ground patch is small and the receiver is fixed in position. The lower right frame shows the adjusted  $\sigma_0$  plotted against transmitter grazing angle. This covers a much wider range of grazing angles.

Figure 75 shows the log of  $\sigma_0$  plotted against the log of the product of the sines of the grazing angles. Each of the subplots covers a range of out-of-plane angles approximately centered on one of the

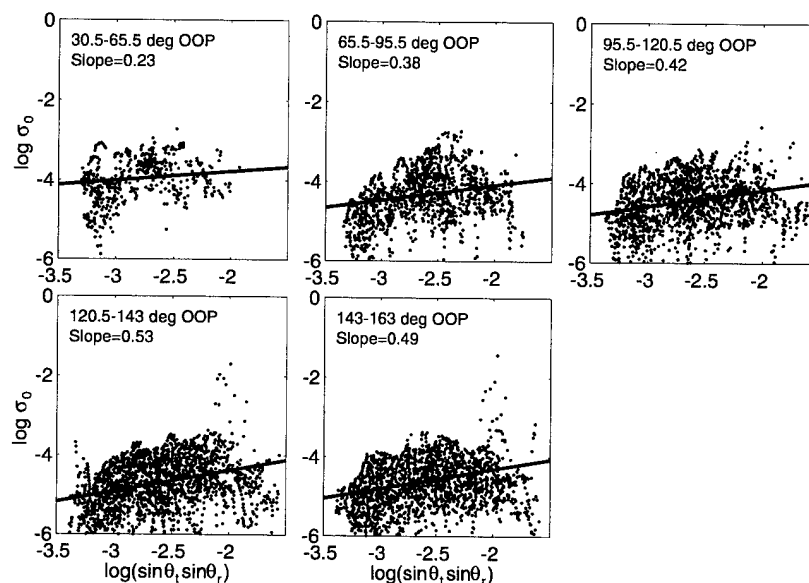


Figure 75. Bistatic Scattering Coefficient vs. Product of Sines of Grazing Angles, Fair Site

radials. Superimposed on each frame is a straight line representing the best fit of the model

$\sigma_0 = \gamma(\sin \theta_t \times \sin \theta_r)^{\alpha(\theta)}$ . Note that  $\alpha$  is allowed to vary with out-of-plane angle while  $\gamma$  is held constant. The value of  $\sigma_0$  at zero on the horizontal axis gives the value of  $\gamma$  and the slope gives the value of  $\alpha$ . For this data set  $\gamma$  is equivalent to -33 dB and  $\alpha$  varies from 0.23 to 0.53 with a mean of 0.41 and a standard deviation of 0.104.

Figure 76 shows the distribution of the amplitudes of  $\sigma_0$  for the Fair Site data. These statistics are obtained by combining the subsets shown in Figure 75. For each subset, the fitted straight line is subtracted from the value of  $\log \sigma_0$  and the result multiplied by 10 to convert to dB. The result is labeled "adjusted  $\sigma_0$ " on the horizontal axis. The values from each subset are then assembled and sorted in order of magnitude. The index of the sorted values, divided by the total number of values, is shown plotted against adjusted  $\sigma_0$  in Figure 76. This curve then gives the proportion of values below the value indicated on the horizontal axis.

The three other curves plotted on this figure, representing Rayleigh, Weibull and lognormal distributions. For each distribution law, the parameters were adjusted to give a least-squares fit to the data. The best fit is with the Weibull distribution.

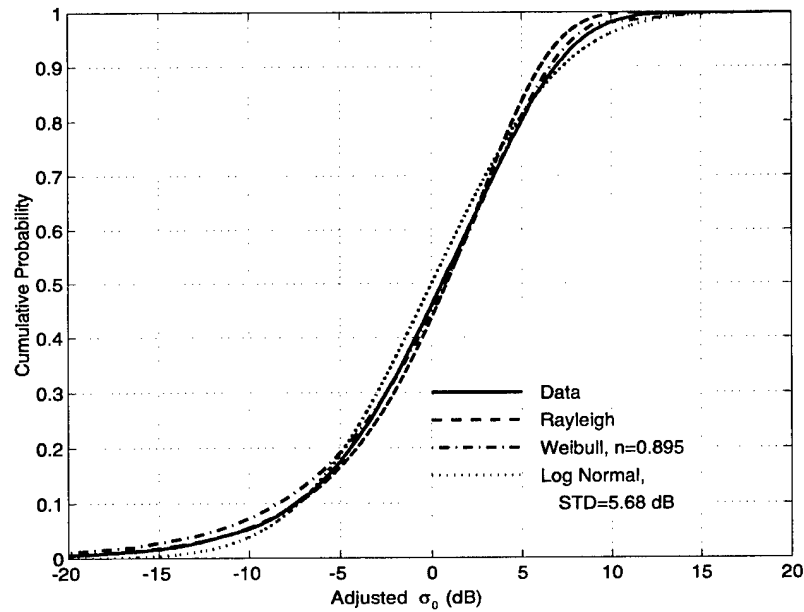


Figure 76. Cumulative Amplitude Distribution, Fair Site, VV

### 15.3 Harriet Site

Harriet Site was located at a distance of 33 km from the receiver. The receiver beam-width was approximately 6 degrees, which gave a width at the site of 3.4 km. The range extent selected for processing was 10 km and was centered on the selected site.

Figure 77 shows some statistical results from the returns from Harriet Site. The upper left-hand frame shows the locations of the aircraft, shown by circles, and the receiver location shown by an asterisk. The points of reflection are indicated by dots but these are hidden by the circles. The upper right frame shows the distribution of  $\sigma_0$  with respect to out-of-plane angle. It can be seen that  $\sigma_0$  falls with increasing out-of-plane angle. A quadratic representing a least-squares-fit to the points is shown. The coefficients of this quadratic, in descending order, are 0.000903, -0.272 and -36.6. The units are dB and degrees. The quadratic has values of -36.6, -53.8 and -56.3 dB at 0, 90 and 180 degrees out-of-plane angle.

The lower two frames show the values of  $\sigma_0$ , with the quadratic function subtracted from them, plotted against receiver grazing angle and transmitter grazing angle. In the lower left frame, it can be seen that the receiver grazing angle covers only a small range, since the ground patch is small and the receiver is stationary. The lower right frame shows that  $\sigma_0$  increases with transmitter grazing angle.

Figure 78 shows the log of  $\sigma_0$  plotted against the log of the product of the sines of the transmitter and receiver grazing angles for a set of ranges of out-of-plane angle. Each of the subplots covers a range of out-of-plane angles approximately centered on one of the radials. Superimposed on each frame is a straight line representing the best fit of the model  $\sigma_0 = \gamma(\sin\theta_t \times \sin\theta_r)^{\alpha(\theta)}$ . Note that  $\alpha$  is allowed to vary with



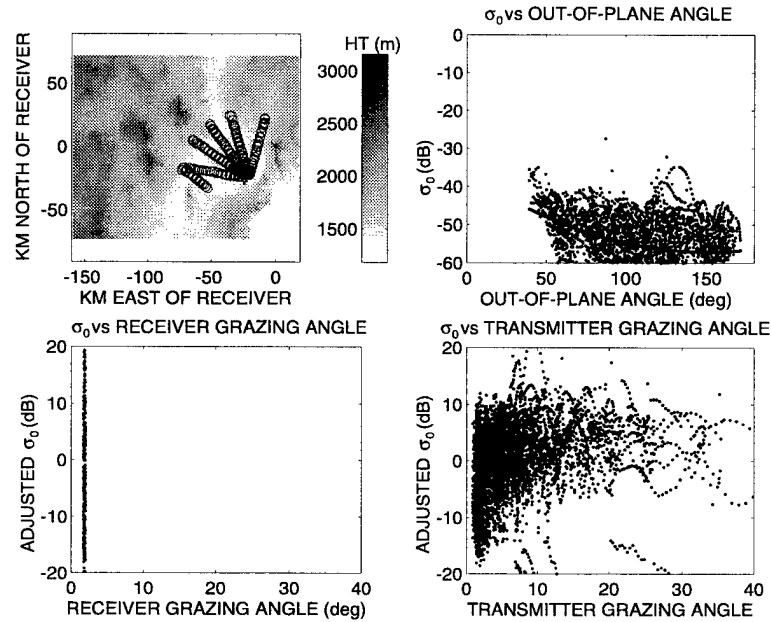


Figure 77. Distribution of Bistatic Scattering Coefficient, Harriet Site, VV

out-of-plane angle while  $\gamma$  is held constant. The value of  $\sigma_0$  at zero on the horizontal axis gives the value of  $\gamma$  and the slope gives the value of  $\alpha$ . For this data set  $\gamma$  is equivalent to  $-41$  dB and  $\alpha$  varies from 0.31 to 0.65, with a mean of 0.52 and a standard deviation of 0.12.

Each subplot is labeled with the slope of the straight line fitted to the data points. This slope corresponds to the value of  $\alpha$  in the Generalized Lambertian Formula. The average of the five  $\alpha$  values is 0.53.

Figure 79 shows the distribution of the amplitudes of  $\sigma_0$  for the Harriet Site data. These statistics are obtained by combining the subsets shown in Figure 78. For each subset, the fitted straight line is subtracted from the value of  $\log \sigma_0$  and the result multiplied by 10 to convert to dB. The result is termed "adjusted  $\sigma_0$ ". The values from each subset are then assembled and sorted in order of magnitude. The index of the sorted values, divided by the total number of values, is shown plotted against adjusted  $\sigma_0$ . This curve then gives the proportion of values below the value indicated on the horizontal axis.

The three other curves plotted on this figure represent Rayleigh, Weibull and lognormal distributions. For each distribution law, the parameters were adjusted to give a least-squares fit to the data. It can be seen that the distribution of the data points is a good fit to the log normal curve with a scale width of 5.5 dB but is also close to the Rayleigh and Weibull curves.

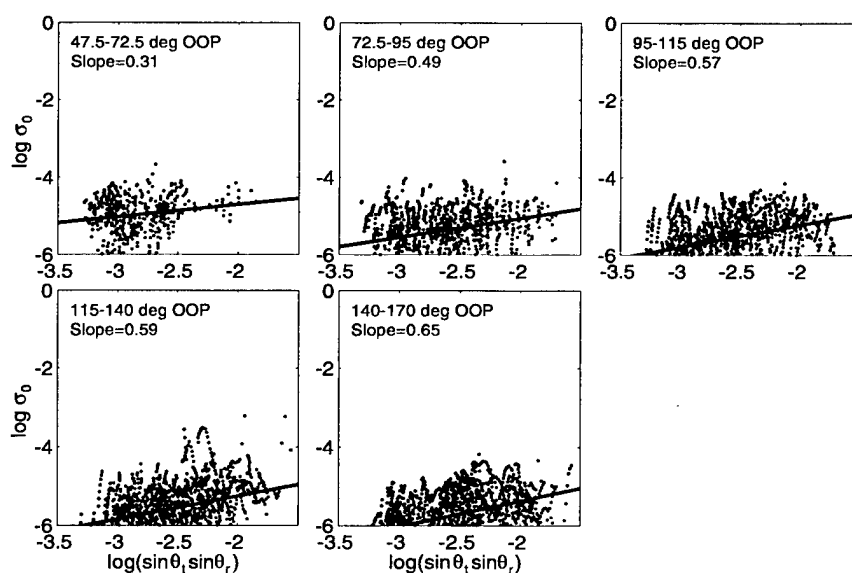


Figure 78. Bistatic Scattering Coefficient vs. Product of Sines of Grazing Angles, Harriet Site

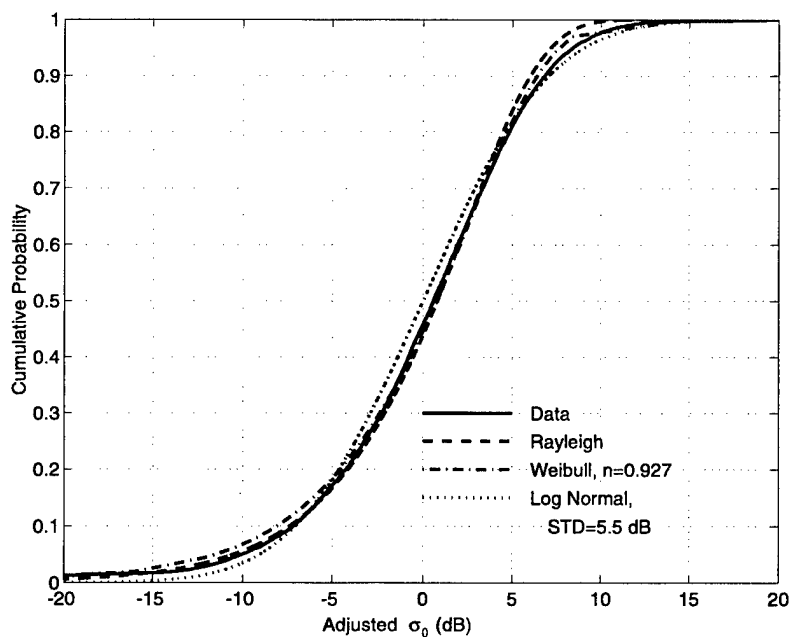


Figure 79. Cumulative Amplitude Distribution, Harriet Site, VV

## 15.4 Carrizozo

Carrizozo is a small town located 47.8 km from the receiver at North Oscura Peak on a bearing of 104 degrees. The receiver antenna beam-width was approximately 6 degrees, which gave a beam-width at the site of approximately 5 km. The range extent selected for processing was 5 km. The selected scattering

area was therefore 5 km square and was centered on the town. The built-up area of the town occupied only a small part of this area.

Figure 80 shows some statistical results from the returns from Carrizozo. The upper left-hand frame shows the locations of the aircraft and the receiver location; these are marked by circles and an asterisk respectively. The upper right frame shows the distribution of  $\sigma_0$  with respect to out-of-plane

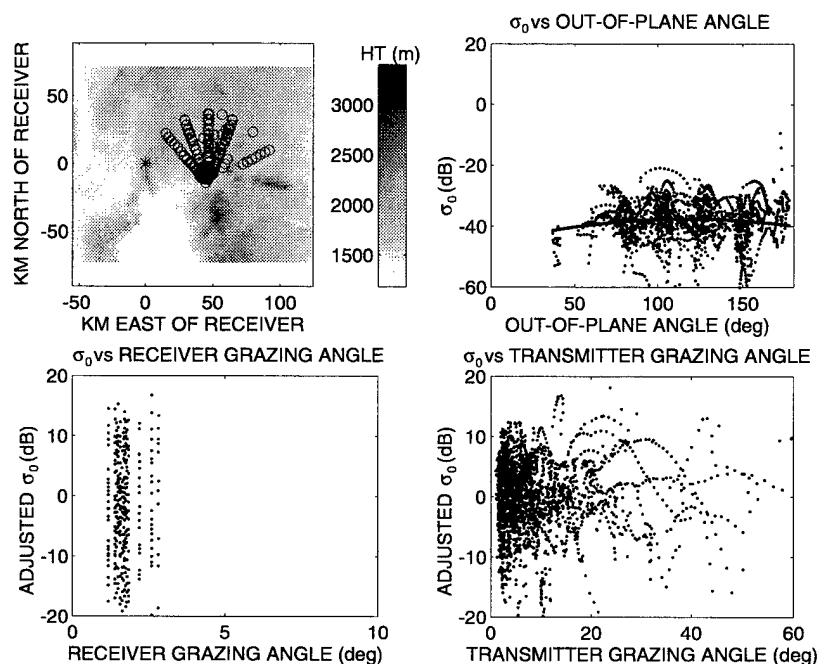


Figure 80. Distribution of Bistatic Scattering Coefficient, Carrizozo, VV

angle. In contrast to the negative slope exhibited by the VV-pol data from the dessert sites,  $\sigma_0$  is constant or increases slightly with increasing out-of-plane angle. A quadratic fitted to the points is shown. The coefficients of this quadratic, in descending order, are  $-0.000586$ ,  $0.137$  and  $-45.7$ . The units are dB and degrees. The quadratic has values of  $-45.7$ ,  $-38.0$ ,  $-39.9$  dB at  $0$ ,  $90$  and  $180$  degrees out-of-plane angle, respectively.

The lower two frames of Figure 80 show the values of  $\sigma_0$ , with the quadratic function subtracted from them (labelled "adjusted  $\sigma_0$ ") plotted against receiver grazing angle and transmitter grazing angle. In the lower left figure, it can be seen that the receiver grazing angle covers only a small range, since the ground patch is small and the receiver is stationary. The lower right frame shows the adjusted  $\sigma_0$  plotted against transmitter grazing angle.

Figure 81 shows the log of  $\sigma_0$  plotted against the log of the product of the sines of the transmitter and receiver grazing angles for different of out-of-plane angle. Each of the subplots covers a range of out-of-plane angles approximately centered on one of the radials. Superimposed on each frame is a straight line

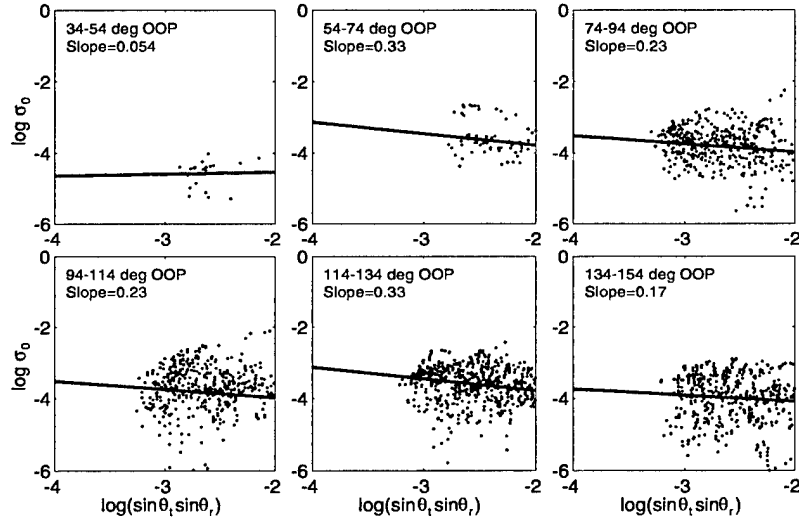


Figure 81. Bistatic Scattering Coefficient vs. Product of Sines of Grazing Angles, Carrizozo

representing the best fit of the model  $\sigma_0 = \gamma(\sin \theta_i \times \sin \theta_r)^{\alpha(\theta)}$ . Note that  $\alpha$  is allowed to vary with out-of-plane angle while  $\gamma$  is held constant. The value of  $\sigma_0$  at zero on the horizontal axis gives the value of  $\gamma$  and the slope gives the value of  $\alpha$ . For this data set  $\gamma$  is equivalent to -44 dB and  $\alpha$  varies from -0.33 to 0.05 with a mean of -0.20 and a standard deviation of 0.13.

Each subplot is labeled with the slope of the straight line fitted to the data points. This slope is equal to the exponent  $\alpha$  in the Generalized Lambertian Formula. Compared to other measurements, these results are unusual in that most of the values of  $\alpha$  are negative. The value of  $\alpha$  averaged over the six out-of-plane angles is 0.10. This result indicates that there is a significant difference between urban and desert terrain in the matter of sensitivity to grazing angles.

Figure 82 shows the distribution of the amplitudes of  $\sigma_0$  for the Carrizozo data. These statistics are obtained by combining the subsets shown in Figure 81. For each subset, the fitted straight line is subtracted from the value of  $\log \sigma_0$  and the result multiplied by 10 to convert to dB. The result is termed "adjusted  $\sigma_0$ ". The values from each subset are then assembled and sorted in order of magnitude. The index of the sorted values, divided by the total number of values, is shown plotted against adjusted  $\sigma_0$ . This curve then gives the proportion of values below the value indicated on the horizontal axis.

The three other curves plotted on this figure, representing Rayleigh, Weibull and lognormal distributions. For each distribution law, the parameters were adjusted to give a least-squares fit to the data. It can be seen that the distribution in the data points is close to Rayleigh except for a slightly longer tail at the upper end.

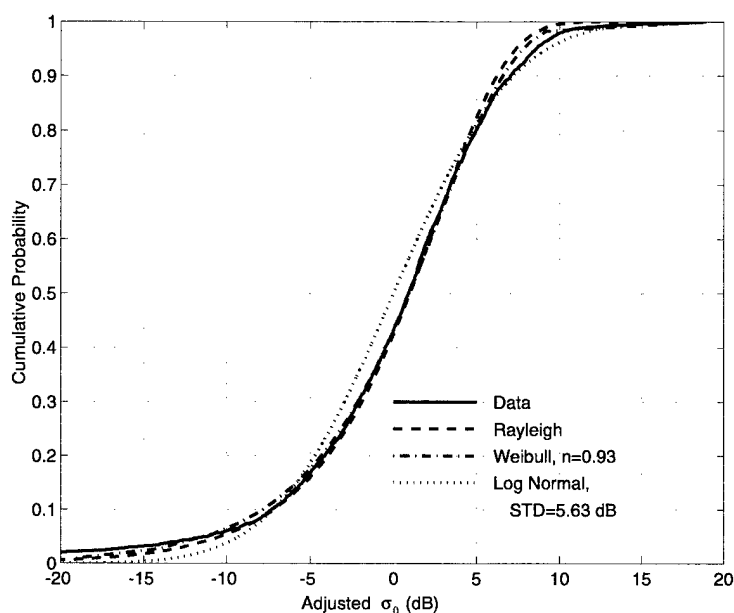


Figure 82. Cumulative Amplitude Distribution, Carrizozo, VV

## 15.5 Comparison with Wide-Area Results

The value of  $\sigma_0$  at 90 degrees out-of-plane angle varied from site to site. For the Fair Site,  $\sigma_0$  was  $-43.9$  dB and was about one dB higher than in the wide-area measurements. For Harriet Site, the value was  $-53.8$  dB, which is almost 10 dB lower than from Fair site. This result is surprising, since the sites were similar. The difference might be due to equipment fault. A check on the direct signal showed that this was also low by about the same amount, suggesting that the transmitter power or transmitter antenna gain was lower than recorded. The town of Carrizozo gave a value for  $\sigma_0$  of  $-38.0$  dB, being about 6 dB higher than Fair Site. The value was expected to be higher because of the presence of houses.

The amplitudes distribution from the three sites were similar in width. The best fit for the lognormal distribution gave widths of 5.66, 5.47 and 5.62 dB for Fair Site, Harriet Site and Carrizozo.

The variation of  $\sigma_0$  with grazing angle was different for Carrizozo than for the other two sites. The values of  $\alpha$  in the Generalized Lambertian Formula were 0.48, 0.53 and  $-0.10$  for Fair Site, Harriet Site and Carrizozo. The marked difference for Carrizozo is in keeping with the notion that scattering from buildings is significantly different from that from the desert foliage.

## 16. DELAY-DOPPLER UHF VV-POL RESULTS

The data discussed in this section is different in many respect from that described in previous sections. The data discussed in previous sections were obtained using the RSTER antenna for receiving. In analyzing the data, the scattering cells were resolved in azimuth and delay. The size of the resolved cell depended on the width of the RSTER antenna receiving beam and the bandwidth of the system. In this section, we deal with data taken using airborne transmitters and receivers, both of which used broad beam antennas. Since angle resolution was poor, Doppler resolution was used in combination with delay resolution to define the scattering cell size and position. For the details of this experiment, see Sections 4.2, 7 and 10.

### 16.1 M3D21\_1003 and M3E21\_1003 Data

There were two valid sets of VV-pol delay-Doppler data available for comparison with the delay-azimuth data. For each of these experiments, the transmitter was flown eastward and the receiver flown northward. The transmitter antenna was on the left-hand side of the aircraft and therefore radiated to the north of track. The receiving antenna was a dipole projecting from the belly of the aircraft and was assumed to have the same gain at all azimuths.

Figure 84 shows a plots of constant delay (solid lines) and constant Doppler (broken lines) for the ground reflection points for data set M3D21\_1003. Figure 83 shows a similar plot for data set

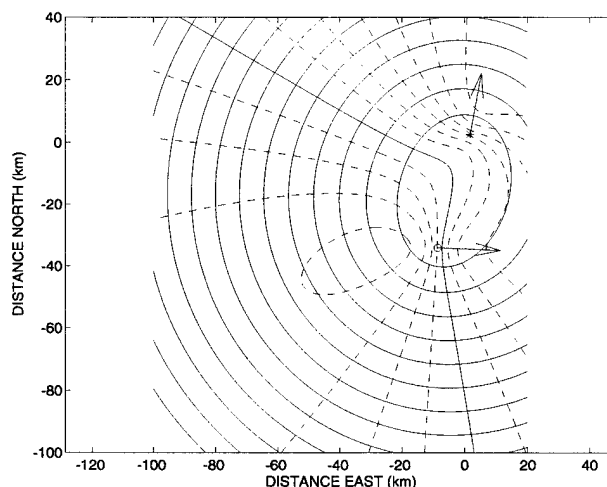


Figure 83. Isodelay & Isodoppler Plots, M3E21\_1003, VV

M3E21\_1003. The position of the east-bound transmitter is shown by a circle and that of the north-bound receiver by an asterisk. The solid Doppler contour indicates zero Doppler shift. To the north and east of

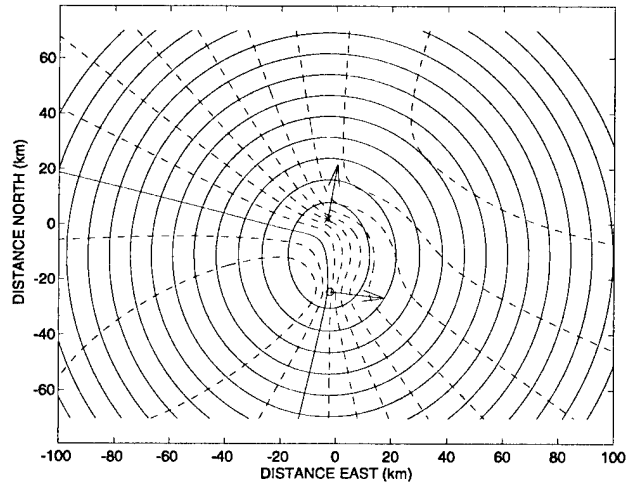


Figure 84. Isodelay & Isodoppler Plots, M3D21\_1003, VV

this line the Doppler shift is positive, i.e. negative range rate. The interval between the constant delay lines is 10 resolution cells. The interval between constant Doppler lines is 5 resolution cells.

Figure 85 shows the combined VV-pol signals for missions M3D21\_1003 and M3E32\_1003. The

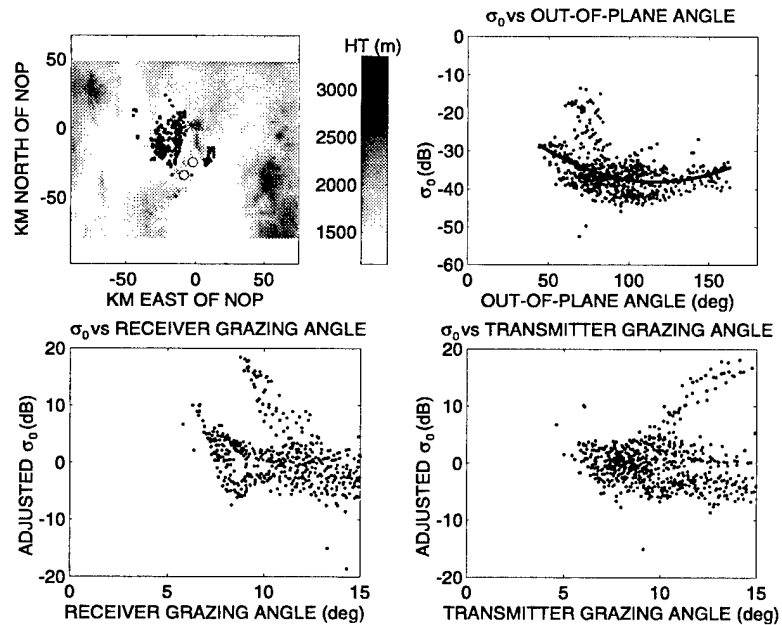


Figure 85. Distribution of Bistatic Scattering Coefficient, M3D21 & M3E21, VV

upper left-hand frame shows the locations of the scatterers that give rise to returns that were 3 dB or more higher than the noise floor (the threshold level was set close to the noise floor to ensure that there were

sufficient data points, at the expense of amplitude errors at the lower values). The locations of the transmitting and receiving aircraft are marked by circles and asterisks, respectively. The upper right frame shows the distribution of  $\sigma_0$  with respect to out-of-plane angle. A quadratic fitted to the points is shown. The coefficients of this quadratic, in descending order, are 0.00224, -0.45 and -22.0. The units are dB and degrees. The quadratic has values of -22.0, -44.2 and -30.1 dB at 0, 90 and 180 degrees out-of-plane angle, respectively. The lower two frames show the values of  $\sigma_0$  with the parabolic function subtracted from them. The values are plotted against receiver grazing angle and transmitter grazing angle. Figure 86 shows the log of the bistatic scattering coefficient against the log of the product of the sines of the grazing angles.

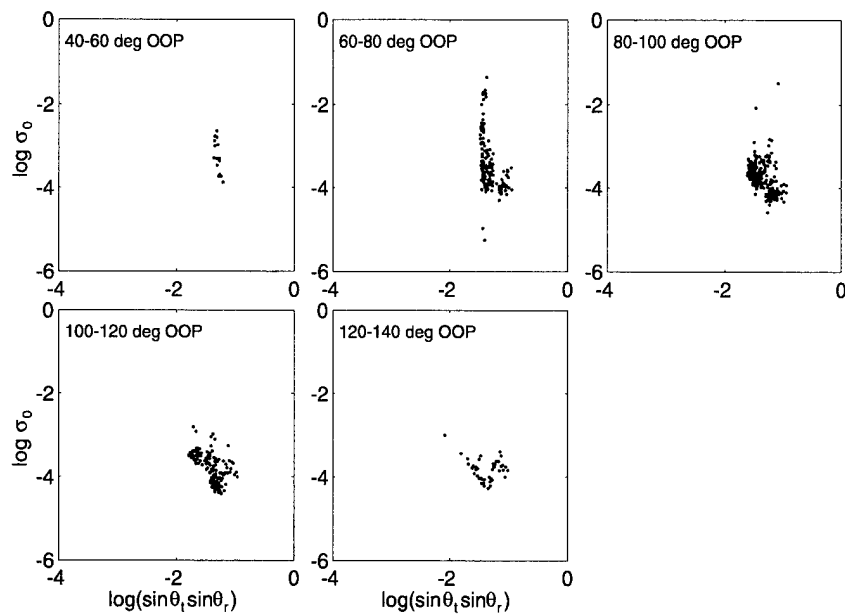


Figure 86. Log of Bistatic Scattering Coefficient vs. Log of Product of Sines of Grazing Angles, M3D21 & M3E21, VV



## 17. DELAY-DOPPLER UHF HH-POL RESULTS

### 17.1 M3D21\_1001 and M3E21\_1001 Data

There were two valid sets of HH-pol delay-Doppler data available that gave estimates of  $\sigma_0$  in the area covered by the delay-azimuth data. In each of these, the transmitter was flown eastward and the receiver flown northward. The transmitter antenna was on the left-hand side of the aircraft and therefore radiated to the north of track. The receiving antenna was a dipole projecting from the rear of the aircraft and was assumed to have the same gain over azimuths of interest as a dipole in free space.

Figure 87 and 88 show plots of constant delay (solid lines) and constant Doppler (broken lines) for the ground reflection points. The position of the east-bound transmitter is shown by a circle and that of

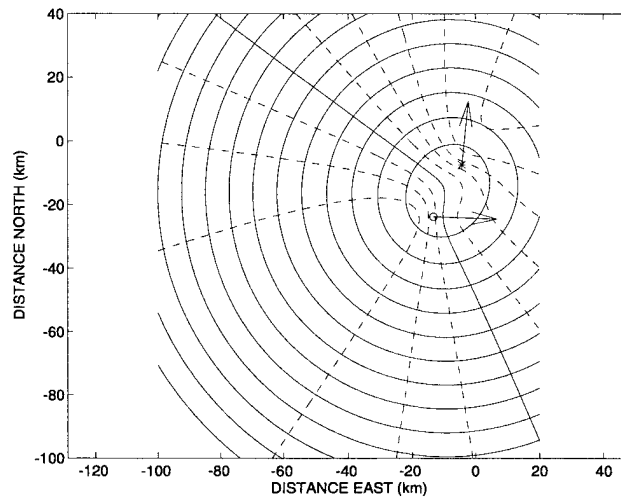


Figure 87. Isodelay & Isodoppler Plots, M3D21\_1001, HH

the north-bound receiver by an asterisk. The solid Doppler contour indicates zero Doppler shift. To the north and east of this line the Doppler shift is positive, i.e. negative range rate. The interval between the constant delay lines is 10 resolution cells. The interval between constant Doppler lines is 5 resolution cells.

Figure 89 shows the combined HH-polarized signals for missions M3D21\_1001 and M3E32\_1001. The upper left-hand frame shows the locations of the scatterers that give rise to returns that are at least 3 dB above the noise floor. The locations of the transmitting and receiving aircraft are marked by circles and asterisks, respectively. The upper right frame shows the distribution of  $\sigma_0$  with respect to out-of-plane angle. A quadratic fitted to the points is shown. The coefficients of this quadratic, in descending order, are 0.00223, -0.50 and 3.22. The units are dB and degrees. The quadratic has values of 3.2, -23.4 and -13.8 dB at 0, 90 and 180 degrees out-of-plane angle, respectively. The lower two

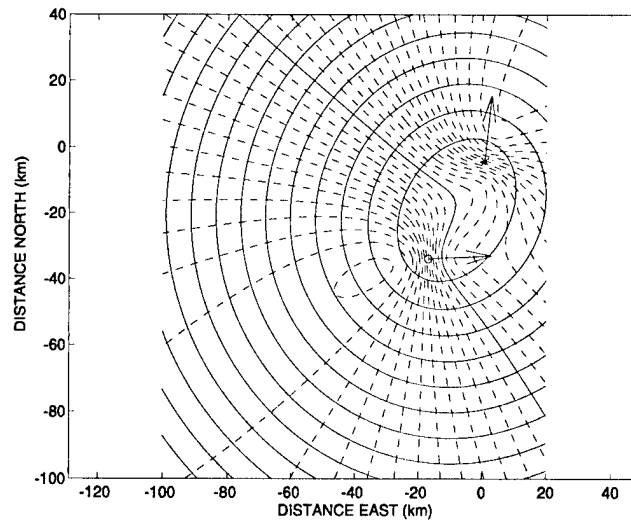


Figure 88. Isodelay & Isodoppler Plots, M3E21\_1001, HH

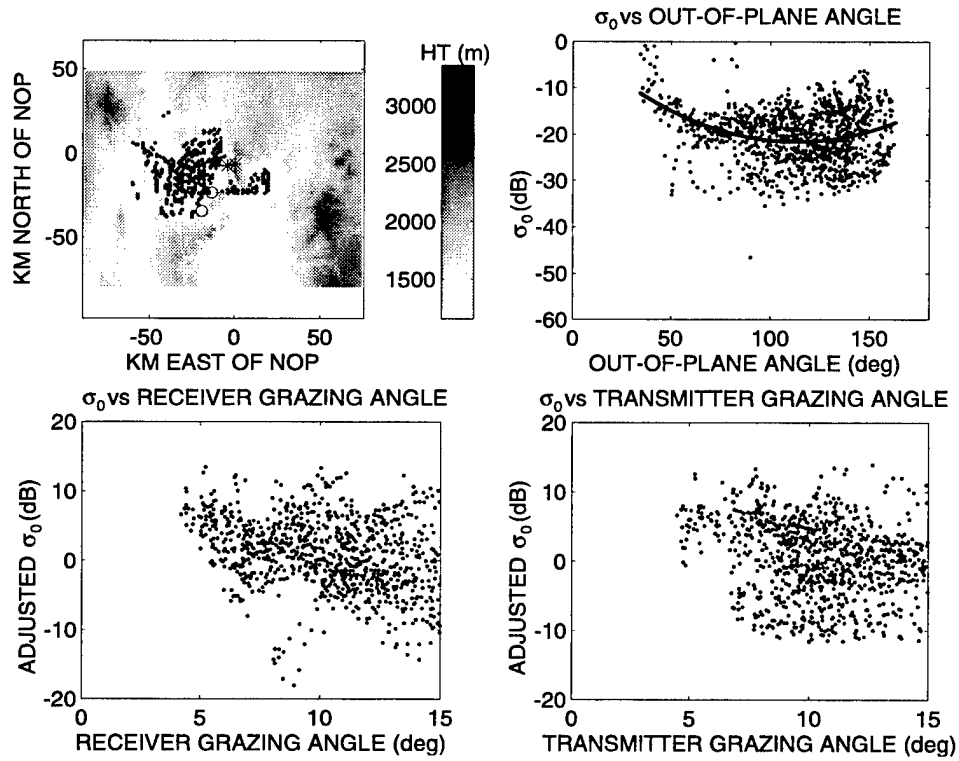


Figure 89. Distribution of Bistatic Scattering Coefficient, M3D21 & M3E21, HH

frames show the values of  $\sigma_0$  with the parabolic function subtracted from them. The values are plotted against receiver grazing angle and transmitter grazing angle.

Figure 90 shows the log of the bistatic scattering coefficient against the log of the product of the sines of the grazing angles.

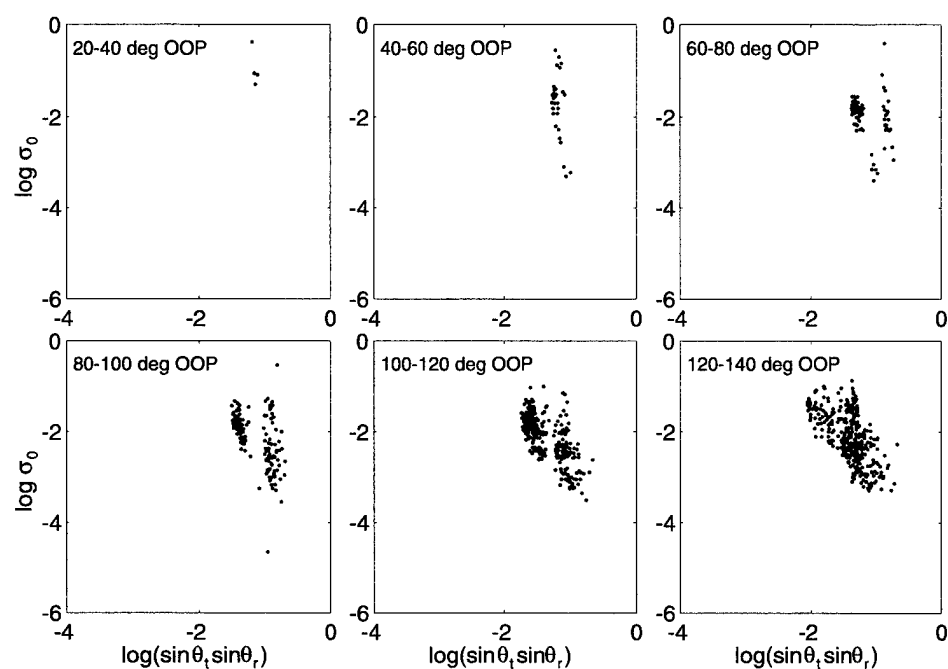


Figure 90. Log of Bistatic Scattering Coefficient vs. Log of Product of Sines of Grazing Angles, M3D21 & M3E21, HH

## 18. DELAY-DOPPLER UHF VH-POL RESULTS

### 18.1 M3D21\_1002 and M3E21\_1002 Data

There were two valid sets of VH-pol delay-Doppler data available that gave estimates of  $\sigma_0$  in the area covered by the delay-azimuth data. In each of these, the transmitter was flown eastward and the receiver flown northward. The horizontally polarized transmitter antenna was on the left-hand side of the aircraft and therefore radiated to the north of track. The receiving antenna was a vertical dipole projecting from the belly of the aircraft and was assumed to have the same gain at all azimuths.

Figure 91 and 92 show plots of constant delay (solid lines) and constant Doppler (broken lines) for the ground reflection points. The position of the east-bound transmitter is shown by a circle and that of

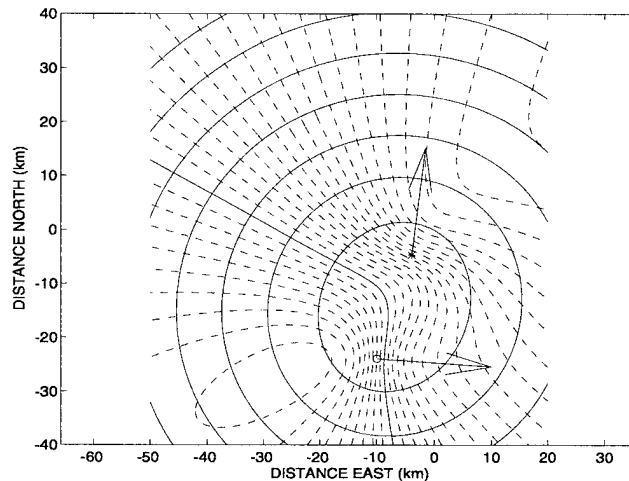


Figure 91. Isodelay & Isodoppler Plots, M3D21\_1002, VH

the north-bound receiver by an asterisk. The solid Doppler contour indicates zero Doppler shift. To the north and east of this line the Doppler shift is positive, i.e., negative range rate. The interval between the constant delay lines is 10 resolution cells. The interval between constant Doppler lines is 5 resolution cells.

Figure 93 shows the combined VH-polarized signals for missions M3D21\_1002 and M3E32\_1002. The upper left-hand frame shows the locations of the scatterers that give rise to returns that are at least 3 dB above the noise floor. The locations of the transmitting and receiving aircraft are marked by circles and asterisks, respectively. The upper right frame shows the distribution of  $\sigma_0$  with respect to out-of-plane angle. A quadratic fitted to the points is shown. The coefficients of this quadratic, in descending order, are 0.00300, -0.53 and -12.8. The units are dB and degrees. The quadratic has values of -12.8, -36.4 and -11.5 dB at 0, 90 and 180 degrees out-of-plane angle, respectively. The lower two

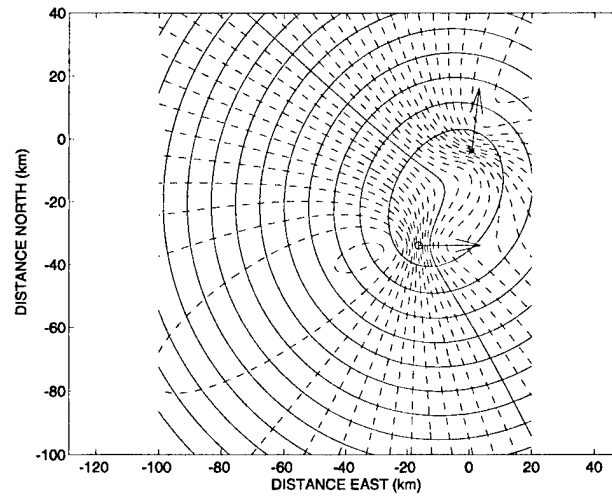


Figure 92. Isodelay & Isodoppler Plots, M3E21\_1002, VH

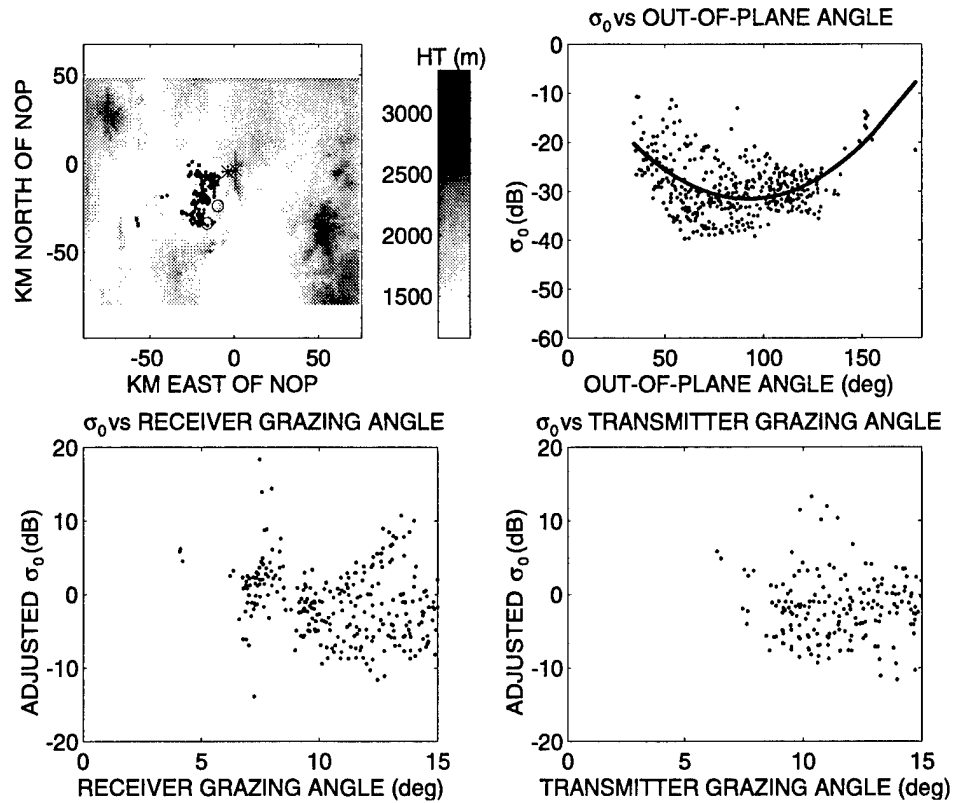


Figure 93. Distribution of Bistatic Scattering Coefficient, M3D21 & M3E21, VH

frames show the values of  $\sigma_0$  with the parabolic function subtracted from them. The values are plotted against receiver grazing angle and transmitter grazing angle.

Figure 94 shows the log of the bistatic scattering coefficient against the log of the product of the sines of the grazing angles.

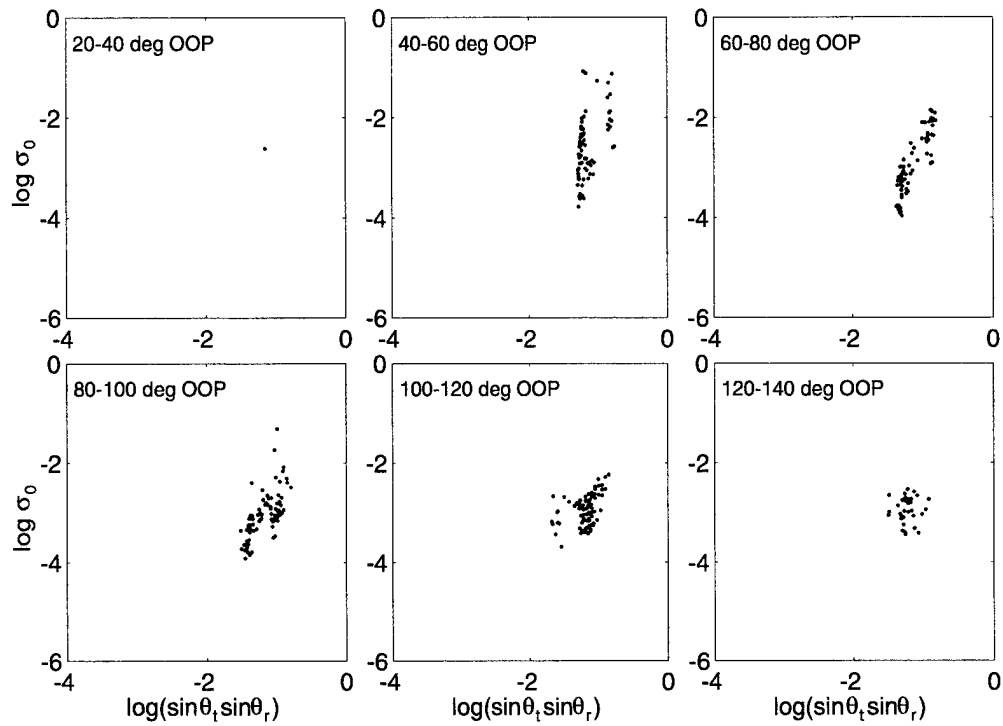


Figure 94. Log of Bistatic Scattering Coefficient vs. Log of Product of Sines of Grazing Angles, M3D21 & M3E21, VH

## 19. COMBINED UHF VV-POL RESULTS

### 19.1 Full Area

Figure 95 shows the result of combining the delay-azimuth and delay-Doppler VV-polarized measurements. The delay-azimuth data include the static and airborne returns associated with Socorro

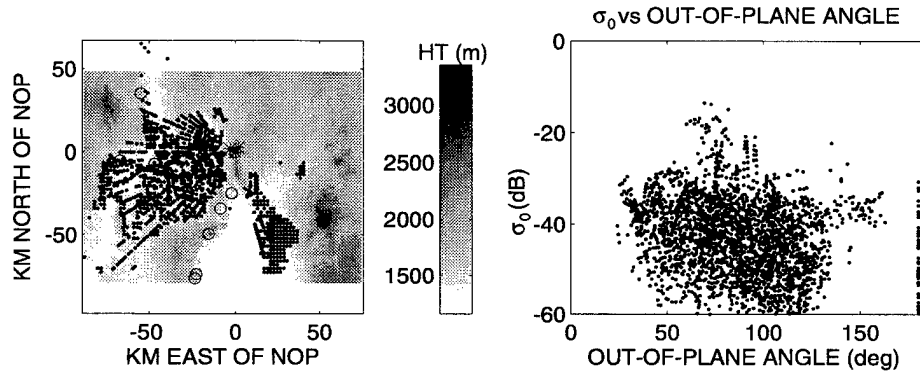


Figure 95. Distribution of Bistatic Scattering Coefficient, Combined Data, UHF, VV

Peak and Salinas Peak, the static returns associated with Sierra Blanca and the monostatic data described in the internal memo by John Jayne, dated October 18, 1993.

The upper left-hand frame of Figure 95 shows the locations of the scatterers that give returns at least 10 dB above the noise floor. The locations of the transmitter and receiver are marked by circles and asterisks, respectively. The upper right frame shows the distribution of  $\sigma_0$  with respect to out-of-plane angle. Note that the monostatic measurements form a vertical line at 180 degrees out-of-plane angle.

Figure 96 shows the log of the bistatic scattering coefficient plotted against the log of the product of the sines of the grazing angles. It can be seen that the returns form two groups. The points to the left of center are provided by the delay-azimuth analysis and those to the right by the delay-Doppler analysis.

Superimposed on each frame of figure 96 is a straight line representing the best fit of the model  $\sigma_0 = \gamma(\sin\theta_i \times \sin\theta_r)^{\alpha(\theta)}$ . Note that  $\alpha$  is allowed to vary with out-of-plane angle while  $\gamma$  is held constant. The value of  $\sigma_0$  at zero on the horizontal axis gives the value of  $\gamma$ . For this data set,  $\gamma$  is equivalent to -31 dB and  $\alpha$  varies from 0.27 to 0.87.

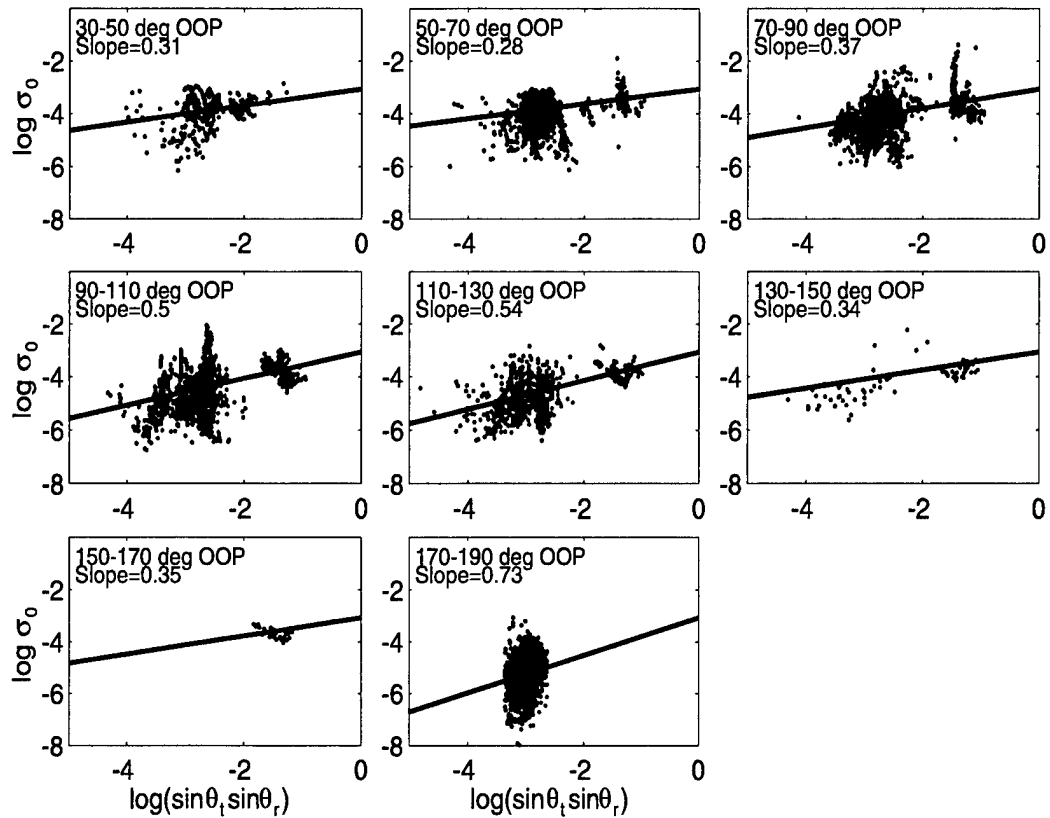


Figure 96. Log of Bistatic Scattering Coefficient vs. Log of Product of Sines of Grazing Angles, Combined Data, UHF, VV

## 19.2 Limited Area

Figure 97 shows the combined VV data when the ground scattering area is limited to a 20 km by 30 km area centered at 30 km west and 15 km south of North Oscura Peak. Figure 98 shows the log of the bistatic scattering coefficient plotted against the log of the product of the sines of the grazing angles. The value of  $\gamma$  for this restricted area is -31 dB, and  $\alpha$  varies from 0.32 to 0.82. These values agree closely with those derived from the full area, supporting the assumption that the full area is substantially uniform in its scattering characteristics.



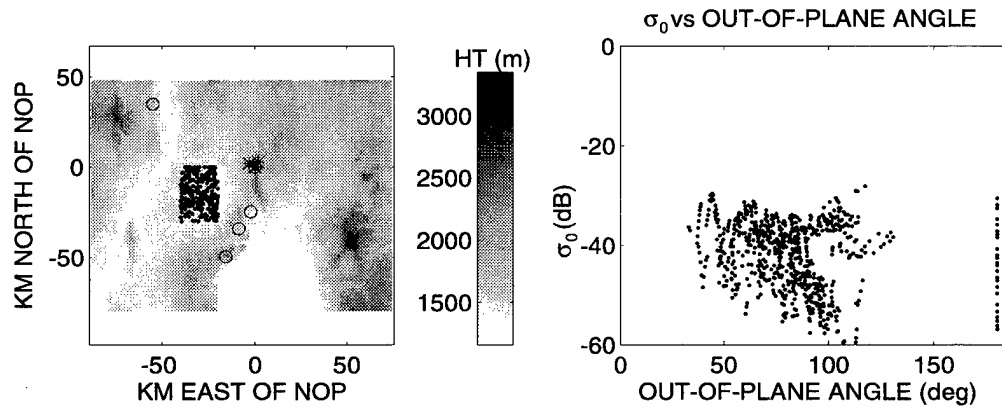


Figure 97. Distribution of Bistatic Scattering Coefficient, Combined Data, Limited Area, UHF, VV

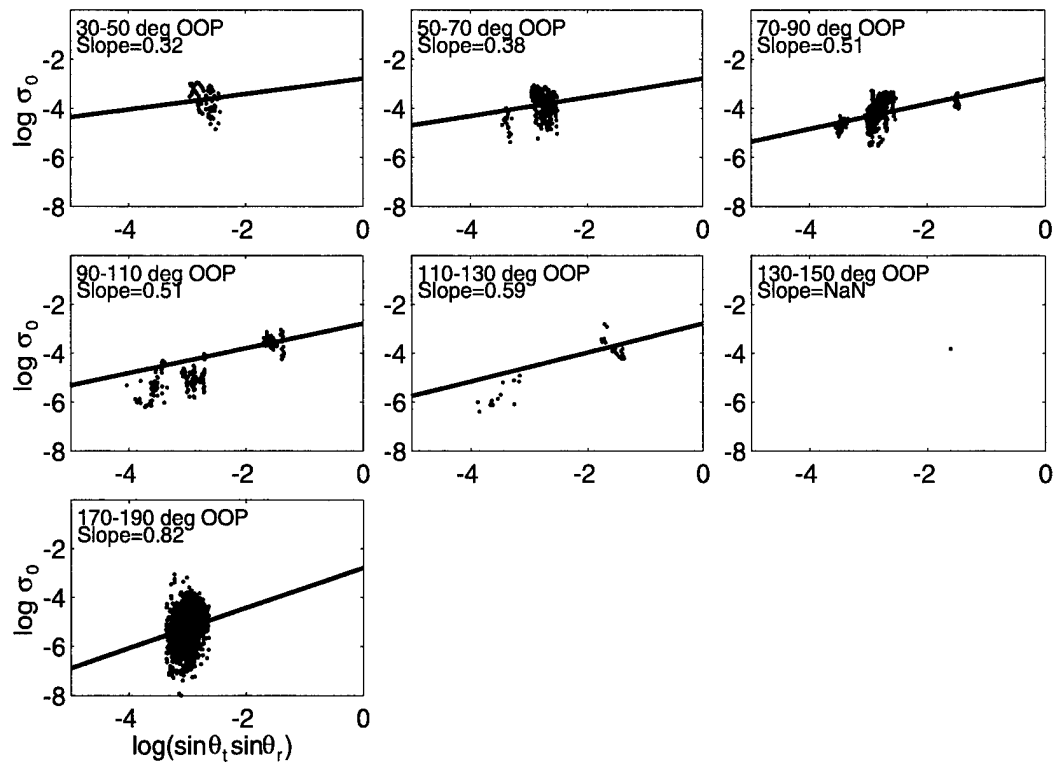


Figure 98. Log of Bistatic Scattering Coefficient vs. Log of Product of Sines of Grazing Angles, Combined Data, Limited Area, UHF, VV

## 20. COMBINED UHF HH-POL RESULTS

### 20.1 Full Area

Figure 99 shows the combined result from the HH-pol delay-azimuth and delay-Doppler measurements. The delay-azimuth data included the bistatic, single-frequency airborne returns associated

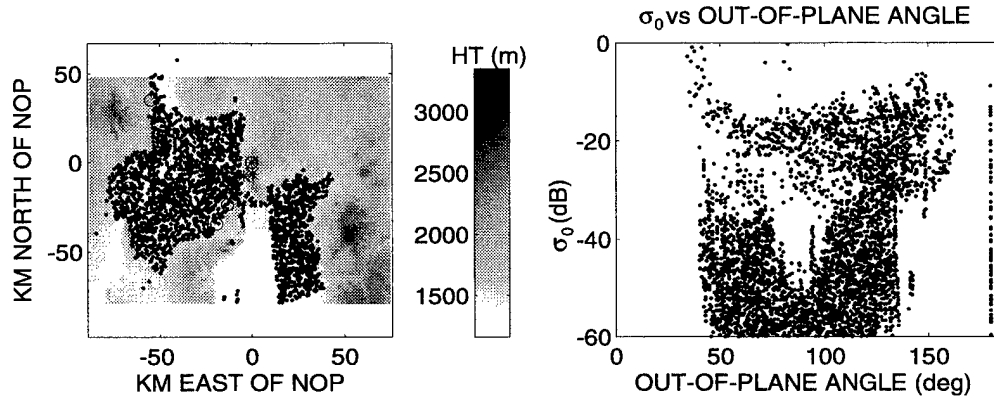


Figure 99. Distribution of Bistatic Scattering Coefficient, Combined Data, UHF, HH

with Socorro Peak, the multi-frequency bistatic ground-based returns associated with Salinas Peak, the quasi-monostatic BINOP measurements conducted on April 4, 1994 at North Oscura Peak and the monostatic measurements collected on August 27, 1993. The delay-Doppler data are from missions M3D21\_1001, M3E21\_1001 and M3D21\_2001.

The upper left-hand frame of Figure 99 shows the locations of the scatterers that give returns at least 10 dB above the noise floor. The locations of the transmitter and receiver are marked by circles and asterisks respectively.

The upper right frame shows the distribution of  $\sigma_0$  with respect to out-of-plane angle. It is apparent that the data points belong to two distinct distributions, the lower set being from the delay-azimuth data taken at small grazing angles and the higher set from the delay-Doppler data taken at higher grazing angles. The delay-azimuth data taken with the RSTER receiving antenna shows a drop in the value of  $\sigma_0$  in the region of 90 degrees out-of-plane angle. The same decrease is not observed in the air-to-air delay-Doppler data. This topic was addressed in Section 2.

Figure 100 shows the log of the bistatic scattering coefficient plotted against the log of the product of the sines of the grazing angles. Following the model described in Section 2, two parallel straight lines are superposed on each frame. These lines represent the best fit to the model defined by  $\sigma_0' = \gamma \vartheta(\phi) (\sin \theta_i \sin \theta_r)^{\alpha(\phi)}$  (Equation 7), where  $\vartheta(\phi) = \frac{1 + a + (1 - a) \cos 2\phi}{2}$  for the delay-

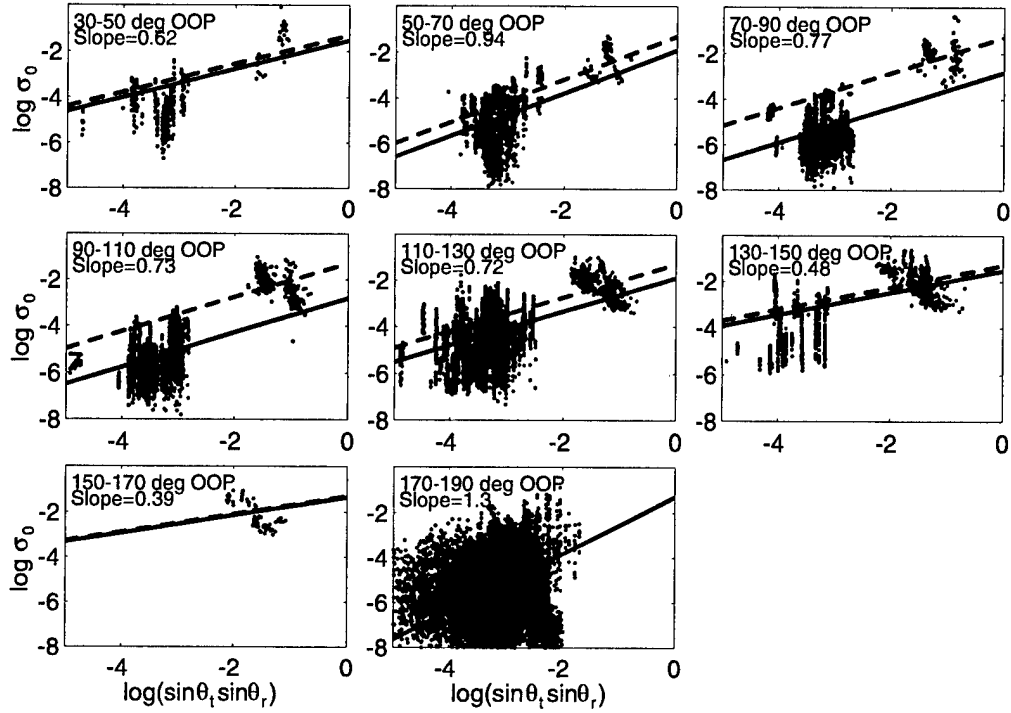


Figure 100. Log of Bistatic Scattering Coefficient vs. Log of Product of Sines of Grazing Angles, Combined Data, UHF, HH

azimuth data and  $\vartheta(\phi) = 1$  for the delay-Doppler data. The value of 0.0001 chosen for  $a$  minimized the variation in  $\alpha$  with changing  $\phi$ . The upper line corresponds to the delay-Doppler data and the lower line to the delay-azimuth data. For this data set  $\gamma$  is equivalent to -15.3 dB. Neglecting the sparse data between 150 and 170 degrees out-of-plane angle, the value of  $\alpha$  varies from 0.35 to 1.1.

## 20.2 Limited Area

Figure 101 shows the combined HH-pol data when the ground scattering area is limited to a 20 km by 30 km area centered at 30 km west and 15 km south of North Oscura Peak. The amplitude plot shows evidence of two distinct distributions, as was the case for the full area data.

Figure 102 shows the log of the bistatic scattering coefficient plotted against the log of the product of the sines of the grazing angles. The least-squares fit gives a value of -6.4 dB for  $\gamma$ . The value of  $\alpha$  varies from 0.96 to 1.38. The values of  $\gamma$  and  $\alpha$  are higher than for the full area. This difference could well be due to a paucity of data points in some regions, rather than to a variation in the scattering characteristics.

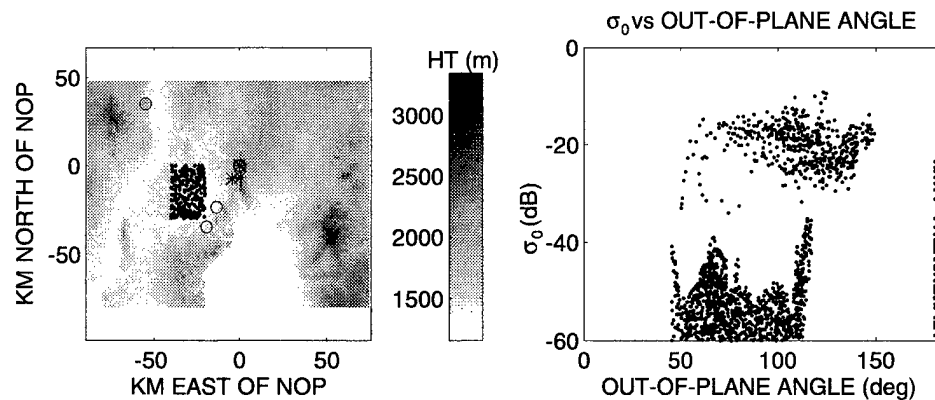


Figure 101. Distribution of Bistatic Scattering Coefficient, Combined Data, Limited Area, UHF, HH

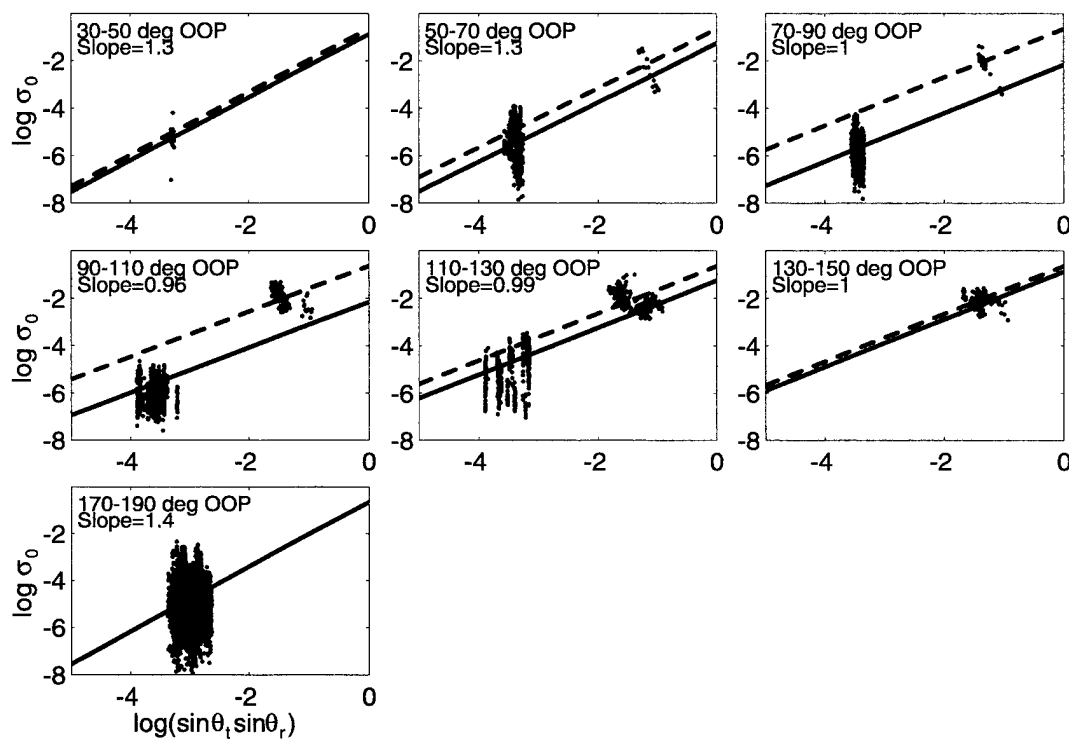


Figure 102. Log of Bistatic Scattering Coefficient vs. Log of Product of Sines of Grazing Angles, Combined Data, Limited Area, UHF, HH

## 21. COMBINED UHF VH-POL RESULTS

### 21.1 Full Area

Figure 103 shows the result of combining the delay-azimuth VH-polarized measurements with the

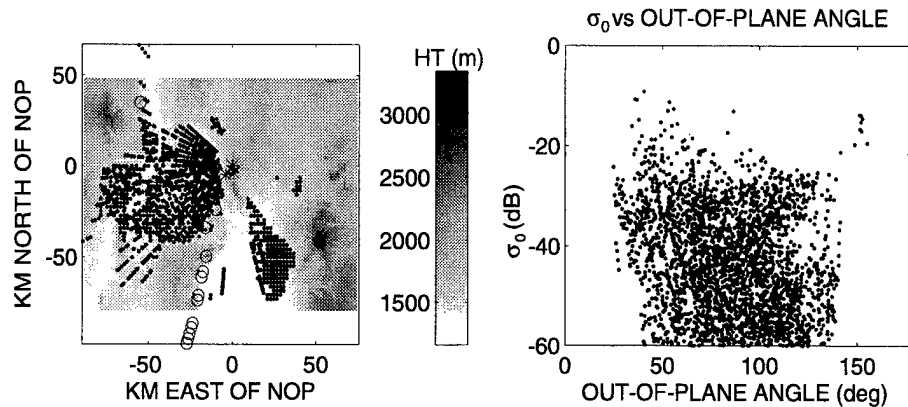


Figure 103. Distribution of Bistatic Scattering Coefficient, Combined Data, UHF, VH

delay-Doppler measurements. The left-hand frame of Figure 103 shows the locations of the scatterers that give returns that are at least 10 dB above the noise floor. The locations of the transmitting and receiving aircraft are marked by circles and asterisks, respectively. The right frame shows the distribution of  $\sigma_0$  with respect to out-of-plane angle. The points belong to two distributions, the lower one being from the delay-azimuth data taken at small grazing angles and the higher one from the delay-Doppler data taken at higher grazing angles.

Figure 104 shows the log of the bistatic scattering coefficient plotted against the log of the product of the sines of the grazing angles. The straight-line fit gives a value of -16 dB for  $\gamma$ . The value of  $\alpha$  varies from 0.8 to 1.2.

### 21.2 Limited Area

Figure 105 shows the combined VV-pol data when the ground scattering area is limited to a 20 km by 30 km area centered at 30 km west and 15 km south of North Oscura Peak. Figure 106 shows the log of the bistatic scattering coefficient plotted against the log of the product of the sines of the grazing angles. The straight-line fit gives a value of -18 dB for  $\gamma$ . The value of  $\alpha$  varies from 0.61 to 0.96. These values agree closely with those derived from the full area, supporting the assumption that the full area is substantially uniform in its scattering characteristics.

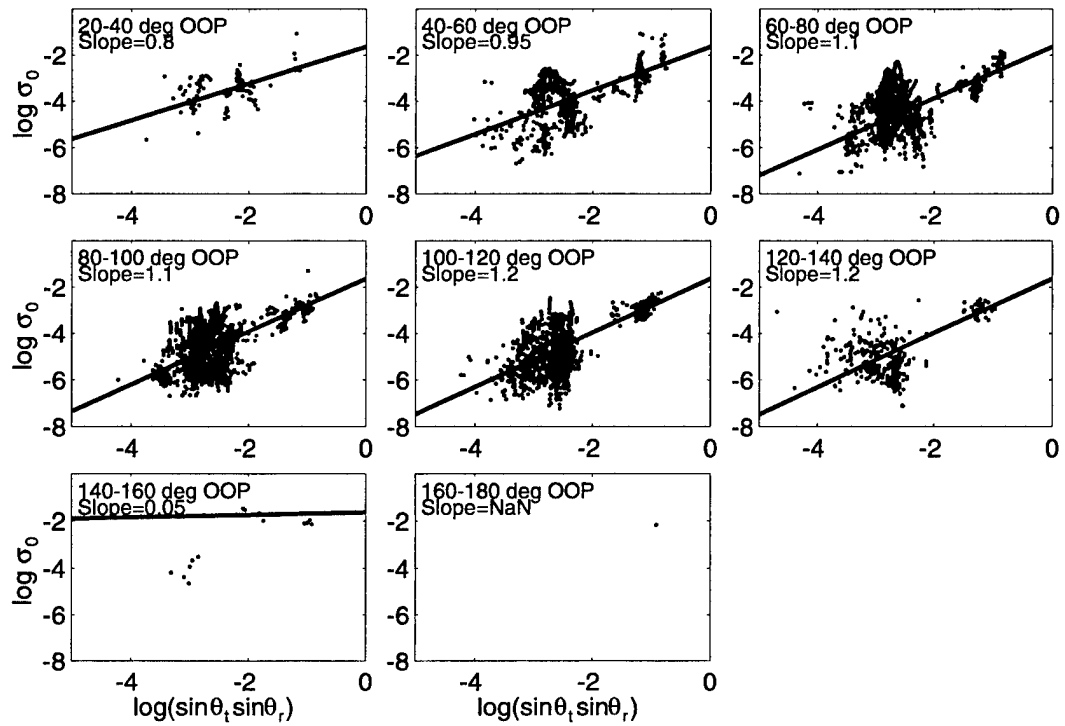


Figure 104. Log of Bistatic Scattering Coefficient vs. Log of Product of Sines of Grazing Angles, Combined Data, UHF, VH

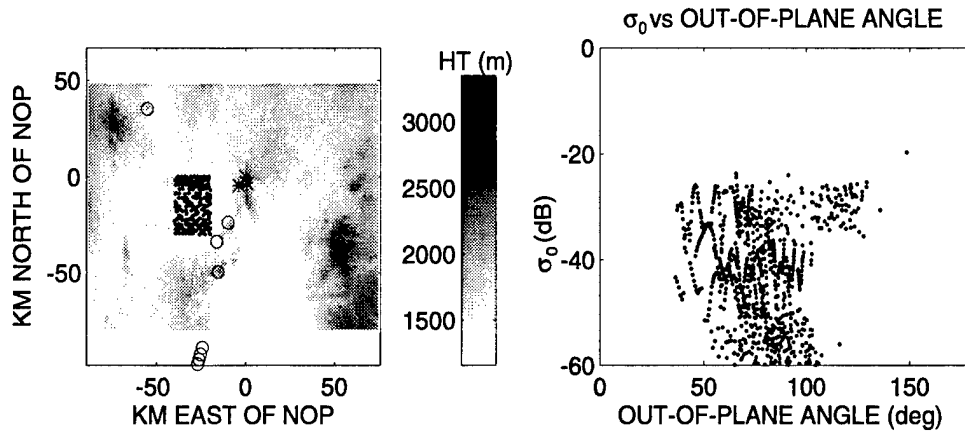


Figure 105. Distribution of Bistatic Scattering Coefficient, Combined Data, Limited Area, UHF, VH

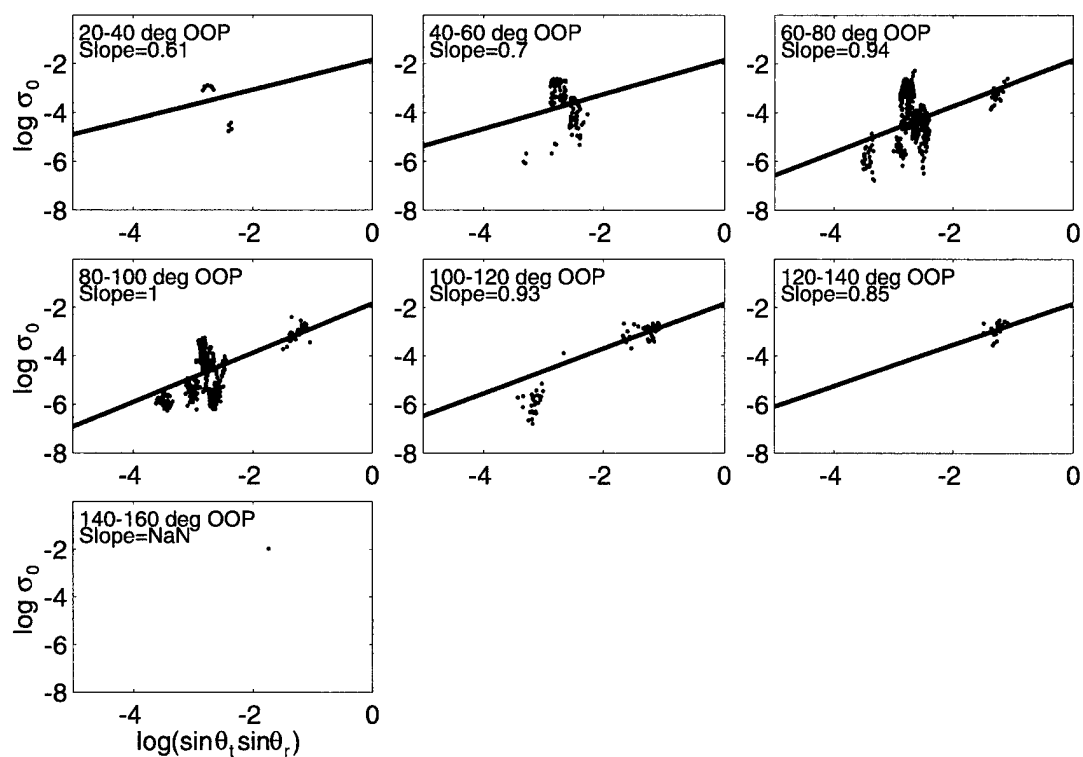


Figure 106. Log of Bistatic Scattering Coefficient vs. Log of Product of Sines of Grazing Angles, Combined Data, Limited Area, UHF, VH

## 22. VHF VV-POL RESULTS

There were four valid sets of VHF, VV-pol, delay-Doppler data available for deriving  $\sigma_0$  in the area covered by the delay-azimuth data. These sets have designators MOD318004, MOD318007, M3D22\_1003 and M3E22\_1003. While the data were being recorded, the receiver and transmitter were flown along the same track with the transmitter trailing the receiver.

### 22.1 MOD318004

The MOD318004 set of VV-pol VHF data was recorded on September 18, 1996 over an area centered on a point approximately 100 km to the west, and 60 km to the south of North Oscura Peak.

Figure 107 shows a plot of constant delay (solid lines) and constant Doppler (broken lines) for the ground reflection points. The position of the transmitter is shown by a circle and that of the receiver by an

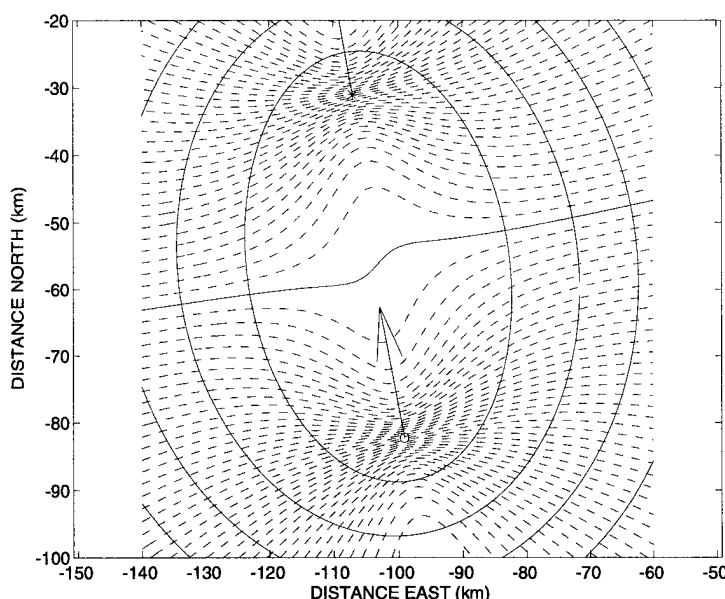


Figure 107. Isodelay & Isodoppler Plots, MOD318004, VHF, VV

asterisk. The single solid Doppler contour indicates zero Doppler shift relative to the direct path Doppler. To the north of this line the Doppler shift difference is positive, i.e. the relative range rate is negative. The interval between the constant delay lines is five resolution cells (7.5 km); the interval between constant Doppler lines is two resolution cells (7.8 Hz).

Figure 108 shows the VV-polarized signals for mission MOD318004. The upper left-hand frame shows the locations of the scatterers that give returns at least 10 dB above the noise floor. The locations of



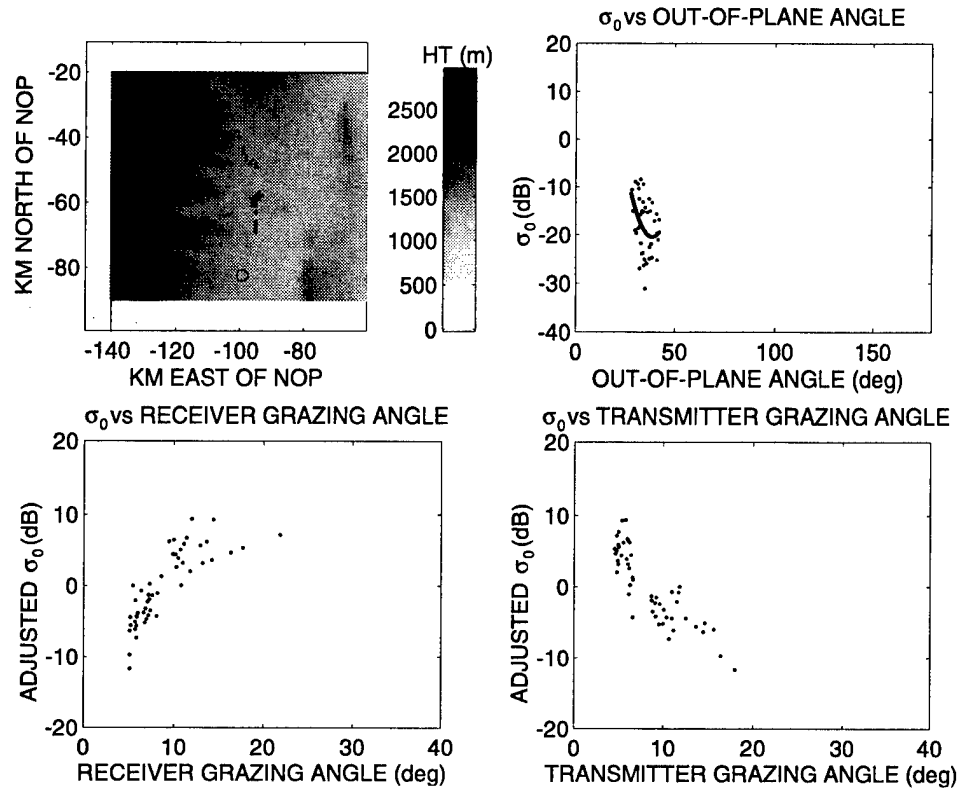


Figure 108. Distribution of Bistatic Scattering Coefficient, MOD318004, VHF, VV

the transmitting and receiving aircraft are marked by a circle and an asterisk, respectively. The upper right frame shows the distribution of  $\sigma_0$  with respect to out-of-plane angle.

Since both transmitting and receiving antennas were vertical dipoles and were therefore omnidirectional in azimuth, antenna beams could not be used to remove the ambiguities associated with mapping from delay-Doppler to cartesian coordinates. As can be seen from Figure 107, each range-Doppler cell will receive energy from two ground patches that are approximately equal in area. This doubling of the area is taken into account in calculating  $\sigma_0$ . Because of the symmetry evident in Figure 107, the pairs of scattering areas will have similar out-of-plane angles and similar grazing angles. The statistics relating to these parameters will therefore be valid.

The data from this mission contained appreciable levels of Radio Frequency Interference (RFI). Most of the RFI was removed using a technique involving the measurement and subtraction of discrete interfering signals. This operation was performed independently for each PRI. Despite this suppression, spurious signals were apparent at specific Doppler frequencies at all delays. These remnants were removed by suppressing the Doppler frequency bands from -6 Hz to 5 Hz and from 30 Hz to 50 Hz. The range of out-of-plane angles was also limited to remove certain spurious signals. Finally, the threshold for selecting returns was set higher than usual at 10 dB above the noise floor.

## 22.2 MOD318007

This set of VV-pol VHF data was recorded on September 18, 1996 over an area centered on a point approximately 110 km to the west, and 70 km to the south of North Oscura Peak.

Figure 109 shows a plot of constant delay (solid lines) and constant Doppler (broken lines) for the ground reflection points; the interval between the constant delay lines is five resolution cells (7.5 km) and

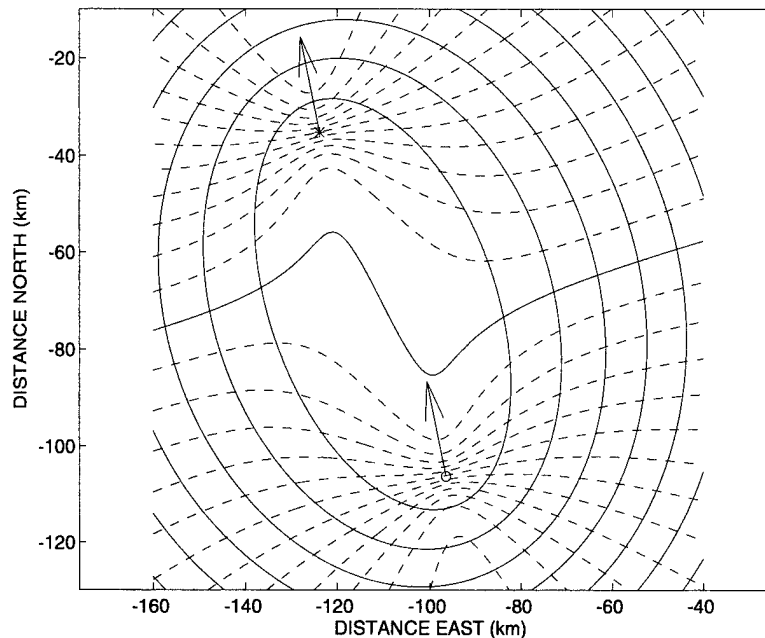


*Figure 109. Isodelay & Isodoppler Plots, MOD318007, VHF, VV*

that between the constant Doppler lines is two resolution cells (7.8 Hz). The position of the transmitter is shown by a circle and that of the receiver by an asterisk. The single solid Doppler contour indicates zero Doppler shift relative to the direct path Doppler. To the north of this line the Doppler shift difference is positive, i.e. the relative range rate will be negative. Because the aircraft were not flying along the same straight path, the contour lines of Figure 109 do not show perfect symmetry about the line between transmitter and receiver.

Since both transmitting and receiving antennas were vertical dipoles, and were therefore omnidirectional in azimuth, antenna beams could not be used to remove the ambiguities associated with mapping from delay-Doppler to cartesian coordinates. As can be seen from Figure 109, each range-Doppler cell receives energy from two ground patches that, except at short delays, have somewhat similar out-of-plane angles and similar grazing angles (to the extent that the patterns are symmetrical). The derived statistics relating to these parameters will therefore represent the average of the pairs of patches.

Because of the ambiguity, both patches contributing to each delay-Doppler cell had to be included in the statistics. This meant that the area could not be limited to the desert floor alone and had to include the rougher elevated ground.

At all bistatic delays, the received signal showed appreciable levels at the Doppler shift associated with the direct path. This may have been due to leakage in the transmitter modulator. This spurious signal was removed from the statistics by rejecting all signals at this frequency and for a band 2 Hz either side.

Figure 110 shows the signals for mission MOD318007. The upper left-hand frame shows the locations of the scatterers that give returns at least 3 dB above the noise floor (the threshold level was set

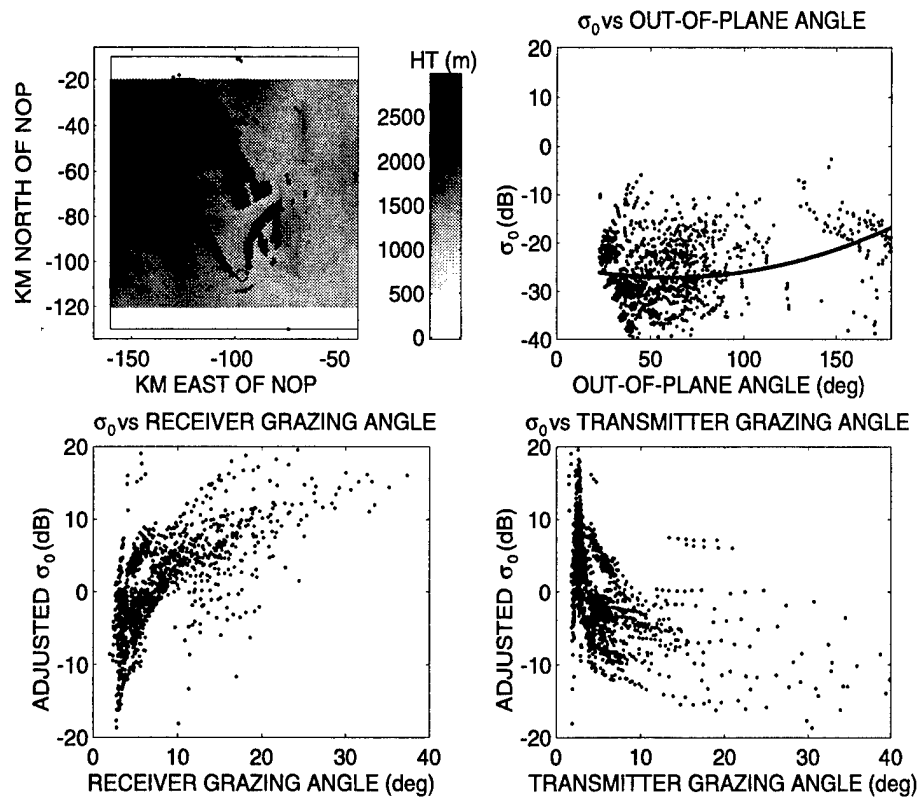


Figure 110. Distribution of Bistatic Scattering Coefficient, MOD318007, VHF, VV

close to the noise floor to ensure that there were sufficient data points, at the expense of amplitude errors at the lower values). The locations of the transmitting and receiving aircraft are marked by a circle and an asterisk, respectively. These returns show the effects of the poor symmetry seen in Figure 109.

The upper right frame of Figure 110 shows the distribution of  $\sigma_0$  with respect to out-of-plane angle along with a least-squares-fitted quadratic. The coefficients of this quadratic, in descending order, are 0.00073 , -0.088 and -24.5. The units are dB and degrees. The quadratic has values of -24.5, -26.5

and  $-16.7$  dB at 0, 90 and 180 degrees out-of-plane angle, respectively. The lower two frames show the values of  $\sigma_0$  with the parabolic function subtracted from them. The values are plotted against receiver grazing angle and transmitter grazing angle.

### 22.3 M3E22\_1003

This set of VV-pol VHF data was recorded on September 22, 1996 over an area centered on a point approximately 80 km to the west, and 50 km to the south of North Oscura Peak.

Figure 111 shows a plot of constant delay (solid lines) and constant Doppler (broken lines) for the ground reflection points; the interval between the constant delay lines is five resolution cells (7.5 km) and

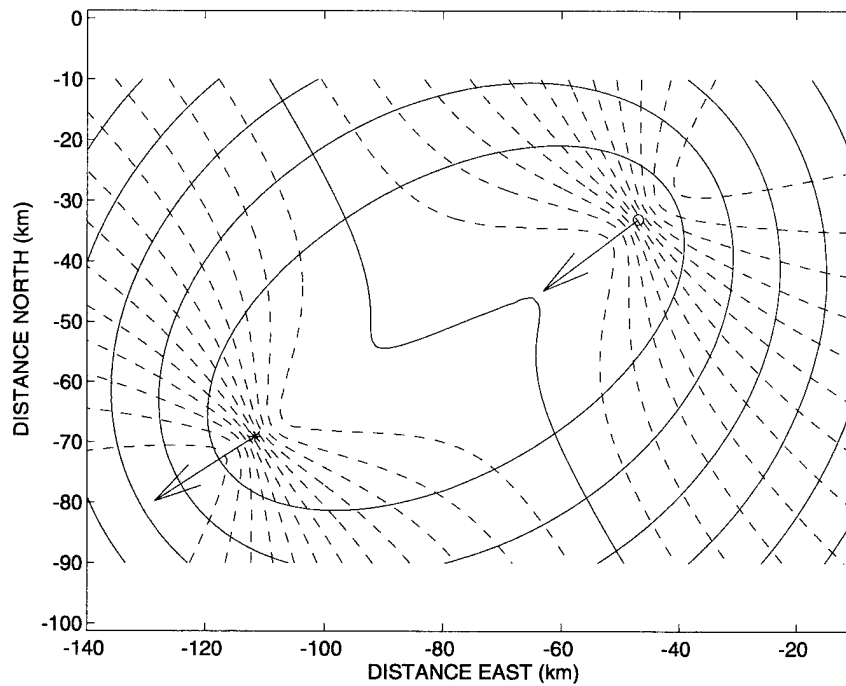


Figure 111. Isodelay & Isodoppler Plots, M3E22\_1003, VHF, VV

that between the constant Doppler lines is two resolution cells (7.8 Hz). The position of the transmitter is shown by a circle and that of the receiver by an asterisk. The single solid Doppler contour indicates zero Doppler shift relative to the direct path Doppler. To the south and west of this line the Doppler shift difference is positive, i.e. the relative range rate is negative.

Figure 112 shows the VV-polarized signals for mission M3E22\_1003. The upper left-hand frame shows the locations of the scatterers that give returns at least 6 dB above the noise floor. The locations of the transmitting and receiving aircraft are marked by a circle and an asterisk, respectively.

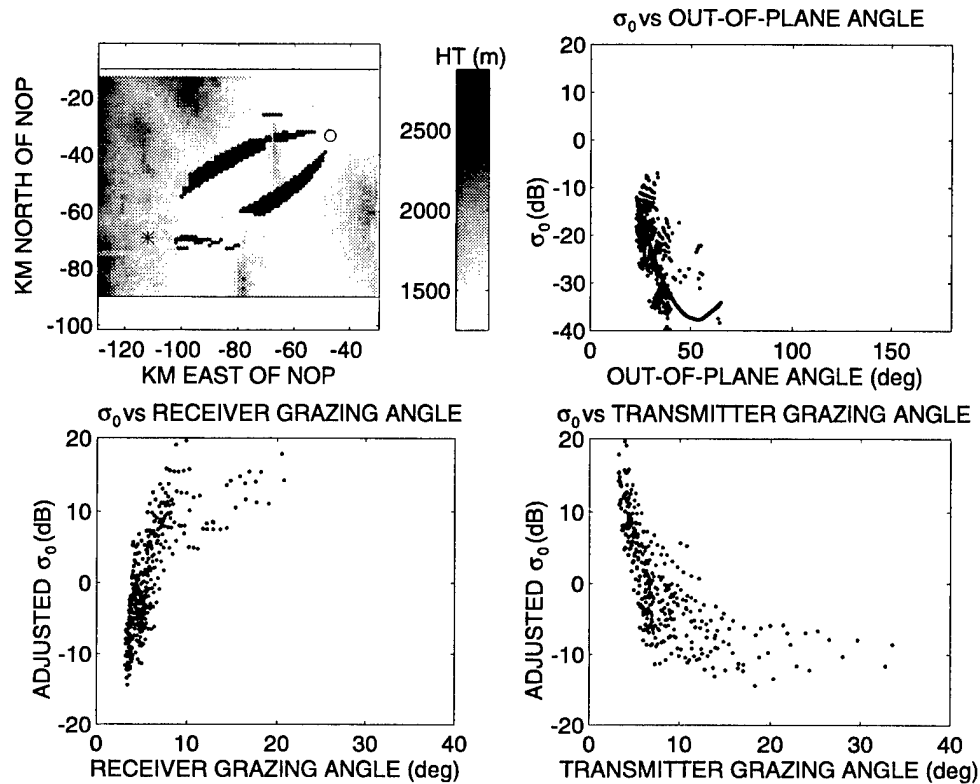


Figure 112. Distribution of Bistatic Scattering Coefficient, M3E22\_1003, VHF, VV

Since both transmitting and receiving antennas were vertical dipoles and were therefore omnidirectional in azimuth, antenna beams could not be used to remove the ambiguities associated with mapping from delay-Doppler to cartesian coordinates. As can be seen from Figure 111, each range-Doppler cell will receive energy from two ground patches that, except at short delays, will have similar out-of-plane angles and similar grazing angles. The derived statistics relating to these parameters will therefore represent the average of the pairs of patches.

The upper right frame of Figure 112 shows the distribution of  $\sigma_0$  with respect to out-of-plane angle along with a least-squares-fitted quadratic. Since there were very few data points beyond 40 degrees out-of-plane angle, the curve in this region should be disregarded. The lower two frames show the values of  $\sigma_0$  with the parabolic function subtracted from them. The values are plotted against receiver grazing angle and transmitter grazing angle.

## 22.4 M3D22\_1003

This set of VV-pol VHF data was recorded on September 22, 1996 over an area centered on a point approximately 90 km to the west, and 45 km to the south of North Oscura Peak.

Figure 113 shows a plot of constant delay (solid lines) and constant Doppler (broken lines) for the ground reflection points; the interval between the constant delay lines is five resolution cells (7.5 km) and

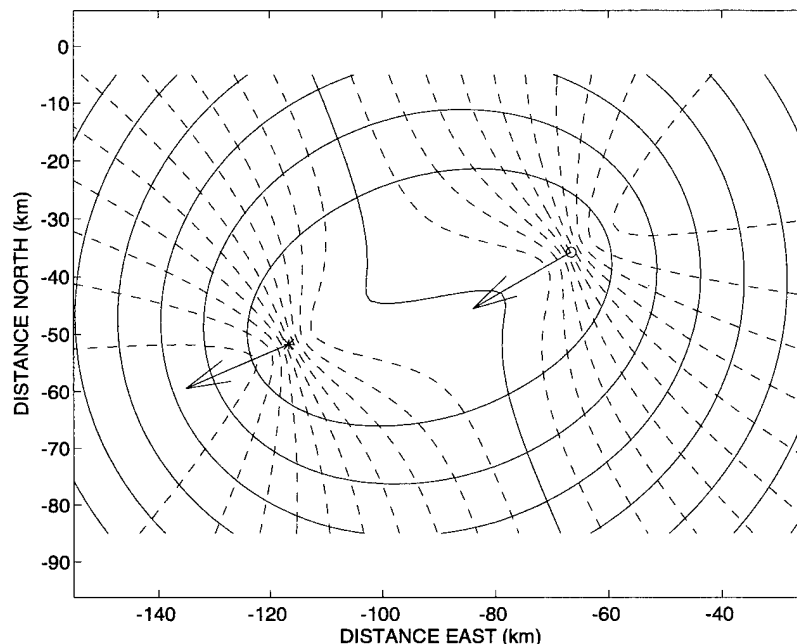


Figure 113. Isodelay & Isodoppler Plots, M3D22\_1003, VHF, VV

that between the constant Doppler lines is two resolution cells (7.8 Hz). The position of the transmitter is shown by a circle and that of the receiver by an asterisk. The single solid Doppler contour indicates zero Doppler shift relative to the direct path Doppler. To the south and west of this line the Doppler shift difference is positive, i.e., the relative range rate is negative.

Figure 114 shows the VV-polarized signals for mission M3D22\_1003. The upper left-hand frame shows the locations of the scatterers that give returns at least 6 dB above the noise floor. The locations of the transmitting and receiving aircraft are marked by a circle and an asterisk, respectively.

Since both transmitting and receiving antennas were vertical dipoles, and were therefore omnidirectional in azimuth, antenna beams could not be used to remove the ambiguities associated with mapping from delay-Doppler to cartesian coordinates. As can be seen from Figure 113, each range-Doppler cell will receive energy from two ground patches that, except at short delays, will have similar out-of-plane angles and similar grazing angles. The derived statistics relating to these parameters will therefore represent the average of the pairs of patches. Because of the ambiguity, both patches contributing to each delay-Doppler cell had to be included in the statistics. This meant that the area could not be limited to the desert floor alone and had to include the rougher elevated ground.

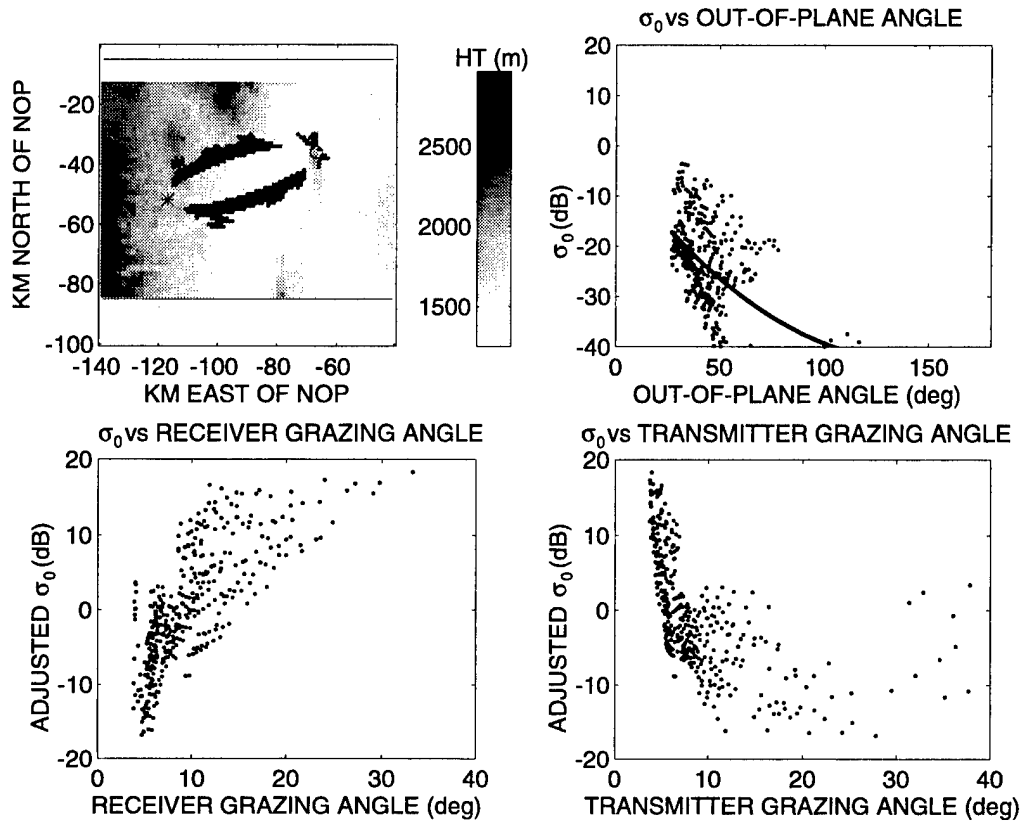


Figure 114. Distribution of Bistatic Scattering Coefficient, M3D22\_1003, VHF, VV

A small amount of RFI was present in the signal and occupied certain Doppler frequency bands. This interference was eliminated by restricting the Doppler range to frequencies less than 20 Hz and rejecting the band between -26 Hz and -9 Hz.

The upper right frame of Figure 114 shows the distribution of  $\sigma_0$  with respect to out-of-plane angle along with a least-squares-fitted quadratic. The coefficients of this quadratic, in descending order, are 0.00198, -0.556 and -3.57. The units are dB and degrees. The quadratic has values of -3.6, -37.5 and -39.2 dB at 0, 90 and 180 degrees out-of-plane angle, respectively. The lower two frames show the values of  $\sigma_0$  with the parabolic function subtracted from them. The values are plotted against receiver grazing angle and transmitter grazing angle.

## 22.5 Combined VHF VV-pol Data

Figure 115 shows the result of combining the four sets of delay-Doppler VV-polarized measurements. The upper left-hand frame shows the locations of the scatterers. The locations of the

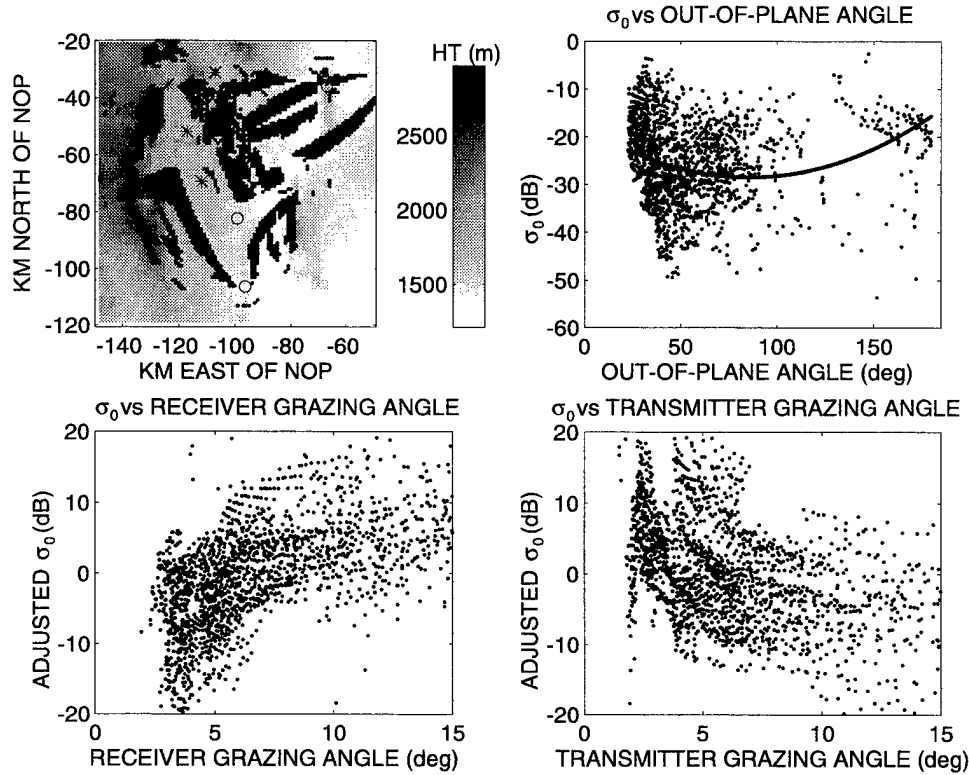


Figure 115. Distribution of Bistatic Scattering Coefficient, Delay-Doppler Data, VHF, VV

transmitting and receiving aircraft are marked by circles and asterisks, respectively. The upper right frame shows the distribution of  $\sigma_0$  with respect to out-of-plane angle. A quadratic fitted to the points is shown. The coefficients of this quadratic, in descending order, are 0.00144, -0.247 and -17.9. The units are dB and degrees. The quadratic has values of -17.9, -28.4 and -15.6 dB at 0, 90 and 180 degrees out-of-plane angle, respectively. The lower two frames show the values of  $\sigma_0$  with the parabolic function subtracted from them. The values are plotted against receiver grazing angle and transmitter grazing angle.

Figure 116 shows the log of the bistatic scattering coefficient plotted against the log of the product of the sines of the grazing angles.



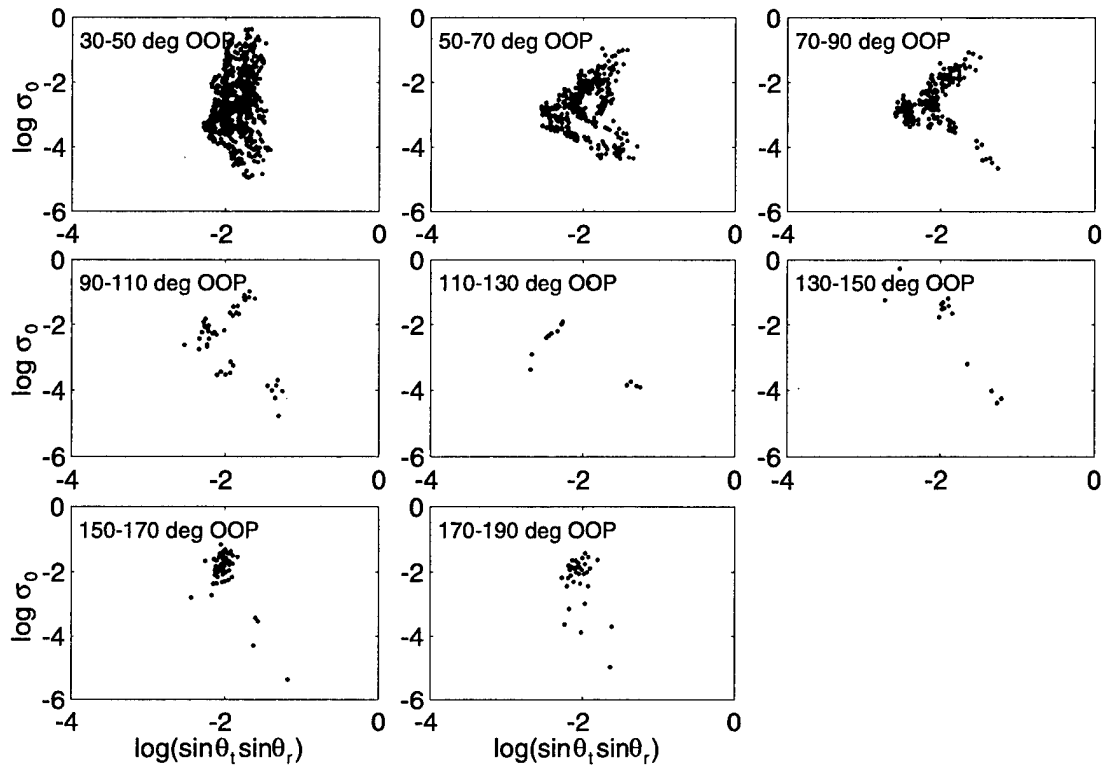


Figure 116. Log of Bistatic Scattering Coefficient vs. Log of Product of Sines of Grazing Angles, Delay-Doppler Data, VHF, VV

## 22.6 Comparison of VV-pol UHF and VHF Results

A comparison was made between the VV-pol values of  $\sigma_0$  obtained at UHF and VHF. The values used in the comparison are those discussed in Sections 19.1 and 22.5.

An inspection of Figures 96 and 116 show that the range of grazing angles covered are different for the two frequencies. For all values of out-of-plane angle at VHF, the values of  $\log(\sin \theta_i \sin \theta_r)$  are concentrated in the range of -1.5 to -2.5, while for UHF, the data from this region is sparse. The comparison was therefore made between the mean VHF value of  $\sigma_0$ , to which is assigned a value of 2 for  $\log(\sin \theta_i \sin \theta_r)$ , and the UHF value of the fitted constant- $\gamma$  function at the same value of  $\log(\sin \theta_i \sin \theta_r)$ .

Figure 117 shows the difference between VHF and UHF VV-pol  $\sigma_0$  as a function of out-of-plane angle. One of the difficulties in interpreting these results lies in the fact that the same ground was not active in the two cases. For the UHF measurements, the returns were obtained from the valley floor in the vicinity of North Oscura Peak, the rough foothills being eliminated by limiting the altitude to 1600 feet. For the VHF data, the scattering area was centered on a point about 100 km to the west of, and about 60 km to the south of North Oscura Peak, there being no overlap between the UHF and VHF areas. Because of the nature of the VV-pol VHF measurements, the terrain could not be limited to the same altitude

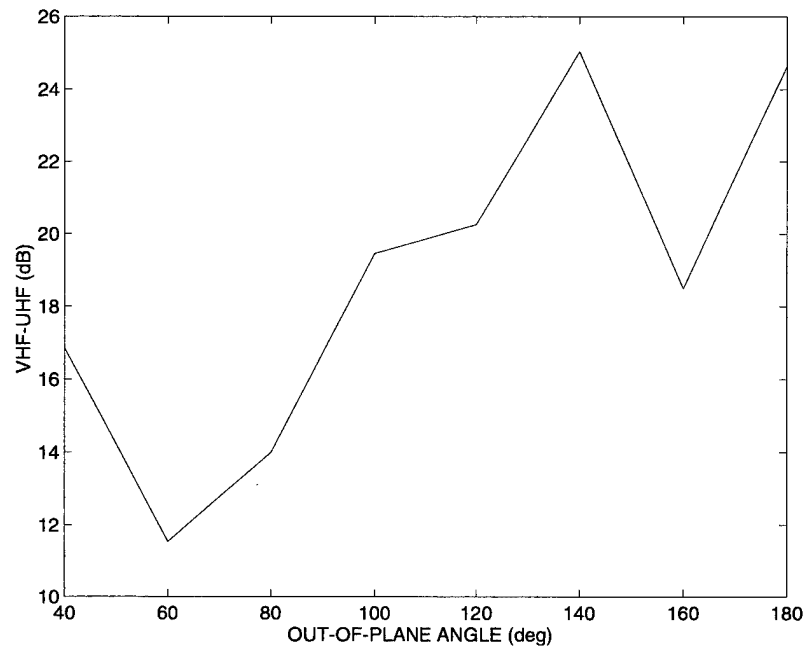


*Figure 117. Comparison of VHF and UHF VV-pol scattering*

regime as for UHF and therefore included higher, rougher ground. Because rougher ground was included in the VHF measurements, it is expected that  $\sigma_0$  would be higher at VHF than at UHF, as is the case.

## 23. VHF HH-POL RESULTS

### 23.1 MOD318002

This set of HH-pol VHF data was recorded on September 18, 1996 over an area centered on a point approximately 100 km to the west, and 70 km to the south of North Oscura Peak.

Figure 118 shows a plot of constant delay (solid lines) and constant Doppler (broken lines) for the ground reflection points; the interval between the constant delay lines is five resolution cells (7.5 km) and

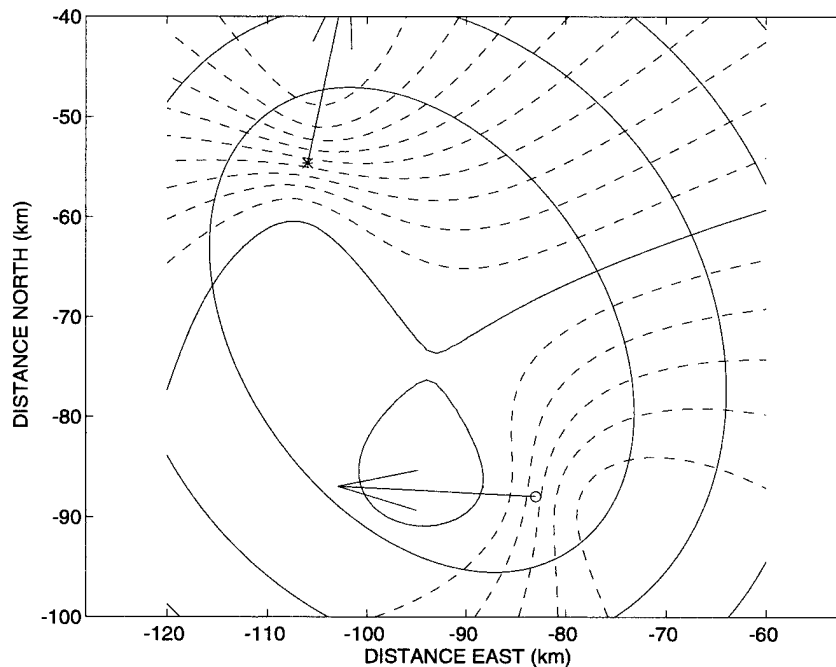


Figure 118. Isodelay & Isodoppler Plots, MOD318002, VHF, HH

that between the constant Doppler lines is two resolution cells (7.8 Hz). The position of the transmitter is shown by a circle and that of the receiver by an asterisk. The single solid Doppler contour indicates zero Doppler shift relative to the direct path Doppler. To the north of this line the Doppler shift difference is positive, i.e. the relative range rate is negative.

The area selected for data extraction was determined by the antenna patterns and the delay-Doppler ambiguities. The transmitting antenna was mounted on the starboard side of the west-bound transmitting aircraft, hence the area to the south of track was in the rear sidelobes of the antenna and therefore received little energy. It can be seen that there are ambiguities associated with most of the illuminated area. The only area that can give unambiguous returns is that to the east of the meridian through the transmitter position, to the north of the latitude line through the transmitter position and giving

Doppler shifts lower than -25 Hz. The area considered was therefore restricted to these limits. Also the ground elevation was restricted to below 1600 m to eliminate returns from the rising ground.

Figure 119 shows the signals for mission MOD318002. The upper left-hand frame shows the locations of the scatterers that give returns at least 3 dB above the noise floor. The locations of the

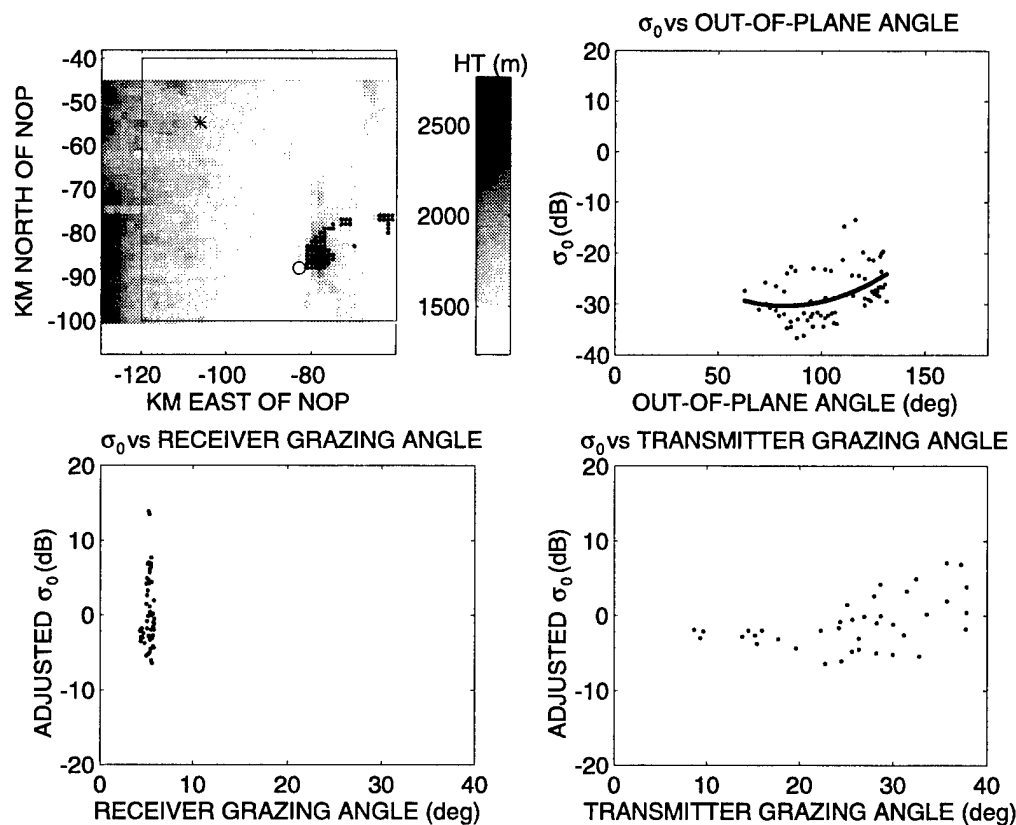


Figure 119. Distribution of Bistatic Scattering Coefficient, MOD318, VHF, HH

transmitting and receiving aircraft are marked by a circle and an asterisk, respectively. The upper right frame shows the distribution of  $\sigma_0$  with respect to out-of-plane angle. A quadratic fitted to the points is shown. The coefficients of this quadratic, in descending order, are 0.00264 , -0.437 and -12.2. The units are dB and degrees. The quadratic has values of -12.2, -30.2 and -5.2 dB at 0, 90 and 180 degrees out-of-plane angle, respectively. The lower two frames show the values of  $\sigma_0$  with the parabolic function subtracted from them. The values are plotted against receiver grazing angle and transmitter grazing angle.

## 23.2 M3E22\_1001

The M3E22\_1001 HH-pol VHF data were recorded on September 22, 1996 over an area centered on a point 70 km to the west, and 45 km to the south of North Oscura Peak.

Figure 120 shows a plot of constant delay (solid lines) and constant Doppler (broken lines) for the ground reflection points; the interval between the constant delay lines is five resolution cells (7.5 km) and

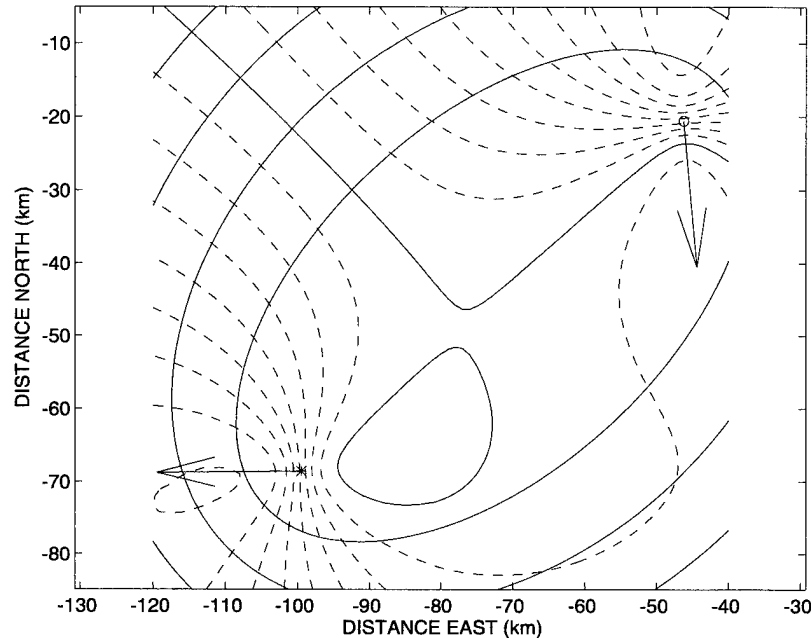


Figure 120. Isodelay & Isodoppler Plots, M3E22\_1001, VHF, HH

that between the constant Doppler lines is two resolution cells (7.8 Hz). The position of the transmitter is shown by a circle and that of the receiver by an asterisk. The single solid Doppler contour indicates zero Doppler shift relative to the direct path Doppler. To the south of this line the Doppler shift difference is positive, i.e. the relative range rate is negative.

The area selected for data extraction was determined by the antenna patterns, the delay-Doppler ambiguities and the ground elevation. The transmitting antenna was mounted on the starboard side of the west-bound transmitting aircraft, hence the area to the south of track was in the rear sidelobes of the antenna and therefore received little energy. It can be seen that there are ambiguities associated with most of the illuminated area. The only area that can give unambiguous returns is that to the north of the latitude line through the transmitter position and giving Doppler shifts greater than 15 Hz. The area considered was therefore restricted to these limits. Also the ground elevation was restricted to below 1600 m to eliminate returns from the rising ground.

Figure 121 shows the signals for mission M3E22\_1001. The upper left-hand frame shows the locations of the scatterers that give returns at least 3 dB above the noise floor. The locations of the

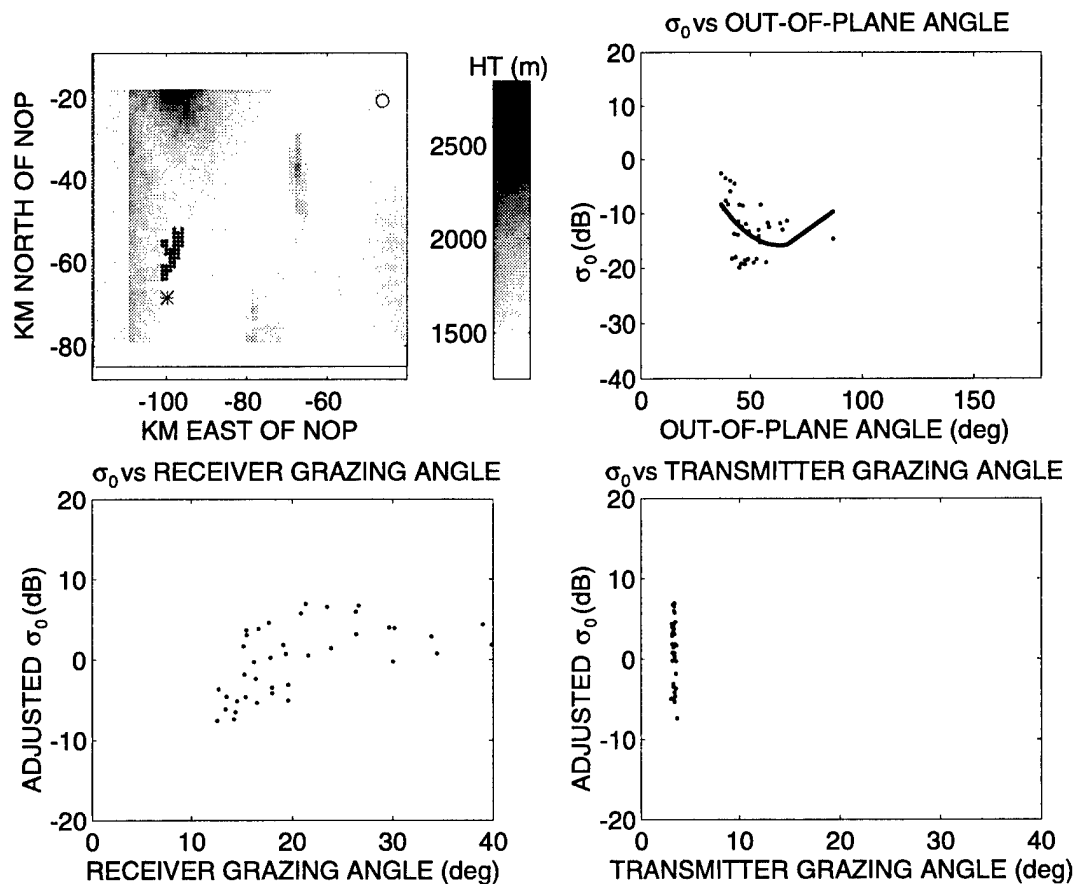


Figure 121. Distribution of Bistatic Scattering Coefficient, M3E22\_1001, VHF, HH

transmitting and receiving aircraft are marked by a circle and an asterisk, respectively. The upper right frame shows the distribution of  $\sigma_0$  with respect to out-of-plane angle. A quadratic fitted to the points is shown. The coefficients of this quadratic, in descending order, are 0.011 , -1.36 and 27.2. The units are dB and degrees. The quadratic has values of 27.2, -8.0 and 132.1 dB at 0, 90 and 180 degrees out-of-plane angle, respectively. The lower two frames show the values of  $\sigma_0$  with the parabolic function subtracted from them. The values are plotted against receiver grazing angle and transmitter grazing angle.

### 23.3 MOD318005

This set of HH-pol VHF data was recorded on September 18, 1996 over an area centered on a point approximately 110 km to the west, and 80 km to the south of North Oscura Peak.

Figure 122 shows a plot of constant delay (solid lines) and constant Doppler (broken lines) for the ground reflection points; the interval between the constant delay lines is five resolution cells (7.5 km) and

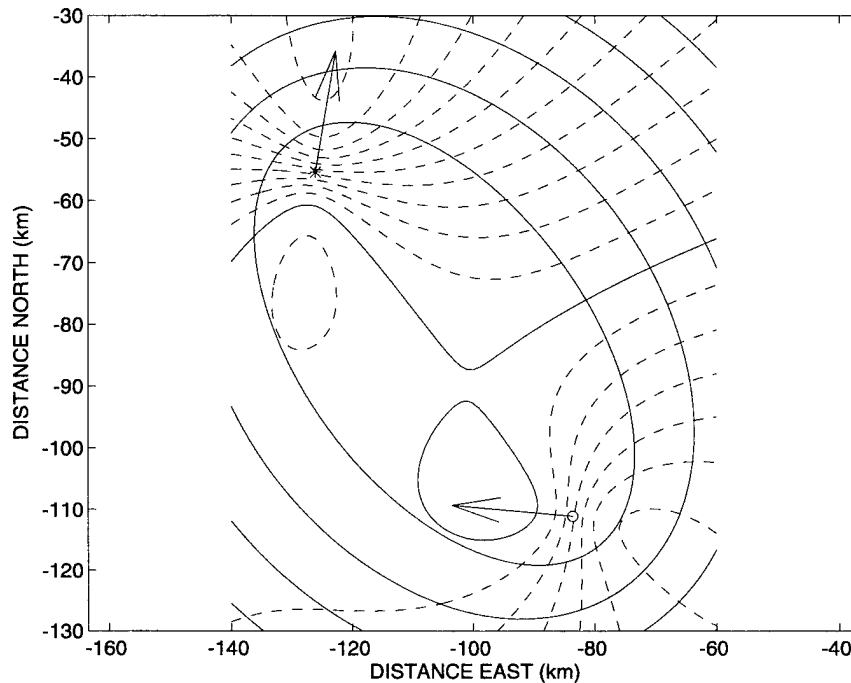


Figure 122. Isodelay & Isodoppler Plots, MOD318005, VHF, HH

that between the constant Doppler lines is two resolution cells (7.8 Hz). The position of the west-bound transmitter is shown by a circle and that of the north-bound receiver by an asterisk. The single solid Doppler contour indicates zero Doppler shift relative to the direct path Doppler. To the north of this line the Doppler shift difference is positive, i.e. the relative range rate is negative.

The area selected for data extraction was determined by the antenna patterns, the delay-Doppler ambiguities and the ground elevation. The transmitting antenna was mounted on the starboard side of the west-bound transmitting aircraft, hence the area to the south of track was in the rear sidelobes of the antenna and therefore received little energy. The only area that can give unambiguous returns is that to the north of the latitude line through the transmitter position and giving Doppler shifts greater than -25 Hz. The area considered was therefore restricted to these limits. Also the ground elevation was restricted to below 1600 m to eliminate returns from the rising ground.

Figure 123 shows the signals for mission MOD318005. The upper left-hand frame shows the locations of the scatterers that give returns at least 3 dB above the noise floor. The locations of the

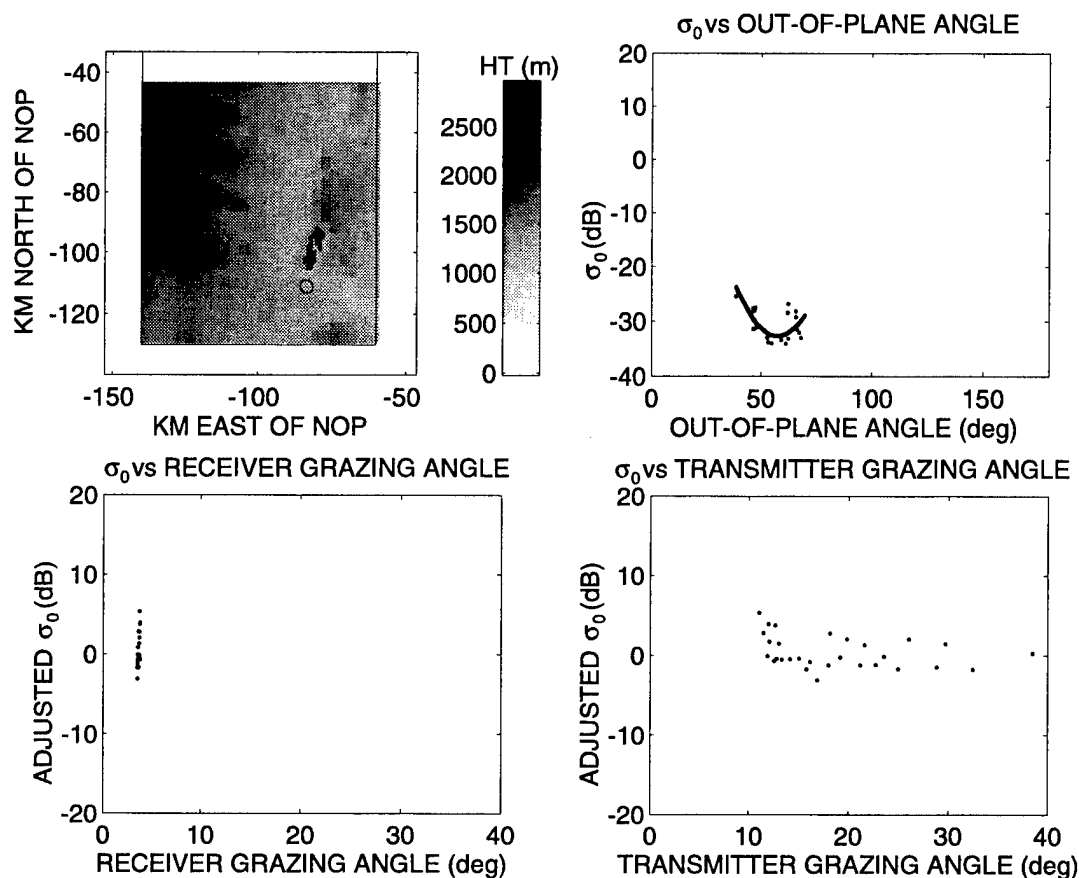


Figure 123. Distribution of Bistatic Scattering Coefficient, MOD318005, VHF, HH

transmitting and receiving aircraft are marked by a circle and an asterisk, respectively. The upper right frame shows the distribution of  $\sigma_0$  with respect to out-of-plane angle. A quadratic fitted to the points is shown. The coefficients of this quadratic, in descending order, are 0.025 , -2.87 and 50.0. The units are dB and degrees. The lower two frames show the values of  $\sigma_0$  with the parabolic function subtracted from them. The values are plotted against receiver grazing angle and transmitter grazing angle.



## 23.4 M3D22\_1001

The M3D22\_1001 HH-pol VHF data were recorded on September 22, 1996 over an area centered on a point 80 km to the west, and 35 km to the south of North Oscura Peak.

Figure 124 shows a plot of constant delay (solid lines) and constant Doppler (broken lines) for the ground reflection points; the interval between the constant delay lines is five resolution cells (7.5 km) and

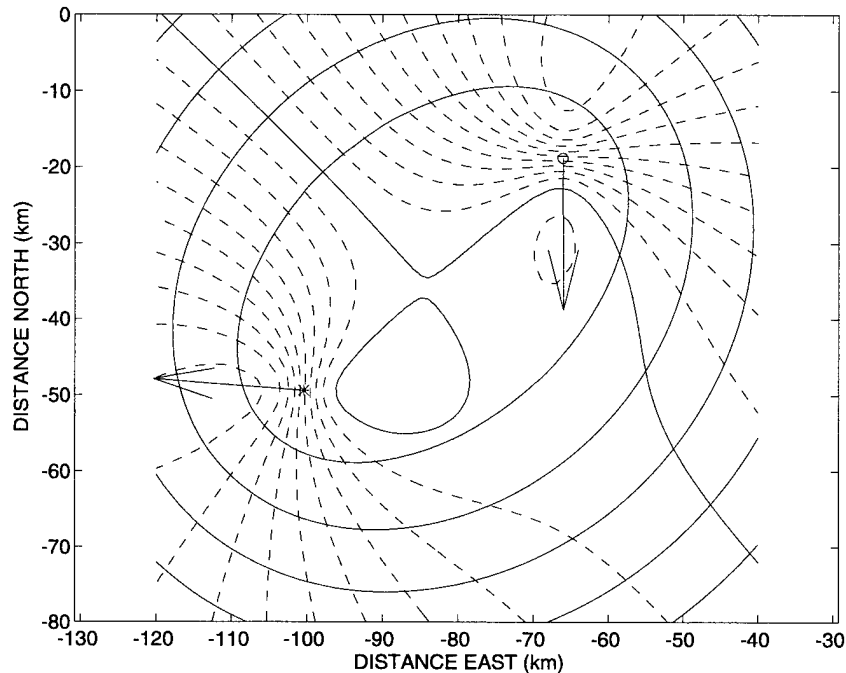


Figure 124. Isodelay & Isodoppler Plots, M3D22\_1001, VHF, HH

that between the constant Doppler lines is two resolution cells (7.8 Hz). The position of the south-bound transmitter is shown by a circle and that of the west-bound receiver by an asterisk. The single solid Doppler contour indicates zero Doppler shift relative to the direct path Doppler. To the north and east of this line the Doppler shift difference is negative, i.e. the relative range rate is positive.

The area selected for data extraction was determined by the antenna patterns, the delay-Doppler ambiguities and the ground elevation. The transmitting antenna was mounted on the starboard side of the transmitting aircraft, hence the area to the east of track was in the rear sidelobes of the antenna and therefore received little energy. There were areas of ambiguity in the region of positive relative Doppler shift. These ambiguities were resolved by rejecting signals whose relative Doppler shifts were greater than - 5 Hz. Also the ground elevation was restricted to below 1600 m to eliminate returns from the rising ground.

Figure 125 shows the signals for mission M3D22\_1001. The upper left-hand frame shows the locations of the scatterers that give returns at least 6 dB above the noise floor. The locations of the

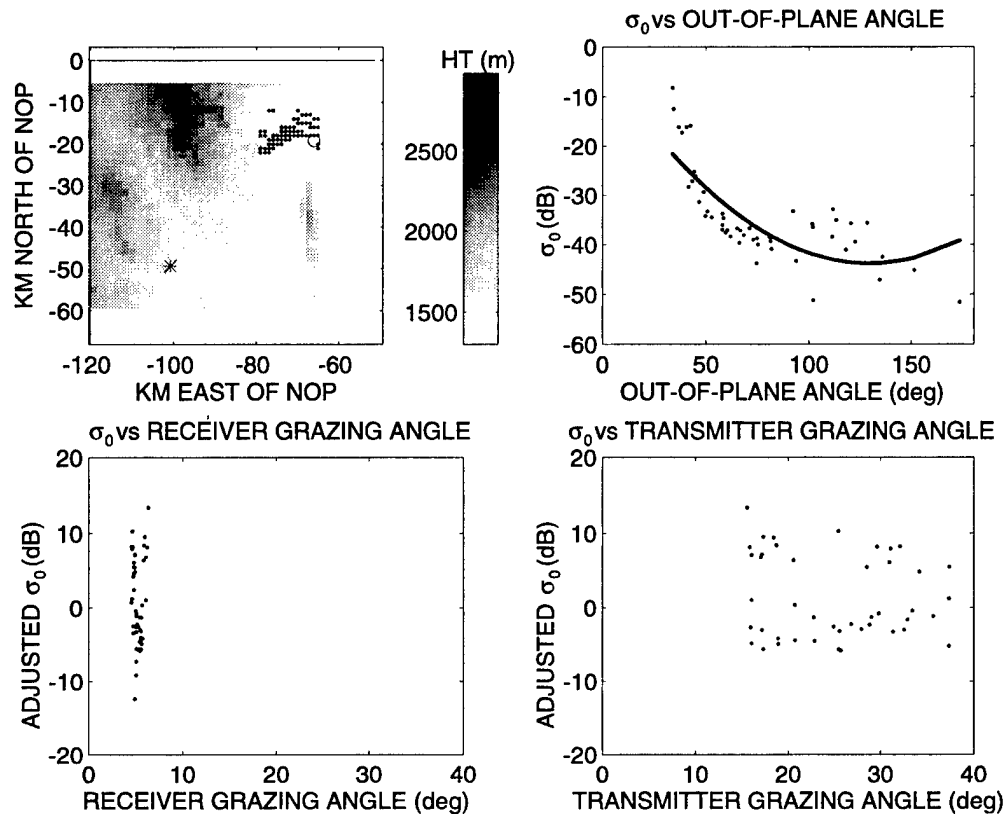


Figure 125. Distribution of Bistatic Scattering Coefficient, M3D22\_1001, VHF, HH

transmitting and receiving aircraft are marked by circles and asterisks, respectively. The upper right frame shows the distribution of  $\sigma_0$  with respect to out-of-plane angle. A quadratic fitted to the points is shown. The coefficients of this quadratic, in descending order, are  $-0.0024$ ,  $-0.628$  and  $-3.07$ . The units are dB and degrees. The quadratic has values of  $-3.1$ ,  $-40.0$  and  $-37.6$  dB at 0, 90 and 180 degrees out-of-plane angle, respectively. The lower two frames show the values of  $\sigma_0$  with the parabolic function subtracted from them. The values are plotted against receiver grazing angle and transmitter grazing angle.

## 23.5 Combined VHF HH-pol Data

Figure 126 shows the result of combining the four sets of delay-Doppler HH-polarized measurements. The data sets were from missions MOD318003, MOD318005, M3E22\_1001, and

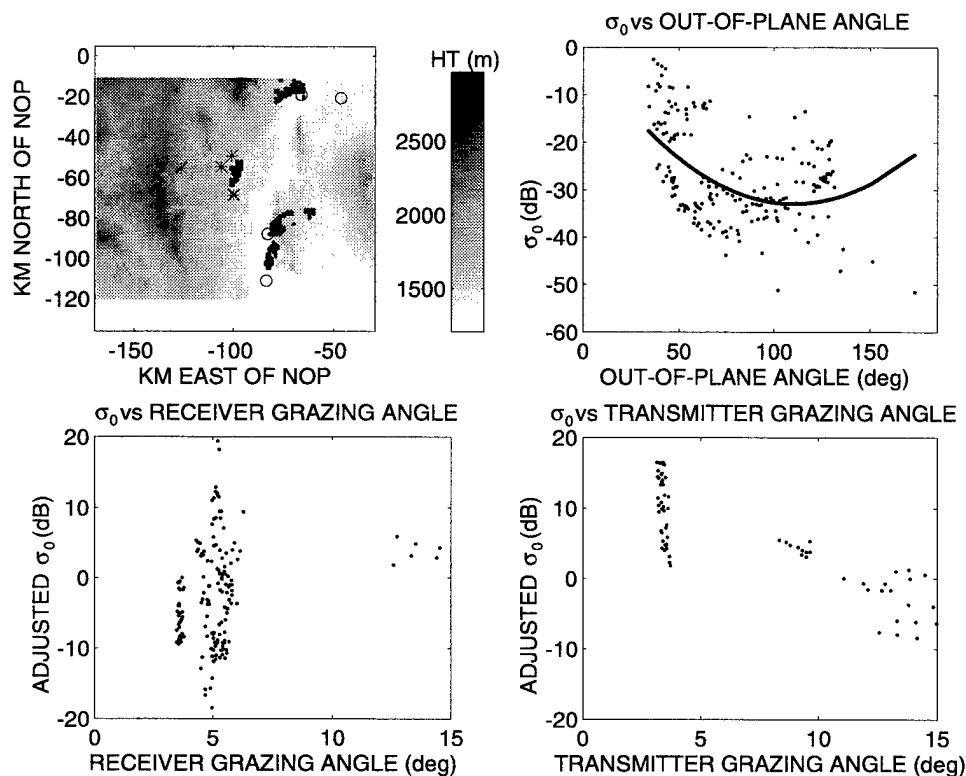


Figure 126. Distribution of Bistatic Scattering Coefficient, Delay-Doppler Data, VHF, HH

M3D22\_1001. The upper left-hand frame shows the locations of the scatterers. The locations of the transmitting and receiving aircraft are marked by circles and asterisks, respectively. The upper right frame shows the distribution of  $\sigma_0$  with respect to out-of-plane angle. A quadratic fitted to the points is shown. The coefficients of this quadratic, in descending order, are  $-0.002618$ ,  $-0.578$  and  $-0.980$ . The units are dB and degrees. The quadratic has values of  $-0.980$ ,  $-31.8$  and  $-20.2$  dB at 0, 90 and 180 degrees out-of-plane angle, respectively. Note that the quadratic curve has its minimum near 90 degrees out-of-plane angle. The lower two frames show the values of  $\sigma_0$  with the parabolic function subtracted from them. The values are plotted against receiver grazing angle and transmitter grazing angle.

Figure 127 shows the log of the bistatic scattering coefficient plotted against the log of the product of the sines of the grazing angles.

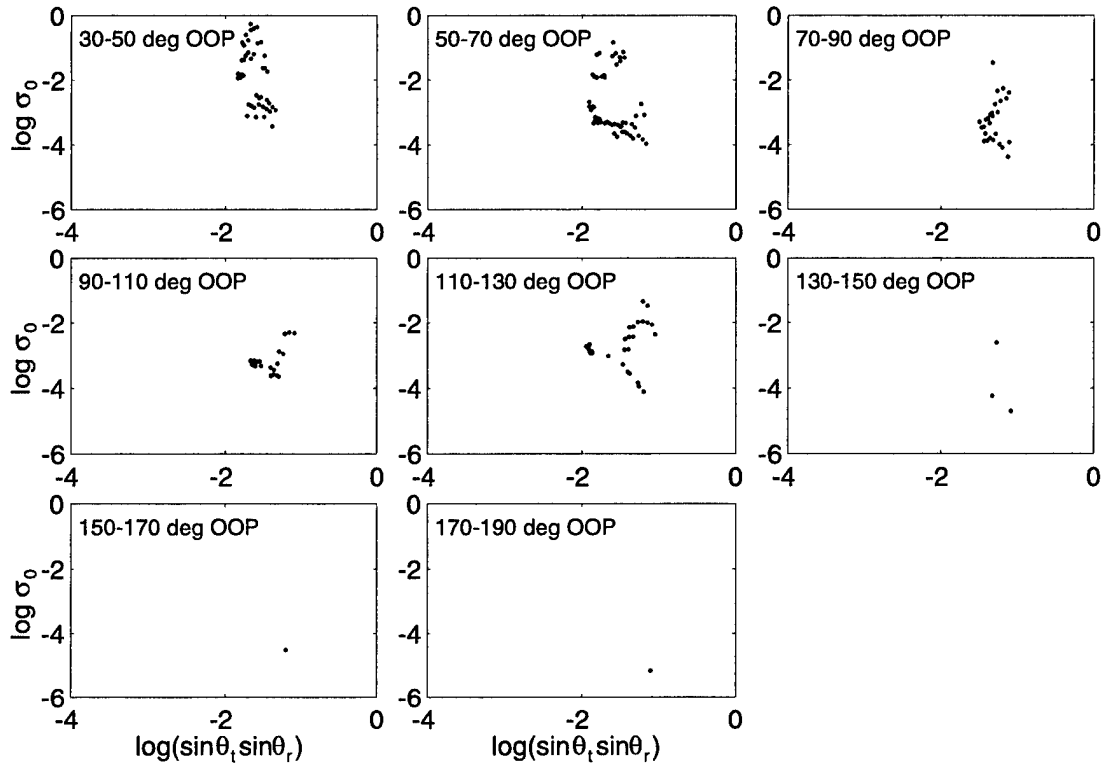


Figure 127. Log of Bistatic Scattering Coefficient vs. Log of Product of Sines of Grazing Angles, Delay-Doppler Data, VHF, HH

## 23.6 Comparison of HH-pol UHF and VHF Data

A comparison was made between the HH-pol values of  $\sigma_0$  obtained at UHF and VHF. The values used in the comparison are those discussed in Sections 20.1 and 23.5.

An inspection of Figures 100 and 127 shows that the range of grazing angles covered are different for the two frequencies. It can be seen from Figure 127 that at VHF, the values of  $\log(\sin \theta_i \sin \theta_r)$  are concentrated in the range of -1.0 to -2.0. In contrast, at UHF, the data from this region of grazing angles is sparse. Rather than comparing the data directly, the comparison was made between the mean value of the  $\sigma_0$  values plotted in Figure 127 and the constant- $\gamma$  function fitted to the UHF data shown in Figure 100, evaluated at  $\log(\sin \theta_i \sin \theta_r) = -1.5$ . Because of the dearth of VHF data at out-of-plane angles beyond 140 degrees, the comparison was limited to the range from zero to 120 degrees.

Figure 128 shows the difference between VHF and UHF VV-pol  $\sigma_0$  as a function of out-of-plane angle. As can be seen in Figures 99 and 126, the areas illuminated were not the same for VHF and UHF. For UHF the returns were from the valley floor in the vicinity of North Oscura Peak. For VHF the area was centered on a point about 80 km to the west of, and about 60 km to the south of North Oscura Peak. There was no overlap between the UHF and VHF areas. However, for both sets of data, the altitude was limited

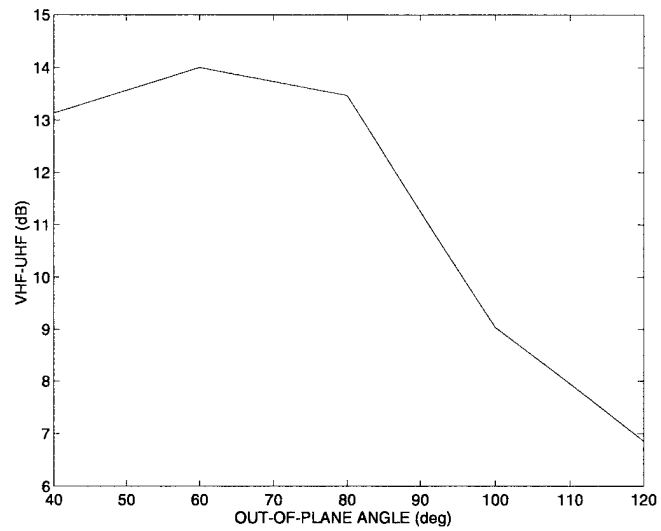


*Figure 128. Comparison of VHF and UHF HH-pol scattering*

to 1600 feet, which should have eliminated the rougher rising ground and ensure that the terrains were similar.

It can be seen from Figure 128 that the VHF values of  $\sigma_0$  are higher than the UHF values. The excess ranges from 14 dB at 60 degrees out-of-plane angle to 7 dB at 120 degrees.

## 24. VHF VH-POL RESULTS

### 24.1 MOD318003

This set of VH-pol VHF data was recorded on September 18, 1996 over an area centered on a point approximately 100 km to the west, and 70 km to the south of North Oscura Peak.

Figure 129 shows a plot of constant delay (solid lines) and constant Doppler (broken lines) for the ground reflection points. The interval between the constant delay lines is five resolution cells (7.5 km) and

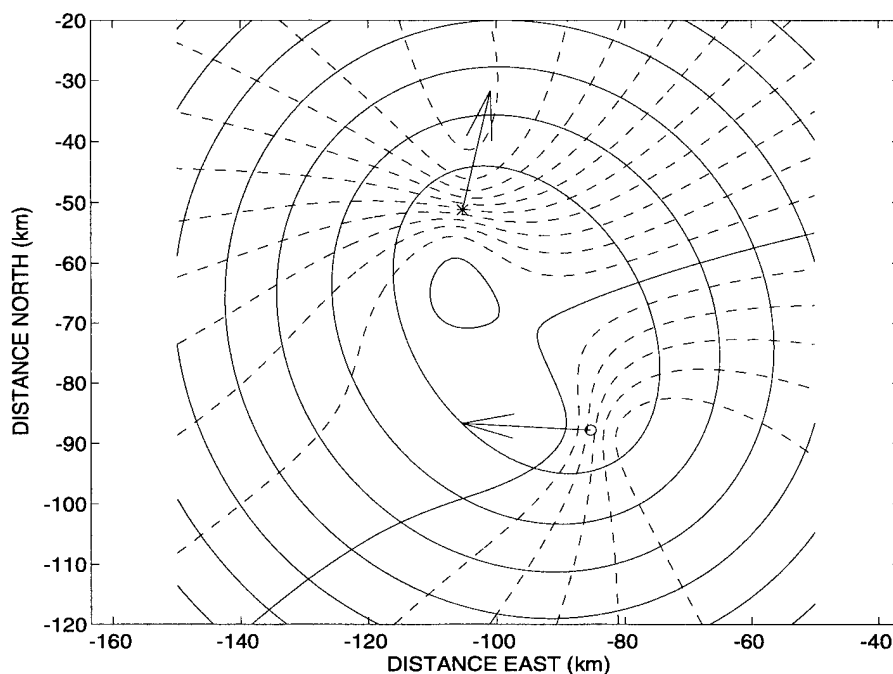


*Figure 129. Isodelay & Isodoppler Plots, MOD318003, VHF, VH*

that between the constant Doppler lines is two resolution cells (7.8 Hz). The position of the west-bound transmitter is shown by a circle and that of the north-bound receiver by an asterisk. The solid Doppler contour indicates zero Doppler shift relative to the direct path Doppler. To the north-west of this line the Doppler shift difference is positive, i.e. the relative range rate is negative.

The area selected for data extraction was determined by the antenna patterns, the delay-Doppler ambiguities and the ground elevation. The H-pol transmitting antenna was mounted on the starboard side of the transmitting aircraft, hence the area to the south of track was in the rear sidelobes of the antenna and therefore received little energy. The V-pol receiving antenna was omnidirectional in azimuth. It can be seen from Figure 129 that there is an ambiguity associated with most of the illuminated area. The only area that could give unambiguous returns was that to the north of the transmitter track and in the area of

negative Doppler shifts. The unambiguous area was selected as being more northerly than the transmitter and having Doppler shifts lower than -10 Hz. Also the ground elevation was restricted to below 1600 m to eliminate returns from the rising ground.

Figure 130 shows the signals for mission MOD318003. The upper left-hand frame shows the locations of the scatterers that give returns at least 3 dB above the noise floor. The locations of the

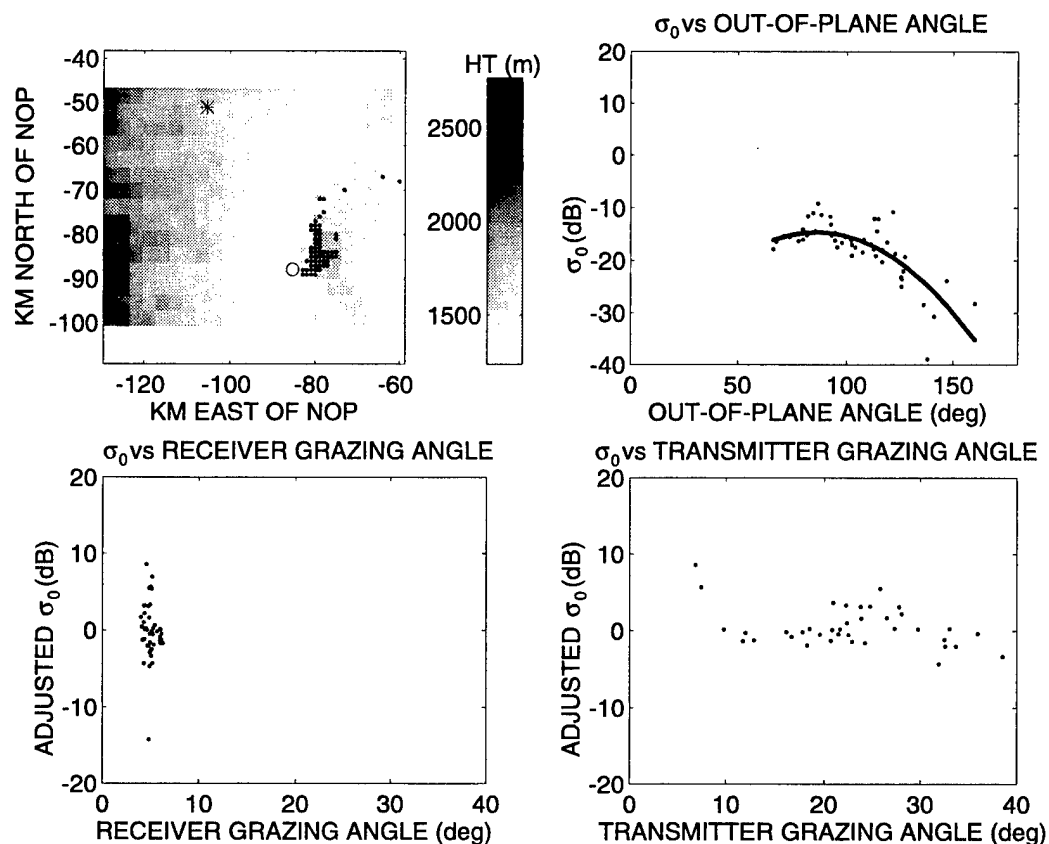


Figure 130. Distribution of Bistatic Scattering Coefficient, MOD318003, VHF, VH

transmitting and receiving aircraft are marked by a circle and an asterisk, respectively. The upper right frame shows the distribution of  $\sigma_0$  with respect to out-of-plane angle. A quadratic fitted to the points is shown. The coefficients of this quadratic, in descending order, are -0.0037, 0.64 and -42.5. The units are dB and degrees. The quadratic has values of -42.5, -14.7 and -47.7 dB at 0, 90 and 180 degrees out-of-plane angle, respectively. The lower two frames show the values of  $\sigma_0$  with the parabolic function subtracted from them. The values are plotted against receiver grazing angle and transmitter grazing angle.

## 24.2 MOD318006

This set of VH-pol VHF data was recorded on September 18, 1996 over an area centered on a point approximately 100 km to the west, and 80 km to the south of North Oscura Peak.

Figure 131 shows a plot of constant delay (solid lines) and constant Doppler (broken lines) for the ground reflection points; the interval between the constant delay lines is five resolution cells (7.5 km) and

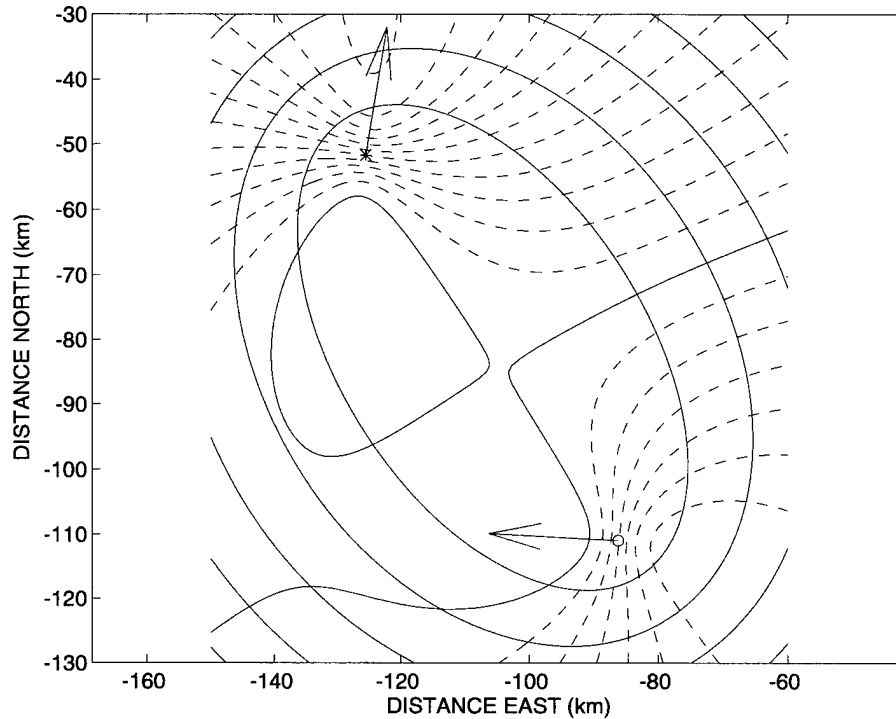


Figure 131. Isodelay & Isodoppler Plots, MOD318006, VHF, VH

that between the constant Doppler lines is two resolution cells (7.8 Hz). The position of the west-bound transmitter is shown by a circle and that of the north-bound receiver by an asterisk. The solid Doppler contour indicates zero Doppler shift relative to the direct path Doppler. To the north-west of this line the Doppler shift difference is positive, i.e., the relative range rate is negative.

The area selected for data extraction was determined by the antenna patterns, the delay-Doppler ambiguities and the ground elevation. The H-pol transmitting antenna was mounted on the starboard side of the transmitting aircraft, hence the area to the south of track was in the rear sidelobes of the antenna and therefore received little energy. The V-pol receiving antenna was omnidirectional in azimuth. It can be seen that there is an ambiguity associated with most of the illuminated area. The only area that could give unambiguous returns was that to the north of the transmitter and in the area of negative Doppler shifts. The unambiguous area was selected as being more northerly than the transmitter and having Doppler shifts



lower than -10 Hz. Also the ground elevation was restricted to below 1600 m to eliminate returns from the rising ground.

Figure 132 shows the signals for mission MOD318006. The upper left-hand frame shows the locations of the scatterers that give returns at least 3 dB above the noise floor. The locations of the

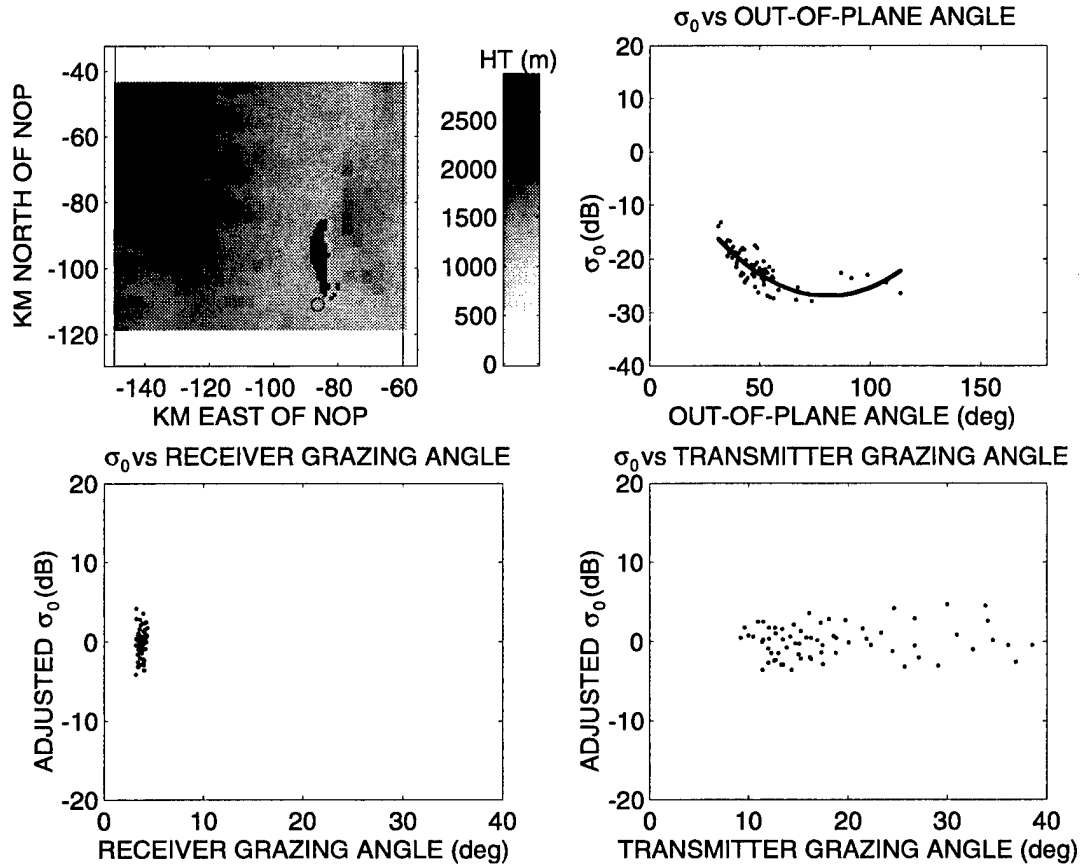


Figure 132. Distribution of Bistatic Scattering Coefficient, MOD318006, VHF, VH

transmitting and receiving aircraft are marked by circles and asterisks, respectively. The upper right frame shows the distribution of  $\sigma_0$  with respect to out-of-plane angle. A quadratic fitted to the points is shown. The coefficients of this quadratic, in descending order, are  $-0.0043$ ,  $-0.69$  and  $1.30$ . The units are dB and degrees. The quadratic has values of 1.3,  $-26.5$  and 15.5 dB at 0, 90 and 180 degrees out-of-plane angle, respectively. The lower two frames show the values of  $\sigma_0$  with the parabolic function subtracted from them. The values are plotted against receiver grazing angle and transmitter grazing angle.

Note that the shape of the quadratic fitted to the values of  $\sigma_0$  in the upper right-hand frame of Figures 130 and 132 are different, despite the fact that the active areas are nearly identical. Considering the probable errors in measurement, and that the data come from different (but overlapping) out-of-plane angles, the difference in shapes is not considered to be significant.

### 24.3 M3D22\_1002

This set of VH-pol VHF data was recorded on September 22, 1996 over an area centered on a point approximately 85 km to the west, and 35 km to the south of North Oscura Peak.

Figure 133 shows a plot of constant delay (solid lines) and constant Doppler (broken lines) for the ground reflection points; the interval between the constant delay lines is five resolution cells (7.5 km) and

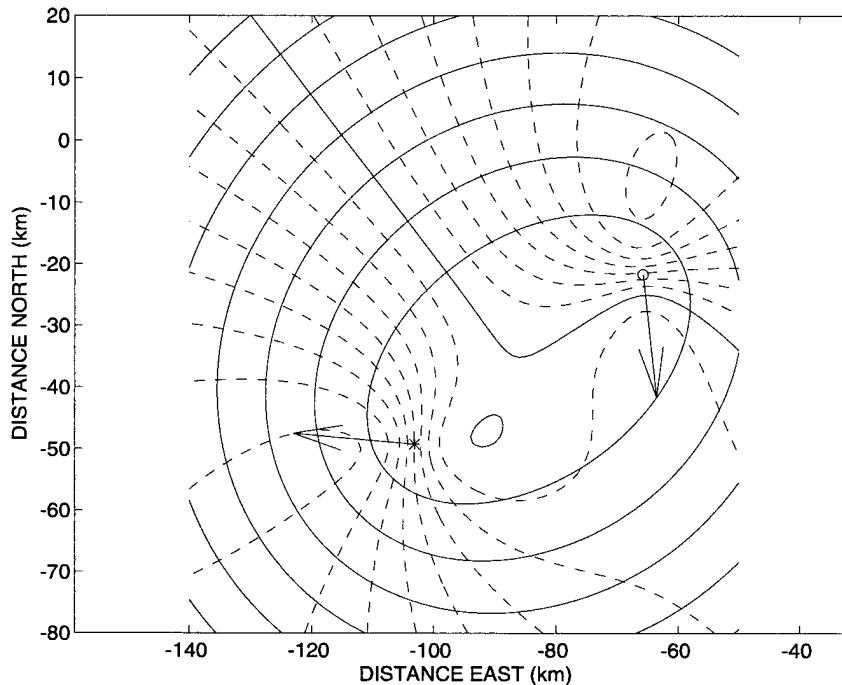


Figure 133. Isodelay & Isodoppler Plots, M3D22\_1002, VHF, VH

that between the constant Doppler lines is two resolution cells (7.8 Hz). The position of the transmitter is shown by a circle and that of the receiver by an asterisk. The single solid Doppler contour indicates zero Doppler shift relative to the direct path Doppler. To the south and west of this line the Doppler shift difference is positive, i.e., the relative range rate is negative.

The area selected for data extraction was determined by the antenna patterns, the delay-Doppler ambiguities and the ground elevation. The transmitting antenna was mounted on the starboard side of the west-bound transmitting aircraft, hence the area to the east of track was in the rear sidelobes of the antenna and therefore received little energy.

It can be seen that there are ambiguities associated with most of the illuminated area. The only area that can give unambiguous returns is that to the west of the meridian through the transmitter position and giving Doppler shifts less than -10 Hz. The area considered was therefore restricted to these limits. Also the ground elevation was restricted to below 1600 m to eliminate returns from the rising ground.

Figure 134 shows the signals for mission M3D22\_1002. The upper left-hand frame shows the locations of the scatterers that give returns at least 3 dB above the noise floor. The locations of the

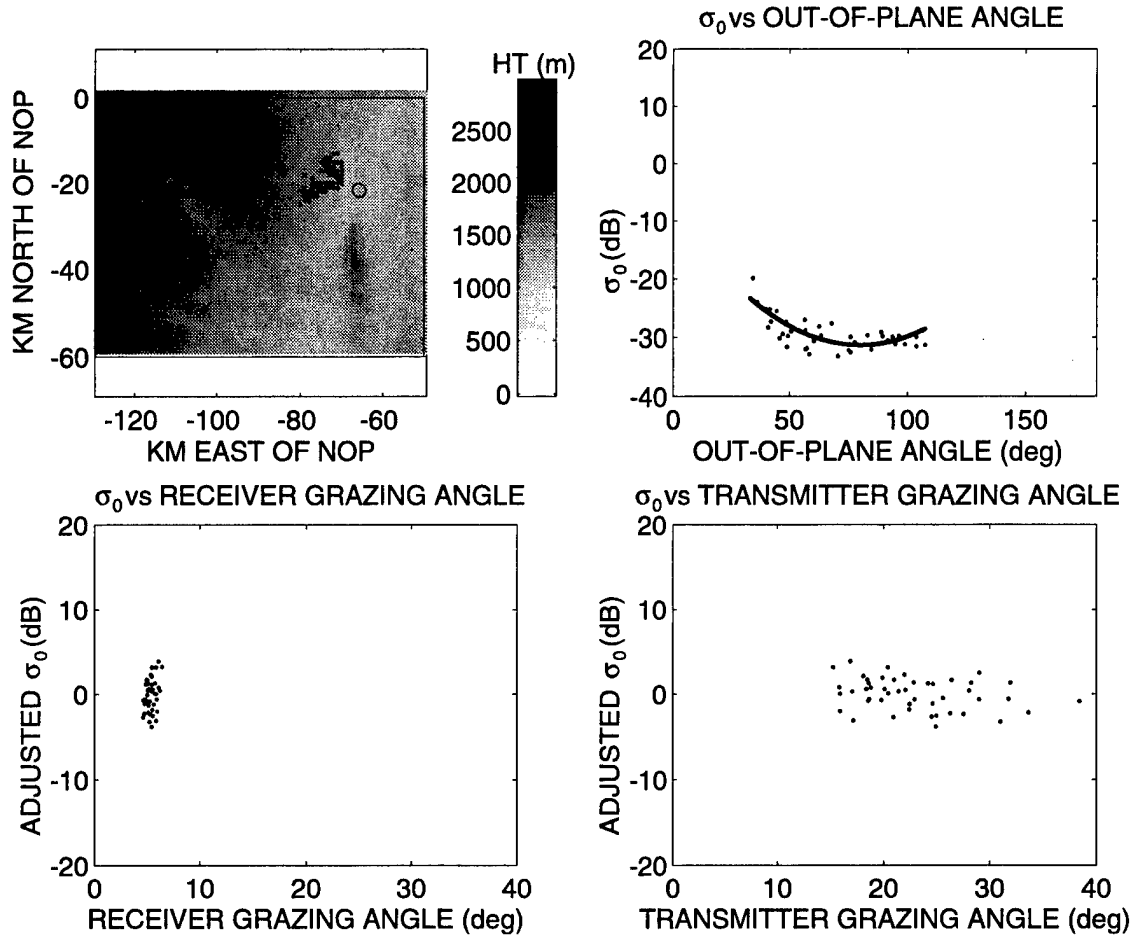


Figure 134. Distribution of Bistatic Scattering Coefficient, M3D22\_1002, VHF, VH

transmitting and receiving aircraft are marked by circles and asterisks, respectively.

The upper right frame of Figure 134 shows the distribution of  $\sigma_0$  with respect to out-of-plane angle along with a least-squares-fitted quadratic. The coefficients of this quadratic, in descending order, are 0.0036,  $-0.582$  and  $-7.98$ . The units are dB and degrees. The quadratic has values of  $-7.9$ ,  $-30.9$  and  $5.1$  dB at 0, 90 and 180 degrees out-of-plane angle, respectively. The lower two frames show the values of  $\sigma_0$  with the parabolic function subtracted from them. The values are plotted against receiver grazing angle and transmitter grazing angle.

## 24.4 Combined VHF VH-pol Data

Figure 135 shows the result of combining the three sets of delay-Doppler VH-polarized measurements. The data sets were from missions MOD318003, MOD318006 and M3D22\_1002. The left-

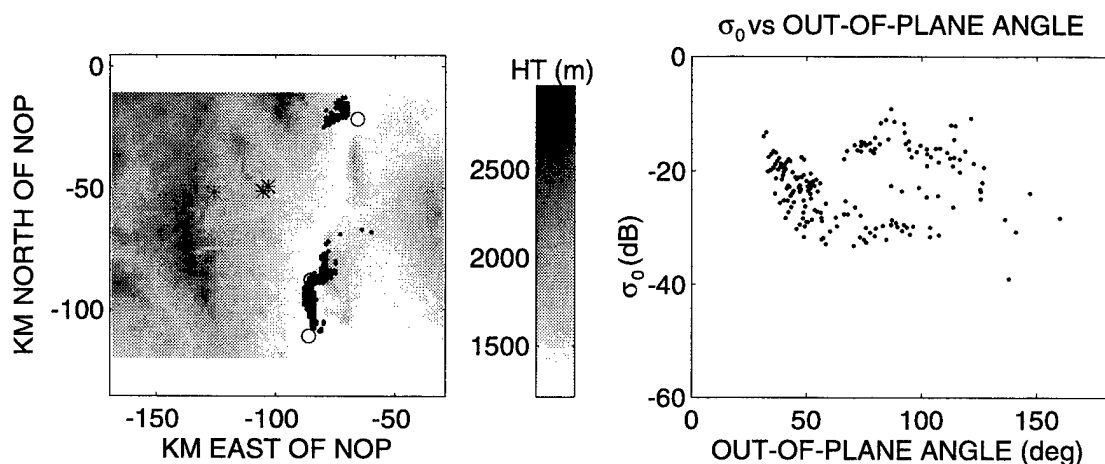


Figure 135. Distribution of Bistatic Scattering Coefficient, Delay-Doppler Data, VHF, VH

hand frame shows the locations of the scatterers. The locations of the transmitting and receiving aircraft are marked by circles and asterisks, respectively.

The right-hand frame shows the distribution of  $\sigma_0$  with respect to out-of-plane angle. It can be seen that the distribution forms two clusters, the lower left being formed by data from MOD318006 and M3D22\_1002, and the upper right from MOD318003. An examination of Figure 130 shows that the small active area for MOD318003 is centered on -80 km east and -85 km north and appears to be on rising ground. The higher value of  $\sigma_0$  suggest that this area is rougher than those pertaining to the other two data sets.

Figure 136 shows the log of the bistatic scattering coefficient plotted against the log of the product of the sines of the grazing angles. Again, there is evidence of clustering in some frames.

## 24.5 Comparison of VH-pol UHF and VHF Data

A comparison was made between the VH-pol values of  $\sigma_0$  obtained at UHF and VHF. The values used in the comparison are those discussed in Sections 21.1 and 24.4.

An inspection of Figures 47 and 136 show that the range of grazing angles covered are different for the two frequencies. For all values of out-of-plane angle at VHF, the values of  $\log(\sin\theta_i \sin\theta_r)$  are concentrated in the range of -1.0 to -2.0. For UHF, the data points are more widely distributed. The

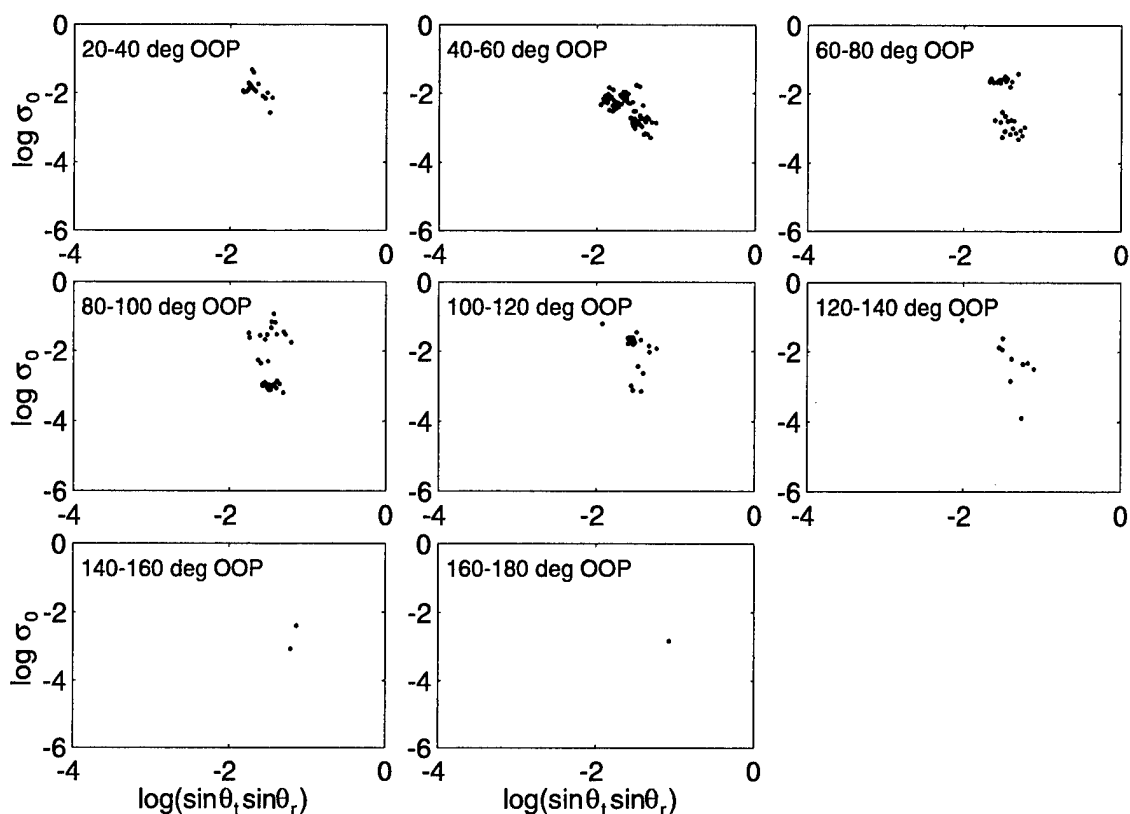
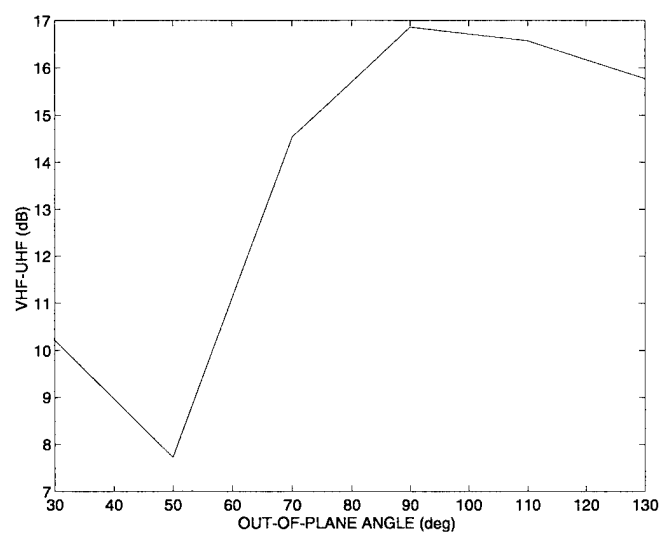


Figure 136. Log of Bistatic Scattering Coefficient vs. Log of Product of Sines of Grazing Angles, Delay-Doppler Data, VHF, VH

comparison was therefore made between the mean VHF value of  $\sigma_0$  and the UHF value of the fitted constant- $\gamma$  function, at  $\log(\sin \theta_i \sin \theta_r) = -1.5$ .

Figure 137 shows the difference between VHF and UHF VH-pol  $\sigma_0$  as a function of out-of-plane angle. The ground areas illuminated were not the same for VHF and UHF. For the UHF measurements, the returns were from the valley floor in the vicinity of North Oscura Peak. For the VHF data, the area was centered on a point about 80 km to the west of, and about 60 km to the south of North Oscura Peak, there being no overlap between the UHF and VHF areas. However, for both sets of data, the altitude was limited to 1600 feet, which should have eliminated the rougher rising ground and ensure that the terrains were similar.



*Figure 137. Comparison of VHF and UHF VH-pol scattering*

## 25. STATISTICAL INDEPENDENCE WITH FREQUENCY VARIATION

Section 15 of this report discusses measurements made at WSMR to evaluate multipath scattering from a small area of terrain at a variety of transmitter-ground depression angles and transmitter-patch-receiver out-of-plane angles. This operation was carried out for three separate areas. In the case of Fair Site, measurements were made at three frequencies to maximize the number of statistically independent samples. This section describes an effort to test the statistical independence of the measurements made at the three frequencies.

If the time-resolution cell is large compared to  $1/F_d$ , where  $F_d$  is the difference between two frequencies, and the number of scatterers in the resolution cell is large, then the values of  $\sigma_0$  at the two frequencies should be independent samples from the same exponential distribution. In the current experiment, the spacing between frequencies was 3 MHz and the time resolution cell was 13  $\mu$ s, which is 39 times  $1/F_d$ . The samples should therefore be independent. The log of the ratio of two independent samples from the same distribution should have a mean of zero and a constant standard deviation. The objective in this analysis was to test if this is true.

### 25.1 Method

The method adopted for comparing the returns at different frequencies was to select range profiles of  $\sigma_0$  for pairs of frequencies and the same aircraft position. This was done by a process of quantizing and sorting. Having obtained pairs of range profiles, values of  $\sigma_0$  were extracted corresponding to a set of ranges within predetermined limits. The mean and standard deviation of the natural log of the ratio of the two samples of  $\sigma_0$  at each range were then calculated.

### 25.2 Results

The frequencies were compared in pairs, 432 with 435, 432 with 438 and 435 with 438 MHz. Table 6 summarizes the results. The first column shows the pairs of frequencies compared. The second column shows the number of independent samples, which were calculated by dividing the actual number of samples by 13, since the transmitted pulse was 13 microseconds long and the signal was sampled at one microsecond intervals. The third and fourth columns show the mean and standard deviations of the log of the ratio of the  $\sigma_0$  values. The bottom row of the table shows matching results using a random sequence with an exponential power distribution (equivalent to a Rayleigh distribution in signal amplitude).

**Table 6. Frequency Dependence**

Frequencies (MHz)	Number of samples	Mean $\ln\left(\frac{\sigma_1}{\sigma_2}\right)$	Std. Dev.
432,435	93	-0.379	1.79
435,438	86	0.457	1.66
432,438	442	0.163	1.89
Exponential	10000	0.011	1.79

It can be seen that the standard deviations in the real data are not significantly different from that in the synthetic data. The lowest value of the standard deviation (1.66) corresponds to about 2% common component in the signals. It is concluded therefore that the measurements at the different frequencies were statistically independent.

The mean values shown in the third column may indicate a frequency-dependent variation in the measurements. To see if these values are statistically relevant, let us consider the largest value of 0.457, resulting from the comparison of 435 and 438 MHz. This measurement was the mean of 86 measurements. If the standard deviation before averaging was 1.66, as shown in the right-hand column, the standard deviation after averaging would be 1.66 divided by the square root of 86. This gives a standard deviation of 0.18. The mean value of 0.457 is 2.55 times this standard deviation. If the mean of the underlying distribution is zero, the probability of this value occurring is 0.001. With such a low probability of random occurrence, the apparent frequency dependence must be considered real.

The frequency-dependent variation in the measurement shown in the third column of the table can be converted to dB by multiplying by 4.34. It can be seen that the measurements taken at 435 MHz were highest, being 2.0 dB higher than the lowest, which were taken at 438 MHz. The measurements taken at 432 MHz were about 0.7 dB above those taken at 438 MHz. Note that the sum of the means from the first two pairs of frequencies is not the same as from the third pair, as might be expected. The discrepancy, however, is only about a quarter of a standard deviation after averaging. There is an 80% probability of this difference occurring.

The analysis has shown that for the bistatic scattering measurements at Fair Site, the spacing of 3 MHz between frequencies gave statistically independent measurements of  $\sigma_0$ . However, the analysis also showed that there is a frequency-dependent variation in the measurements giving a maximum difference of 2 dB between frequencies.



## 26. SUMMARY

### 26.1 Summary of Delay-Azimuth UHF Results

The data have been interpreted in terms of the Generalized Lambertian Formula (GLF), Equation 6,  $\sigma_0 = \gamma(\sin\theta_i \sin\theta_r)^{\alpha(\theta)}$  and the values of  $\gamma$  and the exponent  $\alpha$  estimated from the data. Note that the value of  $\alpha$  for each polarization combination is a function of out-of-plane angle  $\theta$ , while  $\gamma$  is constant for each polarization combination.

Figure 138 shows the values of  $\gamma$  and  $\alpha$  for VV, HH, VH and HV polarization pairs of UHF delay-azimuth wide area data. The results shown here were discussed in Sections 11, 12, 13 and 14.

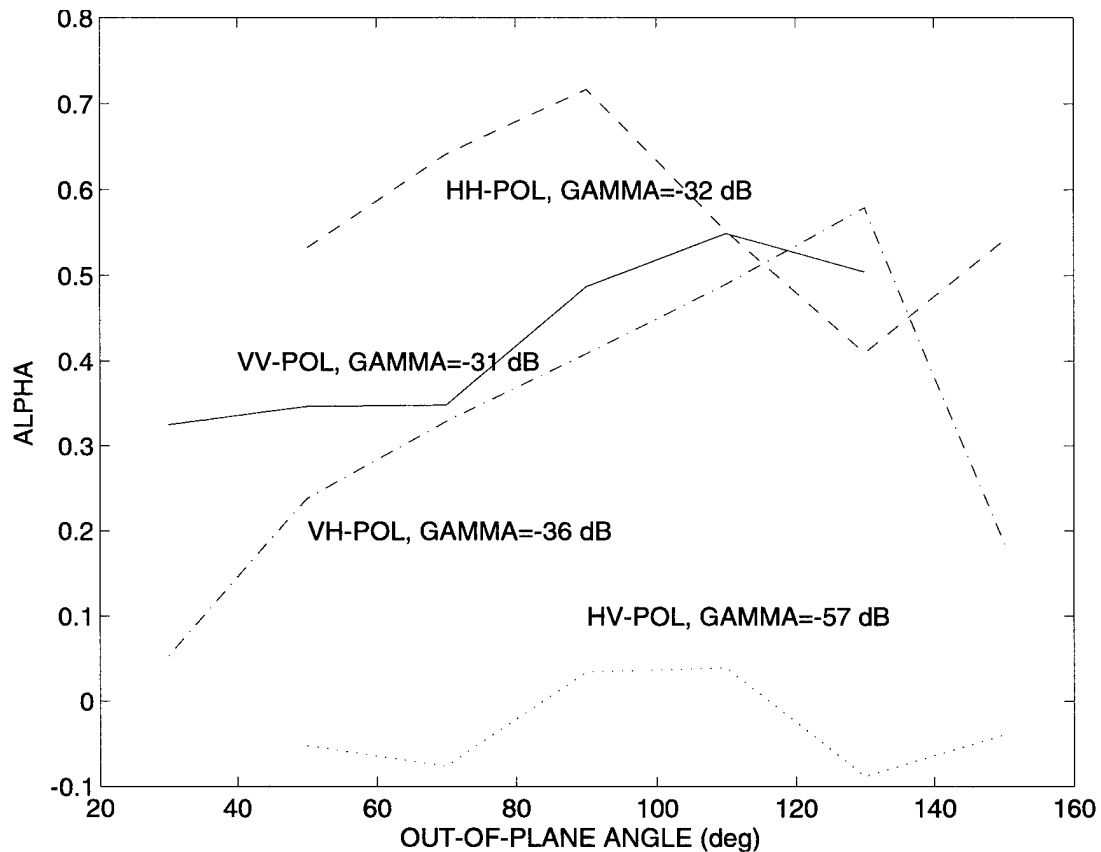


Figure 138. Generalized Lambertian Parameters, Delay-Azimuth, UHF

It can be seen that the values of  $\gamma$  are nearly the same for VV-pol and HH-pol, being -31 and -32 dB, respectively. The value of gamma for VH-pol is a few decibels lower at -36 dB, while that for HV-pol is much lower at -57 dB. The values of  $\alpha$  for VV-pol are close to 0.5, while the values for other polarizations are significantly different. The HH-pol values of  $\alpha$  are higher and those for VH-pol vary over the widest range. For HV-pol the values of  $\alpha$  are near zero.

Table 7 shows the measured  $\sigma_0$  at an out-of-plane angle of 90 degrees for the various polarizations. The first column lists the polarization and sites where applicable; where a site name is not

**Table 7. GLF Parameters**

<b>POLARIZATION</b>	<b><math>\sigma_{0, dB}</math> at 90 deg</b>	<b>Fig. #</b>	<b>Lognormal width (dB)</b>	<b><math>\gamma_{dB}</math></b>	<b><math>\alpha_{mean}</math></b>	<b><math>\alpha_{std}</math></b>
VV	-44.8	22	6.25	-31	0.44	0.16
VV FAIR SITE	-43.9	74	5.66	-33	0.41	0.10
VV CARRIZOZO	-38.0	80	5.62	-44	-0.20	0.13
HH	-51.6	58	8.92	-32	0.59	0.29
VH	-47.2	37	9.24	-36	0.41	0.50
HV	-57.6	70	7.65	-57	0.02	0.50

given, the results are for the wide area measurements. The second column lists the  $\sigma_0$  values at 90 degree out-of-plane angle. The third column lists the figure numbers displaying the relevant data and the fourth column lists the scale width of the lognormal distribution curve fitted to the data. The fifth column shows the value of  $\gamma_{dB}$  and sixth and seventh columns show the mean and standard deviation of the exponent  $\alpha$  in the Generalized Lambertian Formula for grazing angle dependence.

An examination of the  $\sigma_0$  values in the table shows a number of features; first, the VV-pol wide-area  $\sigma_0$  agrees with that for Fair Site; second,  $\sigma_0$  for the town of Carrizozo is 6 dB higher than that for Fair Site; third,  $\sigma_0$  for HH-pol is 6 dB lower than for VV-pol; and fourth, the HV-pol value is 10.2 dB lower than for VH-pol.

The agreement between the VV-pol wide-area and Fair Site results is to be expected and validates some of the assumptions inherent in the wide-area analysis. As well as  $\sigma_0$  at 90 degree out-of-plane being similar, variation with out-of-plane angle are also similar, as can be seen in Figures 22 and 74. Also, the values of  $\alpha$  are consistent.

The higher  $\sigma_0$  for Carrizozo is to be expected because of the presence of houses and other buildings in the scene. Apart from the 90 degree  $\sigma_0$  being higher,  $\sigma_0$ , as a function of out-of-plane angle, shows a relative flat characteristic, compared to the falling characteristic seen in the other VV-pol data. This can be seen in the upper right-hand plots of Figures 22 and 80.

The HH-pol values are 6 dB below the VV-pol values at 90 degree aspect angles but increase as the out-of-plane angle increases or decreases. The values of  $\alpha$  are generally higher than for VV-pol and show a maximum at 90 degrees out-of-plane angle, corresponding to a low value of  $\sigma_0$ .

At 90 degrees out-of-plane angle, the HV-pol  $\sigma_0$  is 10.4 dB lower than the VH-pol value. An examination of Figures 37 and 70 reveals that the variation with out-of-plane angle is also markedly different. Whereas the value for the VH-pol data falls linearly with increasing out-of-plane angle, the value for HV-pol is a minimum near 90 degrees.

The distribution of the magnitude of  $\sigma_0$  was evaluated using the delay-azimuth data. In determining the distribution, the dependence on out-of-plane angle and grazing angles were first determined and then removed from the data. The amplitude distribution of the resultant was then compared with Rayleigh, Weibull and lognormal distributions.

The amplitude distributions of  $\sigma_0$  measured over a wide area were generally found to be much broader than Rayleigh. This suggested that there was a variation in scattering characteristics over the area. The scattering area being considered was then reduced to a 20x30 km patch and the distributions reexamined. As might be expected, these were found to be closer to Rayleigh. The measurements at Fair Site, and Carrizozo were already confined to a relatively small area so there was no need to reduce the measurement area further. The VV-pol  $\sigma_0$  amplitude distribution for the limited patch in the wide-area measurements were found to be closest to Rayleigh. The other polarization combinations varied in width, with the broadest being the VH-pol measurements.

In PCW mode, the transmitter modulator had a leakage between pulses of about -60 dB. Depending on the strength of the direct signal, the constant signal due to modulator leakage could exceed the environmental and receiver noise. Under these circumstances, the distribution of amplitudes were narrower than for random noise. This effect accounts for the short tail at the lower end of the distribution curves seen on some sets of data.

## 26.2 Summary of Combined Delay-Azimuth and Delay-Doppler UHF Results

The data from the delay-azimuth and delay-Doppler measurements were combined and analyzed in a manner similar to that used for the delay-azimuth data.

For VV-pol and VH-pol, the bistatic scattering coefficient,  $\sigma_0$ , was analyzed in terms of the Generalized Lambertian Formula  $\sigma_0 = \gamma(\sin \theta_i \sin \theta_r)^{\alpha(\phi)}$ , Equation 1. For HH-pol data, the Modified Generalized Lambertian Formula  $\sigma_0' = \frac{(1 + \cos 2\phi)}{2}(\sin \theta_i \sin \theta_r)^{\alpha(\phi)}$ , Equation 9, was used to account for the observed null in the region of 90 degrees out-of-plane angle. The individual results are discussed in detail in Sections 19, 20 and 21.

Figure 139 shows the values of  $\gamma$  and  $\alpha$  for the three polarization pairs of UHF data. The value of  $\gamma$  is highest for HH-pol (-15 dB), slightly lower for VH-pol (-16 dB), and lowest for VV-pol (-31 dB). These values of  $\gamma$  have little meaning in themselves, as they reflect the measurements of  $\sigma_0$  at grazing angles between two and 40 degrees extrapolated to 90 degrees. However, in combination with the values of  $\alpha$  they can be used to calculate  $\sigma_0$  in the measurement range.

Excluding out-of-plane angles near 180 degrees, the average value of  $\alpha$  for VV-pol is approximately 0.4, while for HH-pol, it is approximately 0.6. For VH-pol,  $\alpha$  is approximately 1.1.

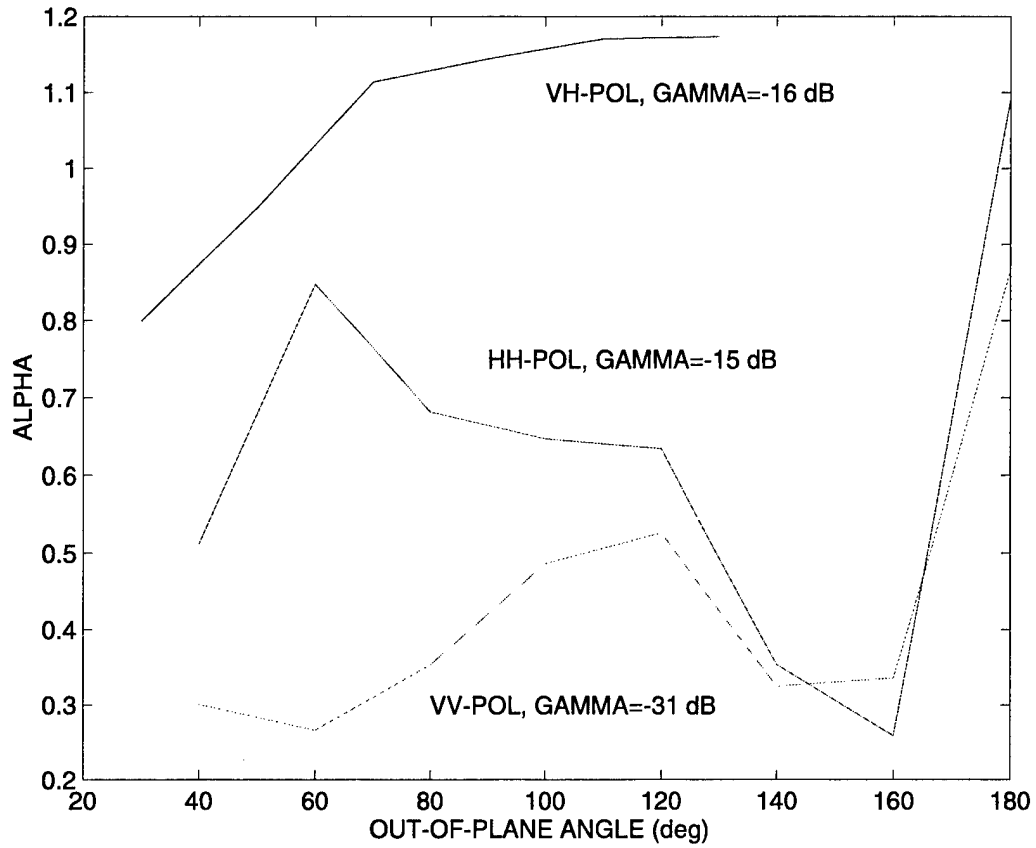


Figure 139. Generalized Lambertian Parameters, Combined Data, UHF

Substituting these values in Equation 1 and Equation 9, the VV-pol data can be modeled by

$\sigma_{0, dB} = -31 + 4\log(\sin\theta_i \sin\theta_r)$ , the VH-pol data by  $\sigma_{0, dB} = -16 + 11\log(\sin\theta_i \sin\theta_r)$  and the HH-pol

data by  $\sigma_{0, dB} = -15 + 10\log\left(\frac{1 + \cos 2\phi}{2}\right) + 6\log(\sin\theta_i \sin\theta_r)$ .

The scattering parameters were calculated for a large ground area in an attempt to cover the largest range of out-of-plane angles and grazing angles. The conclusions were based on the assumption that the scattering characteristics were uniform over this area. To validate this assumption, parameters were calculated for an area measuring 20 by 30 km, for comparison with those from the full area. For VV-pol and VH-pol, there was satisfactory agreement. For HH-pol, there was some disagreement, but this could be due to a paucity of data for some combinations of out-of-plane angle and grazing angle in the limited area.

## 26.3 Comparison of UHF Results

The results of the delay-azimuth analysis shown in Figure 138 and those of the combined data shown in Figure 139 are compared below. Also, by neglecting variations in  $\alpha$  with out-of-plane angle, the results are simplified and summarized.

For both sets of VV-pol results, the value of  $\gamma$  is -31 dB. The values of  $\alpha$  are also similar, those from the combined set being slightly lower. It is assumed that the best accuracy is obtained from the combined data since more data were included. Using the value of  $\gamma$  and a mean value of  $\alpha$  from the combined data, the VV-pol GLF is  $\sigma_{0, dB} = -31 + 4\log(\sin\theta_i \sin\theta_r)$ .

The HH-pol results from the two sets cannot be compared directly since the models were different for the two analyses. For the delay-azimuth data, the GLF was used, whereas for the combined data the GLF was modified to incorporate a null at 90 degrees out-of-plane angle. This difference in model would account for the large difference in  $\gamma$ , the delay-azimuth value being 17 dB lower than the combined data. Since the Modified GLF was the more general model, the combined results are considered to be more accurate. Using the  $\gamma$  and average  $\alpha$  from the combined results, Equation 9 becomes

$$\sigma_{0, dB} = -15 + 10\log\left(\frac{1 + \cos 2\phi}{2}\right) + 6\log(\sin\theta_i \sin\theta_r).$$

Considerable differences are seen in the VH-pol values from the two analyses. The delay-azimuth data gave a  $\gamma$  of -36 dB, compare to -16 dB for the combined data. The problem with the delay-Doppler data is that the cross-polarization isolation was poor, which probably resulted in higher values of  $\sigma_0$ . Because of this limitation, the delay-azimuth results are considered to be more accurate than the combined results. Using the value of  $\gamma$  and a mean value of  $\alpha$  from the delay-azimuth data, the VH-pol GLF becomes  $\sigma_{0, dB} = -36 + 4\log(\sin\theta_i \sin\theta_r)$ .

No delay-Doppler measurements were taken using HV-pol, hence the only results available were from the delay-azimuth data. The delay-azimuth data show a value of  $\alpha$  whose mean is close to zero. Neglecting variations in  $\alpha$ , the GLF reduces to  $\sigma_{0, dB} = -57$ .

## 26.4 Comparison of UHF and VHF Results

Figure 140 shows the difference between measured VHF and UHF values of  $\sigma_0$  as functions of out-of-plane angle. These values were calculated from the GLF and Modified GLF using the parameters derived in the previous sections. It can be seen that for VV-pol the returns are 12 to 25 dB stronger at VHF than at UHF. For VH-pol they are about 8 to 17 dB stronger and for HH-pol, the VHF return are about 7 to 14 dB stronger.

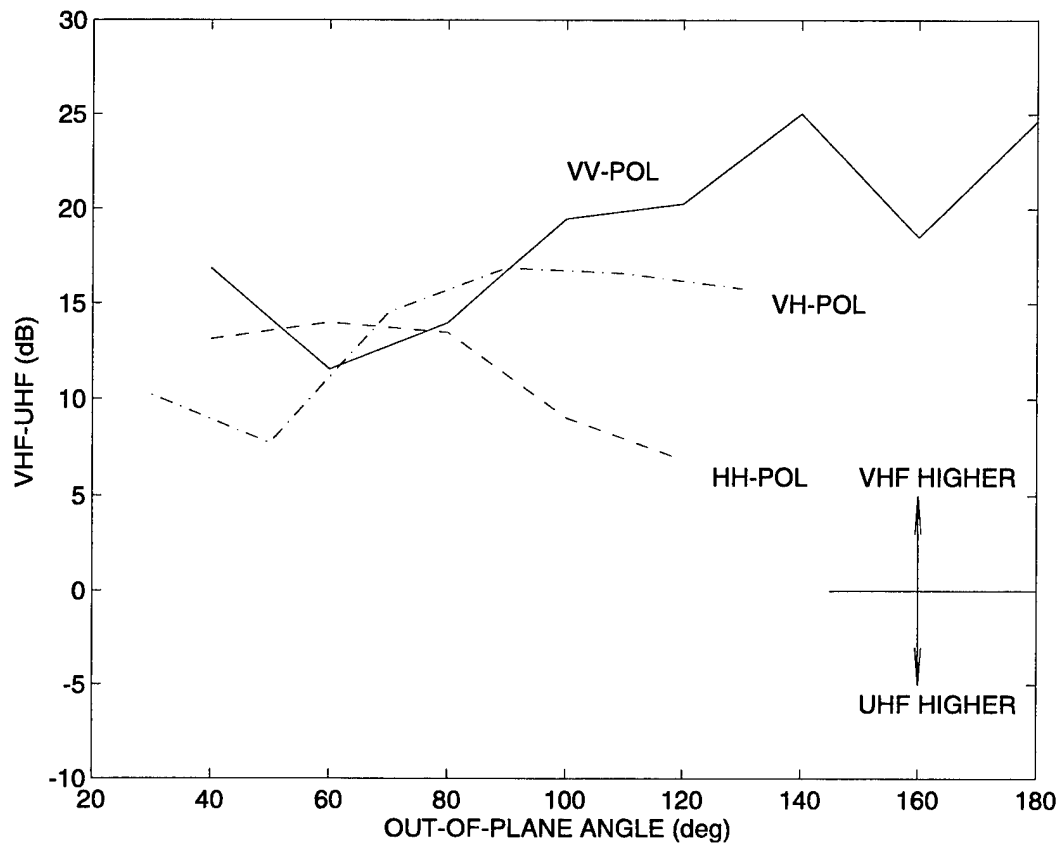


Figure 140. Comparison of VHF and UHF Scattering

## 26.5 Probable Error

In assessing the results of this analysis, the accuracy of the measurements should be considered. The values of  $\sigma_0$  were calculated from the recorded signal by applying the bistatic radar equation, the factors in the equation being determined by measurement and calculation.

The delay-azimuth data was calibrated more precisely than the delay-Doppler data. The antenna gains and receiver gain were subject to rigorous testing. The overall calibration was also validated by comparing the actual direct transmitter to receiver signal with the theoretical. Provided that the system was accurately calibrated, the measured direct signal from transmitter to receiver should have agreed with the theoretical direct-path signal, modified by multipath effects. For 22 of the ground-based VV-pol measurements the direct signal was measured and compared with the theoretical. The average of the measured minus the theoretical (in dB) was  $-1.7$  dB. This small difference could be due to partial cancellation of the direct signal by the signal reflected from the ground.

The calibration of the delay-Doppler data was less accurate, particularly in the determination of antenna gain. Measurements were made from the ground but they did not cover all angles observed and

were corrupted by multi-path effects. To overcome these difficulties, the direct transmitter to receiver signal was employed to provide overall calibration where possible.

For the delay-azimuth data the statistical independence between the measurements at different frequencies were assessed (see Section 25) and a maximum difference of 2 dB found. This difference was between two measurements 3 MHz apart. Most of the measurements used in this report were made over the range from 434.8 to 435.4, a range of 0.6 MHz. The variation in system gain is likely to be less than 1 dB over this range and therefore would not significantly affect the accuracy.

Quasi-monostatic delay-azimuth HH-pol measurements were compared the true monostatic measurements. The quasi-monostatic measurements used RSTER-90 for receiving and a separate antenna for transmitting. The true monostatic measurements used RSTER-90 for both transmitting and receiving. The quasi-monostatic  $\sigma_0$  was found to be 2 dB higher than the true monostatic. Considering that the quasi-monostatic and monostatic measurements were taken months apart, used different transmitting antenna and were analyzed by different analysts using different software, this difference is not considered significant.

## 27. CONCLUSIONS

Bistatic radar measurements of ground scattering, taken at WSMR have been analyzed to obtain an estimate of the bistatic scattering coefficient  $\sigma_0$ . The data have been interpreted in terms of the Generalized Lambertian Formula. Parameters of the formula representing  $\sigma_0$  as a function of grazing angle and out-of-plane angle were derived for VV, VH, HV and HH polarization pairs.

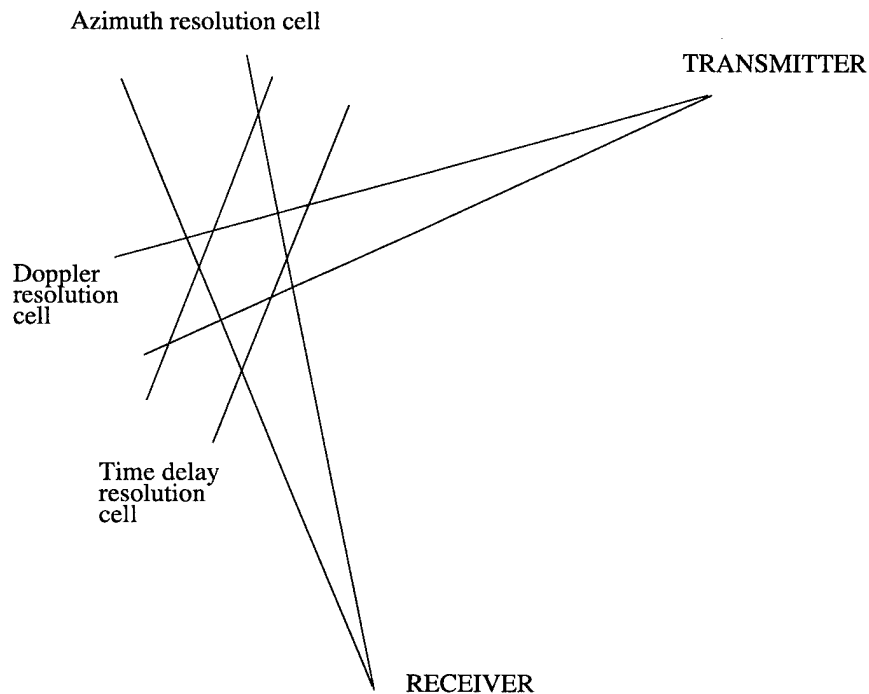
Two sets of measurements were made, the first using the ground-based RSTER antenna for reception in combination with ground-based and airborne transmitters. The second set used airborne platforms for both transmitting and receiving. The two sets were complementary in terms of grazing angles.



## 28. APPENDIX

### Effective Scattering Area

The response at a particular azimuth, delay and Doppler frequency is proportional to the effective scattering area. This scattering area is determined by the combined effects of the receiver beamwidth, time delay cell size and Doppler cell size. More precisely, the effective scattering area is equal to the integral over a horizontal surface of the product of the square of three spacial filtering functions, assuming that each filtering function has a maximum value of unity.



The diagram above illustrates the three filtering functions operating when Doppler processing is used. The two lines originating at the receiver represent the receiver beamwidth, the lines themselves corresponding to fixed amplitudes in the filtering function. The two lines originating at the transmitter represent the Doppler filtering function. The Doppler shift is proportional to the component of the velocity in the direction of the scatterer and is constant along the lines drawn. The third pair of lines represent the time delay cell size. These lines are sectors of ellipses, although they are drawn as straight lines in the diagram. If all three filtering functions had the value of unity between the lines drawn and were zero outside the lines (rectangular functions), the effective scattering area would be the irregular hexagon created by the three pairs of lines.

The shapes of the actual filtering functions depend on the physical antenna structure, the signal processing and the data processing, but can be approximated by rectangular functions or other mathematical shapes. If Doppler processing is not employed, there will be only two intersecting filtering

functions. If the functions are rectangular, the scattering area is simple to calculate and is given by the formula in Paragraph 5.1 (the pairs of lines are assumed to be parallel over a single resolution cell). For three intersecting functions, the calculation of the area of the enclosed figure is difficult if the functions are rectangular; other mathematical shapes prove to be more tractable. The following paragraphs derive the effective scattering area when the shapes are assumed to be gaussian.

In the following derivation of  $A_B$ , each of the three filtering functions is approximated by a gaussian function lying along an axis through the center of the scattering cell. The function is constant

along any line perpendicular to this axis. Each function is of the form  $e^{-\left[\frac{r \cos(\varphi - \theta)}{S}\right]^2}$  where  $r, \varphi$  is the location of the point of interest in polar coordinates, with the origin at the center of the cell,  $\theta$  gives the orientation of the axis of the function and  $S$  is the scale width of the gaussian function. Figure 141 illustrates the meanings of these parameters.

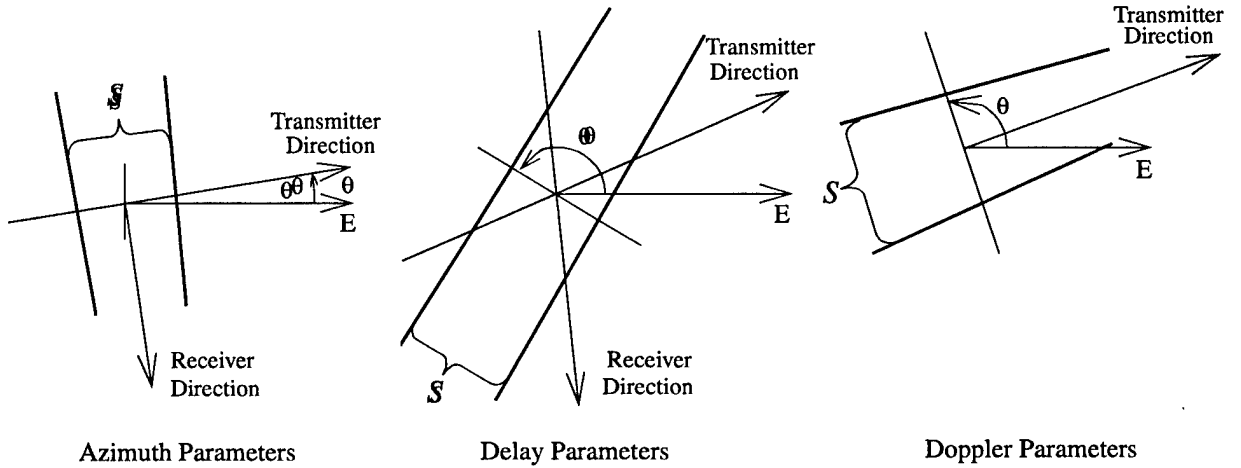


Figure 141. Gaussian Parameters

Note that it is assumed that the three axes intersect at a point. To make this assumption valid, in the data processing the axis of the Doppler function is made to coincide with the intersection of the azimuth and time delay axes by selecting the Doppler cell with the greatest response.

The product of the  $n$  functions ( $n = 3$ ) is

$$g = \prod_{i=1}^n e^{-\left[\frac{r \cos(\varphi - \theta_i)}{S_i}\right]^2} \quad (\text{EQ 21})$$

$$g = e^{\sum_{i=1}^n \left[ \frac{r \cos(\varphi - \theta_i)}{S_i} \right]} \quad (\text{EQ 22})$$

$$g = e^{-r^2 \sum_{i=1}^n \left[ \frac{\cos(\varphi - \theta_i)}{S_i} \right]} \quad (\text{EQ 23})$$

The effective scattering area,  $A_B$ , is the integral of the square of the product of the gaussian functions, thus

$$A_B = \int_0^{2\pi} \int_0^\infty r g^2 dr d\varphi = \int_0^{2\pi} \int_0^\infty r e^{-2r^2 \sum_{i=1}^n \left[ \frac{\cos(\varphi - \theta_i)}{S_i} \right]} dr d\varphi \quad (\text{EQ 24})$$

$$\text{But } \int_0^\infty r e^{-ar^2} dr = \frac{1}{2a} \quad (\text{EQ 25})$$

$$\text{therefore } A_B = \int_0^{2\pi} \frac{1}{n \sum_{i=1}^n \left( \frac{\cos(\varphi - \theta_i)}{S_i} \right)^2} d\varphi \quad (\text{EQ 26})$$

$$A_B = \int_0^{2\pi} \frac{1}{n \sum_{i=1}^n \frac{1}{\frac{1}{2} + \frac{1}{2} \cos 2(\varphi - \theta_i)}} d\varphi \quad (\text{EQ 27})$$

$$A_B = \int_0^{2\pi} \frac{d\varphi}{n \sum_{i=1}^n \frac{1 + \cos[2(\varphi - \theta_i)]}{S_i^2}} \quad (\text{EQ 28})$$

$$A_B = \int_0^{2\pi} \frac{d\varphi}{n \sum_{i=1}^n \frac{1 + \sin 2\varphi \cos 2\theta_i - \cos 2\varphi \sin 2\theta_i}{S_i^2}} \quad (\text{EQ 29})$$

$$\text{Let } 2\varphi = \psi \text{ then } \frac{d\psi}{d\varphi} = 2 \quad (\text{EQ 30})$$

$$A_B = \frac{1}{4} \int_0^{4\pi} \frac{d\psi}{n \sum_{i=1}^n \frac{1}{S_i^2} + \sin \psi \sum_{i=1}^n \frac{\cos 2\theta_i}{S_i^2} - \cos \psi \sum_{i=1}^n \frac{\sin 2\theta_i}{S_i^2}} \quad (\text{EQ 31})$$

$$A_B = \frac{1}{n} \int_0^{4\pi} \frac{d\psi}{4 \sum_{i=1}^n \frac{1}{S_i^2} + \frac{\sum_{i=1}^n \frac{\cos 2\theta_i}{S_i^2}}{1 + \sin \psi \frac{\sum_{i=1}^n \frac{\cos 2\theta_i}{S_i^2}} - \cos \psi \frac{\sum_{i=1}^n \frac{\sin 2\theta_i}{S_i^2}}}{\sum_{i=1}^n \frac{1}{S_i^2}}} \quad (\text{EQ 32})$$

$$A_B = \frac{1}{n} \int_0^{4\pi} \frac{d\psi}{1 + a \cos(\psi - \psi_0)} \quad (\text{EQ 33})$$

$$4 \sum_{i=1}^n \frac{1}{S_i^2}$$

$$\text{where } a^2 = \frac{\left[ \sum_{i=1}^n \frac{\cos 2\theta_i}{S_i^2} \right]^2 + \left[ \sum_{i=1}^n \frac{\sin 2\theta_i}{S_i} \right]^2}{\left[ \sum_{i=1}^n \frac{1}{S_i^2} \right]^2} \quad (\text{EQ 34})$$

$$\text{but } \int_0^{4\pi} \frac{dx}{1 + a \cos x} = 2 \int_0^{2\pi} \frac{dx}{1 + a \cos x} = \frac{4\pi}{\sqrt{1-a^2}} \quad (\text{EQ 35})$$

$$A_B = \frac{1}{n} \frac{4\pi}{4 \sum_{i=1}^n \frac{1}{S_i^2} \sqrt{1 - \frac{\left[ \sum_{i=1}^n \frac{\cos 2\theta_i}{S_i^2} \right]^2 + \left[ \sum_{i=1}^n \frac{\sin 2\theta_i}{S_i} \right]^2}{\left[ \sum_{i=1}^n \frac{1}{S_i^2} \right]^2}}} \quad (\text{EQ 36})$$

$$A_B = \frac{\pi}{\sqrt{\left[ \sum_{i=1}^n \frac{1}{S_i^2} \right]^2 - \left[ \sum_{i=1}^n \frac{\cos 2\theta_i}{S_i^2} \right]^2 - \left[ \sum_{i=1}^n \frac{\sin 2\theta_i}{S_i} \right]^2}} \quad (\text{EQ 37})$$

## REFERENCES

- [1] S. D. Coutts, "Mountaintop Jammer Multipath Mitigation Experiment," Proc. 2nd Adaptive Sensor Array Processing Workshop, Lincoln Lab, March 1994, pp. 595-624.
- [2] L. E. Brennan, "Preliminary Results of Hot Clutter Cancellation Tests Using WSMR Data," Proc. 3rd Adaptive Sensor Array Processing Workshop, March 1995, Vol.2, pp.515-537.
- [3] T. W. Miller and J. M. Ortiz, "An Overview of Issues in Hot Clutter Mitigation," Proc. 4th Adaptive Sensor Array Processing Workshop, Lincoln Lab, March 1996, pp. 193-239.
- [4] R. A. Gabel, "Signal Subspace Issues in TSI Mitigation," Proc. 4th Adaptive Sensor Array Processing Workshop, Lincoln Lab, March 1996, pp.261-283.
- [5] M. Kogon, D. B. Williams, and E. J. Holder, "Hot Clutter Cancellation with Orthogonal Beamspace Transforms," Proc. 4th Adaptive Sensor Array Processing Workshop, Lincoln Lab, March 1996, pp. 315-341.
- [6] F. Marshall and R. A. Gabel, "Simultaneous Mitigation of Multipath Jamming and Ground Clutter," Proc. 4th Adaptive Sensor Array Processing Workshop, Lincoln Lab, March 1996, pp.285-313.
- [7] S. M. Kogon, *et al*, "Joint TSI Mitigation and Clutter Nulling Architectures," Proc. 5th DARPA Hot Clutter TIM, Rome Lab, Sept.1997, pp 199-221.
- [8] D. Rabideau, "Revised STAP Strategies for Modulated Clutter," Proc. 5th DARPA Hot Clutter TIM, Rome Lab, Sept. 1997, pp 222-264.
- [9] T. Slocumb, J. Guerci, and P. Techau, "Hot and Cold Clutter Mitigation Using Deterministic and Adaptive Filters," Proc. 5th DARPA Hot Clutter TIM, Rome Lab, Sept.1997, pp 171-198.
- [10] N. J. Willis, *Bistatic Radar*, Artech House, 1991.
- [11] Sekine & Mao, *Weibull Radar Clutter*, Peregrinus, 1990.
- [12] J.K. Jao, private communication.
- [13] B. D. Carlson *et al.*, "An Ultralow-Sidelobe Adaptive Array Antenna", The Lincoln Laboratory Journal, Summer 1990, Vol. 3, No. 3.
- [14] Nathanson, *Radar Design Principles*, McGraw-Hill, 1969.
- [15] Ruck et al., *Radar Cross-Section Handbook*, Plenum Press, 1970.
- [16] Skolnik, *Radar Handbook, 2nd Ed.*, McGraw-Hill, 1990.
- [17] L. M. Zurk, "Data Sets from Propagation Experiment", MTF-146, October 1996.
- [18] S. D. Coutts, "King Air Instrumentation Radar Calibration Procedure," Internal Lincoln Lab memo, November 1996.
- [19] Kove, P. et. al., "Antenna Calibration for the Propagation and Bistatic Scattering Experiment", ASP-8, January 1997.

- [20] B. Francis, "Determination of Terrain Scattering Coefficients using WSMR Measurements", MTN-108, January 1996.
- [21] J. Jayne, "Two-Dimensional Clutter Maps", Internal Memo, October 1993.

# REPORT DOCUMENTATION PAGE

Form Approved  
OMB No. 0704-0188

Public reporting burden for this collection of information is estimated to average 1 hour per response, including the time for reviewing instructions, searching existing data sources, gathering and maintaining the data needed, and completing and reviewing the collection of information. Send comments regarding this burden estimate or any other aspect of this collection of information, including suggestions for reducing this burden, to Washington Headquarters Services, Directorate for Information Operations and Reports, 1215 Jefferson Davis Highway, Suite 1204, Arlington, VA 22202-4302, and to the Office of Management and Budget, Paperwork Reduction Project (0704-0188), Washington, DC 20503.

1. AGENCY USE ONLY (Leave blank)		2. REPORT DATE 11 June 1999		3. REPORT TYPE AND DATES COVERED Project Report	
4. TITLE AND SUBTITLE  Modeling of UHF and VHF Bistatic Scattering from WSMR Terrain				5. FUNDING NUMBERS  C—F19628-95-C-0002	
6. AUTHOR(S)  Bruce A. Francis					
7. PERFORMING ORGANIZATION NAME(S) AND ADDRESS(ES)  Lincoln Laboratory, MIT 244 Wood Street Lexington, MA 02420-9108				8. PERFORMING ORGANIZATION REPORT NUMBER  MTP-20	
9. SPONSORING/MONITORING AGENCY NAME(S) AND ADDRESS(ES)  Defense Advanced Research Projects Agency/STO 3701 N. Fairfax Drive Arlington, VA 22203				10. SPONSORING/MONITORING AGENCY REPORT NUMBER  ESC-TR-98-056	
11. SUPPLEMENTARY NOTES  None					
12a. DISTRIBUTION/AVAILABILITY STATEMENT  Approved for public release; distribution is unlimited.				12b. DISTRIBUTION CODE	
13. ABSTRACT (Maximum 200 words)  Analysis was performed on bistatic radar data taken at White Sands Missile Range (WSMR) in support of the evaluation of Space-Time Adaptive Processing (STAP) algorithms and the characterization and modeling of monostatic and bistatic scattering. The analysis was confined to data from the flat semi-desert valley floor. Two sets of measurements were made, the first using the ground-based RSTER antenna for reception in combination with ground-based and airborne transmitters. The frequencies were at or near 435 MHz and included VV, VH, HV and HH polarization combinations. The second set of measurements used airborne platforms for both transmitting and receiving and were taken at 141 MHz and 431 MHz for VV, VH and HH polarization combinations. The two sets covered different spans of grazing angles. The data were analyzed to determine the bistatic scattering coefficient of the terrain as a function of out-of-plane angle and grazing angle, and to interpret the results in terms of the Generalized Lambertian Formula.					
14. SUBJECT TERMS White Sands Missile Range WSMR Space-Time Adaptive Processing STAP		bistatic scattering coefficient semi-desert RSTER ground-based airborne		15. NUMBER OF PAGES 184	
		141 MHz 435 MHz multiple polarizations Generalized Lambertian Formula		16. PRICE CODE	
17. SECURITY CLASSIFICATION OF REPORT  Unclassified	18. SECURITY CLASSIFICATION OF THIS PAGE  Unclassified	19. SECURITY CLASSIFICATION OF ABSTRACT  Unclassified	20. LIMITATION OF ABSTRACT  Same as report		